Synthesis and characterization of nanocrystalline UO_2 ceramics

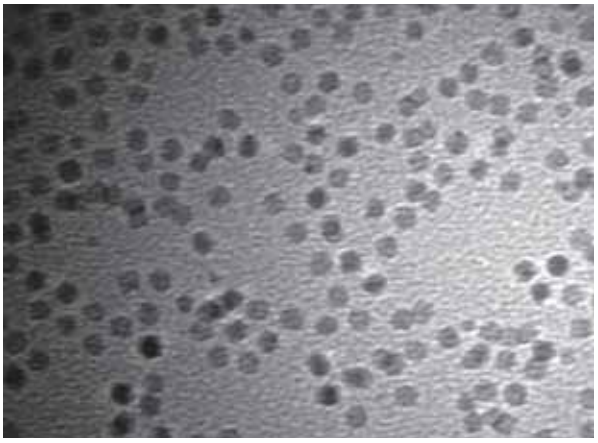
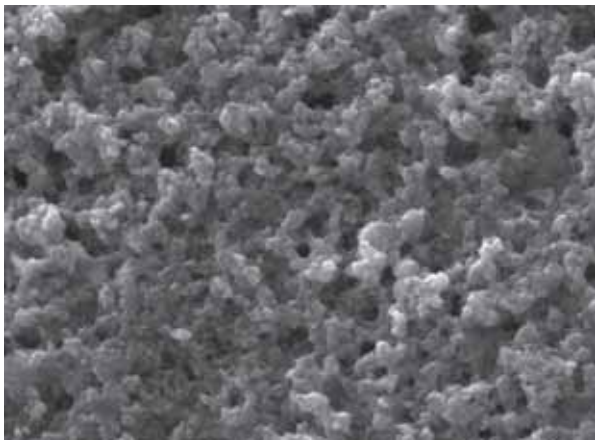

DOCTORAL THESIS

Dissertation by

M.Eng. Raquel Jovani-Abril[1,2]

Directors:

Prof.Dr. Arturo López Quintela[1]
Dr. José Luis Spino[2]

[1] Universidad de Santiago de Compostela (USC), Spain
[2] Institute for Transuranium Elements (ITU), Germany

Santiago de Compostela (Spain), 2014

Memoria de tesis presentada por Raquel Jovani-Abril para la obtención del título de Doctor por la Universidad de Santiago de Compostela dentro del Programa de Doctorado en Ciencia de los Materiales.

Raquel Jovani-Abril

D. Arturo López Quintela, Profesor Doctor Catedrático del Departamento de Química-Física de la Universidad de Santiago de Compostela, y **D. José Luis Spino**, Investigador Doctor Senior del *Institute for Transuranium Elements Joint Research Centre* de la Comisión Europea,

informan:

Que la presente memoria, titulada *"Synthesis and characterization of nanocrystalline UO_2 ceramics"* ("Síntesis y caracterización de cerámicas nanocristalinas de UO_2"), que para optar al título de **Doctor por la Universidad de Santiago de Compostela dentro del Programa de Doctorado en Ciencia de los Materiales** presenta **D$^{\underline{a}}$. Raquel Jovani-Abril**, ha sido realizada en el *Institute for Transuranium Elements Joint Research Centre* de la Comisión Europea en colaboración con el Departamento de Química Física de la Universidad de Santiago de Compostela bajo nuestra dirección.

Considerando que constituye trabajo de Tesis, autorizan su presentación en la Comisión de Tercer Ciclo de la Universidad de Santiago de Compostela.

Y para que así conste, firmamos el presente informe:

Prof.Dr. Arturo López Quintela **Dr. José Luis Spino**

Al fin y al cabo somos lo que hacemos para cambiar lo que somos.
Eduardo Galeano

A Daniel i Jordi

Acknowledgements

The work presented in this study has been carried out in the framework of a European thesis to obtain the degree of Doctor from the University of Santiago de Compostela (USC) and sponsored by the European Commission. This thesis has been enabled by the collaboration and direction of Prof.Dr. Arturo López Quintela from the Department of Physical-Chemistry of the USC, and Dr. José Luis Spino from the Nuclear Fuels Department of the Institute for Transuranium Elements (ITU). I wish to express my gratitude to both of them to take the challenge of the supervision of the thesis and the collaboration in the distance.

I would like to thank the Director of ITU, Prof.Dr. Thomas Fanghänel, for offering me the opportunity to make the research in this renowned institute.

I want to greatly acknowledge Dr. Daniel Baron, Dr. Joaquin Cobos Sabaté, Prof.Dr. Joan de Pablo Ribas, Prof.Dr. Ian Farnan, Prof.Dr. Haas Didier, Dr. Ralph Hania, Dr. Rikard Malmbeck, Prof.Dr. Francisco Rivadulla, Dr. Vicenzo V. Rondinella, Dr. Joseph Somers, Prof.Dr. Carlos Vázquez Vázquez and Dr. Marcus Walter, who accepted without complications to be part of the possible elected members of the jury/revisers for my thesis defence.

I want now to special thank all the colleagues who made that experience possible. I do not use here your title, but your name. Not because I do not want to treat you with the respect you all deserve, but because your title does not say anything about you as a person. It is your name, which represents for me the patience, the love, the time and the laughter we enjoyed together.

First, thank to the Nuclear Fuels Department because, although I was moving around any corner of the institute, this was the unit I was belonging to. I really enjoyed the four years with you.

Thanks to Marc Couland, Herwin Hein and Serge Fourcaudot. You showed me how to move inside this special institute in my first time in ITU as a trainee and later on in the PhD. You opened doors for me which would remain longer closed for a new student. Thanks also for slowly trusting me making your *baby*-experiments. For finishing the preparation of my samples for an urgent project when I needed to fly to Spain without expecting it from one day to the other. Thanks for the office-conversations.

Thanks to Michael Holzhäuser, Co Boshoven, Mairead Murray Farthing, John Mcginley, Sarah Stohr, Patrick Lajarge, Sebastien Gardeur, Antony Guiot, Emmanuel Vermorel, Andrea Cambriani, Alexandre Dockendorf and Annette Küst, who worked in one or other step of the pellet performance. Thank to put your specific experience in this work.

Olivier Pauvert, Chris Selfslag, Ivana Bianchi, Ian Farnan and later Laura Martel, for the patience in the preparation of the NMR samples, the different attempts and posterior interpretation of the results. Marika Vespa for the EXAFS experience in ANKA and Damien Prieur for helping me that much with the interpretation even without knowing us personally. Merci!

Thanks to the electrochemistry group Mathieu Gibilaro, Christophe Nourry, Pavel Souček and Michel Ougier for the experiments together, for the transport of the equipment from one wing to another, from the set-up arrangements. Paul Carbol to borrow me the wing-A fume hood although I was not belonging to his group. Wim de Weerd, Dimitrios Papaioannou and Didier Laux for the SAM tests. Thank to the people working in the Hot Cells Department to allow me to take the cupboard keys each time I was looking for something to set up my experiments. Miriam Weiss, Alfred Morgenstern and Christos Apostolidis for the supply of material for my experiments when I was missing something. Thanks for the strong and warmly *holá* each morning in wing-F.

Eric Colineau and Jean-Christophe Griveau for the first tests to determine magnetic properties of this nc-material. Damien Hudry for our office-discussions late in the evening. Stephen Heathman and Carmen Elena Zvoriste-Walters for the studies about the HP-XRD and nc-UO_2. Special thank to Giorgio Pagliosa, Daniel Bouëxière and Rachel Eloirdi who analyzed and discussed with me no idea how many samples under the XRD and the HT-XRD.

Arne Janssen, Bert Cremer, Hartmut Thiele and Thierry Wiss. I want to thank you for the beautiful TEM/SEM pictures you took from my nanoparticles and from the pellets in all the possible positions always surrounded by the music of Radio Swiss Classic. Markus Ernstberger to teach me about indentation and let me open door to his lab. Sylvain Morel for those first oxygen determination tests. Ondřej Beneš for the time spent with me in the Raman determination. Markus Beilmann to borrow me his glove-box in those last experiments. Darío Manara for the melting point determination tests. Alessandro Zappia and Dragos Staicu for the thermal diffusion determination. Luka Vlahovic for the POLARIS tests. I would like to thank Rudy Konings to let me work with the team and instruments of the Material Research Department although I was not belonging to his unit. Thanks you for the smile that you constantly give.

Asunción Fernández Carretero as my supervisor in my time in ITU as trainee. You were right and in the end (I was not that sure at the beginning) you left me here with a good team of supervisors for the PhD. Roberto Caciuffo to put me in connection with my thesis-Director who for coincidence was also from Spain (but from the opposite side where I am coming from!). I have never imagined I would go to Santiago de Compostela by plane.

I am greatly indebted with der Elektriker, with Fritz, Alfred and all the team of Joachim Küst, who really changed thousand and one things I asked for the set-up of my glove-boxes. Danke, dass ihr immer so schnell und ernst meine Anfragen bearbeitet habt. Danke an die ganze AGS-Gruppe, aber besonders an Rainer Thrun für deine keine Ahnung wie viele Kontrollen. Für deine jeden Tag (das ist überhaupt nicht leicht!) freundliche Art und Weise mit den Menschen umzugehen.

Birgit Christiansen for the effort to get together all the students. Corinne Brossard, Matthias Schulz, Monica Marucci doing easily the not easy task of taking material in and out from ITU. The IT-team but in special to Uemit Zobu, who received the major part of my computer-problem-calls. Klaus Paris und Giovanni von IKFT für das Bauen meines Reaktors.

Many thanks to Krisztina Varga, Petra Strube, Ursula Brettschneider and specially to Anna Matthei-Socha (danke auch für deine vor-Eventmeineslebens-Empfehlungen), Fermín Pérez-Painceiras and Benito Doce, who always immediately resolved any problem I had with the administration work at different stages of the PhD. Muy agradecida!

I wish now to thank all the people with whom I shared this time in a more beautiful and funnier way with excursions, sharing flat, birthdays, meetings at Mühlburger-Tor-Guesthouse, sharing the everyday-forest-bike-journey to ITU, weddings, coffees, bon dia noia com si estigués a Sant Mateu, meals in the canteen, parties in Schlosspark, travels, confidences, advices and friendship distributed now everywhere around the world. Thanks to Cedric Cozzo, Caroline Cozzo, Julie Tondeur, Stefan Maenhout, Simona Nucifora, Matteo Ciucci, Ernesto González Robles, Ernesto Fontana, Gerard Montagnier, Frank de Bruycker, Petronela Gotcu-Freis, Konstantinos Boboridis, Danilo Maddalo, Catherine Ho, Pietro Botazzoli, Rosa Sureda Pastor, Ivana Bianchi, Martin Vargas Zuniga, Joan Horta Domenech, Pedro Amador Celdrán, Ramon Carlos Márquez, Victor Esteban Gran, Ana Isabel Martínez-Ferri, Belén Hurtado, Daniel Serrano Purroy, Eddie López-Honorato, Mathieu Gibilaro, Ondřej Beneš, Carmen García Pérez, Laura Aldave de las Heras, Encarnación Luque Pérez, Mariangela Cardinale, Alfred Jiménez Segarra, Stefanie Kannengiesser, Tomasz Klimczuk, Betül Öztürk, Marco Klipfel, Judit Krajko, Ilaria Marchetti, Peter Pogany, Francesca Quinto, Zeynep Talip, Antonio Garcia Miralles, Joanna Ciezkowska, Robert Böhler, Doroteya Kostadinova, Katalin Bárczi, Octavian Valu Sorin, Michael Welland and Mattia DelGiacco.

Also thanks to the funny people of the course “Science and Technology of Colloids and Interfaces” for the great time discovering together the city of Santiago de Compostela. The climbing club, Ralf Gretter, Arne Janssen, Noreen Lembke, Markus Ernstberger, Sylvain Morel, Markus Beilmann, Stefaan Van Winckel and Philipp Pöml. It was great to learn from you how to “just” trust the person who is down securing you. The Quartier Latin, for the singing evenings even if sometimes we were quite out of tune. Merci to Mark Sierig, Darío Manara, Eglantine Courtois, Ana Sánchez Hernández and specially to Matteo Rini, Alessandro Zappia and Clarita Riva que ya sois como medio de la familia.

To Úrsula Carvajal-Núñez. When you arrived I felt my area invaded. There was no place for two Spanish. But in the end you became the confident of the most of my private worries. Gracias por estar tan loca de venirte hasta España y volverte sin pasar por la Mare de Déu. Para mi es como si hubieses estado allí.

I wish to express my truthful gratitude to Rikard Malmbeck, José Luis Spino and Joseph Somers. It was a great combination because depending on what I needed, I could always ask one or the other for advice. It made me feel I was not belonging to one unit but I was connected to the whole institute. It was a pleasure to speak, discuss

and also argue with you. I have learnt a lot because of the latter.

Thank to Rikard Malmbeck because of everything I learnt from you in the labs. For discussing with me in the afternoon to find solutions for the problems which were appearing at each step. For connecting me to so many people. For having the aptitude to perceive when somebody is not feeling right.

Thank to José Luis Spino because your wonderful source of ideas. For transmitting to me the deep knowledge and passion you have for this novel nano-structure. I tried to defend it in the institute as if the idea was mine. Thanks for the personal friendship we have developed in parallel to this thesis.

Thank to Joseph Somers because you brought clarity and structure to the abstract. Because I took you as referent point when things shifted. Because you told me you would stay there, and it was like that in the end. I am really grateful for your help in the not easy task to conclude the project.

A special thank I want to give to the people who had and has the major influence in the person that today I am.

I want to thank Juan Luis Jovaní Ripoll and Obdulia Abril Ferreres because of the cheerful childhood I had. Because you were there to give me strength in that first important time of my life. Because you worked 25 hours a day to give us the education we have. Because you gave me the values which accompany me everywhere I am. Because the new relationship we are building now together after things have changed that much. Thank to Magdalena Jovaní Ripoll because I know you gave me always, the in-your-own-way best love you had. Thank to Amparo Ripoll Ferrer because even if not being really present in this period of my life, you transmitted me your vigour and the roots, which I grasp when I miss my path. Thank to Ruth Jovaní Abril, because despite of our distance you are the person I know I can always trust. The person, who is always there whatever changes around us.

Finally I want to thank the two most important persons in my today-time, who are responsible for making me continuously think outside the box. Jordi Forchheim-Jovani, thank for your novelty, your each day to day teaching, your smile and laughter, your moment-presence, your energy, your cheerfulness. Because you have given me the present to experience something so precious in my life. Thank to Daniel Forchheim, because you are the one who really supported and encouraged every moment in all this process. The pre, during and after. Thank for your patience and love. It has been astonishing to live so many special moments since we knew each other. Thank to be as cheerful as a child. Thank to be that open to reflect from the difficult situations we had. It is wonderful to grow and grow from all that together. It is really amazing to experience together this deep-revolution in our private-professional-outside-inside-lives.

To all of you who brought me were I am now...

... una abraçada gegant!

Raquel

Abstract

High-performance ceramics with nanosized grains provide today the technical base for a large variety of improved applications in many technologies. This type of microstructure is of special interest as well in the nuclear field as it appears at the periphery of light water reactor (LWR) UO_2 fuels at high burn-up (BU), where the material transforms spontaneously to a closed porous nanocrystalline nc-structure after surpassing a critical dose. The mechanical properties of this newly formed material are superior to those of the fresh fuel due to the nanostructure. Taking this into account, the aim of this work is to develop a fuel consisting of nc-UO_2, which, besides the advantages of enhanced plasticity and faster creep, characteristic of the nc-state, which diminish the pellet clad interaction (PCI) stresses and cladding failure risks, has also the potentiality to develop closed porosity under irradiation, to largely retain fission gases. The study of its behaviour is therefore important, especially during accident conditions under which large amounts of radioactive fission products could be released into the reactor vessel, or to the exterior if the core containment breaks. Its potentiality for retention of fission gas and its improved mechanical properties and resistance to radiation-damage make so the nc-fuel material worthy of deep experimental analysis.

Resumen

Origen del estudio

Hoy en día los combustibles nucleares están hechos en gran medida de dióxido de uranio (UO_2). Se ha alcanzado ya un alto nivel de competencia en este tipo de tecnología con combustibles desde medio hasta alto grado de combustión en el reactor. Sin embargo, se necesitaría un enfoque más radical para alcanzar grados de combustión (BU; *burn-up*) más elevados reduciendo así la cantidad de combustible fresco inicial necesario y por tanto la cantidad de combustible usado (residuos radiactivos). Para ello se requiere una mejora en la capacidad del combustible para retener los gases de fisión, así como una solución para la interacción mecánica y química (PCMI y PCCI; *pellet clad mechanical and chemical interaction*) con el revestimiento de la varilla que contiene las pastillas de combustible. El riesgo de fallo de este revestimiento podría intensificarse a altos grados de combustión debido al incremento de fragilidad del mismo. Así pues, se puso un proyecto en desarrollo con el objetivo de sintetizar polvo nanocristalino (nc)-UO_2 para la fabricación de pastillas (monolitos) de nc-combustible y posterior caracterización de sus propiedades mecánicas fuera de pila, así como su comportamiento bajo irradiación.

El origen de la idea que empujó este estudio se encuentra en minuciosas observaciones previas de la transformación que sufren los combustibles nucleares altamente irradiados. La pastilla de combustible dentro del reactor nuclear es un material sometido a condiciones extremas que van cambiando sus propiedades con el tiempo y la dosis de irradiación. Aparecen daños y defectos locales como intersticiales, bucles y vacantes. Además, la acumulación de productos sólidos de fisión en el parámetro de red, así como la formación de burbujas de gas, disminuyen aún más las propiedades térmicas de la pastilla de combustible. La aparición de grietas en la pastilla debido a las tensiones térmicas sucede desde el primer momento en que se inicia la irradiación. Asimismo se produce un hinchamiento de las pastillas de combustible debido a la acumulación de las burbujas de gas de fisión que se forman en la matriz y de la segregación de productos de fisión de baja densidad (precipitados metálicos y cerámicos). El material combustible se aproxima al revestimiento de la varilla que lo contiene como resultado de este hinchamiento. La interacción física y/o química por contacto con el revestimiento puede inducir el deterioro del revestimiento y su ruptura [Garzarolli et al., 1979]. Este tipo de cambios pueden afectar también el perfil de temperatura de la pastilla de combustible por modificación de las condiciones de transferencia térmica en el espacio entre el combustible y el revestimiento, limitando también el tiempo de vida del combustible (y el grado de combustión o BU) en el interior del reactor en el caso que se produjese una ruptura prematura de la varilla.

El combustible nuclear sufre una transformación en su estructura tras el daño acumulado una vez alcanzado el tercer ciclo de irradiación (alrededor de 40 GWd/tM).

Esta transformación comienza en el borde de la pastilla del combustible y de manera constante progresa hacia el interior mientras se sucede la irradiación [Matzke and Spino, 1997] [Spino and Papaioannou, 2000]. La microestructura original de micro- granos (o granos-grandes) se transforma en una matriz nc-porosa [Nogita and Une, 1994] a través de la reestructuración de los defectos de irradiación acumulados. Se trata de un tipo de acción de "auto-curación", donde el material se cura del daño sufrido reordenándose a sí mismo [Spino et al., 2012]. La nueva nc-estructura que aparece entonces, recibe el nombre de estructura de alto grado de combustión (HBS; *high burn-up structure*), también llamada estructura de borde (rim-structure) porque en los combustibles de UO_2 ésta se inicia en el borde o en las zonas exteriores de las pastillas (región que recibe mayor cantidad de fisiones).

En un principio se pensó que la HBS era la causa de los fallos que observados en el revestimiento de las varillas debido a aumento adicional del volumen (hinchazón) en pila y un supuesto comportamiento frágil del material así transformado [Matzke, 1992]. Además se creyó que esta estructura que aparece en el borde de la pastilla podría actuar como una nueva fuente de liberación de gas. De hecho todavía hay líneas de investigación que defienden esta opinión. Sin embargo, otros estudios han demostrado que el porcentaje de gas liberado desde el borde de las pastillas de combustible, donde aparece la HBS, es bajo en comparación con el gas que viene de las partes internas de la pastilla donde la estructura original todavía está presente [Mogensen et al., 1999]. A esta segunda filosofía le han seguido otras publicaciones que demuestran un evolución en general favorable de las propiedades del combustible con la aparición de esta nueva estructura a altos valores de combustión, en particular el aumento en la retención de los gases de fisión.

Asímismo, las propiedades de la HBS indican una mayor tolerancia a la radiación [Spino et al., 2012]. Este estudio coincide con una evidencia importante e innovadora en la literatura que demuestra que los materiales de granos nano resisten más el daño por radiación que los correspondientes materiales de grano micro, debido a la recombinación de defectos en los múltiples límites de grano [Nita et al., 2005]. Se anticipan también otras tendencias en el material como la mejora de la conductividad térmica y otros efectos de la radiación en las propiedades del material debido a la liberación de estrés en el parámetro de red después de la recristalización [Ronchi et al., 2004], así como el aumento de la tenacidad a la fractura y curación de grietas [Spino et al., 2003].

En lo que concierne a la seguridad, los últimos experimentos realizados en combustibles sometidos a alto grado de combustión en reactores nucleares de agua ligera (LWR; *light water reactor*), no indicaron aumento en la liberación de gas, así como tampoco en la susceptibilidad de fallo durante accidentes de reactividad iniciados (RIA; *reactivity initiated accident*) transitorios [Sasajima et al., 2010] [Fuketa et al., 2006]. También ha sido observada una disminución de la velocidad de corrosión acuosa bajo condiciones típicas de depósito geológico simuladas en combustibles con presencia de HBS [Ekeroth et al., 2009] [Carbol et al., 2009]. Ambos hechos confirmaron la estanqueidad de esta estructura.

Así pues, se ha demostrado que la HBS tiene cualidades excepcionales incluso en comparación con la matriz original (estructura de grano-grande), con una mejora de propiedades que serían muy ventajosas para un combustible. Entonces, ¿por qué no imitar este material recristalizado?. ¿Por qué no imitar esta estructura (HBS) que

aparece en el borde del combustible a altos grados de combustión y se introduce en esta forma como un combustible nuevo en el interior del reactor?. ¿Por qué no sintetizar una matriz de combustible mimetizando la HBS que debido a su aparente resiliencia al daño resistiría tiempos más largos bajo irradiación?.

Aquí es cuando empieza el desarrollo de este proyecto con el objetivo de sintetizar polvo nanocristalino (nc)-UO_2 para la fabricación de pastillas (monolitos) de nc-combustible. Las piezas monolíticas fabricadas a partir de este polvo, tendrían un volumen de aproximadamente 1 cm^3 y una matriz uniforme de granos de un tamaño entre 100 y 250 nm imitando la estructura que aparece a altos grados de combustión (HBS; *high burn-up structure*). Durante este trabajo se consiguió la creación de esta nueva microestructura de combustible pasando por distintas fases. Desde la síntesis del nc-material, a la fabricación de la pastilla de combustible, distintas etapas de este proceso, previamente desconocido o inexplorado, tuvieron que ser especialmente desarrolladas y/u optimizadas.

Síntesis de nc-UO_2 y nc-ThO_2

Un trabajo considerable fue dedicado al desarrollo del polvo inicial para la producción de los monolitos o pastillas de nc-UO_2 imitando la HBS que aparece en los combustibles de los LWR. Dos vías de síntesis química diferentes fueron estudiadas para obtener precipitados defloculados de nc-UO_2 y nc-ThO_2 como compensación a la falta de disponibilidad comercial. El ThO_2 tiene una estructura similar al UO_2 pero tiene, a su vez como ventaja, una sola valencia (IV). Para conseguir obtener mayores cantidades de nc-UO_2 que las publicadas en literatura, y proporcionar así material suficiente para la fabricación de los monolitos, ambos métodos fueron convenientemente ajustados, desarrollados y escalados de acuerdo a las necesidades. El material así producido fue objeto de estudio mediante microscopio electrónico de transmisión (TEM) y difracción de rayos X (XRD).

El primer método desarrollado fue una precipitación controlada que utiliza una disolución acuosa electrolíticamente reducida de nitrato de uranilo como precursor y una solución goteada de NaOH como agente de alcalinización para desencadenar la precipitación del nc-material lo más próximamente posible a la línea de solubilidad del U^{IV}. Este método fue originalmente descrito por [Rousseau et al., 2002], [Rousseau et al., 2006]. Un estudio intensivo de los rango de concentración de U y acidez en los que se produce la precipitación de nc-UO_{2+x} fue llevado a cabo. Se utilizaron para ello disoluciones de nitrato de uranilo electrolíticamente reducidas, usando U-concentraciones más elevadas (10^{-1} M) que las observadas en literatura (10^{-2} M) [Rousseau et al., 2006], y por tanto intervalos de pH de trabajo más bajos, siempre siguiendo la línea de solubilidad del U^{IV}. Como resultado se obtuvieron hasta 10 g de nc-UO_{2+x} por experimento, en lugar de los pocos nanogramos publicados hasta ahora en literatura. La fase sólida así obtenida y estudiada bajo XRD, cristalizó bajo la típica estructura de fluorita UO_2-*fcc* (grupo espacial *Fm-3m*), con un parámetro de red a=0.5417(1) nm y un tamaño de cristal promedio de 3.79 nm, también en concordancia con el tamaño medio observado por TEM de 3.9(8) nm. El difractograma predominante de las muestras correspondía inequívocamente a UO_2 pero en un estado ligeramente oxidado. Esto último se manifestó a través de una contracción del parámetro de red de aproximadamente 0.9% de la fase precipitada (a=0.5417(1) nm) con respecto a los

valores típicos de UO_2 estequiométrico (a=0.547 nm).

El segundo método estudiado fue una descomposición térmica en fase orgánica usando acetilacetonato de uranilo (UAA) como precursor. Éste se añade a una mezcla de ácido oleico y oleilamina calentándose a continuación hasta temperaturas por encima de los 300°C para inducir la precipitación de las nanopartículas de UO_2 por descomposición térmica del UAA. Este procedimiento fue descrito originalmente por [Wu et al., 2006] y fue aquí modificado para reducir la cantidad de agentes tensoactivos respecto al porcentaje de metal utilizado. AsÌ mismo, se escalaron los 0.1 g de nc-UO_2 por experimento obtenidos según lo publicado por [Wu et al., 2006], a 2.3 g de nc-UO_2 por experimento en el presente trabajo. El mismo método fué extrapolado para la síntesis de nc-ThO_2, utilizando acetilacetonato de torio (ThAA) o acetato de torio (ThA) como precursores, obteniéndose finalmente nano-varillas de ThO_2. La razón por la cual se obtuvieron precipitados en forma de varilla, en vez de la forma esférica obtenida para nc-UO_2, es todavía desconocida en este estudio. El rendimiento por experimento (0.3 g nano-varillas de ThO_2) fue más bajo que en la síntesis de nc-UO_2 por el mismo método. Tanto en la síntesis de nc-UO_2 como en la de ThO_2 bajo este método, se probaron diferentes condiciones de trabajo: velocidad de calentamiento, tiempo de envejecimiento de la disolución final, temperatura de envejecimiento, así como distintos precursores iniciales (ThAA y ThA) en la síntesis de nc-ThO_2. No obstante, se encontraron siempre resultados similares en términos de estructura y geometría (esféricas para nc-UO_2 y en forma de varilla para nc-ThO_2) de los precipitados. En el estudio bajo el XRD se determinó una fase sólida perfectamente cristalizada con la típica estructura de fluorita UO_2-*fcc* (grupo espacial *Fm-3m*), un tamaño de cristal promedio (diámetro de la esfera) de 5.52 nm y un parámetro de red de 0.5431(0) nm, también en concordancia con el tamaño promedio observado con el TEM de (4.9(3) nm) y por dispersión dinámica de luz (DLS) de (3.7(1) nm). En las nano-varillas de ThO_2, se encontró una estructura típica de fluorita (grupo espacial *Fm-3m*) ThO_2-*fcc*, con un tamaño de cristalito (diámetro varilla) de 1.42 nm y un parámetro de red de 0.5579(1) nm. No se observó agregación de partículas en las imágenes de TEM del material sintetizado por ambos métodos.

Cristalización y crecimiento de grano en f(T) del nc-UO_2

La composición de los precipitados obtenidos por ambos métodos arriba mencionados y su propensión a la expansión térmica en el estado no consolidado, se estudiaron en el material así sinterizado y recocido a diferentes temperaturas. Para ello se utilizaron técnicas de análisis térmico y de difracción de rayos X, como el análisis termogravimétrico y el análisis térmico diferencial (TGA/DTA), difracción de rayos X (XRD) y difracción de rayos X a alta temperatura (HT-XRD), técnicas espectroscópicas tales como la espectroscopía de absorción de rayos X (XAS), espectroscopía de resonancia magnética nuclear (MAS-NMR), espectroscopía infrarroja (IR), y técnicas de caracterización como la microscopía electrónica de transmisión (TEM).

La evolución del tamaño de los cristales, el parámetro de red y la tensión de red se determinaron para el material así sintetizado y a distintas temperaturas de recocido del material (bajo atmósfera inerte) hasta 1200°C. Para el caso del material nc-UO_2

precipitado en fase acuosa se observó tan sólo un pequeño aumento en el tamaño de los cristales, permaneciendo éstos por debajo de los 7 nm hasta llegar a la temperatura de recocido de 700°C. A partir de esta temperatura, el tamaño de los cristales creció acusadamente y de manera constante con la temperatura, hasta alcanzar un valor de 73 nm a 1200°C. Por el contrario, el incremento mayor del parámetro de red se observó en el intervalo más bajo de temperatura 20°C-700°C. En el intervalo 700°C-1200°C sólo se observó un pequeño aumento en el parámetro de red coincidiendo con la expansión térmica reversible típica del UO_2. Hay que añadir que en la mediciones del parámetro de red a temperatura ambiente y después del tratamiento a temperatura bajo atmósfera estática de He, se observó una recuperación de la estructura típica cristalina del UO_2, pasando del valor de parámetro de red inicial de 0.5417 nm para el nc- UO_2 así sintetizado, a un valor de 0.5473 nm después de la exposición a 1200°C. La contracción del parámetro de red inicialmente medida para el material nc-UO_2 así sintetizado por debajo del valor normal típico para UO_2 (a=0.5470 nm) se atribuyó principalmente a oxidación.

En el caso del nc-UO_2 precipitado por el método en fase orgánica, se observó un comportamiento similar en el crecimiento de las partículas con la temperatura, sin apenas cambio en el tamaño de cristal hasta una temperatura de 700°C (debido al pre-tratamiento a temperatura aplicado), seguido de un crecimiento intenso del tamaño de cristal hasta obtener un tamaño de 150 nm a 1100°C. Se determinó una oxidación inicial de las partículas sintetizadas bajo el método en fase orgánica derivada de los valores de parámetro de red, aunque menos acusada que en las partículas sintetizadas en fase acuosa. Las partículas recobraron el valor típico de parámetro de red para UO_2 a temperaturas de recocido por encima de los 750°C.

En cuanto al parámetro de estrés de red, un comportamiento similar fue también observado para las partículas obtenidas por ambos métodos. La observación principal en ambos casos fue la disminución continua del parámetro de estrés con la temperatura, hasta extinguirse prácticamente a la temperatura en que los cristales empezaron a crecer. Esto confirmaba que la presencia del parámetro de estrés de red actuó en ambos casos como inhibidor del crecimiento cristalino.

Estudio de la estructura y estequiometría del oxígeno mediante XRD, XANES, EXAFS, NMR AND FTIR

La estructura del material nc-UO_2 producido en función de la temperatura pero en este caso bajo atmósfera reductora, se estudió también bajo el XRD y se comparó con el material de referencia $U^{IV}O_2$-grano-grande (granos de tamaño micrométrico). Se midió el parámetro de red del material tras enfriarse después de alcanzar diferentes temperaturas máximas (600°C y 1200°C). Esto permitió la separación de la contribución de la expansión térmica en los valores medidos a temperatura para obtener curvas más limpias de expansión térmica frente a temperatura, y parámetro de red frente a tamaño de cristal. No se encontraron grandes diferencias en el tamaño de cristal, parámetro de red y tensión, entre las mediciones realizadas bajo atmósfera inerte (arriba comentado) y bajo atmósfera reductora (medición realizada tras el enfriamiento) para el material obtenido por el método acuoso. Sin embargo. se observó un cambio notable en el tamaño de los cristales para el material obtenido por el método orgánico al llegar a

temperaturas de recocido de 1100°C bajo atmósfera de He con una talla de cristal de 150 nm, y un tamaño de tan sólo de 12 nm bajo atmósfera de $Ar/5\%H_2$. Comparando el material nc-UO_2 obtenido por ambos métodos, acuoso y orgánico, bajo atmósfera reductora ($Ar/5\%H_2$) y sin ningún otro tratamiento térmico previo del polvo, no se detectaron grandes cambios hasta la temperatura de recocido de 600°C. Pero sí se observaron a la temperatura de 1200°C, obteniendo un tamaño de 82 nm para el material del método acuoso frente a 12 nm para el material del método orgánico. Esto podría ser atribuido a la capa orgánica protectora presente para estas últimas nanopartículas.

Junto al estudio de XRD se llevó a cabo un estudio de XANES para determinar el estado de oxidación de los cationes de U, las fracciones molares correspondientes y la relación de O/U derivada. Los espectros de XANES en el borde U-L_3 mostraron tendencias similares para el nc-UO_2 sintetizado por ambos métodos (acuoso y orgánico): reducción de la estequiometría (x) del UO_{2+x}, al aumentar la temperatura de tratamiento. Se estudiaron muestras de nc-UO_2 así sintetizado y después del tratamiento térmico a 600°C y 1200°C en atmósfera de $Ar/5\%H_2$ y se compararon con el material de referencia $U^{IV}O_2$ (grano-grande), detectándose con la temperatura un ligero desplazamiento del pico de la WL (white line) hacia energías más bajas, así como un aumento de la intensidad y de las oscilaciones en las regiones de XANES. La amplitud de estas oscilaciones disminuyó con el aumento de la temperatura de tratamiento térmico mostrando un mayor orden de la estructura para las muestras recocidas.

Este efecto podría deberse al pequeño tamaño de los cristales del material nc-UO_2 o al simple desplazamiento de la estequiometría del material así producido respecto al material de referencia $U^{IV}O_2$ (grano-grande). Para cuantificar la contribución del tamaño del cristal a este efecto sería necesario un estudio con nc-UO_2 de distintos tamaños de cristal y una estequiometría de oxígeno fija (a ser posible la característica del UO_2 de referencia). Dado que en el momento de realización del estudio esta síntesis selectiva de nc-UO_2 no fue posible, un estudio alternativo para determinar el efecto de la talla del cristal en la estequiometría fue llevado a cabo. Para ello se utilizó un substituto como es el oxido de torio (ThO_2) que cristaliza con la misma estructura de fluorita que el UO_2 y que posee además un único estado de valencia (catión) Th^{IV}.

Se llevo a cabo un estudio de una muestra de nc-ThO_2 así producido (no tratado térmicamente). En los espectros XANES correspondientes al borde Th-L_3, el pico de la WL correspondiente al nc-ThO_2 así sintetizado, se encontró en una posición y amplitud idénticas a las de los espectros del $Th^{IV}O_2$ (grano-grande) de referencia. Tan sólo se detectó una ligera disminución en la intensidad y número de oscilaciones, indicando solo un efecto débil en las distancias interatómicas y el orden reflejado en el espectro de XANES debido a la talla del cristal del material nc-ThO_2. Este prácticamente idéntico comportamiento del material de referencia $Th^{IV}O_2$ (grano-grande) y el nc-ThO_2, sugiere que los desplazamientos observados anteriormente para el material de nc-UO_2 tendrían su origen, no al tamaño de partícula sino más bien al desplazamiento de la valencia-catión hacia un estado más oxidado (U^{VI}) del material así sintetizado. Teniendo esto en cuenta, la determinación de la O/M de nc-UO_2 a partir de la técnica de XANES estaría justificada.

En los espectros de EXAFS k^3-ponderado para el material nc-UO_2 sintetizado por

el método acuoso, las oscilaciones y su amplitud aumentaron con la temperatura de recocido y el creciente tamaño de los cristales, aproximándose gradualmente al espectro típico para la estructura del UO_2 (*fcc*). El material nc-UO_2 así precipitado de 4 nm resultó difícil de ajustar a la estructura de fluorita pura. Los ajustes no eran estables y los datos tenían mucho ruido. La muestra recocida a 600°C y tamaño de cristal de 9 nm mostró un ordenamiento intermedio con oscilaciones claramente identificables. Tanto la muestra original así sintetizada de 4 nm como la muestra recocida a 600°C (9 nm) mostraron claramente distancias de enlace U-O y O-O más cortas en comparación con la referencia de $U^{IV}O_2$-(grano-grande). Esto resultó compatible con los estudios de XRD que mostraron una considerable contracción del parámetro de red para la muestra así sintetizada de 4 nm, siendo ésta menor con la temperatura de recocido. En última instancia, para la temperatura de recocido de 1200°C y un tamaño de cristal de 82 nm, las oscilaciones de EXAFS fueron similares, si no coincidieron totalmente con las del material de referencia $U^{IV}O_2$, indicando misma estructura-*fcc* (*Fm-3m*) y mismas distancias interatómicas. Esto concordó con la similar estructura mostrada en XRD entre la muestra de nc-UO_2 recocida a 1200°C y la referencia de $U^{IV}O_2$-(grano-grande). También resultó coherente con el estudio de XANES que no mostró prácticamente ninguna diferencia respecto a la estructura típica de fluorita para el caso de la muestra nc-UO_2 recocida a 1200°C. Los resultados de los espectros de EXAFS de k^3-ponderada para el material nc-UO_2 de origen orgánico, fueron distintos a los arriba comentados para el material nc-UO_2 de origen acuoso, siendo no sólo el material de 5 nm nc-UO_2 así precipitado difícil de ajustar a la estructura de fluorita pura, sino también las muestras tratadas a 600°C y 1200°C. Todas las muestras presentaron un alto grado de desorden y no se pudieron ajustar al material de referencia $U^{IV}O_2$-(grano-grande), por lo que debería tenerse en cuenta otra fase todavía aquí no identificada.

Se adquirieron espectros de NMR Hahn-echo ^{17}O MAS de muestras tratadas a distintas temperaturas de recocido en atmósfera reductora ($Ar/5\%H_2$). Se identificaron tres tipos diferentes de oxígeno a partir del ajuste del desplazamiento químico de los registros obtenidos para estas muestras, es decir, del desplazamiento del pico ^{17}O de frecuencia de resonancia respecto al del espécimen de referencia y expresado en unidades relativas (ppm). En el presente estudio se tomo como referencia la resonancia del ^{17}O de una muestra de H_2O dopada con ^{17}O y se definió como 0 ppm. La primera identificación correspondió a especies de oxígeno con un desplazamiento químico de casi 900 ppm para las muestras recocidas hasta una temperatura 650°C. Los otros dos tipos de especies de oxígeno identificados aparecieron claramente en el rango de temperatura entre 650°C y 1200°C. Estas especies mostraron una un pico agudo y la otra un pico ^{17}O amplio. Éstos podrían atribuirse a un ^{17}O en un entorno más bien cristalino y en otro entorno más desordenado (debido a la amplitud del pico), respectivamente. Ambos picos disminuyeron fuertemente su desplazamiento químico y su anchura a media altura (FWHM; *Full Width at Half Maximum*) en el intervalo de temperatura de 650°C a 800°C, para converger rápidamente a temperaturas por encima de 800°C a valores cercanos a los de la muestra recocida a 1200°C con 717 ppm (desplazamiento químico) y 5 ppm (FWHM), respectivamente. Este pequeño valor de FWHM es sinónimo de un entorno bien cristalizado, aunque sigue siendo ligeramente más ancho que los 3 ppm encontrados para el $U^{IV}O_2$-(grano-grande) de referencia. A pesar de ello, el desplazamiento químico (717 ppm) fue el mismo que el encontrado para dicha referencia $U^{IV}O_2$-(grano-grande). Puede decirse entonces que el entorno, para la muestra con el cristal de mayor tamaño (∼80 nm), de las posiciones del parámetro de red del oxígeno, está muy próximo al medido para la muestra de referencia

$U^{IV}O_2$-(grano-grande). Basándose en la FWHM puede decirse que para que la señal de UO_2-cristalino sea observable, es necesario llegar a un tamaño de cristal por encima de los 80 nm. Esto estaría en consonancia con la observación hecha mediante XRD para este tamaño de cristal de una estructura UO_2-fcc con parámetro de red 0.5472 nm.

Varias muestras de material nc-UO_2 sintetizadas por el método acuoso y tratadas a distintas temperaturas-clave de recocido, fueron analizadas bajo el espectrómetro de FTIR. Se observaron hasta 4 picos en el intervalo 400-4000 cm^{-1} para la muestra de nc-UO_2 así sintetizada (RT). Estos podrían asignarse a la vibración bending (o de tijereteo) del H-O-H del agua coordinada, y a un posible estado más oxidado del material (UO_{2+x}). Todos los picos disminuyeron en intensidad con la temperatura de recocido de las muestras. Además, para la muestra tratada a la temperatura de recocido de 1200°C, el espectro de IR se asemejaba al espectro de la muestra de referencia de $U^{IV}O_2$. Esto concuerda con los resultados de XANES arriba comentados donde se observó una estructura electrónica diferente para la muestra tratada a 600°C, mientras que la muestra tratada a una temperatura de 1200°C presentó una estructura similar a la de la muestra de referencia de $U^{IV}O_2$. También los resultados del EXAFS se caracterizaron por un orden pobre a 600°C, pero pares de oscilación totalmente ajustados a los de la muestra de referencia de $U^{IV}O_2$ para la muestra tratada a 1200°C.

Se llevo a cabo un estudio isotérmico para el material nc-UO_2 sintetizado, del crecimiento de grano durante periodos de tiempo largos y bajo el HT-XRD. Para las temperaturas de recocido de 500°C, 700°C y 900°C, bajo atmósfera estática e inerte de He, el crecimiento de grano se produjo en las primeras horas de tratamiento a temperatura constante alcanzando un tamaño de cristal promedio estable a dicha temperatura (el crecimiento de grano cesó a partir de ese momento). En el caso de la isoterma a 1200°C y bajo atmósfera estática de He, el material presentó un crecimiento continuo sin llegar a alcanzar un tamaño constante de grano en las primeras 50 h. Se obtuvo una energía de activación de la difusión entre 0.93 eV a 1.25 eV. Estos pequeños valores de energía de activación obtenidos, podrían deberse principalmente a los límites de difusión de grano (superficie e interfaz).

Se midió un parámetro de red de 0.5472 nm para las muestras tratadas durante 50 h a 900°C bajo atmósfera de Ar/H_2 (y tras el enfriamiento del material), obteniendo una talla final de cristal de unos 50 nm. Es por ello que, en principio no sería necesario alcanzar una temperatura de 1200°C (y por tanto una talla de cristal de 80 nm) para conseguir un material con el típico valor de parámetro de red del UO_2 de granos grandes (a=0.5472 nm), como se había comentado más arriba.

Además, un tamaño medio de cristal de 322 nm fue medido a 1200°C durante 50 h en atmósfera estática de He. Teniendo esto en cuenta, durante el proceso de sinterización de los monolitos sería necesaria una temperatura por debajo de 1200°C para evitar el crecimiento extremo de las partículas (>200 nm). Sin embargo, se midió un tamaño final de cristal de 85 nm para las muestras de nc-UO_2 recocidas a 1200°C durante 50 h bajo atmósfera reductora de Ar/H_2. Incluso después de 200 h a esta temperatura en condiciones reductoras, se midió un tamaño final de cristal de 150 nm (bastante menor que el valor de 322 nm observado bajo atmósfera de He y 50 h de tratamiento). Esta diferencia podría deberse al estado inicial de oxidación de las muestras así sintetizadas de nc-UO_2 y su evolución bajo atmósfera estática e inerte de He. Un UO_2 sobreestequiométrico presentaría un aumento mayor de los coeficientes

de auto-difusión y del flujo de masa, incrementando así el movimiento en el límite de grano (o cristal) y crecimiento del grano. De hecho las diferencias entre el coeficiente de difusión del UO_2 de granos grandes y el nc-UO_2, son compatibles con una mejora de los procesos difusión, ya sea por efecto del tamaño de grano o por el ratio O/U>2.

Consolidación y caracterización de monolitos de nc-UO_2

Se probaron diferentes rutas alternativas para la consolidación de los monolitos (ej. prensado convencional uniaxial, float packing, etc). Las pastillas así prensadas, fueron sinterizadas a temperaturas entre 900°C y 1200°C bajo atmósfera de Ar/H_2. Las condiciones óptimas de sinterización se dedujeron a partir del estudio de crecimiento de cristal isotermo durante largos periodos de tiempo bajo atmósferas de He y de Ar/H_2. Esto evitó el riesgo de un crecimiento de grano desproporcionado incluso a la temperatura más alta estudiada de 1200°C. En algunos casos se practicó también un pre-tratamiento térmico del polvo de nc-UO_2 para evitar la formación de grietas durante la etapa de sinterización debido a la presencia de agua o compuestos orgánicos en el material dependiendo de la síntesis utilizada. Las pastillas sinterizadas presentaron una apariencia fuerte aunque se podían observar grietas finas en algunas de ellas. Se obtuvieron densidades de sinterización entre 75.5-90.5% de la densidad teórica (TD_{UO_2}=10.96 g/cm^3). Se obtuvo un tamaño de grano promedio de ∼200 nm, replicando la estructura que aparece a altos grados de combustión (HBS; *high burn-up structure*) para los diferentes tipos de monolitos de nc-UO_2 sinterizados.

También se llevaron a cabo experimentos de dilatometría donde se comparó la contracción entre la pastilla fabricada con material de nc-UO_2, con la pastilla fabricada con el típico UO_2-(grano-grande) y a partir del proceso estándar de fabricación. Se observaron mejores actividades de sinterización a temperaturas inferiores para el material nanocristalino en comparación con las medidas para las pastillas de UO_2-(grano-grande). El rango de temperatura desde el inicio hasta la completa densificación, ocurrió a temperaturas mucho más bajas para las pastillas de nc-UO_2 (200-955°C, con un ratio máximo de sinterización a 740°C), en comparación con las pastillas de UO_2-(grano-grande) [Lahiri et al., 2006] (900-1540°C, con un máximo de sinterización a 1200°C). Esto podría deberse a la mayor superficie presente en el material de nc-UO_2 comparado con el típico UO_2-(grano-grande), lo que llevaría a una sinterización más efectiva (a temperaturas más bajas). Se encontró una energía de activación de la sinterización de $Q = 171 \pm 7\ kJ/mol$ asumiendo difusión de superficie, y $Q = 114 \pm 5\ kJ/mol$ asumiendo difusión de volumen para el monolito de nc-UO_2. La energía de activación determinada para un monolito de UO_2 de grano grande es de $Q = 287\ kJ/mol$ según [Lahiri et al., 2006]. Ambos mecanismos de difusión mostraron pues valores bajos para las energías de activación de sinterización como es típico para los nano-materiales. Esto se traduce en una clara ventaja tecnológica en la fabricación de monolitos de nc-UO_2 debido a su alta capacidad de densificación a temperaturas bajas. El mantenimiento de un rango de temperaturas aceptablemente bajo durante el proceso de sinterización disminuirá costos y simplificará la tecnología de fabricación. Los monolitos de nc-UO_2 ofrecen también la posibilidad de ajustar el tamaño de grano a voluntad mediante la variación de las temperaturas y tiempos de sinterización.

Las macroestructuras de los distintos monolitos de nc-UO_2 se caracterizaron por microscopía óptica (OM). Las microestructuras se caracterizaron por observación de la fractura-fresca a distintas ampliaciones bajo el SEM. En las imágenes de SEM de la fractura-fresca de las pastillas sinterizadas a la temperatura más baja de 900°C, se observaron granos no del todo definidos. La sinterización de los cristales parecía todavía en fase de desarrollo, por lo que a partir de este momento se utilizaron temperaturas de sinterización de 1200°C. Se observaron macro-fisuras en algunas de las pastillas, pero no para los monolitos fabricados con nc-UO_2 sintetizado por el método orgánico con polvo con pre-tratamiento térmico, y tampoco para la muestra del método de consolidación float-packing y polvo sintetizado por el método acuoso. Todas las macroestructuras, con excepción de esta última, mostraron densificación no homogénea (porosidad residual entre las zonas densificadas). También la muestra con prensado convencional de polvo nc-UO_2 pre-deshidratado sintetizado por el método acuoso, mostró una buena calidad en comparación con el resto, desde el punto de vista de la densificación. Sin embargo, es necesario la introducción de mejoras en la formación de los monolitos para evitar el problema de las grietas durante el sinterizado (y por lo tanto disminución de las propiedades del material). En cuanto a la microestructura de la superficie de fractura-fresca, la pastilla de nc-UO_2 sintetizado por el método acuoso y fabricada por consolidación float-packing y sinterización a 1200°C, fue la aproximación más cercana al material HBS obtenido hasta ahora. El tamaño medio de grano para los diferentes monolitos estuvo entre 170 nm y 250 nm. Esto fue un de los grandes logros de este trabajo.

Propiedades mecánicas como la dureza Vickers (H_V), dureza Knoop (H_K) y módulo de Young (E) se determinaron para las pastillas de nc-UO_2 sinterizadas. Un aumento en la dureza (H_V) y valores bajos para módulo-E (de hasta un 30%) fueron en general observados para los diferentes monolitos de nc-UO_2 en comparación con aquellos de UO_2-(grano-grande). También se utilizó microscopía de barrido acústico (SAM) para la estimación y la comparación del módulo de Young obtenido por identación. Los resultados obtenidos por SAM (E=155 GPa) coincidieron con los derivados por micro-indentación (E=155 GPa). La diferencia observada con respecto a pastillas de grano-grande de UO_2 (220 GPa), podría estar influenciada por las imperfecciones de la microestructura (nano-cavidades en las intersecciones de tres granos, poros, grietas, etc.). Sin embargo, esta caída del módulo es todavía demasiado grande como para ser totalmente atribuida a la presencia de cavidades. El mismo tipo de tendencia observado en las muestras de nc-UO_2, es decir, aumento de los valores de H_V y disminución de los valores del módulo-E, ya se había determinado antes en el combustible estándar de UO_2 tras haber alcanzado valores elevados de BU. En este caso la disminución del módulo-E tampoco pudo ser totalmente atribuída a un aumento de la porosidad, y contradijo el efecto de la disolución de los productos de fisión que provoca en realidad un aumento de la rigidez del material. Dado que los combustibles nucleares irradiados se transforman en una estructura nano-recristalizada con el aumento de BUs [Spino et al., 2012], los efectos (parcial) del aumento de H_V (la disolución de los productos de fisión provocan también endurecimiento) y además la disminución del módulo-E (sumado al causado por la porosidad), al igual que los efectos observados en el presente trabajo, podrían atribuirse a la nano-estructura de los combustibles sometidos a elevados BUs.

Se confirmó con éxito la dependencia con el tamaño del cristal, de las propiedades físico-químicas del nc-UO_2. Así, se comprobó que la compresibilidad del nc-UO_2 era

de hecho mayor que la del estándar-UO_2 de tamaño grande. Se confirmó también una dependencia de las propiedades de expansión térmica con el tamaño del cristal para el material de nc-UO_2. La expansión térmica aumentó con la disminución del tamaño de cristal, al mismo tiempo que el módulo de compresibilidad disminuyó. Esto es compatible con la relación Grüneisen que presenta un producto constante entre la conductividad térmica y el módulo de compresibilidad. Sin embargo sigue pendiente la verificación de esta tendencia sobre el calor específico (Cp), necesaria para completar el análisis de la relación de Grüneisen.

En cuanto a la compresibilidad del material bajo difracción de rayos X in situ de alta presión (HP-XRD), se realizó un estudio de la dependencia del módulo de compresibilidad con el tamaño de cristal para el material nc-UO_2. Se estudiaron tres tamaños de nc-UO_2 diferentes (4 nm, 6 nm y 34 nm) hasta una presión de 27 GPa, y se determinaron las constantes de compresibilidad correspondientes B_0 y B_0'. El módulo de compresibilidad del UO_2 sufrió una disminución extrema para las partículas de tamaño dentro del rango nanométrico. Para las partículas de nc-UO_2 de 4 nm se observó un módulo de compresibilidad (B_0) en torno a un 40% menor que el medido UO_2-grano-grande (granos de tamaño micrométrico) [Pujol et al., 2004]. Esto confirmó la dependencia del módulo de compresibilidad con el tamaño de las partículas. Sin embargo, un estudio con partículas de tamaños mayores que los aquí considerados (>34 nm) sería necesario para garantizar que la tendencia observada en estos monolitos (disminución del módulo de elasticidad) se debe al tamaño de los granos, y no sólo debido a las imperfecciones y porosidad posiblemente presente en las muestras.

Los resultados de las pruebas de difusividad térmica para el material de nc-UO_2 compactado mostraron un comportamiento similar al del material UO_2-estándar (micro-grano). La difusividad térmica para las pastillas sinterizadas de nc-UO_2 ($\sim$200 nm, 90% densidad), se determinó en el rango de temperatura 254°C a 1165°C. Se hizo una extrapolación de los resultados obtenidos hasta una densidad de 95% y se encontró la misma difusividad térmica que en las pastillas fabricadas con estándar-UO_2 (grano-grande) y densidad del 95% [Fink, 2000]. Respecto al temido empeoramiento de la conductividad térmica del material en la HBS debido al efecto del tamaño de grano (resistencia Kapitza), quedó aquí demostrado el no-deterioro de las propiedades térmicas para las pastillas de UO_2 con un tamaño de grano de 200 nm imitando la HBS.

Se llevo a cabo la determinación del punto de fusión por calentamiento-láser y detección de la temperatura pirométrica para nc-UO_2-compactado de dos tamaños diferentes de nano-grano (aproximadamente 10 nm y 200 nm), evaluándose su variación con respecto al UO_2-estándar de grano grande. Se encontró una disminución del punto de fusión para el compacto con material nc-UO_2-(10 nm), de aproximadamente 150°K con respecto al valor típico para UO_2-estándar. Esta reducción sería a priori debido al tamaño nano de los granos. Sin embargo, el parámetro de red medido para dicha muestra antes de aplicar la fusión (a=0.5438 nm) resultó inferior al valor típico de la referencia UO_2-estándar (a=0.547 nm), indicando por tanto la presencia de un óxido sobre-estequiométrico el cual también podría ser causante de esta disminución del punto de fusión. Para corroborar la tendencia medida con la reducción de tamaño de grano, sería necesaria una muestra de nc-UO_2 estrictamente estequiométrica. Sin embargo para el compacto con material nc-UO_2-(200 nm) se encontró un punto de fusión igual al de la referencia UO_2-estándar. Una estequiometría de O/M=2.00 del parámetro de red fue medida para esta muestra antes de provocar la fusión. Éste es

un importante resultado tecnológico para el posterior uso de las cerámicas de nc-UO_2 como combustible nuclear. De hecho, un punto de fusión más bajo plantearía un problema para la concesión de licencias de los monolitos como combustible para el reactor. Afortunadamente la posibilidad de un punto de fusión a menor temperatura desaparece para muestras de nc-UO_2 con un tamaño de grano de 200 nm, como también debe ocurrir para el material HBS en el reactor.

Así, dichos nano-efectos tales como la disminución de la conductividad térmica y del punto de fusión se podrían excluir como puntos débiles para el uso de nc-UO_2 como combustible nuclear. Estos efectos pueden ser relevantes para tamaños pequeños de cristal o grano (∼10 nm), pero desaparecen para tamaños de grano de ∼ 200 nm donde convenientemente las propiedades ventajosas de la nano-estructura buscadas (super-plasticidad, baja hinchazón bajo bombardeo de Xe [Spino et al., 2012], crecimiento de grano autolimitado, etc.), permanecen presentes todavía. Ésto anticipa que no existe pérdida de propiedades de las pastillas de nc-UO_2 desarrolladas para aplicaciones técnicas dentro este rango de tamaño.

Recomendaciones para el Futuro

La concesión de licencia para combustible nuclear se hace en base a su seguridad de actuación no sólo bajo condiciones normales de operación, sino también cuando se produce un aumento de temperatura en el combustible. Esto podría ocurrir debido a un accidente por pérdida de refrigerante (LOCA; *Loss of Coolant Accident*) o en un accidente de reactividad iniciado (RIA; *Reactivity Initiated Accident*). Bajo estas condiciones extremas podría ocurrir una fragmentación del combustible. Durante esta tesis se intentó simular un accidente de este tipo mediante un experimento utilizando una muestra de nc-Y-ZrO_2 en vez del nc-UO_2. Esta prueba se realizó en una instalación del ITU (Institute for Transuranium Elements) conocida como POLARIS y que permite un calentamiento por láser de la muestra muy rápido.

El material inicial sometido al POLARIS estaba libre de poros y su superficie era plana. El tratamiento con láser mostró como se produjo una hinchazón local a través de la formación de porosidad. No hubo un perfecto control del experimento, sin embargo es probable que la hinchazón observada se debiese al CO o CO_2 gas generado al reaccionar la impureza de carbono presente en el material con el oxígeno de la atmósfera, causando la formación de poros en un proceso similar a la producción de espuma de vidrio. Un resultado particularmente interesante de la prueba es que los poros formados estaban cerrados y eran sorprendentemente similares a los de la zona-HBS en los combustibles de alto grado de combustión. Sería posible pues, que en este tipo de accidentes de fusión del combustible al menos parte del gas de fisión podría ser atrapado en poros formados potencialmente cerrados, como ocurre en el material de HBS a bajas temperaturas. Aunque estos experimentos son preliminares sugieren un método novel y prometedor para probar la capacidad de retención de gas del combustible nc-UO_2 en condiciones de accidente.

Por último, otro método importante para entender la resistencia de los nc-materiales a la irradiación, podría ser la irradiación de haces de iones. Esto puede llevarse a cabo en instalaciones como las del ANL (Argonne Nacional Laboratory) IVEM-Tandem en Chicago, donde la irradiación con iones de gas inerte (He o Xe) junto con la observación

TEM on-line, proporciona una manera muy útil para implantar los átomos de gas y evaluar cómo se comportan éstos en la matriz (ej. disolución de la misma, formación de burbujas, transporte de burbujas a lo largo de los límites de grano, etc.).

Observaciones finales

Se consiguió con éxito la consolidación de polvo sintetizado de UO_2 nanocristalino en pastillas densas imitando, como sistema ideal, la estructura que aparece a altos grados de combustión (HBS). Desde los diferentes polvos de nc-UO_2 sintetizados (4-5 nm de tamaño de cristal), hasta los compactos monolitos de nc-UO_2 con un tamaño de grano medio de 200 nm y densidad aproximadamente de 90%. Se mostró la estabilidad de ésta estructura después del sinterizado, así como una cinética de crecimiento de grano autolimitada hasta temperaturas de 1200°C. Se confirmó la semejanza entre las pastillas de nc-UO_2 sinterizadas de las propiedades mecánicas fuera de pila (en términos de dureza y módulo de elasticidad), y las propias del material-HBS in pila. Se encontraron propiedades beneficiosas como estabilidad de la estructura, mejora de las propiedades mecánicas y crecimiento autolimitado de grano, lo que alenta a la realización de pruebas de irradiación para verificar este comportamiento en el reactor. Según lo determinado previamente en experimentos fuera de pila con monolitos del sistema nanocristalino hermano nc-Y-ZrO_2 [Spino et al., 2012], una fuerte reducción de la hinchazón por burbujas de gas, estabilidad térmica a largo plazo de la configuración poros-grano, así como un notable comportamiento superplástico y un creep acelerado, se esperarían también para los monolitos de nc-UO_2 aquí desarrollados. Se confirmaron anomalías en las propiedades físicas y químicas del material para tamaños de grano en el nano-intervalo absoluto (<30 nm), en consonancia con lo observado en otros sistemas nanocristalinos. Estos nano-efectos perniciosos, como disminución de la conductividad térmica y el punto de fusión, que podrían significar un punto débil para el uso de nc-UO_2 como combustible, mostraron ser relevantes sólo para tamaños muy pequeños de cristal/grano (<30 nm) desapareciendo para tamaños de grano de ∼200 nm donde convenientemente las propiedades ventajosas buscadas de la nano-estructura (super-plasticidad, baja hinchazón por burbujas de gas, crecimiento de grano autolimitado, etc.), permanecen. Esto anticipa que no existe pérdida de las propiedades de las pastillas de nc-UO_2 desarrolladas para aplicaciones técnicas dentro este rango de tamaño. Finalmente éste ha sido un trabajo muy gratificante con una serie de avances logrados. Se ha aprendido mucho en el tránsito pero aún queda mucho por hacer para determinar el verdadero potencial de este intrigante material.

Summary

Origin of the work

Today's nuclear fuels are largely based on uranium dioxide (UO_2). A high level of proficiency has been reached in this technology with fuels achieving moderate to high burn-up (BU) in the reactor. However, to go beyond the today's achievements a more radical approach may be needed, in order to enable the fuel to reach yet higher BUs. This is desirable for the reduction of the amount of fresh fuel required and the mass of spent fuel inventories (radioactive waste). To achieve these goals, improved fission gas retention capability of the fuel is required as well as a solution to the pellet clad mechanical and chemical interaction (PCMI and PCCI) failure risks problem is needed, which could intensify at high BUs due to boosted cladding embrittlement. A project to synthesize nanocrystalline (nc)-UO_2 powders for the manufacture of bulk nc-fuel compounds for the characterization of their out-of-pile mechanical properties and irradiation behaviour was built.

The kicking idea of the above development was originated after careful observations of the transformations in the highly irradiated nuclear fuels. Indeed, the fuel pellet working inside the nuclear reactor is a material subjected to extreme conditions that change its properties with time and irradiation dose. Damage in the material and local defects like interstitials, loops and vacancies are created. Furthermore, accumulation of solid fission products in the lattice and formation of gas bubbles make the pellet thermal conductivity to decrease. Fuel cracks appear from the beginning of the irradiation due to thermal stresses and make the thermal properties to decrease even more. The fuel pellets swell owing to the accumulation of fission gas bubbles in the matrix and the segregation of low-density fission-products phases (metallic and ceramic precipitates). As a result of the swelling, the fuel approaches the clad. Physical and/or chemical interaction can occur upon contact, which can induce clad deterioration and rupture [Garzarolli et al., 1979]. These types of changes can affect also the temperature profile of the fuel pellet by modification of the gap thermal transfer conditions, limiting as well the life-time of the fuel (and BUs) inside the reactor, if premature rod rupture occurs.

After all this accumulated damage, nuclear fuels approximately at the end of the third irradiation cycle (about 40 GWd/tM) undergo then a structure transformation which begins at the edge of the fuel pellet and steadily progresses to its centre as the irradiation proceeds [Matzke and Spino, 1997] [Spino and Papaioannou, 2000]. The original microstructure of micro-grains (or larger-grains) transforms into a nc-porous matrix [Nogita and Une, 1994] through restructuring of the accumulated irradiation defects. This is a sort of "self-healing" action where the material gets cured from damage by reordering itself [Spino et al., 2012]. The new nc-structure appearing is called high burn-up structure (HBS). It is called also rim-structure because in UO_2 fuels it

initiates at the rim or outer zones of the pellets (region which receives the most fissions).

At the beginning it was thought that the HBS could be responsible for cladding failures due to additional in-pile volume increase (swelling) and a supposed brittle behaviour of the transformed material was postulated [Matzke, 1992]. Also, it was thought that the rim-structure could act as a new source of gas release. Indeed, there are still investigation-lines that defend this opinion. However, other studies found that the percentage of gas liberated from the rim of the fuel pellets, where the HBS appeared, was low in comparison with the gas coming from the inner parts of the fuel where the original structure is still present [Mogensen et al., 1999]. This philosophy has been followed in other publications, which demonstrate a generally beneficial evolution of the fuel properties, in particular the retention of the fission gases, after the structure transformation.

Besides that, the properties of the HBS indicate an enhanced radiation tolerance as reported by [Spino et al., 2012]. This study coincided with the important novel evidence in the literature that nano-grained materials are more resilient to radiation damage than their large-grained pairs due to defects-recombination at their multiple grain boundaries [Nita et al., 2005]. Also improvement of the thermal conductivity and other radiation-defects-depending properties were found due to lattice-strain release after recrystallization [Ronchi et al., 2004], as well as fracture toughness increase and crack-healing tendency were anticipated [Spino et al., 2003].

Moreover, in relation to safety issues, the latest experiments on the high BU-LWR (Light Water Reactor) fuels indicated no increase in the gas release and in the failure susceptibility during reactivity initiated accident (RIA) transients [Sasajima et al., 2010] [Fuketa et al., 2006]. Also diminution of the aqueous corrosion rate under simulated geologic repository conditions for fuels containing HBS was found out [Ekeroth et al., 2009] [Carbol et al., 2009]. Both last facts confirmed the tightness of the structure.

So it has been demonstrated that the HBS has exceptional qualities even in comparison with the original fresh matrix (large-grain structure), with a number of improved properties that are really advantageous for a fuel. Then, why not imitate this recrystallized material?. And why not imitate the structure appearing in the rim (HBS) and introduce it in this form as a fresh fuel inside the reactor?. Why not synthesize a fuel matrix like this HBS, which due to its apparent damage-resilience would withstand longer times under irradiation?.

Here is were the project to synthesize nanocrystalline (nc)-UO_2 powders for the manufacture of bulk nc-fuel compounds began. The produced monolithic pieces from these powders would have a volume of approximately 1 cm^3 with a uniform matrix of grains with size between 100 and 250 nm to mimic the rim-structure. The creation of this novel fuel microstructure has been achieved in this work by passing through very different steps. From the nc-material synthesis to the fuel pellet manufacture, many individual process stages, previously unknown or unexplored, had to be specifically developed and/or optimized.

Synthesis of nc-UO_2 and nc-ThO_2

Regarding the initial powder for synthesizing nc-UO_2 monoliths mimicking the HBS of LWR-fuels (nanostructured), considerable work was devoted to the development of two different chemical synthesis routes leading to deflocculated nc-UO_2 and nc-ThO_2 precipitates to compensate for their lack of commercial availability. ThO_2 is similar in structure to UO_2 but has the advantage of a single valence state (i.e. IV). To obtain large amounts of nc-UO_2 as required for pellets forming, both methods were conveniently adjusted, developed and scaled-up according to the aim needs. The material in the as-produced condition was studied by transmission electron microscopy (TEM) and X-ray diffraction (XRD).

The first method developed was a controlled precipitation that uses an electrolytically reduced aqueous solution of uranyl nitrate as precursor and a dropped NaOH-solution as alkalinisation agent that is used to trigger the precipitation of the nc-material in the vicinity of the U^{4+} solubility line. This method was originally described in [Rousseau et al., 2002] [Rousseau et al., 2006]. An intensive study of the range of U-concentration and acidity for nc-UO_{2+x} precipitation from electrolytically reduced uranyl nitrate solutions was endeavoured, using higher U-concentration (10^{-1} M) ranges as the observed in literature (10^{-2} M) [Rousseau et al., 2006], and therefore lower pH ranges, following the solubility line of U^{IV}. As a final result, 10 g of nc-UO_{2+x} per batch were obtained, instead of the few nanograms of yield appearing hitherto in the literature. The resulting solid phase, as studied by XRD, was found to crystallize with the typical UO_2-*fcc* fluorite structure (*Fm-3m* space group), with a lattice parameter a=0.5417(1) nm and average crystallite size of 3.79 nm, also in agreement with an average size observed by TEM of 3.9(8) nm. The predominant diffractogram of the samples corresponded unmistakably to UO_2, but in a slightly oxidized state. The latter was manifested through a lattice contraction of about 0.9% of the precipitated phase (a=0.5417(1) nm) with respect to the values of stoichiometric UO_2 (a=0.547 nm).

The second method studied concerned the thermal decomposition of an organic phase using uranyl acetylacetonate (UAA) as precursor, which was added to a mixture of oleic acid and oleylamine, which was then heated as a whole up to temperatures above 300°C to induce the precipitation of UO_2 nanoparticles by thermal decomposition of the UAA. This original procedure was described in [Wu et al., 2006]. Reduction of surfactant quantities with respect to the metal content, as well as scale up of the method from 0.1 g of nc-UO_2 as reported by [Wu et al., 2006] to 2.3 g of nc-UO_2, was achieved. The same method was extrapolated for the synthesis of nc-ThO_2, using thorium acetylacetonate (ThAA) or thorium acetate (ThA) as precursor, from which ThO_2 nanorods have been obtained. The reason for the rod-shape of the precipitates is hitherto unknown. Batch sizes of 0.3 g ThO_2 nanorods were obtained by this means, i.e. with a much lower production yield than in the case of UO_2 nanoparticles. Different conditions for the heating rate, ageing time, ageing temperature and initial precursors (ThAA and ThA) were explored for the UO_2 and ThO_2 cases. However, similar results were always found, in terms of the structure and geometry (round-shaped for nc-UO_2 and rod-shaped for nc-ThO_2) of the precipitates. Perfectly crystallized solid phases, as studied by XRD, with the typical UO_2-*fcc* fluorite structure (*Fm-3m* space group), with an average crystallite size (spheres diameter) of 5.52 nm and a lattice parameter of 0.5431(0) nm were found for the UO_2 case, also in agreement with the average size observed by TEM (4.9(3) nm) and DLS (3.7(1) nm). For the ThO2 nanorods, also the typical ThO_2-*fcc* fluorite structure (*Fm-3m* space group), with a crystallite size (rods

diameter) of 1.42 nm and a lattice parameter of 0.5579(1) nm, was found. In both cases, no aggregation of the precipitated nanoparticles has been observed on the TEM images.

Crystallization and grain growth in f(T) for nc-UO_2

To study the composition of the precipitates obtained by both methods above mentioned and their propensity to thermal growth in the unconsolidated state, further analysis of the precipitated material annealed at different temperatures was performed by applying the thermal analytical and X-ray diffraction techniques like thermogravimetric analysis and differential thermal analysis (TGA/DTA), X-ray diffraction (XRD) and high temperature X-ray diffraction (HT-XRD), and spectroscopic techniques such as X-ray absorption spectroscopy (XAS), magic angle spinning nuclear magnetic resonance spectroscopy (MAS-NMR) and infrared spectroscopy (IR) and characterization techniques like transmission electron microscopy (TEM).

The evolution of the crystallite size, the lattice parameter and the lattice strain were determined from ambient temperature up to 1200°C under inert atmosphere. For the aqueous precipitated nc-UO_2, only a weak effect of temperature on the crystallite size occurred below 700°C, remaining this below 7 nm in this temperature range. On exceeding 700°C, the crystal size grew, however, steadily with temperature, to reach the value of 73 nm at 1200°C. Opposite, the strongest lattice parameter increase was measured in the lowest temperature range 20°C-700°C, whereas in the temperature range 700°C-1200°C only a weak lattice expansion was observed, which almost coincided with the reversible thermal expansion of UO_2. Thus, on the base of measurements done after cooling, a recovery of the UO_2 typical crystal structure was achieved during this annealing under static He atmosphere, passing from the initial lattice parameter value of 0.5417 nm for the as-produced nc-UO_2, to the value of 0.5473 nm after exposure to 1200°C. The verified initial lattice contraction of the as-produced nc-UO_2 below the normal value of bulk stoichiometric UO_2 (a=0.5470 nm) is attributed mainly to oxidation.

For the organic precipitated nc, a similar particle-growth behaviour with temperature was observed, with almost no crystal-dimension changes up to 700°C (because of the pre-thermal treatment performed), followed by an intense crystal-growth between this temperature threshold and the final annealing temperature of 1100°C, obtaining a final crystal size of 150 nm. As for the derived oxygen stoichiometry from the lattice parameter values, also an initial oxidation of the nc-particles produced by the organic method was confirmed, although in lower extent as for the case of the particles produced by the aqueous method. The particles recovered the normal lattice dimension of bulk stoichiometric UO_2 for annealing temperatures above 750°C.

As for the determined lattice strain, also a similar behaviour was observed for particles obtained from both preparation methods. The main observation in both cases was that the lattice strain decreased continuously with temperature, until being practically extinguished at the temperature at which the boosted crystal growth started. This confirmed the lattice strain to having acted in both cases as crystal-growth inhibitor.

Structure and oxygen-stoichiometry studies by XRD, XANES, EXAFS, NMR AND FTIR

The structure of the produced nc-UO_2 material as a function of temperature and, in this case under reducing atmosphere, was also studied by XRD and compared to the reference bulk-$U^{IV}O_2$. The lattice constant of the material in the cooled state after reaching different maximum temperatures (600°C and 1200°C) was measured. This allowed the separation of the thermal expansion contribution in the high-temperature values to obtain cleaner curves of thermal expansion vs. temperature and lattice dimension vs. crystal size. No big differences in crystal size, lattice and strain, were observed between measurements made under inert (above commented) and reducing atmospheres (measurement after cooling) for the material obtained by the aqueous method. However, a notable change in the crystallite size was observed for the material obtained with the organic method at 1100°C, which showed a size of 150 nm under He and a size of only 12 nm under Ar/5%H_2. Comparing the aqueous and organic produced material under reducing atmosphere (Ar/5%H_2) and without pre-thermal treatment, no big change was observed until 600°C anneal, but at 1200°C. At the last temperature, a size of 82 nm was measured for the aqueous method material compared to the 12 nm obtained for the particles from the organic method at the same temperature under reducing atmosphere (Ar/5%H_2), were measured. That could be ascribed to the surface layer protecting the organic precipitated nanoparticles.

In addition to the XRD studies, XANES was used to determine the oxidation state of the U cations and the corresponding molar fractions and the derived O/U ratios. The XANES spectra at the U-L_3 edge for the aqueous method material and for the organic method material, showed similar improving trends with increasing temperature and as the stoichiometry shift (x) decreased (UO_{2+x}). The samples studied were nc-UO_2 as produced and after thermal treatment at 600°C and 1200°C under Ar/5%H_2. Compared to the reference sample of bulk (large grain) $U^{IV}O_2$ material, the peak of the WL shifted slightly to lower energies and increased in intensity, and the oscillations within the XANES regions increased. The amplitude of these oscillations decreased with the increasing temperature of thermal treatment showing a higher structural order of these annealed samples.

This effect could be either due to the small crystal size of nc-UO_2 samples or to the stoichiometry shift of the synthesised material. To quantify these contributions a dedicated study with nc-UO_2 with fixed oxygen stoichiometry and different crystal sizes would be needed. Since at this moment this kind of selective synthesis of nc-UO_2 was not possible, an alternative separate study of the size effect in the stoichiometric nano-oxide-material was attempted using the substitute thorium dioxide (ThO_2), known to crystallize with the same fluorite structure as UO_2 and to maintain a unique cation-valence state Th^{IV}.

In this work, a study of as-produced nc-ThO_2 (not thermally treated) was done. In the corresponding XANES spectra at the Th-L_3 edge, the peak of the WL corresponding to nc-ThO_2 at RT (as-produced) had an identical position and amplitude as the one of the reference spectra of large-grain bulk $Th^{IV}O_2$. Only a slight peak intensity decrease and somewhat fewer oscillations were detected, which indicated only a weak effect of the crystal size on the interatomic distances and ordering reflected in the XANES spectra. This identical behaviour of the large grain $Th^{IV}O_2$ and the

nc-ThO_2 suggested that the displacements observed formerly for nc-UO_2 would have been not due to the particle size, but rather to the shift of the cation-valence towards the oxidised state (U^{VI}). Having that into account, determining the O/M of nc-UO_2 from the XANES shift seems to be justified.

In the k^3-weighted EXAFS spectra of nc-UO_2 particles from the aqueous method the oscillations and their amplitude increased with the annealing temperature and the resulting growing crystal size, approaching gradually those typical of the UO_2(*fcc*)-structure. The as-precipitated 4 nm as-precipitated sample was very difficult to fit with a pure fluorite structure, as the fits were non stable and the data noisy. The 600°C annealed 9 nm sample showed an intermediate ordering with clearly identified oscillations. Both the original 4 nm-sample and the 600°C-annealed 9 nm-sample showed clearly shorter U-O and O-O bond-distances compared to the reference bulk-$U^{IV}O_2$ sample. This was compatible with the XRD studies showing considerable lattice contraction for the as-received sample and in lower extent, with intensity decreasing with temperature, for the annealed samples below 1200°C. Ultimately, for particles annealed at 1200°C and with a crystal size of 82 nm, the EXAFS oscillations were similar, if not entirely matching, to those of the bulk-$U^{IV}O_2$, indicating the same *fcc*-structure (*Fm-3m*) and same interatomic distances and substantial crystal perfection. That was in agreement with the structure-similarity shown in the XRD analysis between the nc-UO_2 sample annealed at 1200°C and the reference large-grain bulk-$U^{IV}O_2$ sample; and was also consistent with the XANES studies, showing no departure from the fluorite structure for the fully annealed UO_2 nanoparticles. In the k^3-weighted EXAFS spectra of the UO_2 nanoparticles from the organic origin, the results were different as above, being not only the as-precipitated 5 nm sample very difficult to fit with a pure fluorite structure, but the samples treated at 600°C and 1200°C, too. All samples presented a high degree of disorder and could not match at all the reference signature of bulk-$U^{IV}O_2$, with the meaning that another unidentified phase must be taken into account in this case.

NMR Hahn-echo ^{17}O MAS spectra could be acquired for samples prepared by the aqueous method after annealing at different temperatures under reducing atmosphere ($Ar/5\%H_2$). Three different oxygen environments could be identified from the fitting of the chemical-shift signatures of these samples, i.e., the records of the ^{17}O-resonance-frequency peak displacement with respect to that of a reference specimen, expressed in relative units (ppm). In the present case, the ^{17}O-resonance of a ^{17}O-dopped H_2O sample was taken as reference, and defined as 0 ppm. The first identification corresponded to oxygen species having a chemical shift of nearly 900 ppm and was found for samples annealed up to 650°C. The two other types of oxygen species identified appeared clearly in the temperature range 650°C-1200°C. These new species, i.e., one showing a sharp and the other a broad ^{17}O-peak, could be respectively attributed to ^{17}O in a well crystalline environment and in a more disordered one; the last due to the larger peak broadening. Both peaks diminished strongly their chemical shifts and half-maximum widths in the temperature range 650°C-800°C, to converge rapidly at temperatures above 800°C to values near those of the sample annealed at 1200°C, i.e., respectively, 717 ppm (chemical shift) and 5 ppm (FWHM), which due to very small peak broadening (FWHM) indicated a very well crystallized environment. This last was still slightly bigger than the 3 ppm found for $U^{IV}O_2$-bulk. Despite this, the chemical shift (717 ppm) was the same as that found for $U^{IV}O_2$-bulk. Hence, one can say that the environment around the oxygen lattice positions in the case

of the sample with the biggest crystallite size (∼80 nm) was very close to that of $U^{IV}O_2$-bulk. Based on the FWHM, one can say that to observe the signal of crystalline UO_2 a crystallite size above 80 nm should be reached. This is in line with the observation by XRD of an UO_2-*fcc* structure with lattice parameter 0.5472 nm in this case.

Several samples from the aqueous method at key annealing temperatures were also analysed under the FTIR spectrometer. In the case of nc-UO_2 in the as-produced condition (RT), four peaks in the range 400-4000 cm^{-1} could be observed. They could be assigned to the bending vibration of H-O-H of the coordinated water, and to a possible more oxidised state (UO_{2+x}). All these peaks diminished in intensity with the annealing temperature. Hence, at 1200°C the IR spectra looked like the one of the $U^{IV}O_2$ reference sample. That was also in agreement with the above commented XANES results where a different electronic structure was seen at 600°C, while at 1200°C a similar structure to bulk-$U^{IV}O_2$ was found. Also EXAFS was characterized by poor ordering at 600°C but entirely matching with the bulk-$U^{IV}O_2$ oscillation pairs at 1200°C.

Isothermal grain-growth study of the synthesized nc-UO_2 was then performed by XRD and HT-XRD. For the annealing temperatures of 500°C, 700°C and 900°C and a static and inert atmosphere of He, the grain growth took place in the first hours of isothermal hold until a stable average crystal size was established at the applied temperature, at which time grain growth ceased. For the isotherm at 1200°C and a static atmosphere of He, the material had a continuous growth not reaching a constant grain value in the first 50 h. An activation energy of diffusion of 0.93 eV to 1.25 eV was obtained. The low activation energies obtained could be related predominantly to grain boundary (surface and interface) diffusion.

A lattice parameter of about 0.5472 nm was already found for the samples treated at 900°C after 50 h dwell time under Ar/H_2 obtaining a final size about 50 nm. Therefore a temperature of 1200°C (and in consequence a final crystallite size of 80 nm) would be, in principle not necessary to reach the typical lattice parameter of the reference large-grained UO_2 (a=0.5472 nm), as above commented.

An average crystal size of 322 nm was measured after cooling for the heat treatment at the highest temperature of 1200°C after 50 h dwell time under He. Taking that into account, it appears that a temperature below 1200°C would be necessary in the sintering process of the monoliths to avoid extreme growth of the particles (>200 nm). Nevertheless for the nc-UO_2 samples annealed at 1200°C during 50 h under Ar/H_2 dynamic atmosphere, a final crystal size of 85 nm was measured after cooling. Even after 200 h dwell time at this temperature under reducing atmosphere, a final crystal size of 150 nm was seen (quite far from the 322 nm observed under He atmosphere after 50 h). This difference could be due to the initial oxidation state of the nc-UO_2 samples and their evolution under a static He atmosphere. An hyperstoichiometric UO_2 would present a stronger increase of the self-diffusion coefficients and in the same way raise the mass-flow, for which enhanced grain-boundary motion and grain (or crystal) growth will occur. In fact the differences in the diffusion coefficient between bulk-large-grain-UO_2 and nc-UO_2 are compatible with an enhancement of the diffusion processes either by a diminishing of the grain size or by O/U>2 effects.

nc-UO_2 monolith consolidation and characterization

Different alternative routes for consolidation into green bodies (e.g. conventional uniaxial pressing, float packing, etc.) have been tested. Afterwards the green bodies were sintered at temperatures between 900°C and 1200°C under Ar/H_2 atmosphere. The optimum sintering conditions were deduced from the long-isothermal crystallite growth studies under He and Ar/H_2 atmosphere. This ensured lack of disproportionate grain growth risks even at the highest temperature used of 1200°C. Also thermal pre-conditioning of the powder before pressing was in some cases done to avoid cracks during the sintering step due to the presence of water or organics (depending on the case) in the material. The pellets sintered presented a strong appearance although fine cracks were visually observable in some cases. Sintering densities between 75.5-90.5% of the theoretical density (TD_{UO_2}=10.96 g/cm^3), were obtained. An average grain size of ∼200 nm, replicating the HBS, was obtained for all the different sintered nc-UO_2 pellets.

Additional dilatometry experiments were performed to compare the shrinkage of the fabricated nc-UO_2 pellet with that of bulk-UO_2 (large grain) produced by a standard fabrication process. Enhanced sinter activities of the nanocrystalline materials compared to microcrystalline UO_2 were found at lower temperatures. The temperature range from onset to completion of the densification occurred at much more lower temperatures for the nc-UO_2 (200-955°C, with a maximum sintering rate at 740°C), compared to the bulk-UO_2 [Lahiri et al., 2006] (900-1540°C, with a maximum sintering at 1200°C). The reason of that might be the higher surface present in the nc-UO_2 compared with the bulk-UO_2 material, rendering the sintering to become more effective (at lower temperatures). The sintering activation energy was determined as $Q = 171 \pm 7\ kJ/mol$ assuming surface diffusion and $Q = 114 \pm 5\ kJ/mol$ assuming volume diffusion for the nc-UO_2 monolith, compared to $Q = 287\ kJ/mol$ determined for bulk-UO_2 in the literature [Lahiri et al., 2006]). Both diffusion mechanisms showed low values of the sintering activation energies as typical for nanopowders. That means a clear technological advantage in the fabrication of nc-UO_2 monoliths due to its high densification capacity at low temperatures. Furthermore, the nc-UO_2 offered the possibility of adjusting the grain size at will by varying sintering temperatures and times. Maintaining an acceptably low temperature range in the sintering process, it will diminish the costs and simplify the manufacturing technology.

Characterization of macrostructures by optical microscopy (OM), and microstructures by fresh-fracture observation by SEM, for different samples at different magnifications, was performed. Not well defined grains were observable in the fresh-fracture SEM images of the pellets sintered at low temperature of 900°C. The sinter of the crystals was still under development, therefore sintering temperatures of 1200°C were used afterwards. Macrocracks across different samples were observed, but not for the monoliths from nc-UO_2 synthesized by the organic-route with powder thermal pre-treatment, and not for the monoliths from the float-packing consolidation method and powder of the aqueous-synthesis. All macrostructures, with exception of the last one, showed non-homogeneous densification (residual porosity between densified areas). Also the conventional pressed sample of pre-dehydrated powder from the aqueous route showed a good quality in comparison to the rest, from the point of view of the densification. However, improvements in the performance of the monoliths would be necessary to avoid the problem of cracks in the sintered pellets (and therefore the diminishing material's properties). Looking at the fresh fracture surfaces, the microstructure of the aqueous-route-powder pellet produced by float

packing consolidation and sintering at 1200°C, was the closest approximation to the HBS material obtained until now. The average grain size for the different monoliths was in the 170 nm to 250 nm range. Here a major success of this work was achieved.

Mechanical properties as Vickers Hardness (H_V), Knoop Hardness (H_K) and Young's modulus (E) were determined for sintered nc-UO_2 pellets. An increase in hardness (H_V) and low values for E-modulus (up to 30%) were in general seen for the different nc-UO_2 monoliths in comparison with bulk-UO_2. Also scanning acoustic microscopy (SAM) was used for the estimation and comparison of the Young's E-modulus obtained by indentation. The results by SAM (E=150 GPa) matched the ones derived from microindentation (E=155 GPa). This difference observed with respect to bulk-UO_2 pellets (220 GPa), could be influenced by microstructure imperfections (nanocavities at triple-grain junctions, pores, cracks, etc.). However, the drop was still too large to be attributed only to the presence of cavities. The same type of tendency observed in the nc-UO_2 specimens, i.e. with increase of H_V values and decrease of the E-modulus values, has been found before in irradiated standard-UO_2 fuel at high BUs. In this case also the E-modulus decrease could not be fully attributed to a porosity increase and was to contradict the effect of the fission products dissolution, which causes in reality an increase of the material's stiffness. Since with the increase of BU the irradiated nuclear fuels transform into a nano-recrystallized structure [Spino et al., 2012], the effects of (partial) H_V-increase (fission products dissolution causes as well hardening) and additional E-modulus decrease (beside that caused by porosity) like the effects observed in the present work could be attributed in high BU fuels due to the nanostructure.

The confirmation of the size-dependent physical-chemical properties of nc-UO_2 has been successfully accomplished. So the compressibility of nc-UO_2 was proved in fact to be larger than that of standard-UO_2. A size-dependence of the thermal expansion properties of nc-UO_2 was also confirmed. The thermal expansion was shown to increase with the size-decrease, at the time that the bulk modulus decreased. This is compatible with the Grüneisen relationship showing a constant product between the thermal conductivity and the bulk modulus. However, verification of the trend in the specific heat (Cp) is still lacking, which is indeed neeeded to complete the Grüneisen-relationship analysis.

Regarding the material's compressibility, in-situ high pressure X-ray diffraction (HP-XRD) has been performed for the study of the bulk modulus dependence on the crystal size in nc-UO_2. Three different nc-UO_2 sizes (4 nm, 6 nm and 34 nm) were studied up to a pressure of 27 GPa and the corresponding compressibility constants B_0 and $B_0^{'}$ determined. The bulk modulus of UO_2 suffered an extreme decrease in the nano-size particle range. For the 4 nm-size nc-UO_2-particles, a bulk modulus (B_0) around 40% lower than the one measured for bulk-UO_2 (micron-size grains) [Pujol et al., 2004], has been observed. This confirmed the dependence of the bulk modulus with the crystallite size. However, studies with bigger particle sizes as the ones here studied (>34 nm) would be necessary to guarantee that the tendency observed in the monoliths (decrease of E-modulus), is due to the size of the grains and not just because of imperfections and porosity possibly present in the samples.

The results of thermal diffusivity tests of the compacted nc-UO_2-material showed similar behaviour as that of standard, nuclear grade UO_2 (bulk). The thermal diffusivity for sintered nc-UO_2 (∼200 nm, 90% density), was determined between

254°C to 1165°C. Extrapolation to 95% density was done and same thermal diffusivity as standard bulk-UO_2 pellet [Fink, 2000] with 95% density was found. Regarding the feared worsening of the thermal conductivity of the HBS material due to grain-size effect (Kapitza resistance), it has been here shown that no thermal properties deterioration has to be expected for the 200 nm-UO_2 pellet material mimicking the HBS.

Determination of the melting point by laser-heating and pyrometric temperature detection has been performed for compacted nc-UO_2 with two different nano-grain sizes (about 10 nm and 200 nm) and their variation with respect to bulk-UO_2 (large-grain), assessed. A melting point depression of about 150°K with respect to the normal value of bulk-UO_2 was found for the 10 nm-size nc-UO_2 sample. This reduction would be a priori due to the nano-size grains. However, the measured lattice constant of the sample before melting (a=0.5438 nm) was below the value of bulk-UO_2 (a=0.547 nm) and indicated in reality a hyperstoichiometric oxide, which would also cause a melting point decrease. To corroborate the measured tendency with the grain-size reduction, a strictly stoichiometric nc-UO_2 sample would be needed. However, an identical melting point as for bulk-UO_2, was found for the 200 nm-sample for which a stoichiometry of O/M=2.00 was confirmed from the lattice constant measurement before melting. This is an important technological result for the use of nc-UO_2 ceramics as nuclear fuel. Indeed, a lower melting point would pose a problem for the licensing of the monoliths as a fuel for the reactor. Fortunately the possibility of a lower melting point disappears for the 200 nm-UO_2 samples, as it would occur for the HBS material in the reactor, too.

So, postulated nano-effects such as diminution of the thermal conductivity and the melting point could be here excluded as weak points for the use of nc-UO_2 as a nuclear fuel. These effects might be relevant for very low crystal/grain sizes ($\sim$10 nm) but they disappear for grain sizes of $\sim$ 200 nm, where, conveniently, the sought advantageous properties of the nano-structure (super-plasticity, low swelling under Xe-bombardment [Spino et al., 2012], self-limiting grain growth, etc.), still remain. This anticipates the lack of property loss of the developed nc-UO_2 monoliths for technical applications in this size range.

Future Recommendations

The licensing of nuclear fuel is made on basis of its safety performance not just only under normal operation conditions, but also when a temperature rise occurs in the fuel. This could be caused in a Loss of Coolant Accident (LOCA) or in a Reactivity Initiated Accident (RIA). Under such extreme conditions fuel fragmentation could occur. During this thesis, one attempt was made to mimic such an accident in an out of pile experiment using nc-Y-ZrO_2 as a sample instead of nc-UO_2. This test was made in a facility at ITU (Institute for Transuranium Elements) known as POLARIS, which permits very rapid laser heating of the sample.

The initial material tested in POLARIS was pore free and its surface was flat. The laser treatment showed that a local swelling occurred through formation of porosity. This experiment was not perfectly well controlled, but it is likely that the observed swelling was due to CO or CO_2 gas generated when the carbon impurity in the material reacted with oxygen from the atmosphere, which caused pore formation, in a process similar to the production of foamed glass. A particularly interesting result

of the test is that the formed pores were closed and astonishingly similar to those of the HBS-zone in high burn-up fuels. Chances appear therefore that during such kind of postulated fuel melting accident, at least part of the fission gas could be trapped in potentially forming closed pores, as it occurs in the HBS material at low temperatures. Although these experiments are preliminary they suggest a promising novel method to test the gas retention capability of the nc-UO_2 fuel under accident conditions.

Finally, another important method to understand the resistance of nc-materials to irradiation can be provided by ion beam irradiation tests. This can be done at facilities like the ANL (Argonne National Laboratory) IVEM-Tandem facility in Chicago, where irradiation with inert gas ions (He or Xe) with on-line TEM observation provides a very useful way to implant the gas atoms and to evaluate how they behave in the matrix, e.g. dissolution therein, formation of bubbles, transport of bubbles along grain boundaries, etc.

Concluding remarks

Successful consolidation of the synthesized nanocrystalline UO_2 nanopowders into dense pellets mimicking of the High Burn-up Structure (HBS) as ideal system has been achieved. From the different synthesized nc-UO_2 powders (4-5 nm size) to the nc-UO_2 compacted monoliths with 200 nm average grain size and about 90% density were achieved. Stability of the structure after ageing and self limiting grain growth kinetics up to temperatures of 1200°C, were shown. The out-of-pile mechanical properties of sintered pellets (in terms of hardness and elastic modulus) were confirmed to closely resemble those of the HBS-material in-pile. Beneficial properties found, like stability of the structure, enhanced mechanical properties and self-limiting grain growth, strongly encourage the performance of irradiation tests to verify the in-reactor behaviour. As determined previously in out-of-pile tests of monoliths of the brother system of nanocrystalline nc-Y-ZrO_2 [Spino et al., 2012], a strong reduction of the gas bubble swelling, long term thermal stability of the pore-grain configuration, and striking superplastic behaviour and accelerated creep, would be expected as well for the developed nc-UO_2. Confirmation of anomalies in the physical properties of the material for grain sizes in the absolute nanorange (<30 nm), consistent with observations in other nc-systems was also achieved. These pernicious nano-effects, as diminution of the thermal conductivity and the melting point, which could be a weak point for the use of nc-UO_2 as a fuel, were found, however, to become relevant only at very low crystal/grain sizes (<30 nm) and to disappear for grain sizes of ∼200 nm, where, suitably, the other searched beneficial properties of this nanostructure super-plasticity, low gas-bubble swelling, self-limiting grain growth, etc., remain. This anticipates the lack of property loss of the developed nc-UO_2 monoliths for technical applications in this size range. This has been a very rewarding work, with a number of breakthroughs achieved. Much has been learned, but more needs to be done to determine the true potential of this intriguing material.

Contents

Abstract xii

Resumen xxvi

Summary xxxviii

List of Symbols and Abbreviations xliii

1 Introduction 1
- 1.1 Background and state of the art. . . . 1
- 1.2 Goal of the thesis. . . . 10

2 Analytical and characterization techniques 13
- 2.1 Electrochemical analysis . . . 13
  - 2.1.1 Cyclic Voltammetry (CV) . . . 13
  - 2.1.2 Electrolysis . . . 14
- 2.2 Spectroscopy . . . 15
  - 2.2.1 Ultraviolet-visible spectroscopy (UV-Vis) . . . 15
  - 2.2.2 Dynamic Light Scattering (DLS) . . . 15
  - 2.2.3 X-ray Absorption Near Edge Structure (XANES) and Extended X-ray Absorption Fine Structure (EXAFS) . . . 16
  - 2.2.4 Nuclear Magnetic Resonance spectroscopy (NMR) . . . 17
  - 2.2.5 Infrared spectroscopy (IR) . . . 17
- 2.3 Electron microscopy . . . 18
  - 2.3.1 Scanning Electron Microscopy (SEM) . . . 18
  - 2.3.2 Transmission Electron Microscopy (TEM) . . . 18
- 2.4 X-ray scattering . . . 18
  - 2.4.1 Room Temperature X-Ray Diffraction (RT-XRD) . . . 19
  - 2.4.2 High Temperaure X-Ray Diffraction (HT-XRD) . . . 19
- 2.5 Thermogravimetry/Differential Thermal Analysis (TGA/DTA) . . . 19
- 2.6 Dilatometry . . . 20
- 2.7 Mechanical Characterization . . . 20
  - 2.7.1 Microindentation . . . 20
  - 2.7.2 High Pressure X-Ray Diffraction (HP-XRD) . . . 20
  - 2.7.3 Scanning Acoustic Microscopy (SAM) . . . 21
- 2.8 Thermophysical characterization . . . 21
  - 2.8.1 Thermal Diffusivity . . . 21
  - 2.8.2 Melting Point . . . 22

3 Synthesis of nc-UO_2 by controlled massive precipitation in Aqueous phase 25
3.1 Introduction and principles. . . . 25
3.1.1 U-stability: environmental studies. . . . 25
3.1.2 U-redox chemistry pertinent to nc-UO_2 synthesis. . . . 26
3.1.3 nc-UO_2 synthesis principles. . . . 27
3.2 Mother solution preparation. . . . 28
3.3 U^{IV}/U^{VI} cyclic voltammetric and spectrophotometric study. . . . 28
3.3.1 Cyclic voltammetric study of the mother solution. . . . 28
3.3.1.1 Experimental arrangement. . . . 28
3.3.1.2 Results and discussion. . . . 37
3.3.2 Electrochemical reduction of the mother solution. . . . 38
3.3.2.1 Experimental arrangement. . . . 38
3.3.2.2 Results and discussion. . . . 39
3.3.3 UV-Vis spectrophotometry of the solution. . . . 39
3.3.3.1 Experimental. . . . 39
3.3.3.2 Results and discussion. . . . 41
3.4 Precipitation and separation of the UO_2-nanocrystals. . . . 43
3.4.1 Introduction remarks. . . . 43
3.4.2 Experimental steps. . . . 44
3.4.3 Spectrophotometry of the solution. . . . 45
3.5 Characterisation of the as-produced nanocrystals. . . . 46
3.5.1 Precipitates morphology and composition. . . . 46
3.5.2 Precipitates crystal structure. . . . 46
3.6 Results and discussion. . . . 47

4 Synthesis of nc-UO_2 and nc-ThO_2 by a precursor thermal decomposition in Organic phase 55
4.1 Introduction and principles. . . . 55
4.2 Experimental. . . . 57
4.2.1 Solution preparation. . . . 59
4.2.1.1 UO_2 nanocrystals preparation. . . . 59
4.2.1.2 ThO_2 nanocrystals preparation. . . . 59
4.2.2 Reaction step. . . . 60
4.2.2.1 UO_2 nanocrystals production. . . . 60
4.2.2.2 ThO_2 nanocrystals production. . . . 61
4.3 Precipitation and separation of the nanocrystals. . . . 62
4.3.1 UO_2 nanocrystals recovery. . . . 62
4.3.2 ThO_2 nanocrystals recovery. . . . 62
4.4 Characterisation of the as produced nanocrystals. . . . 64
4.4.1 Precipitates morphology and composition. . . . 64
4.4.1.1 UO_2 nanocrystals morphology. . . . 64
4.4.1.2 ThO_2 nanocrystals morphology. . . . 64
4.4.2 Precipitates crystal structure. . . . 66
4.4.2.1 UO_2 nanocrystal structure. . . . 67
4.4.2.2 ThO_2 nanocrystal structure. . . . 68
4.5 Results and discussion. . . . 70

5 Crystallization and Grain Growth in f(T) for nc-UO_2 by Aqueous route 73
5.1 Generalities. . . . 73
5.2 Thermal evolution and mass changes as probed by TGA/DTA. . . . 73
5.3 Lattice parameter and crystal growth in neutral atmosphere. . . . 74
5.3.1 Grain growth as a function of temperature under neutral atmosphere. . . . 75
5.3.2 Lattice parameter and linear thermal expansion coefficient as a function of temperature. . . . 76
5.3.3 Lattice strain evolution as a function of temperature. . . . 80
5.4 Lattice parameter and crystal growth under reducing conditions. . . . 80
5.4.1 Crystal size and lattice parameter evolution as a function of temperature as probed by XRD. . . . 80
5.4.2 O/M ratio as a function of temperature as probed by XANES. . 83
5.4.3 Order and disorder probed by local methods, as Debye-Waller EXAFS, NMR and FTIR, as a function of crystal size. . . . 87
5.4.3.1 Local structures as probed by Debye-Waller EXAFS distances. . . . 87
5.4.3.2 Local structure and valence state as probed by MAS NMR. . . . 89
5.4.3.3 Local structure and valence state as probed by FTIR. . 94
5.5 nc-UO_2 long-isothermal grain growth as probed by XRD under neutral and reducing conditions. . . . 98
5.6 Results and discussion. . . . 103

6 Crystallization and Grain Growth in f(T) for nc-UO_2 by Organic route 111
6.1 Generalities. . . . 111
6.2 Thermal evolution and mass changes as probed by TGA/DTA. . . . 111
6.3 Lattice parameter and crystal growth in neutral atmosphere. . . . 111
6.3.1 Grain growth as a function of temperature under neutral atmosphere. . . . 113
6.3.2 Lattice parameter and linear thermal expansion coefficient as a function of temperature. . . . 114
6.3.3 Lattice strain evolution as a function of temperature. . . . 117
6.4 Lattice parameter and crystal growth under reducing conditions. . . . 117
6.4.1 Crystal size and lattice parameter evolution as a function of temperature as probed by XRD. . . . 117
6.4.2 O/M ratio as a function of temperature as probed by XANES. . 119
6.4.3 Order and disorder probed by local methods, as Debye-Waller EXAFS, as a function of crystal size. . . . 124
6.5 Results and discussion. . . . 124

7 nc-UO_2 monolith consolidation and characterization 129
7.1 Introduction and principles. . . . 129
7.2 Compaction methods . . . 130
7.2.1 Conventional uniaxial pressing . . . 130
7.2.2 Float-packing . . . 131
7.3 Characterization of the nc-UO_2 monoliths. . . . 132
7.3.1 Green Specimens. . . . 132
7.3.1.1 Conventional pressed pellets of nc-UO_2 from aqueous route. With/without thermally pre-treated powder. . . 132

7.3.1.2 Float packing consolidation of nc-UO_2 from aqueous route in pellet form. . . . 133
7.3.1.3 Conventional pressed pellet of nc-UO_2 from organic route. Thermally pre-treated powder. . . . 133
7.3.2 Sintered of the nc-UO_2 green bodies. . . . 134
7.3.3 Macro and microstructural characterization of the nc-UO_2 monoliths. . . . 138
7.3.4 Results and discussion. . . . 145
7.4 Mechanical properties of nc-UO_2. . . . 147
7.4.1 Hardness and Young's modulus of nc-UO_2 monoliths as probed by Vickers and Knoop indentation. . . . 147
7.4.2 Young's modulus as probed by scanning acoustic microscopy (SAM). . . . 152
7.4.3 Bulk and Young's modulus of nc-UO_2 as a function of the crystal size by high pressure XRD. . . . 153
7.4.4 Results and discussion. . . . 158
7.5 Thermophysical properties of nc-UO_2 monoliths. . . . 162
7.5.1 Thermal Diffusivity in nc-UO_2 monoliths. . . . 163
7.5.2 Melting Point Depression in nc-UO_2 monoliths. . . . 163
7.5.3 Results and discussion. . . . 165
7.6 Results and discussion. . . . 166

8 Overall Discussion and Conclusions 171
8.1 Synthesis of nc-UO_2 and nc-ThO_2. . . . 171
8.2 Crystallization and Grain Growth in f(T) for nc-UO_2. . . . 173
8.3 Structure and oxygen-stoichiometry studies by XRD, XANES, EXAFS, NMR AND FTIR. . . . 175
8.4 nc-UO_2 monolith consolidation and characterization. . . . 179

9 Future Recommendations 183
9.1 Synthesis of the nanoparticles. . . . 183
9.1.1 Synthesis of ThO_2 nanoparticles to study a unique valence system. 183
9.1.2 Synthesis of PuO_2 nanoparticles and ^{238}Pu doping to enable damage in the nc-UO_2. . . . 183
9.1.3 Synthesis of nanoparticles of different controlled sizes. . . . 183
9.1.4 Use of ThO_2 nanorods as reinforcement in the the nc-monoliths to increase strength. . . . 183
9.2 Basic science of nc-actinide oxides. . . . 184
9.3 Alternative monolith compaction and sintering methods. . . . 184
9.3.1 Sintering of commercial nc-Y-ZrO_2 by spark plasma sintering (SPS), as substitute of nc-UO_2. . . . 184
9.3.2 Centrifugal casting 185
9.4 nc-UO_2 in extreme conditions. . . . 186

Institute for Transuranium Elements (ITU) 194

List of Tables 195

List of Figures 199

Bibliography 214

List of Symbols and Abbreviations

α Thermal Diffusivity ($m \cdot s^{-1}$)

ΔE_0 Threshold energy shift (eV)

λ Thermal Conductivity ($W \cdot m^{-1} \cdot K^{-1}$)

ρ Density ($g \cdot cm^{-3}$)

σ^2 Debye-Waller factor ((Å^2))

τ Relaxation time (h)

θ Diffraction angle (°)

υ Poisson modulus

a Knoop- long diagonal (mm)

b Knoop- short diagonal (mm)

B_0 Compressibility modulus (GPa)

c cubic

C_p Heat capacity at constant pressure

C_v Heat capacity at constant volume

CN Coordination Number

d Vickers- average diagonal (mm)

D_i Diffusion coefficient (m^2/s)

E Potential (V)

e Lattice strain

F Faraday constant

F Load (N)

f fix parameters

fcc face centered cubic

G_0 Starting grain size (nm)

G_L Limited grain size (nm)

H Hardness (GPa)

H_K Knoop Hardness number (-)

H_V Vickers Hardness number (-)

I Intensity (A)

i Current density (mA/cm^2)

k_B Boltzmann constant ($8.6173324 \cdot 10^{-5} eV \cdot K^{-1}$)

KIc Fracture toughness ($MPa \cdot m^{\frac{1}{2}}$)

m monoclinic

Q Charge (C)

Q_{diff} Activation energy of diffusion (eV)

R Interatomic distance ((Å))

t tetragonal

V_R Rayleigh wave velocity (m/s^{-1})

1H NMR Hydrogen Nuclear Magnetic Resonance

%FIMA % Fissions per Initial Metal Atom

a Lattice parameter

a.u. arbitrary units

am amorphous

An Actinide

atm. atmosphere

BM-EOS Birch-Murnaghan equation of state

BU Burn-Up

c crystalline

CV Cyclic Voltammetry

DLS Dynamic Light Scattering

DSC Differential Scanning Calorimeter

DW Debye-Waller factor

E Young's modulus (GPa)

EDX Energy-Dispersive X-ray spectroscopy

EELS Electron Energy Loss Spectroscopy

EOS Equation of state

EXAFS Extended X-ray Absorption Fine Structure

FP Fission products

FT Fourier Transform

FTIR Fourier Transform Infrared spectroscopy

FWHM Full Width at Half Maximum

GB Grain boundary

Gen Generation

GOF Goodness of fit value

GWd/tM Gigawatt-days per ton of fissile metal atoms

HAADF High Angle Annular Dark Field

HBS High Burn-up Structure

HP High Pressure

HP-XRD High Pressure X-Ray Diffraction

HRTEM High Resolution TEM

HT-XRD High Temperaure X-Ray Diffraction

IR Infrared spectroscopy

ITU Institute for Transuranium Elements

LAF Laser Flash

LIBD Laser-Induced Breakdown Detection

LOCA Loss of Coolant Accident

LP Low Pressure

LTE Linear Thermal Expansion

LTEC Linear Thermal Expansion Coefficient

LVDT Linear Variable Differential Transformer

LWR Light Water Reactor

M Molarity (mol/L)

MAS-NMR Magic Angle Spinning Nuclear Magnetic Resonance

nc Nanocrystalline

NIR Near InfraRed

NMR Nuclear Magnetic Resonance spectroscopy

NPs Nanoparticles

O/M Oxygen to metal ratio

OA Oleic Acid

OAM Oleylamine

ODE Octadecene

OM Optical Microscopy

OOA N-(*cis*-9-octadecenyl)oleamide

PCCI Pellet Clad Chemical Interaction

PCI Pellet Clad Interaction

PCMI Pellet Clad Mechanical Interaction

PCS Photon Correlation Spectroscopy

PTT previous Powder Thermal Treatment

PWR Pressurized Water Reactor

R_f Goodness of fit (%)

RIA Reactivity Initiated Accident

rpm Revolutions per minute

RT Room Temperature

SAED Selected Area Electron Diffraction

SAM Scanning Acoustic Microscopy

SEM Scanning Electron Microscopy

SF SIMFUEL or simulated nuclear fuel

SPS Spark plasma sintering

STEM Scanning Transmission Electron Microscopy

TD theoretical density (%)

TEM Transmission Electron Microscopy

TGA/DTA Thermogravimetry/Differential-Thermal Analysis

ThA Thorium Acetate

ThAA Thorium AcetylAcetonate

TODS 3,6,9-Trioxadecanoic acid

TZP Tetragonal Zirconia Polycrystals

UAA Uranyl AcetylAcetonate

V-EOS Vinet equation of state

WL White-Line

XANES X-ray Absorption Near Edge Structure

XAS X-ray Absorption Spectroscopy

XRD X-Ray Diffraction

Y-ZrO_2 4 mol% $Y_2O_3ZrO_2$

Chapter 1

Introduction

1.1 Background and state of the art.

Today's nuclear fuels are largely based on uranium dioxide (UO_2). A high level of proficiency has been reached, with fuels achieving moderate to high burn-up (BU) in the reactor. In nuclear power technology, BU (also known as fuel utilisation) is a measure of the amount of energy extracted from the primary nuclear fuel source. It is defined as the fraction of fuel atoms that underwent fission in % fissions per initial metal atom (%FIMA). But also as the actual energy released per mass of initial fuel in gigawatt-days per ton of fissile metal atoms (GWd/tM).

To go beyond the today's achievements a more radical approach may be needed, which will enable the fuel to reach yet higher BUs. This is desirable for the reduction of the amount of fresh fuel required and the mass of spent fuel inventories (radioactive waste). To achieve these goals, improved fission gas retention capability of the fuel is required as well as a solution to the pellet clad mechanical and chemical interaction (PCMI and PCCI) failure risks problem is needed, which could intensify at high BUs due to boosted cladding embrittlement.

The current nuclear electricity plants are based predominantly on light water reactors (LWR). The fuel is produced, after enrichment, by conversion of UF_6 (uranium hexafluoride) to UO_2. The product is a powder which is pressed and sintered at high temperature to provide a solid fuel generally in the form of cylindrical pellets. The pellets are stacked into zircalloy tubes known as cans or clads. The filled cans sealed with arc-welded end plugs are known as rods or pins. The sealed zircalloy (alloy of zirconium and tin) clad provides a tight encapsulation that serves as a barrier between the fuel and the coolant (water), and avoids the escape of radioactive fission-products. Between the pellet and the cladding there is initially a gap of 80-100 μm under cold conditions. It cannot be too large or it would cause the fuel to operate at higher temperatures because of the larger separation to the coolant. But this small space is fundamental to avoid or delay the possible fuel-cladding contact because of pellet expansion during irradiation. The fuels rods are held together with a fixed (usually square type) configuration by several spacer grids, which constitute altogether the fuel assemblies that are loaded into the core of the reactor (Fig. 1.1).

The fission energy is transformed to heat in the fuel pellet due to collision of fission fragments with the surrounding fuel material and by gamma ray emission and radioactive decay of the produced isotopes, which delivers a great amount of heat.

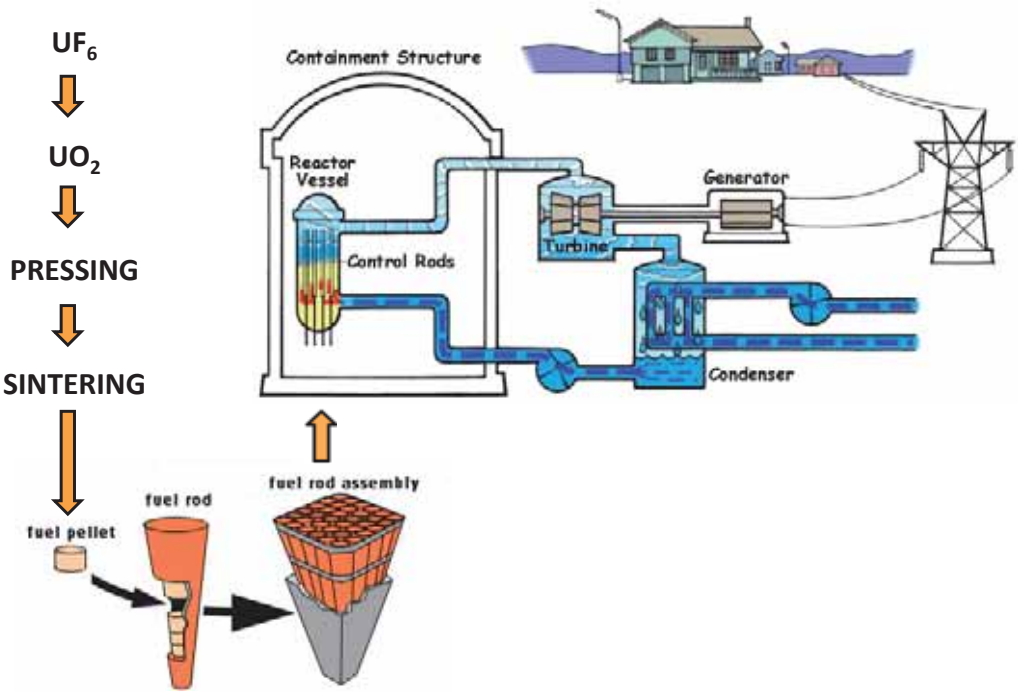

Figure 1.1: Light Water Reactor [The energy net, 2012] [U.S.NRC, 2012].

This heat is transferred to the coolant (water), which passes by the clad, generating water vapour. This steam feeds conventional generators (steam-driven turbines) in the primary (for BWR) or secondary (for PWR) loop which produce the electricity.

The fuel pellet inside the nuclear reactor is a material subjected to extreme conditions which change its properties with time and irradiation dose. Each atom in the fuel is displaced several times during its irradiation history but many return to equivalent crystallographic positions. Damage and local defects like interstitials, loops and vacancies are created. UO_2 is a poor heat conductor, therefore the heat transfer from the centre to the surface of the pellet is slow. A typical temperature profile of a LWR pellet is shown in Fig. 1.2 [Konings et al., 2011]. Furthermore, accumulation of solid fission products in the lattice and formation of gas bubbles make the pellet thermal conductivity to decrease. The fission gases precipitate in bubbles and lead eventually to compositional and microstructural changes, swelling of the fuel, as well as to embrittlement and hardening of the cladding. Other effects occur in the central sections of the fuel pellet (at higher temperature) and include grain growth, porosity build-up and an augmented gas release [Kleykamp, 1979] [Stehle et al., 1975]. Fig. 1.3-*left* shows a fuel decorated with cracks after four reactor cycles (approximately four years). On the right side of the figure, the evolution of the geometry of the pellets inside a rod can be observed. Fuel cracks appear from the beginning of the irradiation due to thermal stresses. The fuel pellets swell owing to the accumulation of fission gas bubbles in the matrix and the segregation of low density fission-products phases (metallic and ceramic precipitates). As a result of the swelling, the fuel approaches the clad. Physical and/or chemical interaction can occur upon contact, which can induce clad deterioration and rupture [Garzarolli et al., 1979]. These type of changes can affect also the temperature profile of the fuel pellet (Fig. 1.2) by modification of

the gap thermal transfer conditions, limiting the life time of the fuel (and BUs) inside the reactor, if premature rod rupture occurs.

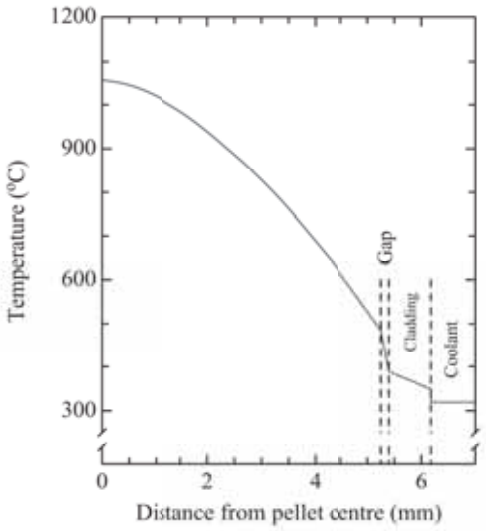

Figure 1.2: A typical temperature profile of a LWR fuel as a function of the fuel pin radius [Konings et al., 2011].

A vast amount of work has been made in the last decades to characterise the behaviour of high BU fuels and to deepen the knowledge of the underlying phenomena, with the aim to increase the usage time of the fuel in the reactor [Watteau et al., 2001]. Besides that, in the last 20 years also a large increase of the research activities in nanocrystalline (nc)-materials for different aims and applications has been ostensible [Kulisch et al., 2009] [Mathur and Singh, 2009]. The question arises whether these two apparently disconnected research areas would overlap and whether a link between nc-materials and high BU nuclear fuel materials would exist. The answer to this question is attempted below.

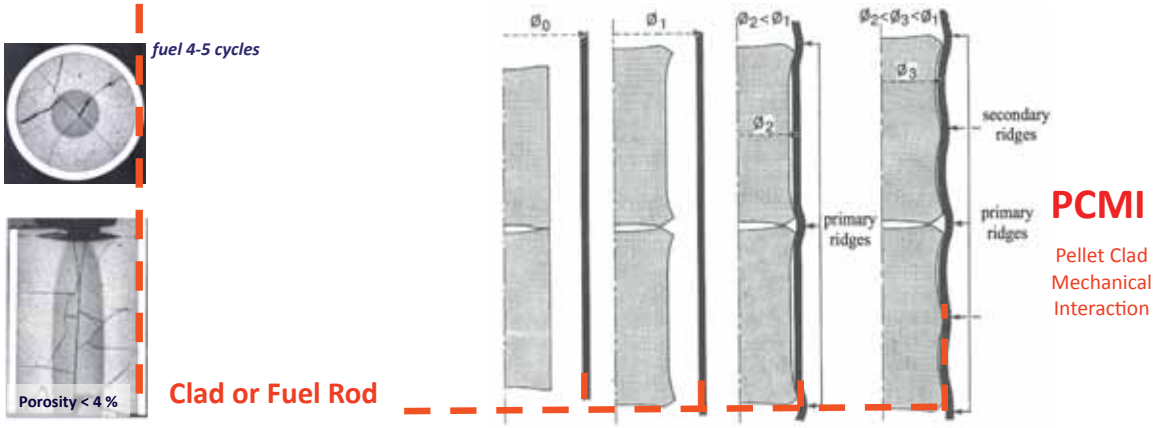

Figure 1.3: Macrograph of a fuel pellet after irradiation showing the typical radial cracks *(left)*. Pellet inside the pin illustrating the swelling with the irradiation time *(right)*. [Bailly et al., 1996].

Indeed, nuclear fuels approximately at the end of the third irradiation cycle

(about 40 GWd/tM) undergo a structure transformation which begins at the edge of the fuel pellet and steadily progresses to its centre as the irradiation proceeds [Matzke and Spino, 1997] [Spino and Papaioannou, 2000]. The original microstructure transforms into a nc-porous matrix [Nogita and Une, 1994] through restructuring of the accumulated irradiation defects. This is a sort of "self-healing" action where the material gets cured from damage by reordering itself [Spino et al., 2012]. Fig. 1.4 shows two ceramographs of different fuel zones at increasing local BU and where the mentioned change in the structure is clearly appreciated. The new nc-structure appearing (Fig. 1.4-*right*-micrograph) is called high burn-up structure (HBS). It is called also rim-structure because in UO_2 fuels it initiates at the rim or outer zones (r/R>0.98) of the pellets (colder periphery of the pellet; Fig. 1.4-*right*). This happens because the rim is the region which receives the highest dose (the most fissions) and therefore is exposed to highest local increase of BU (∼70 GWd/tM in the third cycle, at temperatures rarely exceeding 800°C [Sonoda et al., 2002]), and so the highest radiation damage, too.

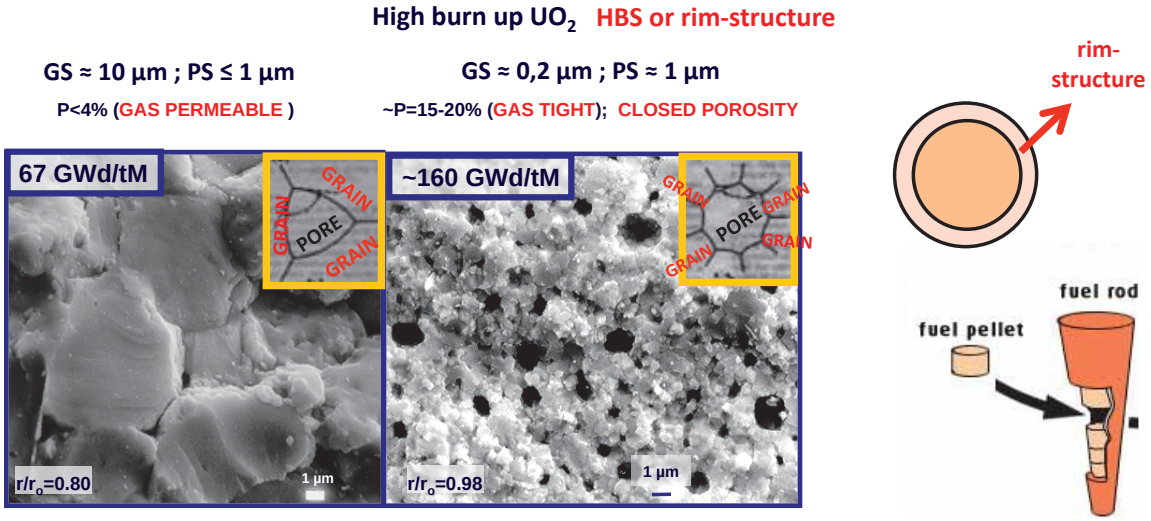

Figure 1.4: Micrographs at different pellet radius areas [Spino and Papaioannou, 2008]. High burn-up structure (HBS or rim-structure) transformation [The energy net, 2012].

Most of the properties observed in the HBS, resemble those seen in the nanomaterial's structures. Likewise heavily cold worked metals which after severe plastic deformation show grains in the nm-size range [Villegas and Shaw, 2009], the heavily damaged high-BU fuel region at the rim of the pellets display a profound modification of the microstructure on exceeding a critical dose. After this threshold, the original nuclear fuel with large-grains (10-20 μm) suffers progressively grain subdivision (low-angle sub-grain formation or low coordination number) and recrystallization (high-angle sub-grain formation or high coordination number) changes (Fig. 1.5) at the end of which a new structure (the HBS) with uniformly nm-sized grains (100-250 nm) appears [Spino et al., 2012]. This transformation to a structure with nm-grains at the edge (rim) of the pellet results in lattice contraction [Spino and Papaioannou, 2000]. Furthermore, formation of new 1 μm-sized pores embedded in the matrix (Fig. 1.5) occurs, which entraps most of the created fission gas [Spino et al., 1996]. This porosity can reach values above 20%.

At the beginning it was thought that the HBS could be responsible for cladding failures due to additional in-pile volume increase (swelling), which, in addition to

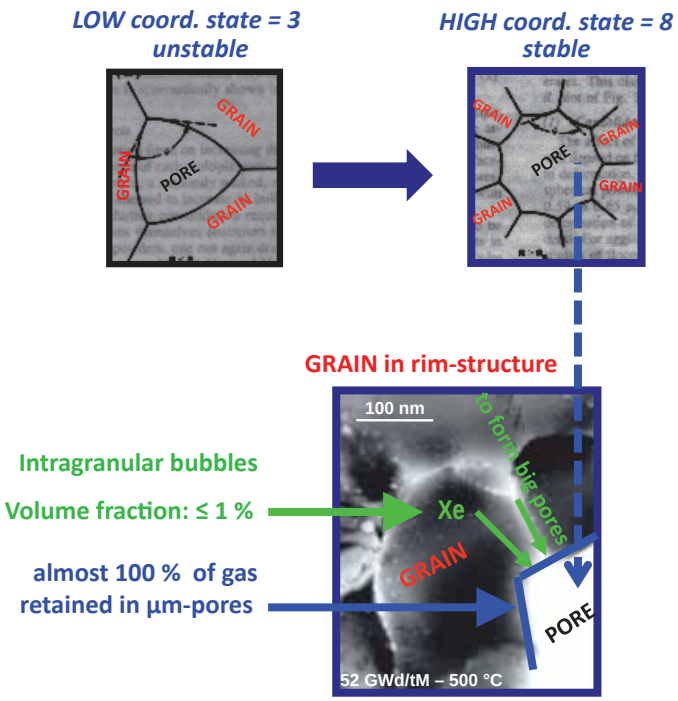

Figure 1.5: Coordination state change in the transformation to the HBS (or rim-structure).

the supposed brittle behaviour of the transformed material [Matzke, 1992], lead to proposals of pellet-design changes to counteract the transformation [Swam, 1997] [Tulenko and Wang, 2008]. Also, it was thought that the rim-structure could act as a new source of gas release. In fact, one could think that the larger the grains (e.g. 10-20 μm, as in the original fuel or the fuel with lower high-BUs), the longer the pathways for the fission gases towards the grain boundaries and the exterior, and consequently, the more generally improved fission gas retention behaviour in comparison with the small grains of the HBS (0.2 μm grains). Indeed, there are still investigation lines which defend this opinion.

However, other studies found that the percentage of gas liberated from the rim of the fuel pellets, where the HBS appeared, was low in comparison with the gas coming from the inner parts of the pellet where the original larger-grain structure is still present [Mogensen et al., 1999]. This philosophy has been followed by other publications, which demonstrates a generally beneficial evolution of the fuel properties, as in particular the retention of the fission gases, after the structure transformation [Rondinella and Wiss, 2010], [Spino et al., 2012]. Specifically, it has been observed that the HBS does not develop an open pore structure with interconnected channels, even at higher porosities [Noirot et al., 2008].

In fact, it has been seen that structures with large grains (10-20 μm) and with 1 μm pores and porosities below 4% (in the original fuel and the fuels with low BUs; Fig. 1.4-*left*), are permeable to the flow of gases. In contrast, the rim-structure with small grains (100-250 nm) and with 1 μm pores and 20% porosity (Fig. 1.4-*right*), was suggested to remain gas tightly because of the formed closed porosity [Spino et al., 2004] [Hiernaut et al., 2008]. Moreover the larged-grained structures are found to retain large amount of dislocation loops and gas bubbles inside the grains, which diminishes the mechanical properties (creep strain), increasing the risk of

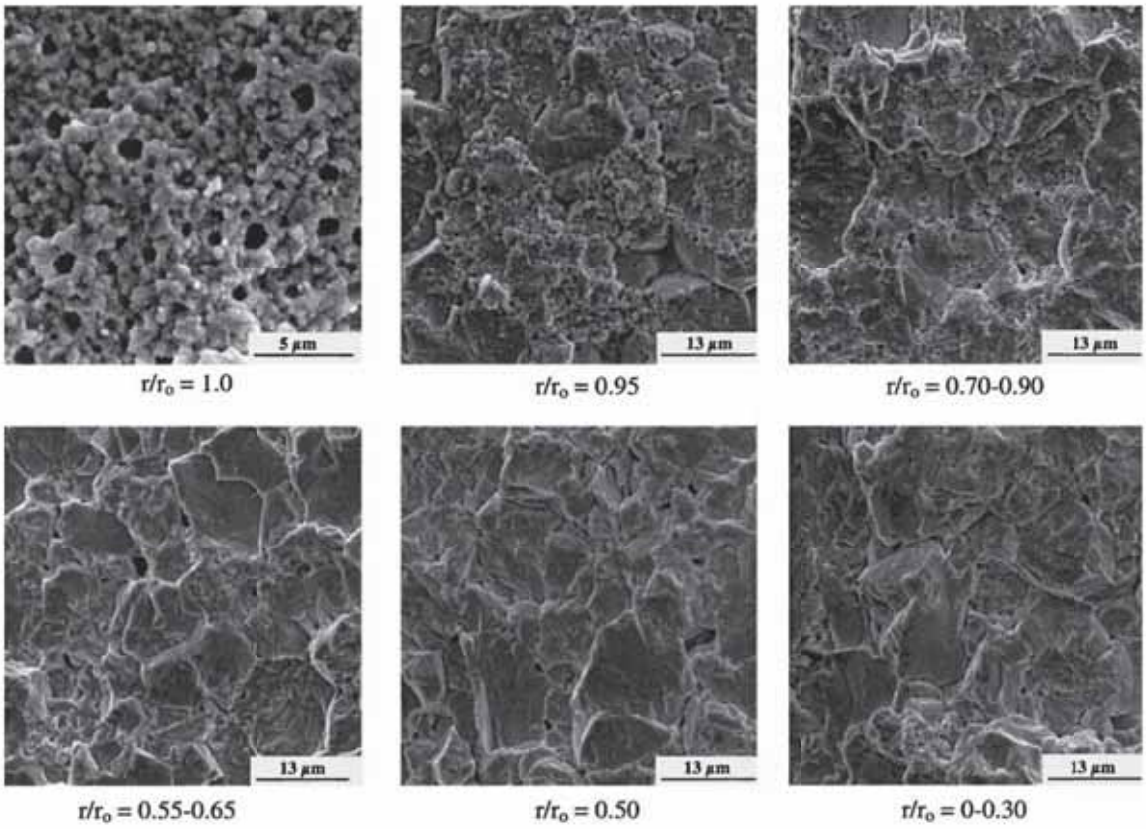

Figure 1.6: SEM micrographs of a fuel pellet at high-BU from the outer radius or rim (HBS in the first micrograph) to inner radial positions from [Manzel and Walker, 2002].

PCMI. In contrast, the small-grained structures with their high-angle sub-grain (high coordination state; Fig. 1.5) facilitating the GBs sliding deformation mechanisms, show improvement of the plasticity and creep strain, diminishing the PCMI-failure risks [Chung and Davies, 1979] [Spino et al., 2008].

Besides that, the properties of the HBS indicate an enhanced radiation tolerance as reported by [Spino et al., 2012]. This study coincided with important evidence in the literature that nano-grained materials are more resilient to radiation damage than the corresponding large-grained materials due to defect recombination at their multiple grain boundaries has been reported by [Nita et al., 2005]. Also improvement of the thermal conductivity and other radiation-defects depending properties was found due to lattice-strain release after recrystallization [Ronchi et al., 2004], as well as fracture toughness increase and crack-healing tendency were anticipated [Spino et al., 2003].

Moreover, in relation to safety issues, the latest experiments on the high BU LWR fuels indicated no increase in the gas release and in the failure susceptibility during reactivity initiated accident (RIA) transients [Sasajima et al., 2010] [Fuketa et al., 2006]. Also diminution of the aqueous corrosion rate under simulated geologic repository conditions for fuels containing HBS was found out [Ekeroth et al., 2009] [Carbol et al., 2009]. Both facts confirmed the tightness of the structure.

So it has been demonstrated that the HBS has exceptional qualities even in comparison with the original matrix (large-grain structure), with a number of improved properties that are really advantageous for a fuel. Then, why not imitate this recrys-

tallized material?. And why not imitate the structure appearing in the rim (HBS) and introduce it in this form as a fresh fuel inside the reactor?. Why not synthesise a fuel matrix like this HBS, which due to its apparent damage-resilience would withstand longer times under irradiation?.

This is a radical step in nuclear fuel conception, hitherto not considered, since, as indicated before, the general thinking of the industry (fuel providers and utilities) was until now just the contrary one, i.e. trying to make larger and larger grains, under the premise to improve only one aspect of the fuel performance, namely the fission-gas release under steady state conditions, disregarding the implied worsening of the fuel plasticity due to grain-size increase, and also its poorer behaviour under power-ramps.

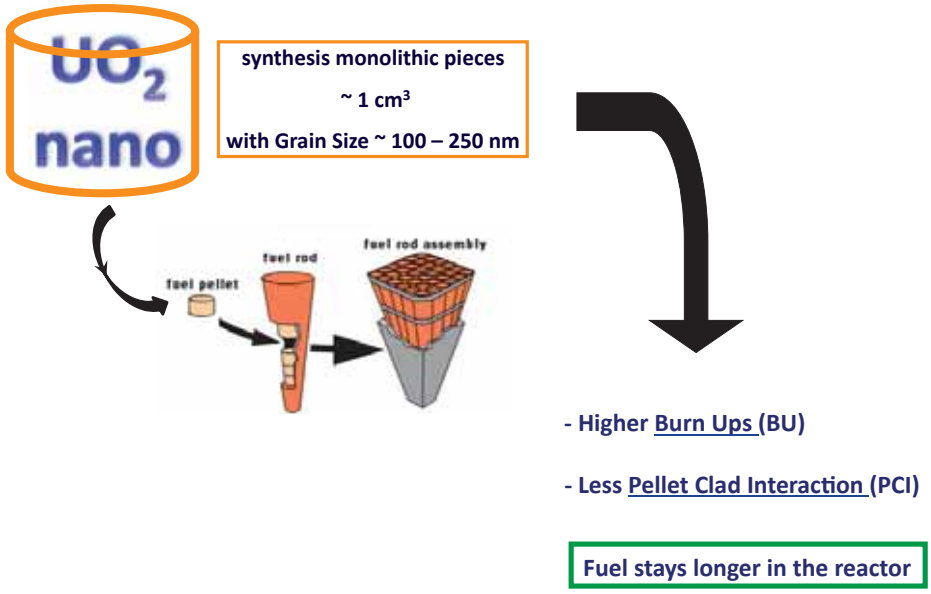

Figure 1.7: A novel fuel microstructure: nc-UO_2 [The energy net, 2012].

On the contrary, apart from its still unproven improved resistance against radiation-damage (e.g. reduced swelling), the principal virtues of nc-fuels in-pile compared to conventional fuels will be the faster relaxation of PCI stresses through the higher plasticity induced by grain-refinement, plus the possibility of retention of most fission gases in formed closed pores. As a potential technological application, and as inspired in the behaviour of HBS-material in pile, the nc-fuel could retain fission gases inside the pores up to very high-BUs (>300 GWd/tM). Up to these BUs values, the porosity could increase up to 30%, until incipient pore interconnection would first begin [Konings et al., 2011].

The main aim here is thence to synthesise nc-UO_2 powders for the manufacture of bulk nc-fuel compounds for the characterization of their out-of-pile mechanical properties and irradiation behaviour. The produced monolithic pieces would have a volume of approximately 1 cm^3, with a uniform grain size between 100 and 250 nm to mimic the rim-structure.

The first question which appears is how to obtain enough amount of nc-UO_2 powder for fabrication trials of bulk-pieces, when the known methods of nanoparticle synthesis are generally tuned to yield just small amounts of material (mg range), primarily

dedicated to analytical or research uses [Rousseau et al., 2002] [Mennecart et al., 2004] [Wu et al., 2006] [Rousseau et al., 2006] [Opel et al., 2007] [Rousseau et al., 2009]. The second important interrogate that arises then is how to obtain thereof dense large monoliths with uniform grain size around 200 nm, when the achievement of bulk nc-bodies is today one of the most demanding challenges in nanotechnology.

The traditional methods for the production of UO_2 are based on the precipitation of U^{VI} salt from liquid solutions. Then the precipitated material is oxidised to U_3O_8 by oxidative thermal treatment and afterwards the conversion to UO_2 (U^{IV}) is reached by a second heat treatment under reducing conditions (800°C under Ar/H_2). All these processes together provide a powder material which is further conditioned by different physical-chemical/mechanical methods to give a compositionally stable (in air) and free-flowing agglomerate, suitable to be compacted by standard powder metallurgy techniques (basically uniaxial-bidirectional pressing). The standard characteristics of commercial "ready-to-press" UO_2-powders have a $UO_{2.1}$ composition, agglomerate particle size 20-40 μm and crystallite size 200-500 nm. After pressing to desired geometry, final sintering of the compact (1600°C during 16 h) is necessary to get the desired density, of 95 to 98% of the theoretical density (TD_{UO_2}=10.96 g/cm^3). However, the final grain size obtained by this conventional material synthesis route is in the range of 5-10 μm, which is far above the goal here (100-250 nm).

1.2 Goal of the thesis.

The main goal in the present work was to develop an accessible route to produce defect-free nc-UO_2-based monolithic ceramic specimens with tailored grain/pore microstructure. The target configuration consisted of a dense, uniform matrix with 100-250 nm sized grains with porosity levels of 10 to 20% to reproduce out-of-pile the properties of the HBS material, using similar methods as utilized in the previously studied case of nc-Y-ZrO_2 [Santa-Cruz, 2009]. Once this goal was accomplished, a study to determine their physical-chemical properties and their damage resistance in comparison with micron-grained materials was performed.

The creation of the above novel fuel microstructure has been achieved in this work by passing through very different steps. From the material synthesis to the fuel pellet manufacture, many individual process stages, previously unknown or unexplored, had to be specifically developed and/or optimized. Hence, regarding the initial powder, considerable work was devoted to the development of two different chemical synthesis routes leading to deflocculated nc-UO_2 and nc-ThO_2 precipitates. ThO_2 is similar in structure to UO_2 but has the advantage of a single valency (i.e. IV).

Although much information can be found about nano-chemistry and actinides-chemistry, not very much information on the synthesis of nanoparticles with actinides compounds is available. The objective of the few reported works is, in the majority of cases, concerned with the issue of radionuclide release control during spent fuel geological disposal, namely the ultimate dissolution/re-precipitation of actinides in a in a fractured geological repository, by non-excludable contact of damaged spent fuels with water [Rousseau et al., 2002], [O'Loughlin et al., 2003]. The target in these cases is to examine the radiological hazards which could emerge from these situations and to quantify the effect of radioactivity release (and potential environment contamina-

tion) on possible long-term permanence of spent fuels in contact with groundwater [Mennecart et al., 2004], [Rousseau et al., 2006]. Also the study of the elementary oxidation mechanisms occurring on an atomic scale on fuel/water contact during spent fuel storage has been performed with actinide oxide colloids [Opel et al., 2007], [Rousseau et al., 2009]. Other nanostructures based on uranium oxides have been used for catalytic purposes [Wang et al., 2008]. In other cases, the possible study of size-dependent physical and chemical properties has motivated the synthesis of high-quality colloidial of UO_2 [Wu et al., 2006].

Despite that, no publications of the above describe the production of nc-actinides other than as in the very small quantities needed for research or analytical studies. Although enough for these purposes, no monolith ceramic as desired in this work could be achieved with such (small) amounts of material. For the mimicking of the HBS nc-microstructure in whole UO_2-pellet between 0.5 and 1.0 g of nc-UO_2 powder are needed. Therefore, a method with a definitely higher material's yield must be developed.

In the present work, two of the above reported methods for the synthesis the nc-UO_2 were chosen and developed as a source for the nc-powder needed to perform the described monoliths. In Chap. 3 the first one is described. This is a controlled precipitation method that uses an electrolytically reduced aqueous solution of uranyl nitrate as precursor and dropped NaOH-solution as alkalinisation agent to trigger the precipitation of the nc-material in the vicinity of the U^{4+} solubility line, which was originally described in [Rousseau et al., 2002], [Rousseau et al., 2006]. The second method, described in Chap. 4, is a thermal decomposition of an organic phase containing uranyl acetylacetonate (UAA) as precursor, which is added to a mixture of oleic acid and oleylamine which is then heated as a whole up to temperatures around 300°C to induce the precipitation of UO_2 nanoparticles by thermal decomposition of the UAA. This original procedure was described in [Wu et al., 2006]. To obtain larger amounts of nc-UO_2 as required, both methods were conveniently adjusted, developed and scaled-up according to the aim needs. The material in the as-produced condition was studied by TEM and XRD. Crystallization and grain-growth kinetics of the synthesized powders as a function of the temperature and time, as well as structure characterization at the different temperatures, follow in Chap. 5 and Chap. 6, for the aqueous controlled precipitation and the organic precipitation, respectively. Tools such as TGA/DTA, XRD, HT-XRD, TEM, NMR, IR and XANES/EXAFS were used for this purpose. The results on thermally treated powders provided useful information for the selection of ideal sintering conditions for the posterior synthesis nc-monoliths. In Chap. 7 the consolidation of the green monoliths, as well as different thermal routines for the drying and sintering steps, which represent a challenge for the achievement of crack-free dense specimens, were explored. Optical, mechanical and thermophysical characterization of the sintered bodies followed to verify their aptitude to meet nuclear reactor fuel specifications. Characterization techniques as SEM, indentation, HP-XRD, SAM, thermal diffusivity and melting point were used. Chap. 8 summarizes the discussions of the different chapters in a final conclusion of the overall results. Finally Chap. 9 concentrates different future recommendations for the project. Some of them have been already initiated during the thesis and presented here, e.g., alternatives for monoliths compaction, study of nc-UO_2 magnetic properties and out-of-pile simulation experiments.

Chapter 2

Analytical and characterization techniques

2.1 Electrochemical analysis

The instrument used was a SP-50 voltammeter from BioLogic Science Instruments (working ranges 2.8-10 V and 10 μA - 400 mA).

2.1.1 Cyclic Voltammetry (CV)

A three electrode system configuration was utilized. A working electrode (~1 mm thick rod in spiral form, composition Pt/Ir 90/10% metal from Heraeus and Fisher type with introduced area=1.885 cm^2 Fig. 2.1a), an auxiliary or counting electrode (net, composition Pt/Ir 90/10% metal from Heraeus and Fisher type with 0.12 mm net-wire thickness, 38 mm in diameter and 50 mm in height Fig. 2.1a), and a reference electrode (Ag/AgCl InLab® Reference saturated from Mettler Toledo). A 150 mL glass-reactor built for these experiments was also used (Fig. 2.1b).

(a) Net, spiral, frit (b) Reactor

Figure 2.1: Cyclic voltammetry experimental arrangement.

In a cyclic voltammetry (CV) analysis, the current density i (mA/cm^2) is plotted versus the applied voltage or potential E (V). Where i is the intensity or current at the

working electrode I (A), divided by the area of the working electrode (spiral) introduced in the solution. The conductivity of the solution supported by the addition of an electrolyte solution (NaCl, HCl). For comparison, the different cyclic voltammogram scans should be performed with the same immersed area of the working electrode.

The scan of current density vs. voltage produces a peak for any component in the solution that is reduced/oxidized (depending on the initial scan direction) throughout the range of potentials scanned. The current increases as the potential reaches the corresponding values for the reduction of the different species present in solution, and that are redox active, inside the potential window. But then falls off as the concentration of the system is depleted close to the electrode surface.

The redox reaction $UO_2^{2+} + 4H^+ + 2e^- \longleftrightarrow U^{4+} + 2H_2O$ occurs at the working electrode (spiral). The potential was measured between the reference electrode and the working electrode. The current applied by the potentiostat was measured between the working electrode and the counter electrode (net).

2.1.2 Electrolysis

In the electrochemical reduction the potential is measured between the reference electrode (Ag/AgCl saturated) and the working electrode (net). The current applied by the potentiostat is measured between the working electrode (net) and the counter electrode (spiral). The expected cell reactions during electrochemical reduction of U^{VI} are for the cathode (or working electrode):

$$UO_2^{2+} + 4H^+ + 2e^- \longleftrightarrow U^{4+} + 2H_2O \tag{2.1}$$

and for the anode (or counting electrode),

$$2H_2O \longleftrightarrow 4H^+ + 4e^- + O_2 \tag{2.2}$$

providing the global reaction,

$$2UO_2^{2+} + 4H^+ \longleftrightarrow O_2 + 2H_2O + 2U^{4+} \tag{2.3}$$

The intensity passing across the solution was plotted as a function of the time and the real charge (Q_{real}) passed across the solution was then calculated as:

$$Q = I \cdot t \tag{2.4}$$

where

I= current in amperes (A)

t = time in seconds (s)

The theoretical charge ($Q_{theoretical}$) required to reduce the UO_2^{2+}/U^{+4} species, was calculated as,

$$Q = F \cdot n(e^-) \tag{2.5}$$

where

Q = Charge in coulombs (C)

F = Faraday constant = 96500 C $\cdot$ mol^{-1}

$n(e^-)$ = moles of electrons = 2 $\cdot$ $n(e^-)_{UO_2^{2+}}$ (from Eq. 2.1)

where $n(e^-)_{UO_2^{2+}}$ corresponds to the number of moles of U present in the initial solution.

The conversion rate as a function of time was controlled by monitoring the charge passed across the solution and by the decrease of the intensity of the peak UO_2^{2+}/U^{+4}, which is proportional to the presence of U^{VI} in the liquid, in the different CV measurements done while running the experiment. The corresponding expressions are:

$$Conversion\ rate = \frac{I}{n(e^-) \cdot F} = flux = \frac{dC}{dt} \tag{2.6}$$

$$Conversion\ rate\ (\%) = \frac{Q_{real}}{Q_{theoretical}} \cdot 100\ (\%) \tag{2.7}$$

$$Conversion\ rate\ (\%) = \frac{(i_0 - i)}{i_0} \cdot 100\ (\%) \tag{2.8}$$

where

Q_{real} = Charge in coulombs (C) applied to the solution.

$Q_{theoretical}$ = Charge in coulombs (C) theoretically necessary to be applied to reduce the U-moles added to the solution.

i_0 = current intensity of the UO_2^{2+}/U^{+4} peak observed in the CV run before the beginning of the electrochemical reduction.

i = current intensity of the UO_2^{2+}/U^{+4} peak observed in the CV at each time during the electrochemical reduction.

2.2 Spectroscopy

2.2.1 Ultraviolet-visible spectroscopy (UV-Vis)

The UV-Vis absorption spectres were recorded using a Lambda 9 UV-Vis/NIR spectrophotometer (Perkin Elmer) in the wavelength range from 360-470 nm with a scan speed of 15 nm/min (slit width 0.5 nm).

The ultraviolet-visible spectroscopy (UV-Vis) uses light in the range close to UV and near infrared (NIR). The absorption in the UV range is directly dependent with the solution color changes, and therefore with the presence amount of one or other ion.

2.2.2 Dynamic Light Scattering (DLS)

Dynamic Light Scattering (DLS) (also known as Photon Correlation Spectroscopy (PCS)) measures Brownian motion and relates this to the size of the particles. It does this by illuminating the particles with a laser and analysing the intensity fluctuations in the scattered light.

A Nano ZS system from Malvern with working ranges 0.3 nm to 5 μm, has been used to measure the rate of the intensity fluctuation and then to calculate the size of the particles. A quartz cell was used to performance the measurement.

2.2.3 X-ray Absorption Near Edge Structure (XANES) and Extended X-ray Absorption Fine Structure (EXAFS)

Bulk-XAS data at the U-L_3 and Th-L_3 edges were collected at the INE Beamline at the Ångströmquelle Karlsruhe (ANKA) [Brendebach et al., 2007] [Rothe et al., 2012]. The beamline is equipped with a Ge(422) double-crystal monochromator coupled to collimating and focusing rhodium-coated mirrors was used. The monochromator angle was calibrated in transmission mode for the U-L_3 and Th-L_3 edges by assigning the energy of 17038 eV to the first inflection point of the K-edge absorption spectrum of yttrium metal foil. For each X-ray absorption near-edge structure (XANES) measurement, the spectra of the reference foil was systematically collected at the same time. All measurements were recorded at room temperature in transmission mode using argon filled ionization chambers at one bar pressure. The E_0 values at the absorption edge were taken at the first inflection point using the first zero-crossing value of the second derivative. The energy of white-line (WL) maximum at the edge was selected using the first zero-crossing of the first derivative. Several acquisitions (four to six spectra depending on the edge) were performed on the same sample to improve the signal-to-noise ratio. To determine the oxidation states of U in the studied samples, XANES spectra at L_3 edge of reference materials were collected during the same experimental run using the same experimental arrangement. UO_2 and ThO_2 were used as reference for the *IV*-valence of U and Th, respectively. In addition, the extended X-ray absorption fine structure (EXAFS) measurements of UO_2 was analysed to ensure that stoichiometric compounds were obtained. The valence of U and the corresponding molar fractions of U^{IV}, U^{V} and U^{VI} were determined according to a linear combination of UO_2 (pure U^{IV}), U_4O_9 (mixture of U^{IV} and U^{V}) and U_3O_8 (mixture of U^{IV} and U^{VI}). The energy position of the absorption edge of an U-L_3 edge XANES spectrum is directly related to the chemical state of U. Therefore, the U oxidation state can be estimated by comparison of an "unknown" spectrum with a set of spectra of suitable reference compounds.

All EXAFS spectra oscillations were extracted from raw absorption data with the *ATHENA* interface of the IFFEFIT software [Newville, 2001] [Ravel and Newville, 2005]. Experimental EXAFS spectra were Fourier-transformed using a Hanning window over the full k-range available at the respective edges. The FT peaks of interest were selected and fitted in reciprocal space with the *ARTEMIS* interface of the IFFEFIT software [Ravel and Newville, 2005]. Amplitude and phase shifts functions were calculated using FEFF 8.40 [Rehr et al., 1998]. Spherical 7.5 Å clusters of atoms built using the UO_2 fluorite-type structure (space group *Fm-3m*) were used for FEFF calculations. This symmetry can be described as a simple cubic

packing of anions with cations in the cubic (eight-coordinate) holes. Thus, the U cations are surrounded by shells of 8 O anions, 12 U cations and 24 O anions. For each shell, the coordination numbers were fixed to these theoretical values and were fitted separately. Considering the negligible difference in the calculated amplitude and phase shifts, cation-cation shells were modelled using one metallic backscattering element. In addition, the multiple-scattering paths were also considered in the FEFF calculations. The amplitude factor (S_0^2) was set at 0.90 for the U shell. The shift in the threshold energy (ΔE_0) was varied as a global parameter.

The U in this study were derived from existing stocks of uranyl nitrate powder (for the synthesis of nc-UO_2 by the aqueous route Chap. 3) and from commercial UAA, ThAA and ThA powder (for the organic route Chap. 4). Sample preparation involved crushing of nanocrystalline UO_2, blending it with MgO as a support matrix, and compaction of the mixture into a disk for X-ray absorption measurements. The disk was mounted in a special holder, and double-sealing it by means of two polyethylene bags. Sample integrity and homogeneity were checked prior to shipment using X-ray radiography. UO_2 and ThO_2 μm size were used as reference samples for the measurements. The reference UO_2 was thermally treated at 1600°C under Ar/5%H_2 for 6 hours to provide an oxygen/metal ratio (O/M) of 2.00.

2.2.4 Nuclear Magnetic Resonance spectroscopy (NMR)

Solid-state Nuclear Magnetic Resonance (NMR) is a very efficient probe of the local environment in materials. This technique is based on the analysis of the nuclear spin. To obtain high resolution spectra, the sample is spun at an angle of 54.74° with respect to the static magnetic field. This technique is named magic angle spinning (MAS). For the study of our uranium dioxides, ^{17}O is the only nucleus which can be detected. As its natural abundance is of 0.038% an enrichment of the samples is required. A synthesis of nc-UO_2 by controlled precipitation following the method described in Chap. 3 in ^{17}O 10% enriched aqueous phase was performed. To achieve that, 5 mL of water enriched at 90% with ^{17}O was added to the initial $UO_2(NO_3)_2$-solution. The total U concentration in solution was smaller (0.19 M) as the one used in a normal process (0.5 M). The objective was just to have enough material (about 2 g of UO_2 were obtained) for all the analyses needed, having the maximum concentration in ^{17}O. During precipitation of the nc-UO_2 by addition of NaOH 3 M solution, the experiment solution passed from an enrichment of ^{17}O 11.84% to ^{17}O 8.74% because of the dilution.

The series of nc-UO_2 enriched in ^{17}O were afterwards annealed at the following temperatures: 200°C, 600°C, 650°C, 700°C, 800°C and 1200°C. The heating was done under dry Ar/5%H_2 for 15 minutes. As a reference, a standard UO_2 ($\sim \mu$m crystal size) sintered at 1600°C under Ar/5%H_2 for 6 h and measured during the same campaign, was used.

All the ^{17}O experiments were acquired on a 9.4 T Bruker spectrometer using a 1.3 mm probe-head. The ^{17}O rotor-synchronised Hahn-echo MAS-NMR spectra were acquired at 55 kHz (typically operating temperature of 40°C). The ^{17}O peak of a $H_2^{17}O$ sample was used as reference and defined as 0 ppm. First and second pulse durations were set to 3 μs ($\pi/2$) and 6 μs (π), respectively, with an echo delay of 2 rotor periods (9.1 μs). As the longitudinal relaxation time (T_1) is fast, a recycling delay of 100 ms was used for all the samples.

2.2.5 Infrared spectroscopy (IR)

Infrared spectroscopy (IR) gives information on the composition and chemical structure of a component. In this case nc-UO_2 samples were analysed. The nc-UO_2 synthesized were annealed at 200°C, 600°C and 1200°C. The heating was done under dry Ar/5%H_2 for 15 min. As a reference, a standard UO_2 ($\sim$ μm crystal size) sintered at 1600°C under Ar/5%H_2 for 6 h and measured during the same campaign, was used. All the samples were measured in an Alpha FT-IR Spectrometer from Brucker able to measure in the spectral range from 375 to 7500 cm^{-1}.

2.3 Electron microscopy

2.3.1 Scanning Electron Microscopy (SEM)

From the initial samples a small piece was broken (fresh fracture) for microstructure characterization using scanning electron microscopy (SEM), energy dispersive and wave length dispersive X-ray analysis (EDX-WDX) and X-ray diffraction (XRD). Some of the samples were sputtered with gold for SEM-EDX-WDX observations but good images were obtained without sputtering because the conductivity of UO_2.

The SEM used was a Vega Tescan TS 5130-LSH, 200 eV-30 KeV, with a magnification range of 3-1000000 times and a resolution of 3 nm. The SEM was equipped with an EDX-detector (10 mm^2, Si(Li), 110 eV-80 KeV, resolution <138 eV) and a WDX-analyser (4 diffracting crystals = LiF, PET, TAP, LSM80, spectral resolution $\leq$ 2 eV) of Oxford Instruments.

The scanning electron microscope (SEM) used was a Vega Tescan TS 5130-LSH, 200 eV-30 KeV, with a magnification range of 3-1000000 times and a resolution of 3 nm. The SEM was equipped with an EDX-detector (10 mm^2, Si(Li), 110 eV-80 KeV, resolution <138 eV) and a WDX-analyser (4 diffracting crystals = LiF, PET, TAP, LSM80, spectral resolution $\leq$ 2 eV) of Oxford Instruments.

2.3.2 Transmission Electron Microscopy (TEM)

The morphologies and dimensions of the samples were revealed by transmission electron microscope (TEM). The TEM investigations were conducted with a specially modified FEI Tecnai G2 F20 XT apparatus for the analyses of radioactive materials. This unique design provides excellent capabilities for the analysis of radioactive specimens. The TEM is operating at 200 kV and equipped with a Gatan GIF Triedem, an additional Gatan slow scan camera and an EDAX EDS Genesis System. A beryllium window is used to protect the EDS detector against alpha radiation. To avoid radioactive contamination during the sample transfer, a glove box with controlled atmosphere was mounted around the measuring unit (FEI CompuStage).

The specimens for TEM imaging were prepared by suspending the solid particles in ethanol or hexane (depending on the sample), with the suspension being placed in

an ultrasonic bath and sonicated agitated for 15 min. A drop of the well dispersed suspension was loaded on a carbon coated 200 mesh copper grid, which was dried under ambient conditions, before the grid was placed on the sample holder of the microscope. TEM techniques provide direct information on both size and shape of the nanoparticles and at the same time the structure of the single particles can be determined.

2.4 X-ray scattering

The average crystallite size, lattice parameter and micro-strain of the different powder analysed, have been determined by the X-ray diffraction (XRD) Rietveld refinement of the Bragg peaks with the HighScore Plus software [HSP-PAN, 2011], and used also to characterize the microstructure of the material. This analysis is based on the change of the profile parameters, compared to a standard sample. Those are depending on the instrument settings used for data collection and on the profile function used for the refinement [HSP-PAN, 2011]. A peak shape described by a Pseudo-Voigt function has been used for the microstructural refinement. The shape and width of the diffraction peak are a convolution of the instrumental broadening and the sample broadening. In general, data were taken at steps of 0.0146° in 2θ (θ = diffraction angle) with counting steps of 2 s, in the range 2θ = 10°-120°.

$$D = \frac{180}{\pi} \frac{\lambda}{(W - W_{std})^{0.5}} \tag{2.9}$$

where D is the crystallite size, λ is the wavelength of the radiation and W parameter contains the information about the size broadening.

$$e = \frac{[(U - U_{std}) - (W - W_{std})]^{0.5}}{\frac{1}{100}\frac{180}{\pi} \cdot 4 \cdot (2 \cdot Ln2)^{0.5}} \tag{2.10}$$

where e is the micro-strain and U parameter contains the information about the strain broadening.

2.4.1 Room Temperature X-Ray Diffraction (RT-XRD)

The XRD measurements were performed with a θ-2θ diffractometer D8 (Bruker AXS, Karlsruhe) operating in the Bragg-Brentano mode, with a Ge monochomator and a Cu-Kα_1 source (λ=0.15406 nm). The calibration (alignment and zero position checks) of the device was done with reference material LaB_6 (lanthanum hexaboride). The samples analysed were loaded on a flat specimen-holder of Si-911-crystal providing low background, which was continuously rotated during the measurements for better particle statistics.

2.4.2 High Temperaure X-Ray Diffraction (HT-XRD)

In situ HT-XRD patterns were acquired with a Bruker D8 powder diffractometer mounted in a Bragg-Brentano configuration, with a curved Ge monochromator [111],

a Cu X-ray tube (40 kV, 40 mA), and a Position Sensitive detector Braun covering an angular range of 6°(2θ) and an Anton Paar HTK2000 heating chamber. The alignment of the machine is done with reference material MgO at different temperatures.

2.5 Thermogravimetry/Differential Thermal Analysis (TGA/DTA)

Thermogravimetric analysis for the determination of mass changes and decomposition temperatures were carried out with a simultaneous thermogravimetry differential thermal analysis (TGA-DTA) system (NETZSCH Simultaneous Analyzer STA 449 Jupiter). For the tests Al_2O_3 crucibles were employed. For the correction of the gas buoyancy effect, base lines were measured with empty crucibles using the same experimental conditions as for the investigated samples.

2.6 Dilatometry

The sintering behaviour of green monoliths was determined by differential dilatometry with a Bähr Thermoanalyse DIL-802 S. The length change of the monolith was measured as a function of temperature relative to the length changes of a parallel reference sample (polycrystalline Al_2O_3) with similar dimensions.

2.7 Mechanical Characterization

2.7.1 Microindentation

The microindentations were performed with a Frank-Finotest hardness-tester according to the standard methods for advanced ceramics, ASTM C1327 for Vickers indentation hardness and ASTM C1326 for Knoop indentation hardness. The form of the these typical indenters is shown in Fig. 7.24. Loads of 1.96 N, 4.90 N and 9.80 N were applied for 15 seconds. For comparison an instrumented microindenter developed in ITU, was also used. In this case, loads of 0.49 N, 0.98 N, 1.96 N, 4.90 N and 9.80 N were applied also for 15 seconds. The acquisition of test data points was at room temperature. At least 3 to 5 different indentations (at different locations throughout the sample) were performed for each load applied and the average value taken for the calculations. Minimum distances between indentations were respected following the respective ASTM methods. Random representative areas of the material were always taken for the tests.

The samples were embedded in hard epoxy-resin, followed by grinding and polishing of the test surface. Special holders with two-sides plane-parallel geometry were used to ensure the perpendicularity of the indenter to the sample and, surface and in consequence, symmetrical indentations. Grinding of the samples was carried out with SiC paper (600 to 1200 mesh), as well as a final polishing with diamond suspensions was done, reducing progressively the particle size from 15 μm to 1 μm. A fine polishing was needed to achieve a perfect flat mirror surface and to avoid the addition of errors in

the determination of the indentation lengths due to surface roughness and imperfections.

2.7.2 High Pressure X-Ray Diffraction (HP-XRD)

The compressibility study of the different nano-sized UO_2 was performed by means of in-situ X-ray diffraction (XRD). The samples were loaded in a Diacell-type membrane diamond anvil cell with 500 μm culet size using pre-indented Re gaskets with 200 μm diameter holes. Pressure was determined using the ruby scale [Piermarini et al., 1975] and Cu equation of state (Cu-EOS). Silicone oil was used as pressure transmitting medium. High pressure X-ray diffraction (HP-XRD) was performed using a modified Bruker D8 x-ray diffractometer with focusing mirror optics installed on a molybdenum rotating anode source (Mo $K_{\alpha 1}$=0.70926 Å), coupled with a Bruker SMART Apex II Charged-Coupled Device (CCD). The recorded diffraction images were integrated using the ESRF FIT2D software [Rodríguez-Carvajal, 1993].

2.7.3 Scanning Acoustic Microscopy (SAM)

The scanning acoustic microscopy were performed in a collaboration with the group of Prof. Laux as part of a collaboration with IES (Institut d'Electronique du Sud) at University of Montpellier with an acoustic microscope in ITU developed (Fig. 2.2). The device includes a translation stage, micrometric motors, echographic bench, and acoustic focused sensors with spherical lens with an aperture angle of 50°. The samples should have a thickness of about 1 mm. Afterwards the samples are embedded in a resin and polished to obtain a smooth surface. The sample is introduced in an aluminium basked and methanol coupling liquid is poured until the embedded sample is completely submerged. After horizontal alignment with two adjusting screws the acoustic sensor is lowered avoiding to trap any air bubble which could lead to false readings. The sensor is further lowered until a few μm distance from the sample and defocusing is started in order to get an acoustic image. The signal from the sensor is converted to an optical signal to be displayed on a computer screen.

2.8 Thermophysical characterization

2.8.1 Thermal Diffusivity

The measurements of the thermal diffusivity are performed in a laser-flash device (LAF I) [Ronchi et al., 1999] inside a lead-shielded glove box with remote manipulators. The sample is heated up (Ar atmosphere of 10^{-2} mbar) in a high frequency furnace to the measurement temperature. A laser pulse is applied to one of the surfaces of the sample. At the opposite surface , the out-temperature perturbation is recorded by a photo-diode pyrometer (0.05°K sensitivity) with an in ITU developed log-amplifier with a rise-time of the order of 50 μs. The experimental set-up and the measurement technique are explained in detail by [Staicu, 2007].

The thermogram is recorded by a 14 bit digitalizer ($T = T(t)$ consisting of several thousands of points) and is analysed by a realistic and accurate mathematical model of the pulse propagation in the sample. The thermal diffusivity and heat losses are

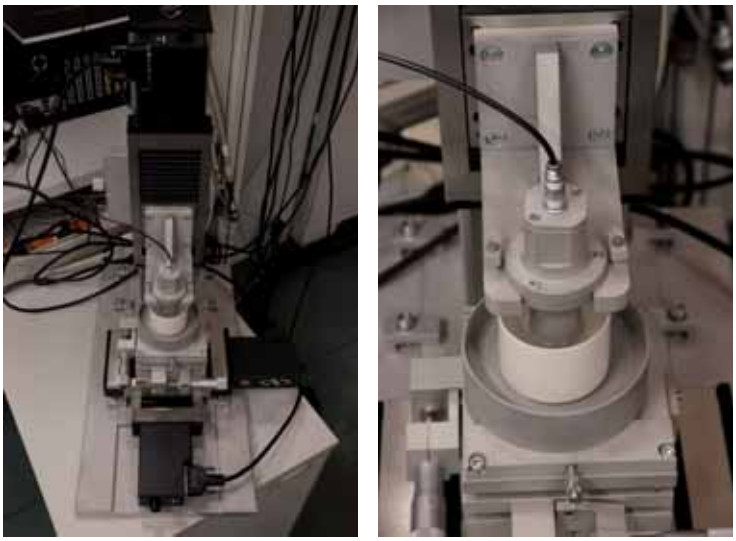

(a) (b)

Figure 2.2: Overview of the acoustic microscope (in ITU developed) device showing acoustic sensors, coupling liquid holder, sample platform and translation stages.

calculated by a numerical fitting method. Correct measurements of thermal diffusivity can be obtained even with samples of small sizes and irregular contours, due to the highly homogeneous probe laser-beam. The precision of the individual measurements is better than 1%. Nevertheless, the accuracy of the measured thermal diffusivity is lower than the precision of the method, being principally determined by sample thickness variations.

2.8.2 Melting Point

Same conditions as described in [Cappia et al., 2013] were used. A schematic of the laser heating experimental set-up can be also there seen and here reproduced (Fig. 2.3). The sample is introduced in an autoclave under controlled atmosphere and heated by a 4.5 kW cw Nd:YAG TRUMPF® laser. The power in function of the time profile is programmable with a resolution of 1 ms. The onset of melting is detected by the appearance of vibrations in the signal of a probe Ar^+ laser reflected by the sample surface (reflected light signal technique) [Manara et al., 2008]. The cooling of the sample occurs when the laser beam is switched off. Thermal arrests corresponding to solidification can then be observed on the thermograms recorded by fast pyrometers. These operate in the visible-near infrared range between 488 nm and 900 nm. The reference pyrometer wavelength is here 655 nm. This was calibrated according to the procedure reported in [Manara et al., 2008] [Böhler et al., 2012]. A dense sample of at least several microns in thickness are needed in order that the measurement is not influenced by the sample support. The normal spectral emissivity of urania has been assumed to be equal to 0.83 [Manara et al., 2005] [Cappia et al., 2013]. In Fig. 2.4 a picture of the sample melting point set-up, is shown.

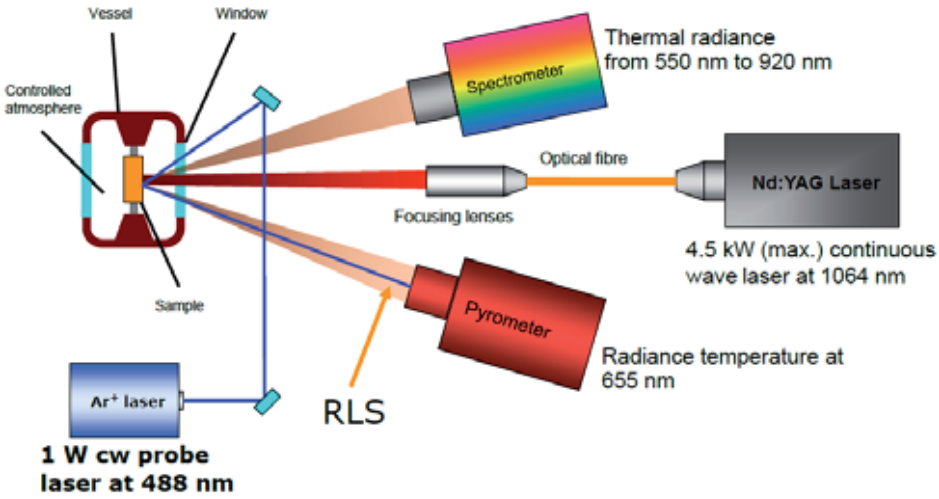

Figure 2.3: Laser heating experimental set-up [Cappia et al., 2013].

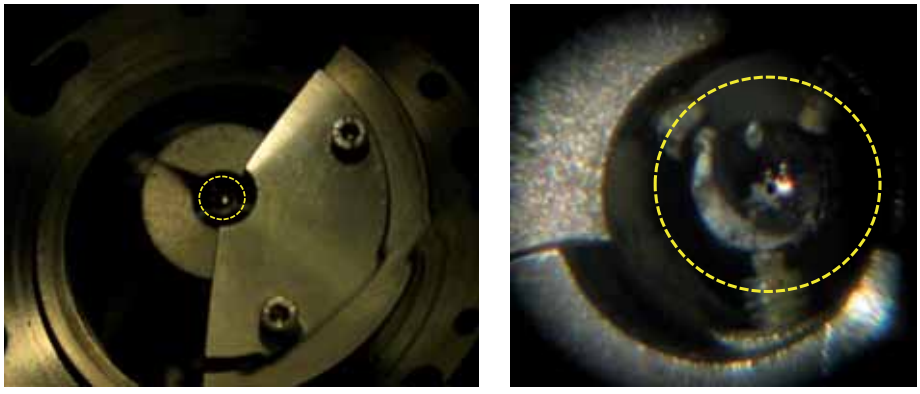

Figure 2.4: Sample melting point setup. In the yellow area, the nc-UO_2 pellet hold with three screws is observable.

Chapter 3

Synthesis of nc-UO_2 by controlled massive precipitation in Aqueous phase

3.1 Introduction and principles.

3.1.1 U-stability: environmental studies.

The control of used and present uranium mines, spent nuclear fuels and waste repositories installations is an ongoing subject. Related to the surveillance of these sites, the understanding of the dissolution/re-precipitation and transport behaviour of different radionuclides at different pH in aqueous media is essential to the avoidance of the contamination of the groundwater [Ryan and Rai, 1983]. The behaviour in water of U in its various forms, particularly as UO_2 in crystalline and amorphous states, needs to be understood. In the case of reducing conditions the disposal is facilitated by immobilization of the soluble U^{VI} species by its reduction and precipitation as insoluble U^{IV} in form of UO_2, and posterior removal after localization from the aqueous media [Lovley and Phillips, 1992].

The increase in the solubility and mobility of U^{IV} or U^{VI} species due to complexation with chloride [Hennig et al., 2005], carbonate [Suzuki et al., 2006] or sulphate [Hennig et al., 2007] anions, constitutes also a subject of attention for radiological issues. The possible of oxidative remobilization of the nanometer-sized precipitates [Suzuki et al., 2002] [Ling et al., 2008] by accidental contact with atmospheric O_2 [Zhong et al., 2005] or by radiolytical induced oxidation in water [Mennecart et al., 2004], is also matter of study.

A variety of parameters influence the systems involving UO_2 colloids. In particular, the precipitation/solubility of U colloids in aqueous media is affected by two issues. The trend to oxidation from U^{IV} to U^{VI}, as well as the hydrolysis of U^{IV} at very low pH (pH$\sim$1) by complexation of U^{4+} into $U_m(OH)_n^{(4m-n)}$ in solution ($mU^{4+} + nH_2O \longleftrightarrow U_m(OH)_n^{(4m-n)} + nH^+$) [Neck and Kim, 2001]. The presence of the colloids in solution is also function of the degree of acidity of the media. Finally, the colloids aggregation state (crystalline, amorphous), also plays a role in their precipitation/solution trends [Opel et al., 2007] [Rai et al., 2003].

3.1.2 U-redox chemistry pertinent to nc-UO_2 synthesis.

The precipitation in aqueous media of uranium colloids species at different pHs has been studied to gain a better understanding of these processes, with the objective to examine the radiological hazards implied in the deep disposal of radioactive waste [Rousseau et al., 2002]. The elementary mechanisms occurring on an atomic scale during fuel oxidation storage have been also studied with actinide colloids [Opel et al., 2007], [Rousseau et al., 2009].

The calculated equilibrium solubility lines of U^{IV} and U^{VI} species in aqueous solution as a function of pH have been reported by [Neck and Kim, 2001] [Fanghänel, Th. and Neck, 2002]. A plot of these results as compiled by [Gil et al., 2010] is shown in (Fig. 3.1). There are several orders of magnitude difference between the solubility of U^{IV} in presence of its crystalline dioxide phase, UO_2(c), or in presence of the amorphous form of this phase (hydrated uraninite, $UO_2 \cdot xH_2O$(am)). Also several orders of magnitude separate the two lasts with the solubility line of U^{VI} in the presence of the crystalline hydroxide phase schoepite, $UO_2(OH)_2$(s) (Fig. 3.1) [Gil et al., 2010]. Also valuable experimental data of the oxidation state of U in the precipitates and of the size of the corresponding colloids and their agglomerates, along the solubility line have been reported at different pH and low U-concentrations [Opel et al., 2007] [Rai et al., 2003] [Fujiwara et al., 2003] [Fujiwara et al., 2005]. The data show precipitates sizes of UO_2 ranging from 8-13 nm at around pH=1 in the crystalline state, to 80-150 nm at pH>2.5 in the amorphous state (Fig. 3.1). One can conclude that by provoking the precipitation close to the U^{IV} solubility line at lowest pH, the smallest and more crystalline form, of the precipitates can be obtained, avoiding possibly the precipitation of any uranium hydroxide compound.

According to the hitherto experience, the synthesis of nc-material using this method results, however, in small quantities of material produced and large quantities of waste. The concentrations of U per batch were of the order of 10^{-3} to 10^{-3} M [Rousseau et al., 2002] [Rousseau et al., 2006] [Opel et al., 2007] [Rousseau et al., 2009]. A challenge to tackle in this work will be hence to study the feasibility of this synthesis method for nc-UO_2 species, but extrapolated to quantities of product as high as 1 g per batch or higher so as to be able to produce dense monoliths with such material.

In the publications of [Rousseau et al., 2002] [Rousseau et al., 2006] [Rousseau et al., 2009], two methodologies to obtain nano-precipitates were used. Two pH ranges were studied, $\leq$4 and $\geq$4, with uranyl nitrate ($UO_2(NO_3)_2$) solutions dissolved in chloride media with U-concentrations of 0.005 M and 0.03 M, respectively. In both intervals, UO_{2+x} precipitates with elementary size 20 nm (without excluding agglomeration) and O/U ratio $\sim$ 2.19 were obtained [Suzuki et al., 2006] [Rousseau et al., 2002]. In the first method, an aliquot of U^{VI} solution was added to the precipitation reactor where reducing conditions were applied by a galvanostat (constant intensity) at a fixed pH. The dropped U^{VI} was reduced electrochemically to U^{IV} at a fixed pH and UO_{2+x} was so precipitated. In the second method used by these authors, the U^{VI}-solution was first reduced electrolytically to U^{IV} (to avoid precipitation of U^{VI} compounds which begins at pH$\geq$4) and thereafter it was slowly dropped into the precipitation vessel under reducing conditions, which were kept by application of constant potential. Simultaneously, the pH was held constant by

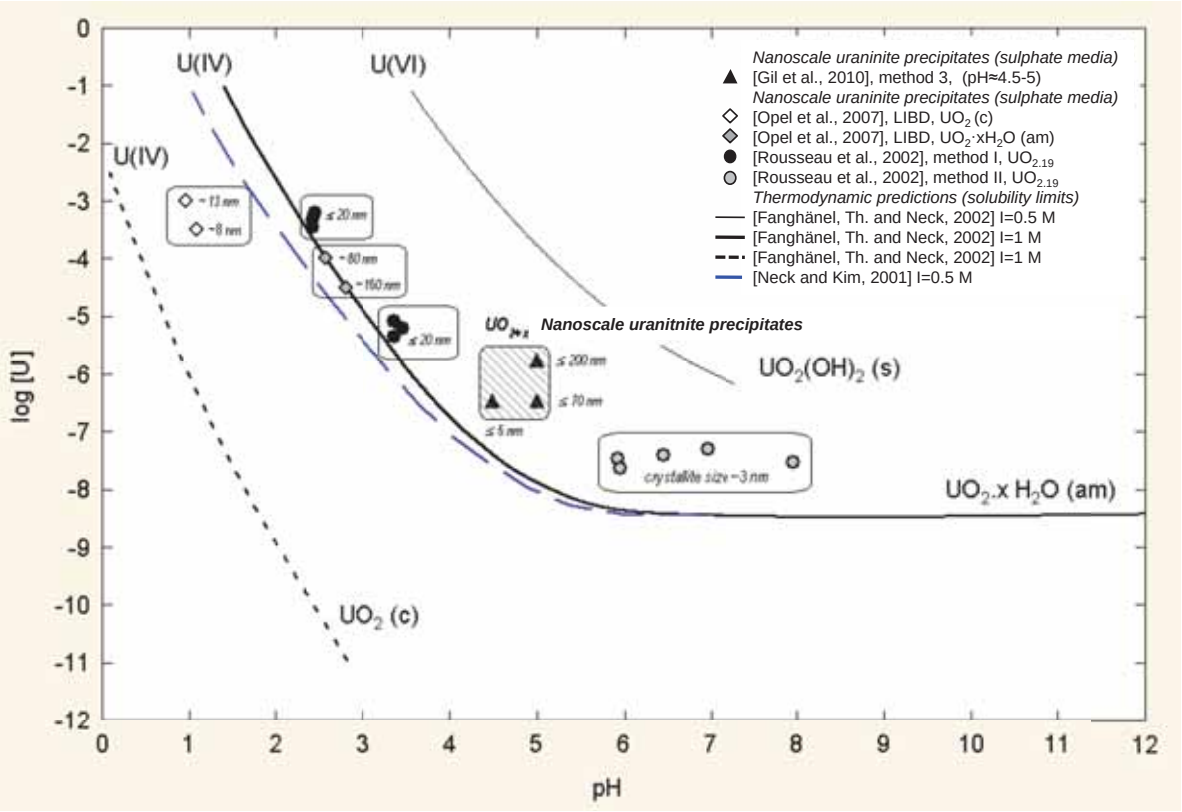

Figure 3.1: Theoretical solubility limits of U^{IV} and U^{VI} species in aqueous solutions [Fanghänel, Th. and Neck, 2002] [Neck and Kim, 2001] and experimental determinations for U-sulphate [Gil et al., 2010] and U-chloride solutions [Rousseau et al., 2002] [Opel et al., 2007]. Compounds shown beside each equilibrium line show the precipitated solid phase when these conditions are exceeded.

balancing the acidity of the U solution with controlled NaOH additions. Precipitation occurred thence instantaneously.

An intensive study of the range of U-concentration and acidity for nc-UO_{2+x} precipitation from electrolytically reduced uranyl nitrate ($UO_2(NO_3)_2$) solutions is hence endeavoured in the present work, using higher concentrations ranges, and therefore lower pH ranges, following the solubility line of U^{IV}. The use of higher concentrations and their correspondingly lower precipitation pH range, was already suggested but not tested by [Opel et al., 2007]. In their perchlorate system, these authors proposed moving upwards the U^{IV}-precipitation line towards lower pHs as a means to obtain nano-UO_2 precipitates in its crystalline form but upon diminishing the size of the agglomerates. In the present chapter, the same kind of concept will be applied.

3.1.3 nc-UO_2 synthesis principles.

For the nc-UO_2 synthesis by controlled precipitation in aqueous media, the starting $UO_2(NO_3)_2$ solution was reduced from U^{VI} to U^{IV}, before being precipitated by adding NaOH to the system. An initial study of the electrochemical reduction by cyclic voltammetry (CV) and an optimization of the different parameters have been also performed. A typical set-up used for the reduction and controlled precipitation, is shown in Fig. 3.2.

It consisted of a glove-box to house the entire configuration under inert atmosphere and as the first radioprotection barrier for the handling toxic materials. A seven-necked reactor was used where pH-electrode, reference electrode, counter electrode, working electrode, Ar-flow inlet tube, NaOH dosing tube and out-gas neck, were placed.

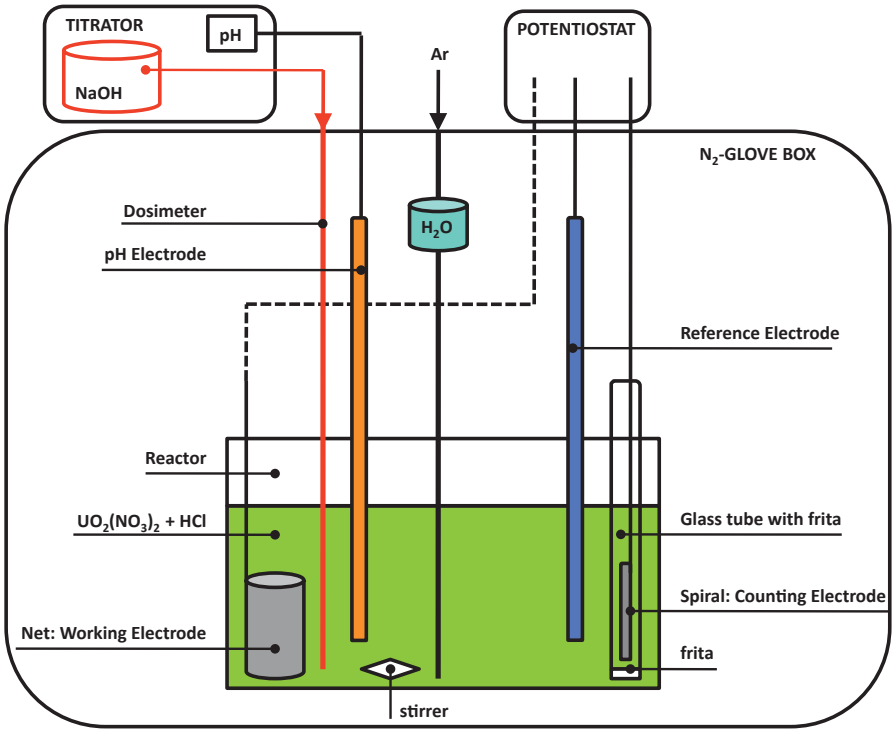

Figure 3.2: General set-up for reduction and controlled precipitation in a aqueous media method.

A flow chart showing the different steps performed in the process are shown in Fig. 3.3. The solution containing the U-salt was prepared and the pH was adjusted by HCl addition. The pH was kept below 1 to avoid hydrolysis of the U^{4+} cation (see Sec. 3.1.1) once the reduction of the U^{VI}-solution began.

In a second step, the initial U^{VI}-solution was electrochemically reduced at constant potential to U^{IV}, keeping the acidity of the solution below the precipitation pH for the given initial U-concentration in the solution (U^{IV}-solubility line Fig. 3.1). The state of electrolysis of the solution was controlled by continuous CV-checks, at the time that UV-vis absorption tests were performed.

After reduction of the solution, precipitation proceeded. Aliquots of NaOH were added into the solution where a series of stepwise precipitations were carried out. In the method reported by [Rousseau et al., 2009] the procedure was the other way around. In that case [Rousseau et al., 2009] aliquots of U-solution (reduced or unreduced depending on the method used) were added in a solution with higher pH where the precipitation was immediately taking place. The quantities of material per day and batch obtained were very small. By changing the procedure, and by increasing at the same time the U-concentrations in the solution (i.e. with respect to the ones

used by [Rousseau et al., 2009] and [Gil et al., 2010]), an increase of the yield of the precipitates was searched.

Black nc-UO_2-precipitates appeared so continuously until no more U^{IV}-cation was present in the solution. All reduction and precipitation experiments were conducted under anoxic conditions in a glove-box under N_2 atmosphere (oxygen $< 0.5\%$).

Centrifugation of the blackened solution was then performed to collect the precipitates. Removal of the Na^+ and Cl^- species still present on the surface of the wet nc-UO_2-precipitates was achieved by repeated washing with deionised water and sonification. Centrifugation after each washing step was needed to separate the precipitates from the water containing the dissolved Na^+ and Cl^- species washed.

In the course of the above experiments, the uranyl containing solutions changed its colour from yellow-green, characteristic of the uranium nitrate hexahydrate salt, to green dark colour, once the specie U^{VI} was reduced to U^{IV}. In both cases (oxidised and reduced), the solution had intense colour but no turbidity was observed. Once the first aliquots of NaOH were dropped into the reactor, the green coloured transparent U^{IV}-solution began to acquire turbidity because of the incipient UO_2 crystals precipitated. This green-turbid colour changed progressively to black with the following precipitation (see Fig. 3.3).

The morphology and structure of the obtained nc-UO_2 were characterized by means of Transmission Electron Microscope (TEM) and confirmed by X-Ray Diffraction (RT-XRD).

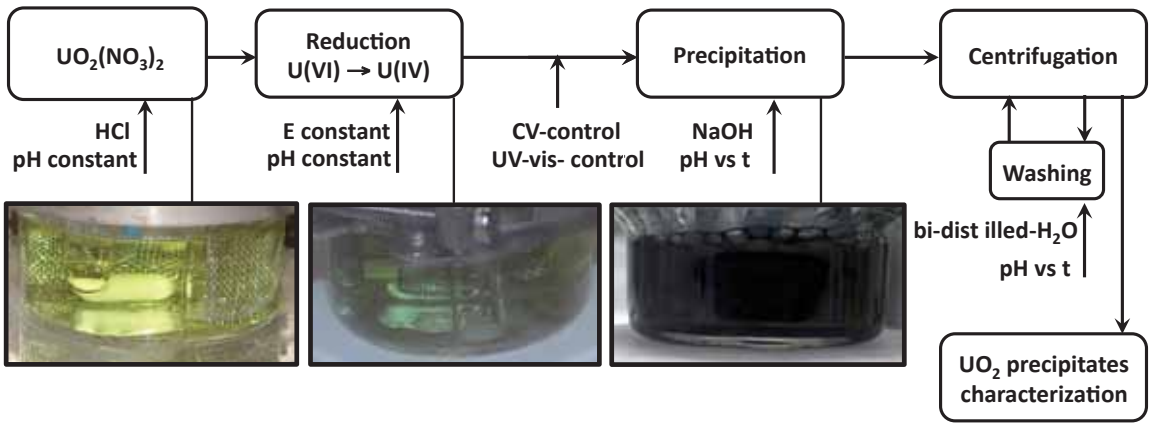

Figure 3.3: Controlled massive precipitation in aqueous phase steps.

3.2 Mother solution preparation.

The mother solution was prepared by dissolution of $UO_2(NO_3)_2$ powder (CAS: 10102-06-4; yellow green crystals; Fig. 3.4) in deionised water by continuous stirring at 80°C to reach a solution concentration of 500 gU/L. This mixture at room temperature (RT) was diluted in a NaCl 1 M solution to obtain final uranium concentrations in the

range 0.02-0.06 M.

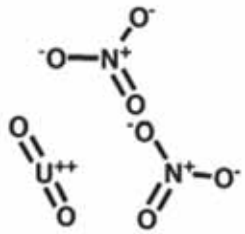

Figure 3.4: Uranyl Nitrate molecular structure.

Eventually, uranium concentrations of 0.5 M were used. Increasing the U-concentration, diminishes the pH at which the U^{IV}-oxide precipitates start to appear following the U^{IV} solubility line (Fig. 3.1). Therefore for higher U concentrated solutions, the 1 M NaCl was completely substituted by 1 M HCl to guarantee an initially sufficiently low pH to avoid any precipitation or hydrolysis of the U^{IV} during the electrolytic reduction. Deionised water and analytical grade reagents (HCl and NaOH from Alfa Aesar) were used to prepare the different solutions.

3.3 U^{IV}/U^{VI} cyclic voltammetric and spectrophotometric study.

3.3.1 Cyclic voltammetric study of the mother solution.

3.3.1.1 Experimental arrangement.

The electrochemical reduction characteristics were studied by cyclic voltammetry (CV) which is a voltamperometric technique. The study of the uranyl ion system under the influence of different parameters as use of separated compartment for the anode, different ion concentrations, acidic aqueous media and scan rates, were analysed. The study was carried out in a glove-box under anoxic conditions (nitrogen atmosphere with oxygen<0.5%) with a SP-50 voltammeter. A three electrode system configuration was utilized. A working electrode (spiral), an auxiliary or counting electrode (net) and a reference electrode (Ag/AgCl saturated). The three electrodes were immersed in the prepared solution using a 150 mL glass-reactor built for these experiments. CV-technique description and characteristics of the instrument, as well as the different electrodes and reactor used, are detailed in Sec. 2.1.

The set-up used was similar to the one shown in Fig. 3.2 but with some minor changes, which are reflected in Fig. 3.5. In the CV-studies, the net was used as counter electrode. Otherwise in the reduction of the solution the net was used as a working electrode. During the CV-studies, the dimensions of the working electrode must be kept small in order to enhance its tendency to become polarized. However, during the reduction of the pair UO_2^{2+}/U^{+4}, a bigger area of the working electrode is desired to achieve higher reduction rates. Therefore the use of the net (with bigger surface compared to the spiral) in the reduction as a working electrode, was preferred over the spiral one. A separated compartment (12 mm diameter glass tube with frit on the

bottom (see Fig. 3.5) was used in some of the CV-experiments to study its possible influence (acceleration of the reduction) in the posterior reduction of the solution (possible increase/diminution of reduction yield).

The solution contained the analyte $UO_2(NO_3)_2$ and an excess of the supporting electrolyte NaCl. The junction of the electrolyte, solvent and specific working electrode material determined the range of the potential to be applied. In this case, the U-analyte was redox active inside the experimental potential window (-0.4 V to +1.4 V vs. Ag/AgCl saturated).

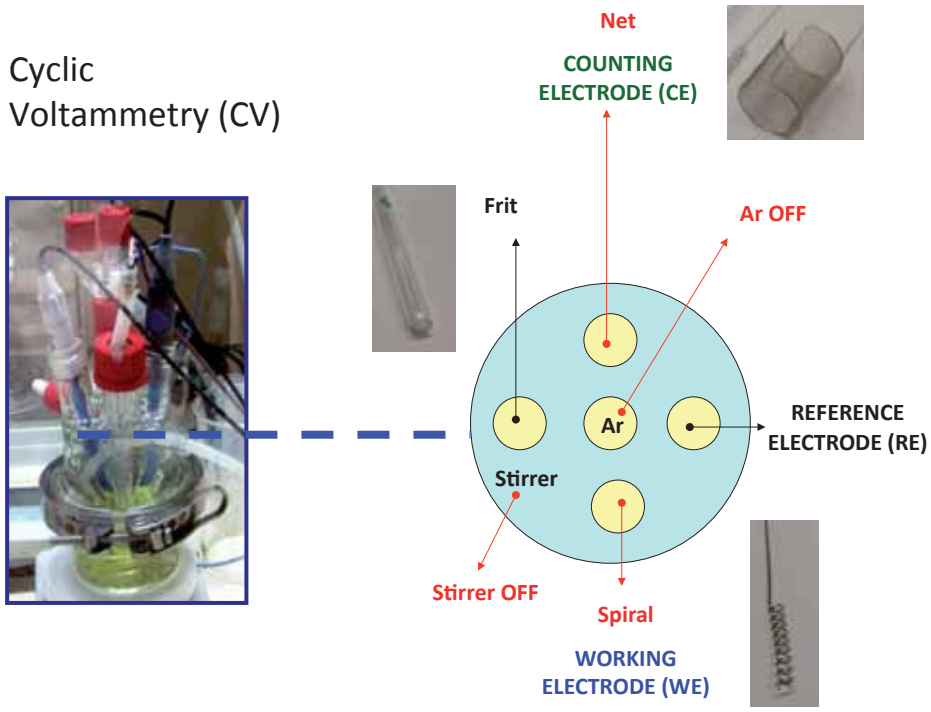

Figure 3.5: Cyclic voltammetry set-up.

Before beginning the CV analysis, the pH was measured with a pH glass electrode (iEcotrode Plus Metrohm 3 M KCl) in combination with a Titrando 906 instrument from Metrohm. Adjustment with HCl 1 M was made to achieve a solution with the desired pH depending on the experiment. Introduction of inert Ar gas, as well as stirring of the solution was made before beginning the CV runs during 15 min. The objective was to achieve the effective removal of the possible O_2 traces as well as a good mixing of the solution. During the CV measurement, the Ar supply and the stirrer agitation were stopped to avoid mechanical disturbance. For each CV study performed, new initial solution was used and careful cleaning of the electrodes was carried out. The Ar gas was passed through a deionised water bottle before entering into the reactor to avoid the solution to dry.

The potential was scanned as said between -0.4 and +1.4 V vs. Ag/AgCl saturated reference electrode, using different scan rates depending on the study. In this potential range, the NaCl (or the HCl) solution itself exhibited so called cathodic and anodic waves (peak at -0.4 for the reduction of the solvent and peak at +1.4 for the oxidation

of the solvent Fig. 3.6).

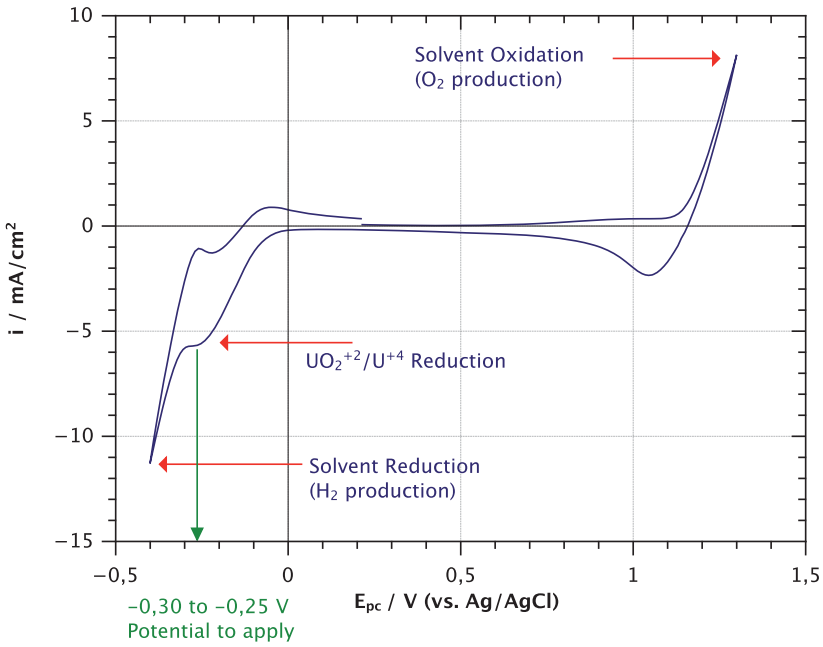

Figure 3.6: Cyclic voltammogram 0.1 M U and pH 0.5. $UO_2(NO_3)_2$ solution in NaCl 1 M scanned between -0.4 and +1.4 V vs. Ag/AgCl saturated at a scan rate of 0.1 V/s.

A single cathodic peak (E_{pc}) was observed between -0.30 and -0.25 V vs. Ag/AgCl corresponding to the reduction reaction of UO_2^{2+}/U^{+4}. The peak intensity is proportional to the amount of U^{VI} present in the solution. The coupled anodic peak (E_{pa}) expected for a reversible two-electron transfer process at 0.12 V was not always observed (theoretically $\triangle E_p = E_{pc} - E_{pa} = 0.12$ V).

Different experiments were conducted to optimize the conditions necessary to observe the UO_2^{2+}/U^{+4} reduction peak, and to check the influence of the different parameters on the system. The use of a separate containment for the anode, different analyte concentrations and scan rates, as well as different acidity levels of the solution, were examined.

In first instance, the use of a glass tube with a frit on the bottom (Fig. 3.5) as a separated compartment for the anode (introduced in the glass tube) during the reduction step was tested. Having both electrodes in the same bath, as proposed by [Rousseau et al., 2009] and [Gil et al., 2010], O_2 was continuously created inside the bath which caused species re-oxidation. The objective of the frit was to avoid as much as possible the passage of O_2 produced on the anode electrode, without influencing the free pass of the electrolyte. In this form, the reduction reaction was expected to be reinforced in front of the oxidation reaction.

Various porosity-grade (40, 100 and 160 μm) frits were studied but just the most porous one brought a real advantage with respect to the not use of the frit. For less porous frits, the reduction yield was slowed because the frit acted not only as a barrier for O_2 but also for the electrolyte. Opposite, with the use of more porous frits, the U-reduction was speeded in comparison to the case where the both electrodes stayed

nude in the same bath (no use of frit), as free pass of electrolyte was possible but major pass of O_2 was avoided. The time of the reduction reaction was thus notably decreased.

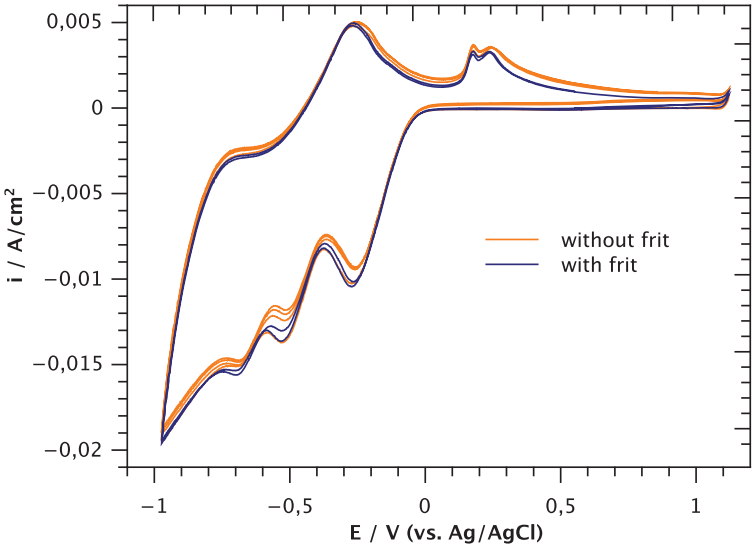

Figure 3.7: Influence of the frit on the system. Cyclic voltammogram 0.02 M U and pH=3. $UO_2(NO_3)_2$ solution in NaCl 1 M scanned between -1.0 and +1.2 V vs. Ag/AgCl saturated at a scan rate of 0.1 V/s.

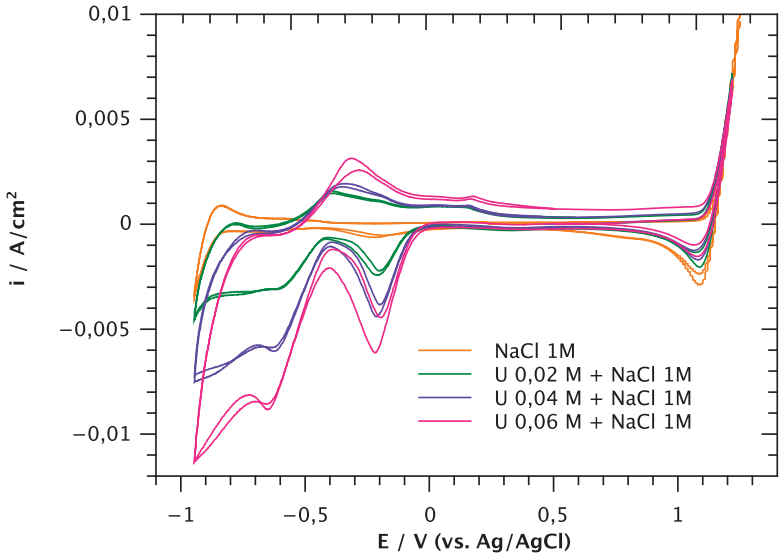

Figure 3.8: Influence of the concentration on the system. Cyclic voltammogram 0.02 M, 0.04 M and 0.06 M U and pH∼3. $UO_2(NO_3)_2$ solution in NaCl 1 M scanned between -1.0 and +1.2 V vs. Ag/AgCl saturated at a scan rate of 0.1 V/s.

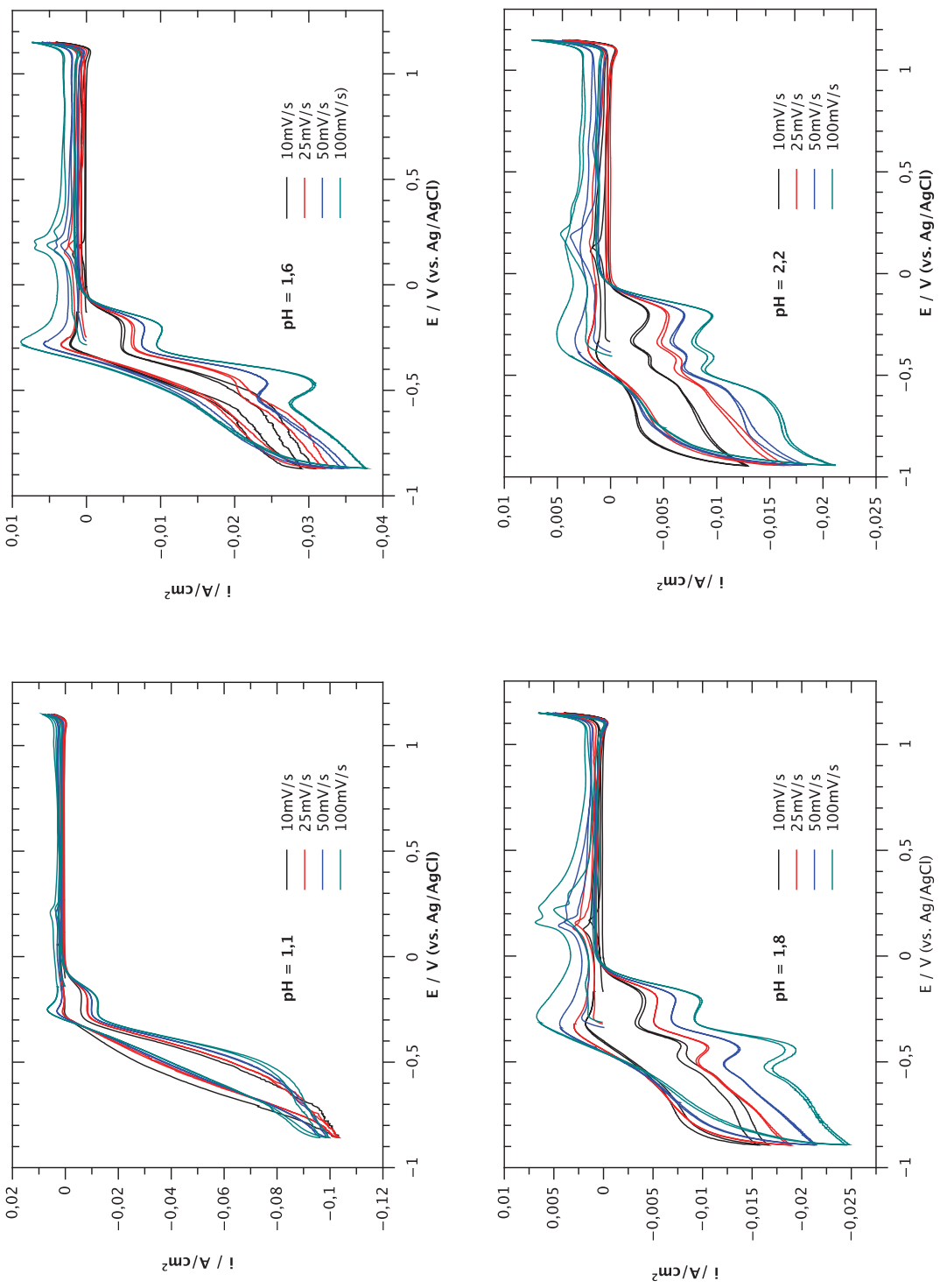

Figure 3.9: Influence of the acidity and scan rate on the system. Cyclic voltammogram 0.02 M U at different pH (1.1, 1.6, 1.8 and 2.2) and rates (0.01, 0.02, 0.05 and 0.1 V/s). $UO_2(NO_3)_2$ solution in NaCl 1 M scanned between -1.0 and +1.2 V vs. Ag/AgCl saturated.

No difficulty in the observation of the UO_2^{2+}/U^{+4} cathodic peak was hence found when using the frit. In Fig. 3.7 two different experiments are represented using the same initial solution, i.e. one with and one without the frit (anode and cathode in the same bath). No difference in the CV plots was observed.

The redox potential in CV studies was scanned between -1.0 and +1.2 V vs. Ag/AgCl (saturated) at different scan rates (0.01, 0.02, 0.05 and 0.1 V/s) and for different acidity degrees in the aqueous media (pH 1.1, 1.6, 1.8 and 2.2 Fig. 3.9). The intensity of the UO_2^{2+}/U^{+4}-peak increased with the scan rate making it more at every pH, making the peak more visible.

The influence of the analyte concentration on the UO_2^{2+}/U^{+4} peak was also studied. Various experiments with different U-concentrations (0.02 M, 0.04 M and 0.06 M) in acid conditions were performed and are shown in Fig. 3.8. On increasing the concentrations of U-analyte, an increase of the redox feature UO_2^{2+}/U^{+4} was observed.

3.3.1.2 Results and discussion.

Based on the CV study of the uranyl ion (analyte) redox reaction under variation of different parameters, the conditions for the electrochemical reduction of these species could be defined.

The U-analyte was redox active inside the experimental potential window -0.4 V to +1.4 V vs. Ag/AgCl saturated. The UO_2^{2+}/U^{+4} cathodic peak was shown to appear in the range of -0.300 and -0.250 V vs. Ag/AgCl saturated. That is in agreement with the literature, where the potential necessary to reduce the pair UO_2^{2+}/U^{+4} is cited as 0.280 V [Mikeev, 1989]. Therefore a redox potential of -0.300 V (vs. Ag/AgCl saturated electrode) was to be applied during the electrolysis, which corresponds to -0.101 V relative to the standard hydrogen electrode (SHE) (-0.300 V/(Ag^0/AgCl/Cl^-)=-0.300+0.199=-0.101 V/H^+/H_2).

The use of a separate containment for the anode electrode accelerated the electrolytic reduction of the analyte but a glass-frit with high porosity (40 μm) was necessary to ensure the free passage of the electrolyte. Therefore, the use of the frit during the posterior step of electrochemical reduction was introduced as routine.

Increasing the concentration of U-analyte favoured the observation of the redox peak UO_2^{2+}/U^{+4} for the CV-checks done along the electrolysis, so as to obtain the highest peak intensity.

A better identification of the UO_2^{2+}/U^{+4} was possible using high scan rates. In light of these test results, a scan speed as high as 0.1 V/s was afterwards always used in the CV-checks done along the electrolysis.

3.3.2 Electrochemical reduction of the mother solution.

3.3.2.1 Experimental arrangement.

The experimental arrangement used for the electrochemical reduction was in essence that shown in the general illustration of the precipitation method in Fig. 3.2. The general principles for the electrolysis are described in Sec. 2.1.2. Three electrodes were so immersed in the prepared solution in a 150 mL glass reactor built for these experiments. The solution containing the U-analyte ($UO_2(NO_3)_2$) was prepared at different concentrations between 0.02 until 0.5 M in U (depending on the experiment). And an excess of the supporting electrolyte (1 M NaCl or 1 M HCl) was added here, too. The experimental set-up of the reduction cell used is shown in Fig. 3.10, where some modification can be appreciated with respect to one used for the CV-tests (see Fig. 3.5). In the CV experiments, the net electrode was used as counter electrode, but for the present case (reduction of the solution), the net was used as a working electrode (cathode). During the reduction of the pair UO_2^{2+}/U^{+4}, a larger working electrode area is desired to achieve higher reduction rates, for which the net electrode (with larger surface that of the spiral electrode) was employed for that purpose. The spiral was used as a counter electrode (anode).

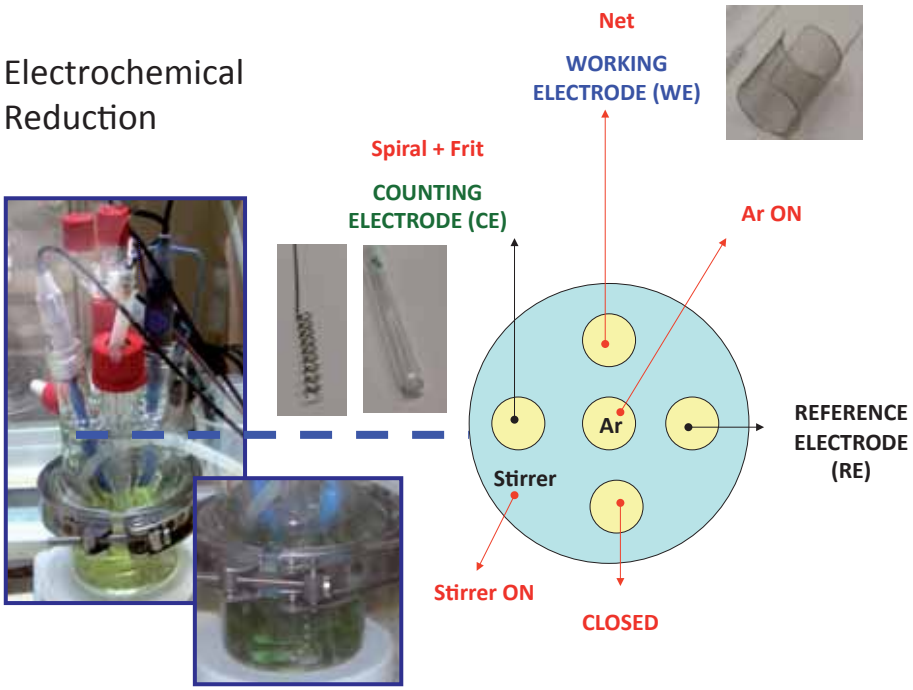

Figure 3.10: Electrochemical reduction set-up.

To prevent the re-oxidation of the obtained U^{IV} to U^{VI} because the anodic (counting electrode or spiral) produces oxygen, the anode was introduced in a separated glass tube of 12 mm in diameter, with a glass-frit (40 μm as determined in the CV study) on its bottom. This is seen as a fundamental modification of the approach adopted by [Rousseau et al., 2009] and [Gil et al., 2010] where cathode and anode were immersed in the same bath. The frit allows the passage of the electrolyte but partially avoids the passage of the oxygen to the solution, so that the entire process is more effective

speeding the reduction process.

Continuous bubbling of the solution with inert gas (Ar) was applied to avoid any traces of O_2 which could pass through the frit. A humidification bottle was installed between the argon supply and the reactor vessel, so that the Ar was pre-bubbled and saturated with water before entering in the reactor. This ensures dry Ar gas is saturated with water and the losses of liquid during the experiment are minimised. The bubbling together with the stirring reinforced the homogenization of the mixture (stock solution) during the whole experiment. Same as in the CV-tests, all reduction and precipitation experiments were conducted under anoxic conditions in a glove-box under N_2 atmosphere (O_2<0.5%).

In a typical experiment, an aliquot of the uranyl (U^{VI}) nitrate stock-solution was diluted in a 1 M NaCl solution to yield a final U-concentration of 0.1 M in a 75 mL batch. Before beginning any electrochemical reduction step, the pH was measured with a pH glass electrode (iEcotrode Plus Metrohm 3 M KCl) in combination with a Titrando 906 measuring instrument from Metrohm. Adjustment with HCl 1 M was pursued to maintain the solution with a pH<1 to avoid the hydrolysis (see Sec. 3.1.1) of the already reduced U^{4+}, before the onset of the precipitation was induced by controlled NaOH-alkalinisation.

The reduction of U^{VI}-solution to U^{IV} was performed under a constant potential (-0.3 V vs. Ag/AgCl as determined in the CV study) and the current varied between |-50| to |-5| A. Therefore the calculation of the needed time for the electrolysis was approximated. The reduction was rapid at first but slowed as the ion concentration decreased as would be expected from Ohm's Law ($V = I \cdot R$), i.e. at constant voltage, the current is inversely proportional to the resistance.

The U^{VI}-solution was proved to be electrochemically reduced to U^{IV} almost entirely. Continuous checks of the reduction status were carried out by CV-tests during the electrolysis of the solution to verify the extent of reduction of the U^{VI} cations amount (on observing the intensity diminution of the UO_2^{2+}/U^{+4} cathodic peak). Thus, the reduction was temporarily halted and the typical experimental CV arrangement was adopted in each check (Fig. 3.5). The spiral was disposed outside the glass-frit and put inside the reactor bath in direct contact with the reducing solution. Ar flow and stirrer agitation were stopped to avoid disturbances. Scan speed as high as 0.1 V/s was used as determined in the CV-study.

During the reduction, the reactor was showing increasingly evidence of an already reduced green U^{IV}-solution, while inside the glass tube with the frit a yellow U^{VI}-solution was still observed, due to the continuous O_2 production on the anodic side (spiral).

3.3.2.2 Results and discussion.

Fig. 3.11 shows different CV plots recorded at different times during the reduction step. The plots show the decrease of the cathodic peak UO_2^{2+}/U^{+4} with increasing electrochemical reduction time, in terms of the current of density (A/cm^2) passing between the two inert Pt electrodes at the corresponding potential. The electrochemical resistance of the media increased with time because the ions concentration of the

species to reduce diminished. The diffusion to the cathode of the ions, which are still not reduced, became hence more difficult, explaining so the decreased cathodic current.

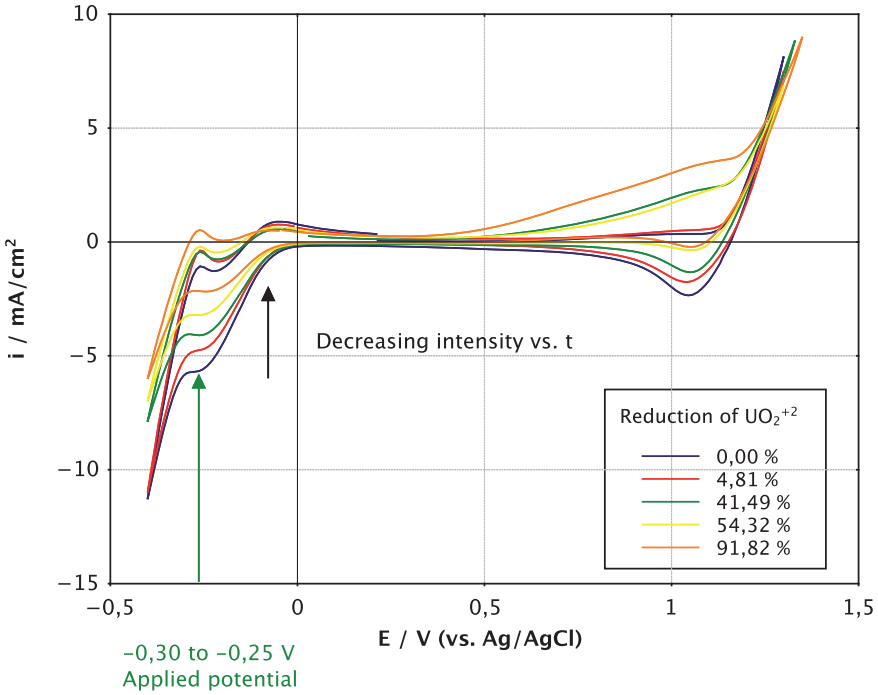

Figure 3.11: Cyclic voltammogram 0.1 M U and pH<1. $UO_2(NO_3)_2$ solution in HCl 0.33 M scanned between -0.4 and +1.4 V vs. Ag/AgCl (saturated) at a scan rate of 0.1 V/s. The theoretical reduction rate of the ion UO_2^{2+} at each moment was calculated with Eq. 2.7.

The pH rose from 0.2 to 0.6 at the end of the electrochemical reduction. That could be due to the acid consumption during the electrolytic reduction of the uranyl ion (cathodic reaction; see Eq. 2.1). That could be relevant if a pH>1 was in the end obtained because hydrolysis of U^{IV} is expected.

3.3.3 UV-Vis spectrophotometry of the solution.

3.3.3.1 Experimental.

Different Aliquot samples were taken along the electrolysis for ultraviolet-visible spectroscopy (UV-Vis) analysis, which were performed to monitor the valence state of U before and during the controlled potential reduction of $UO_2(NO_3)_2$ in HCl solution (Fig. 3.12). The UV-Vis/NIR spectrophotometer used to record the UV-Vis absorption spectres is described in Sec. 2.2.1. The tint of the solution was changing along the reduction from an initial clear-yellow colour typical of UO_2^{2+} ion, to a dark-green colour typical of U^{4+} at the end of the process (see Fig. 3.13 showing the progressive colour change of the U-solution upon its reduction).

3.3.3.2 Results and discussion.

The absorption bands in the range from 375 to 500 nm, which are characteristic to the absorption of uranyl (U^{VI}) ions, gradually decreased and finally disappeared with

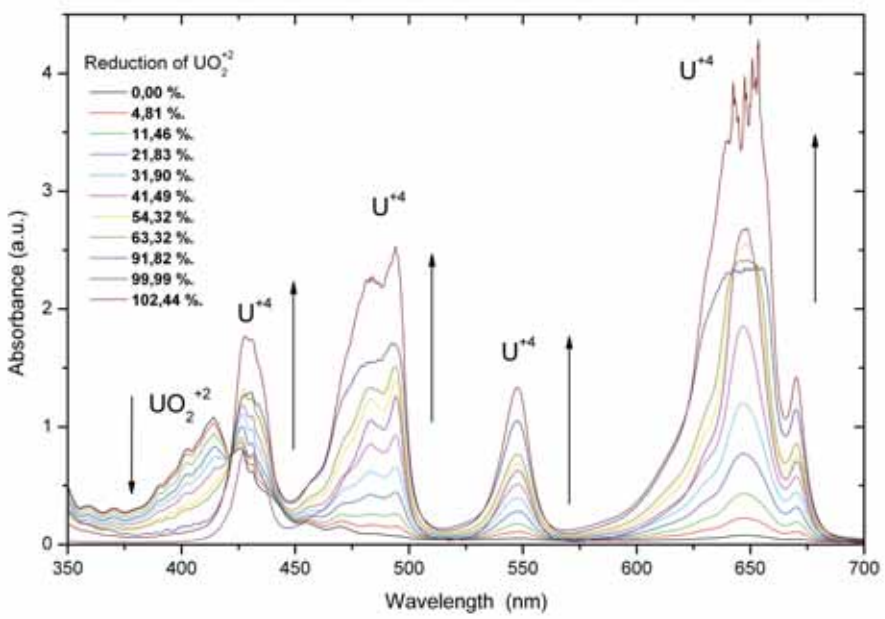

Figure 3.12: Change in visible absorption spectra for the reduction of 0.1 M U and initial pH<1. $UO_2(NO_3)_2$ solution in HCl 0.33 M. The theoretical reduction rate of the ion UO_2^{2+} at each moment was calculated with Eq. 2.7.

increasing the electrolysis reduction time. At the same time, the absorption bands from 400 to 700 nm, which are consistent with absorption typical peaks for U^{IV} (426, 492, 548 and 646 nm), appeared with stronger intensity as the time of electrochemical reduction of the solution increased. That was in agreement with the intensity decrease of the UO_2^{2+}/U^{+4} cathodic peak observed in the CV tests of the solution (Fig. 3.11) with the time of reduction. This result strongly supports the fact that UO_2^{2+} in the acidic solution was almost fully reduced to U^{IV} at the Pt electrode. The progress of the electrochemical reduction, as analysed by spectrophotometry, is shown in Fig. 3.12.

In Fig. 3.14, the intensity peak decrease by both cyclic voltammetry (e.g. UO_2^{2+}/U^{+4} cathodic peak, Fig. 3.11) and UV-spectrophotometry (e.g. UO_2^{2+} absorption peak

Figure 3.13: U-solution at different steps during electrochemical reduction

at 412.43 nm, Fig. 3.12), are plotted as a function of the percentage of $UO_2(NO_3)_2$ electrochemical conversion (analysis performed on the same aliquots of solution). Correspondence between both methods in the determination of the UO_2^{2+}/U^{+4} conversion, is very satisfactory.

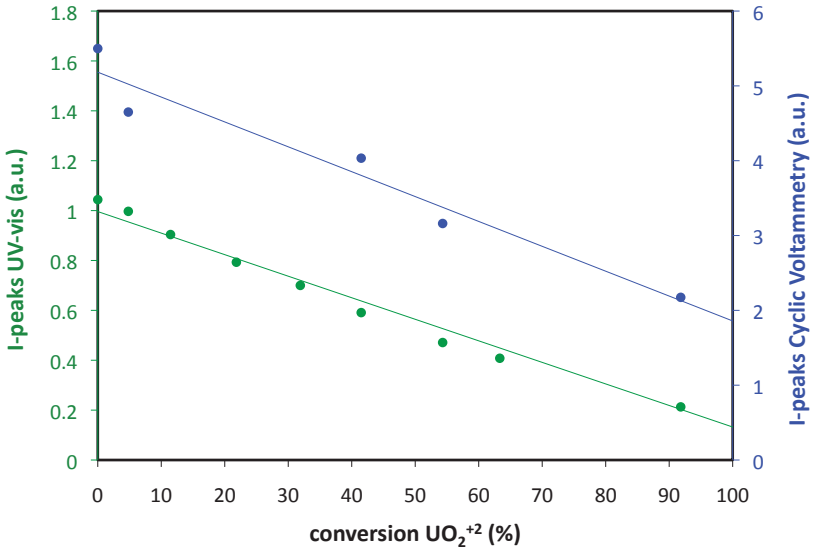

Figure 3.14: Intensity peak decrease by both CV (e.g. UO_2^{2+}/U^{+4} cathodic peak, Fig. 3.11) and UV-spectrophotometry (e.g. UO_2^{2+} absorption peak at 412.43 nm, Fig. 3.12) as a function of the percentage of $UO_2(NO_3)_2$ electrochemical conversion.

3.4 Precipitation and separation of the UO_2-nanocrystals.

3.4.1 Introduction remarks.

The precipitation from the electrochemically reduced U^{IV}-solution (0.5 M U for the highest concentration) was achieved by gradual alkalinisation of the solution following as close as possible the theoretical solubility limit line of U^{IV} species in aqueous media Fig. 3.1. This was pursued to avoid significant agglomeration of the precipitates (UO_2(c) or $UO_2 \cdot xH_2O$(am)), which was faired to occur if the system entered in the region of frank supersaturation, as it could be induced by uncontrolled brusque alkalinisation (pH-increase much beyond the equilibrium line).

Indeed, the theory of precipitation from supersaturated solutions and a number of dedicated experimental works indicate that the size of the nuclei-precipitates is inversely proportional to the supersaturation degree, while the number of nuclei is directly proportional to it (homogeneous precipitation) [Lifshitz and Slyozov, 1961] [Bristow et al., 2001] [Wu et al., 2008] [Maeda et al., 2009]. However, under consideration of kinetic aspects (e.g. coagulation rates), also considerable number of studies exist indicating that the supersaturation degree is a key factor triggering the agglomeration of precipitates, with the evidence found that the larger the supersaturation degree the larger the size of the agglomerates formed (including both homogeneous and heterogeneous precipitation) [Yu et al., 2007] [Claassen and Sandenbergh, 2006]

[Zumstein and Rousseau, 1989] [Packter, 1958] [Sarig et al., 1978].

The quantity of NaOH theoretically needed to reach a given pH can be calculated as the sum of $[OH^-]mols_A + [OH^-]mols_B$, where the first term A indicates the number of OH mols needed to increase the initial pH to the wished final pH, as given by:

$$[OH^-]mols_A = [H^+]mols_{Initial} - [H^+]mols_{End} \tag{3.1}$$

where

$[H^+]mols_{Initial} = 10^{-pH_{Initial}}$

and

$[H^+]mols_{End} = 10^{-pH_{End}}$

and the second term B indicates the number of OH mols needed to precipitate the species U^{+4} as UO_2, as given by the reaction:

$$U^{4+} + 4OH^- \leftrightarrow UO_2 + 2H_2O \tag{3.2}$$

and where

$$[OH^-]mols_B = 4 \cdot U^{4+}mols \tag{3.3}$$

This theoretically amount of NaOH needed to set a given pH was hence estimated and was taken into account as indicative value for the subsequent precipitation step.

3.4.2 Experimental steps.

The precipitation was performed in the same reactor used for the electrolysis experiments. The arrangement used for this step is shown in Fig. 3.15. No potential was applied during the precipitation but the atmosphere conditions were maintained in the same way as in the electrochemical reduction step: i.e. the arrangement was kept inside a glove-box under anoxic conditions (N_2 atmosphere with O_2<0.5%) and dynamic Ar gas flow (passed through a humidification bottle to saturate it with water before entering in the reactor to avoid the dryness of the solution), was applied.

The pH at the beginning of the precipitation, was below 0.5. A series of stepwise precipitations between pH<0.5 and 3 were then carried out by addition of 3 M NaOH solution at a rate of 10-20 μl/min, as controlled by a dosage instrument (Titrando 906 from Metrohm). The slow alkalinisation was automatically stopped when the solution reached the pH desired, and was re-started when the pH evolved backwards (through precipitation, Eq. 3.3) and was again below the set pH.

Black nc-UO_2-precipitates appeared around pH∼1 and the solution began to look turbid from this point onwards. The pH variation during the precipitation step was

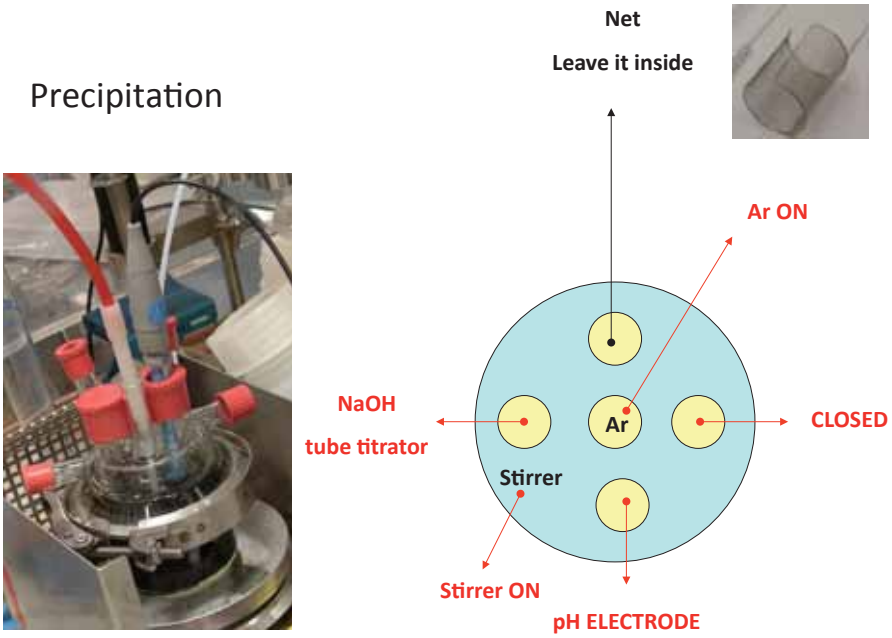

Figure 3.15: Precipitation of nc-UO_2 set-up.

monitored continuously. An example of this variation with time for the case of the highest U-concentration used in the experiments (0.5 M) is shown in (Fig. 3.16). In the displayed case, a constant dosage rate of the alkalinising NaOH-solution of approximately 1.2 ml/h was used. Small pH-drifts occurred because of the formation of nc-UO_2 crystals. In addition to this, on reaching the pH the value of 1, a main jump or abrupt slope increase was observed in the pH vs. t curve (Fig. 3.16), which revealed the main precipitation of UO_2 crystals in the solution has already occurred, when the pH surpassed this precipitation threshold.

The quantity of NaOH theoretically needed to reach the set pH was calculated as previously indicated as the sum of $[OH^-]mols_A + [OH^-]mols_B$. The NaOH-solution was slowly added at constant rate and the pH was monitored (Fig. 3.16). The NaOH additions stopped automatically after approximately 30 h of precipitation on reaching the pH the value 3. After this point, no further essential modifications of the pH were registered during at least 3 days more (>100 h after initiation of the process), indicating that the precipitation had been already almost completed when the pH achieved the value 3.

Centrifugation (3500 rpm and 30 min) of the blackened solution was performed to gather the precipitates. Na^+ and Cl^- species were present in the final solution because of the initial additions of HCl to acidify solution and the posterior additions of NaOH used to precipitate the U^{IV}-species as oxide in the solution. The wet nc-UO_2-precipitates hold these impurity species on its surface, which will precipitate as small NaCl crystals once the final product dries. Therefore, the wet nc-UO_2-precipitates were re-dispersed in deionised water and sonificated for diluting and washing out the possible Na^+ and Cl^- species concentration present. Subsequent centrifugation, to

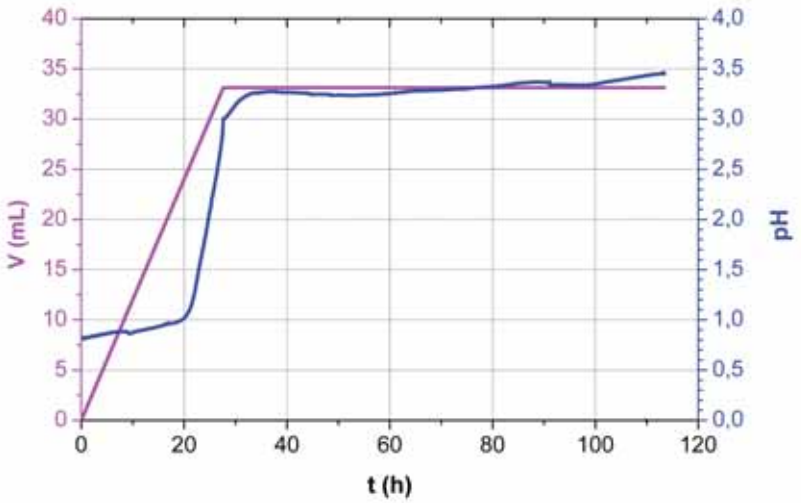

Figure 3.16: Controlled nc-UO_2 precipitation from a electrochemically reduced U^{IV}-solution 0.5 M U in HCl 1M. pH monitoring vs. NaOH addition and time.

separate the nc-UO_2-precipitates from the water containing the dissolved Na^+ and Cl^- species, was done. This washing-centrifugation step was performed 5 times using a volume of 40 ml of deionised water pro washing operation and a partial charge of 1.25 g nc-UO_2 each tube (4 tubes were centrifuged in parallel). For the highest U-concentrations of (0.5-0.6 M), around 10 g of nc-UO_2 precipitates were obtained in total from each precipitation batch.

3.4.3 Spectrophotometry of the solution.

The UV-spectrophotometer was used during the precipitation process to identify the decrease in U concentration in the solution (see Fig. 3.17 where the absorption band at 647.04 nm typical from U^{+4}, has been monitored). With increasing of the pH (addition of NaOH to the solution), increasing of nc-UO_2 precipitates occurred and reduction of the U^{IV} in solution diminished. The change in the visible absorption spectra could not be observed effectively till the end of the precipitation because of the turbidity of the solution. A picture of the reduced green U^{IV}-solution before to begin the precipitation and the black final solution containing the nc-UO_2-precipitates, is shown in Fig. 3.18.

With the solubility constants for UO_2 (c) and UO_2 (am), and the stability constants for U^{IV} hydrolysis reported by [Guillaumont et al., 2003], a graph with the speciation of all uranium entities present at different pH in the solution as well as the solubility lines for UO_2 (c) and $UO_2 \cdot xH_2O$ (am) can be represented, as it was undertaken in Fig. 3.19. The speciation curves add knowledge of what is happening in the solution as the pH is increased in the precipitation step. The yellow line represents the piece of solubility/precipitation line followed during precipitation. The yellow circles represent the experimental precipitation points observed in the UV-absorption spectra (Fig. 3.17) having in account the different intensities obtained. These experimental precipitation point fall all on the theoretical precipitation line.

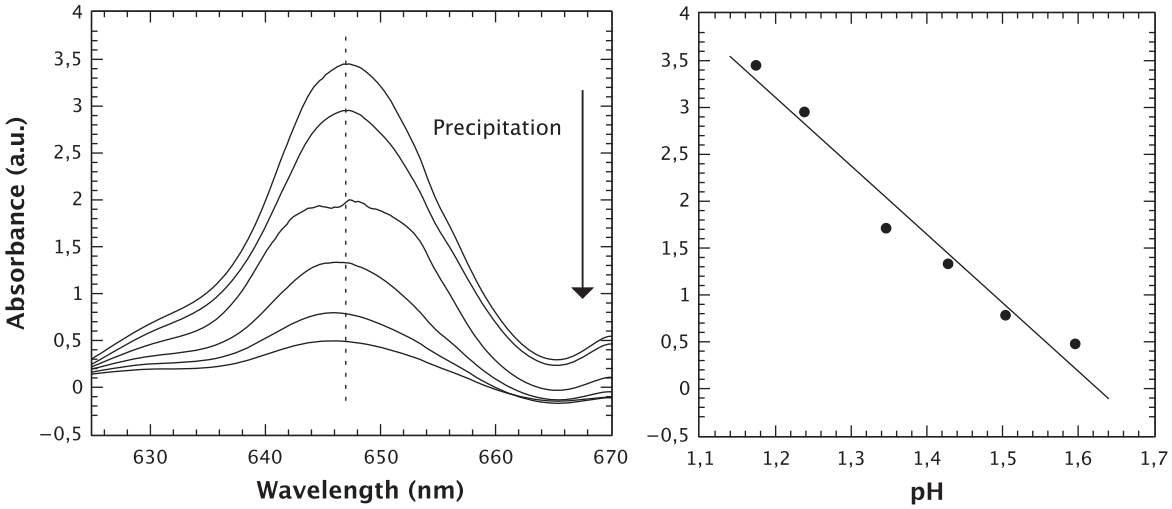

Figure 3.17: Change in visible absorption spectra of the typical U^{IV} band between 630 and 665 nm, of a controlled nc-UO_2 precipitation from a electrochemically reduced U^{IV}-solution 0.1 M U in HCl 1 M and pH<1 *(left)*. Diminishing of intensity with increasing of the pH because the precipitation of the U^{+4} in solution as nc-UO_2 *(right)*.

(a) U^{IV}-electrochemically reduced solution 0.5 M U in HCl 1M and pH<0.5.

(b) ∼10 g of black nc-UO_2 precipitates

Figure 3.18: U-solution before and after the precipitation.

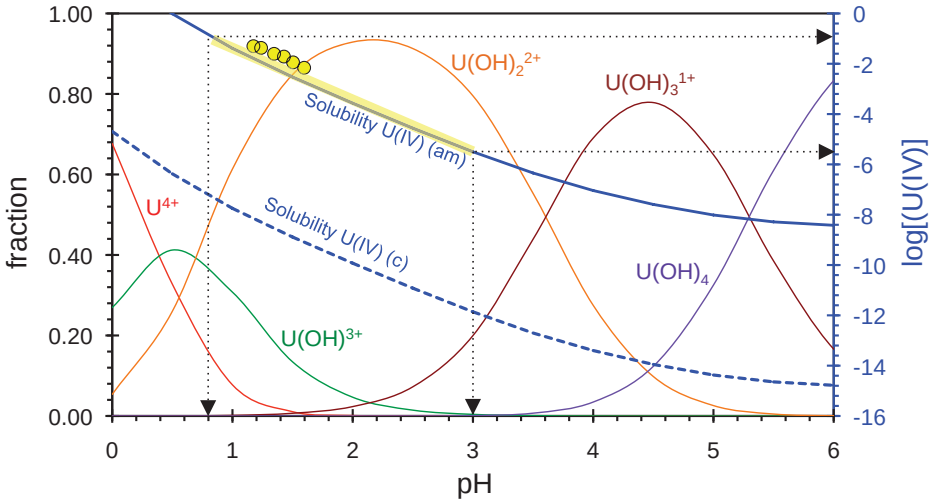

Figure 3.19: Uranium Speciation at different acidic media and solubility lines for UO_2 (c) and $UO_2 \cdot xH_2O$ (am) represented with the constants data by [Guillaumont et al., 2003]. *Yellow circles* represent experimental points. *Yellow line* represents the piece of solubility line followed during precipitation.

3.5 Characterisation of the as-produced nanocrystals.

The morphology and structure of the obtained nc-UO_2 particles were characterized by means of transmission electron microscope (TEM) and the structure confirmed by X-ray diffraction (XRD).

3.5.1 Precipitates morphology and composition.

Qualitative composition analysis of the precipitates obtained was carried out by TEM. The characteristics of the instrument used, as well as the preparation of the analysed specimens are described in Sec. 2.3.2.

Fig. 3.21 shows the TEM image of nc-UO_2 synthesised by the presently described method. The average precipitate size was of 3.9(8) nm, as obtained from the size distribution (Fig. 3.20). The particles showed agglomerates of 50 nm (Fig. 3.21a). However, very often separated nanoparticles exist in suspension in the original solution, but one sees agglomerates on the TEM grid, due to the preparation of the TEM sample.

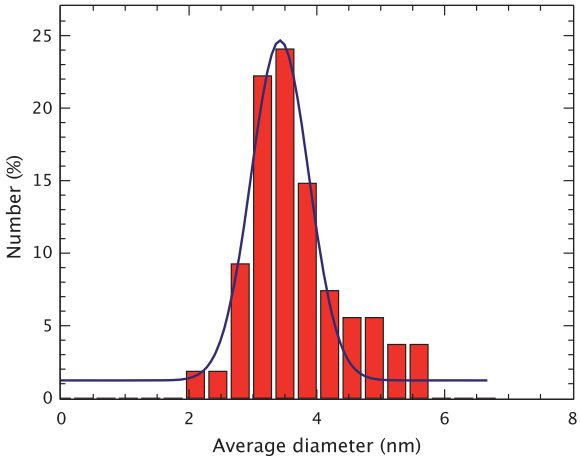

Figure 3.20: Size distribution histogram from TEM measurements of nc-UO_2 synthesized by precipitation in aqueous media. Diameter average size of 3.9(8) nm diameter average size.

The collected black precipitates presented the typical *fcc* fluorite structure of UO_2. The selected area electron diffraction (SAED) pattern (inset of Fig. 3.21c) revealed the polycristallinity of the material with the *fcc* structure. The calculated interference fringe spacing in the HRTEM image (Fig. 3.21c) was about 0.315 nm, which was in agreement with the interplanar distance of the [111] plane in the *fcc* fluorite structure (0.3153 nm for the UO_2 standard 00-041-1422-ICCD).

3.5.2 Precipitates crystal structure.

The crystal structures and crystal size of the as synthesised nc-UO_2 observed in the TEM analysis were confirmed by XRD. The characteristics of the instrument used are described in Sec. 2.4.1. The crystal structure of the nano-precipitates was

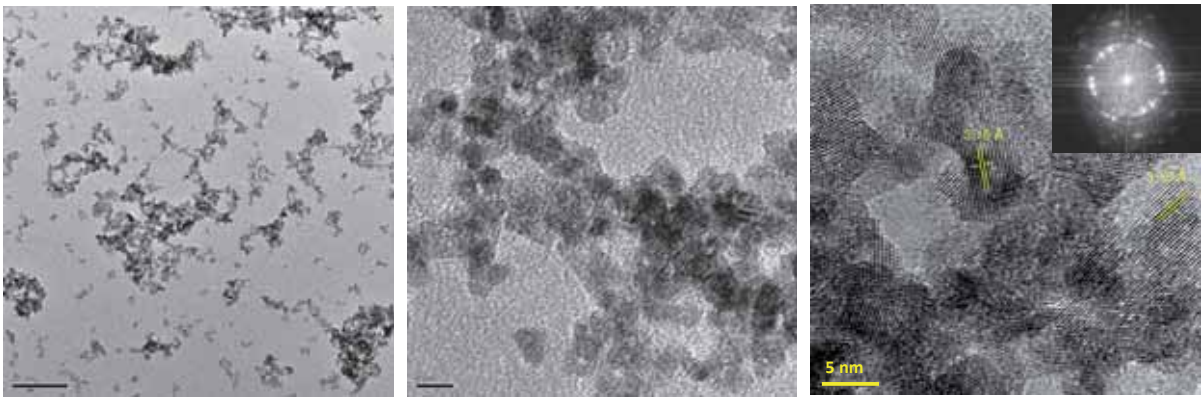

(a) The scale bar is 50 nm. (b) The scale bar is 5 nm. (c) The scale bar is 5 nm. The inset of the figure shows selected area electron diffraction (SAED).

Figure 3.21: TEM micrographs of UO_2 at low resolution, showing an assembly of nanocrystals, and at high resolution, revealing lattice imaging of the nanocrystals.

determined by Rietveld refinement (Sec. 2.4) using bulk-UO_2 as standard. The whole diffraction pattern was taken in account. The agreement between the measured and fitted diffraction lines profiles is shown in Fig. 3.22. The overall fit quality as described by the measured R-values and the goodness of the fit (GOF) was, despite broadness of the peaks (typical for nanocrystals), satisfactory (R(expected)/%=4.39, R(profile)/%=4.32, GOF=1.51). A *fcc* fluorite structure (*Fm-3m* space group) with a lattice parameter of 0.5417(1) nm (a=0.547 nm for the UO_2 standard 00-041-1422-ICCD) and 3.79 nm crystallite size in agreement with the average size observed by TEM of 3.9(8) nm, was found. All diffraction peaks showed a small shift to the higher 2θ, which suggests either a slightly higher oxidation state relative to stoichiometric UO_2, or a mechanical distortion (contraction) of the lattice due to surface stresses induced by the small particle size [Boswell, 1951] [Qi et al., 2002] [Fukuhara, 2003] [Park and Qian, 2010].

The Bragg diffraction peak positions and relative intensities for the refined XRD pattern of as produced UO_2 nanocrystals in comparison with standard diffraction patterns of UO_2, U_4O_9 and U_3O_8, are also shown in Fig. 3.23. The peaks show to be compatible with an oxide structure between those of UO_2 and U_4O_9, both *fcc*-phases, but with an oxidation degree closer to that of U_4O_9 (systematic peaks shift towards higher diffraction angles compared to UO_2, i.e., higher oxygen stoichiometry). The figure shows also fully disagreement of the measured diffraction pattern with that of the phase U_3O_8, which excludes hence such an extreme oxidation of the precipitation product.

The interplanar distance of the [111] plane in the *fcc* fluorite structure was of 0.3147 nm for the XRD pattern Fig. 3.22 (0.3153 nm for the UO_2 standard 00-041-1422-ICCD). Calculated interference fringe spacing for single crystals in the HRTEM image of 0.315 nm was obtained (Fig. 3.21c).

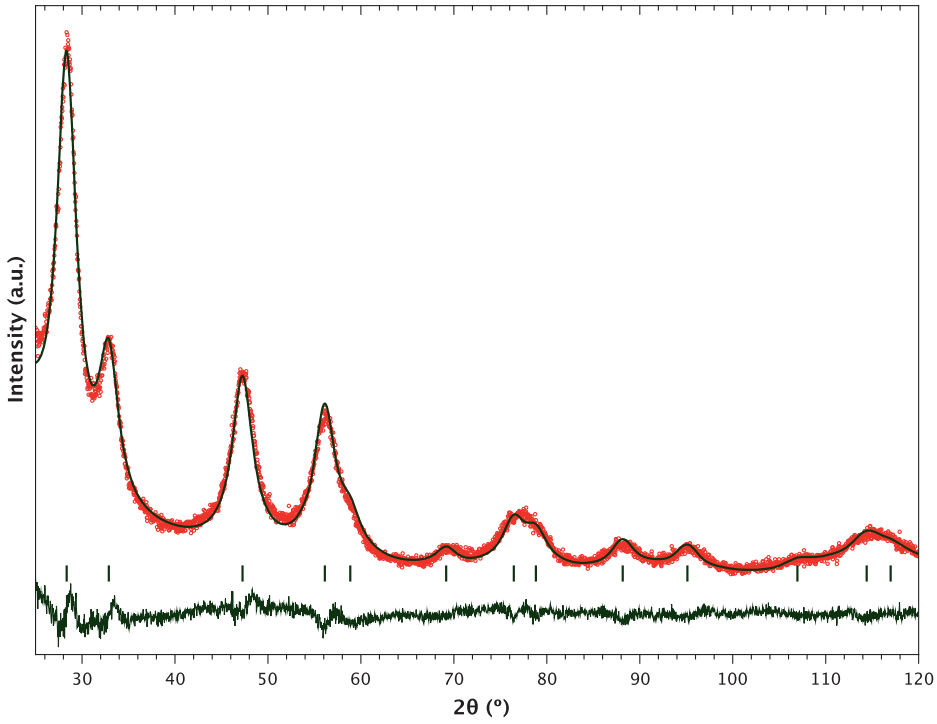

Figure 3.22: XRD pattern of nc-UO_2 experimental data, fitted pattern, Bragg peak positions and experimental-fitted difference.

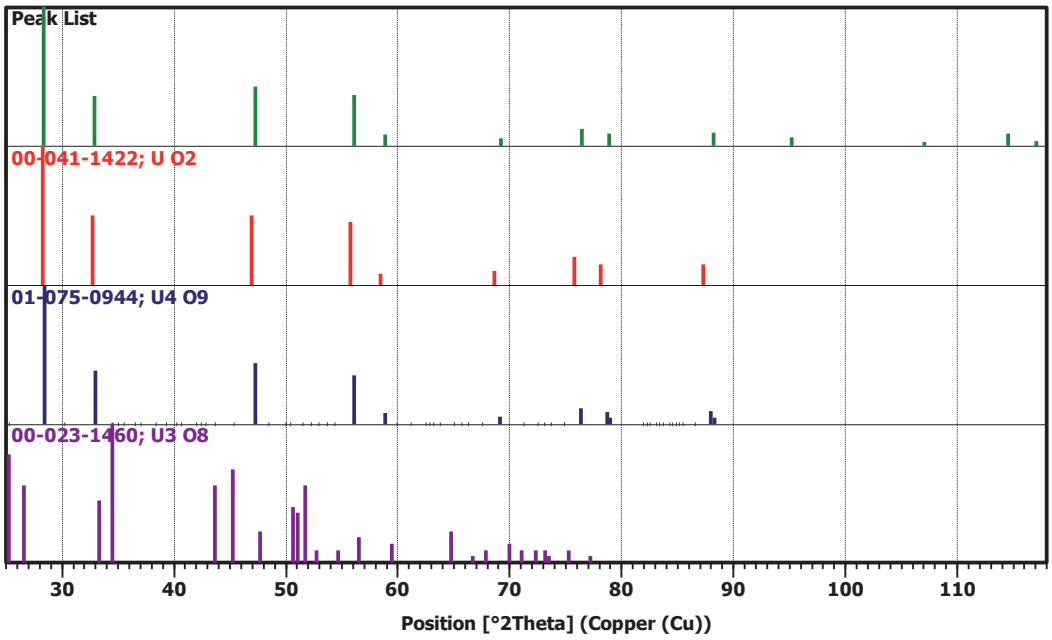

Figure 3.23: Bragg diffraction peak positions and relative intensities for the refined XRD pattern of nc-UO_2 by aqueous route (*green*), standard UO_2 (00-041-1422-ICCD - *red*)), U_4O_9 (01-075-0944-ICCD - *blue*)) and U_3O_8 (00-023-1460-ICCD - *lila*)), respectively ([ICCD, 2012] database).

3.6 Results and discussion.

An intensive study of the range of U-concentration and acidity for nc-UO_{2+x} precipitation from electrolytically reduced uranyl nitrate solutions was endeavoured, using

higher concentration (10^{-1} M) ranges as the observed in literature (10^{-2} M), and therefore lower pH ranges, following the solubility line of U^{IV}.

The electrochemical reduction characteristics of the uranyl ion by cyclic voltammetry (CV). The study of the uranyl ion system under the influence of different parameters as use of separated compartment for the anode, different ion concentrations, acidic aqueous media and scan rates, were analysed. In light of this CV study, the conditions for the electrochemical reduction of these species could be defined. Electrochemical reduction was pursued following the later defined parameters. Continuously control of the reducing solution by CV and UV-Vis spectrophotometry was done along the electrolysis step. Correspondence between both methods in the determination of the UO_2^{2+}/U^{+4} conversion, was satisfactory.

Precipitation from the electrochemically reduced U^{IV}-solution was achieved by gradual alkalinisation of the solution following as close as possible the theoretical solubility limit line of U^{IV} species in aqueous media. nc-UO_{2+x} precipitation was achieved in the pH range of ∼1 to 3 and for U-concentrations as high as 0.5 M. Washing-centrifugation steps of the blackened solution were performed to gather the precipitates. As a result, 10 g of nc-UO_{2+x} per batch have been obtained. This represents not only an improvement of the method studied but a major achievement in its use for the synthesis of meaningful quantities of such material.

The solid phase, as obtained by XRD, was found to crystallize with the typical UO_2-*fcc* fluorite structure (*Fm-3m* space group), with a lattice parameter a=0.5417(1) nm and average crystallite size of 3.79 nm, also in agreement with an average size observed by TEM of 3.9(8) nm and DLS of 3.7(1) nm. The predominant diffractogram of the samples corresponded unmistakably to UO_2, though in a poorly crystallized form, or as finely aggregated nc-particles, which caused peak broadening. This phase, which has also been described in the literature as amorphous-hydrated uraninite [Ryan and Rai, 1983] [Opel et al., 2007] [Rai et al., 2003] [Fanghänel, Th. and Neck, 2002] and [Neck and Kim, 2001], was however shown in the present XRD measurements to correspond to crystalline UO_2 but in a rather oxidized state. The latter was manifested through a lattice contraction of about 0.9% of the precipitated phase (a=0.5417(1) nm) with respect to the values of stoichiometric UO_2 (a=0.547 nm). An effect which could be also caused by surface stresses induced by the small particle size, as frequently observed in nanoparticles. Further studies will be then undertaken in chapters hereafter to clarify this influence. Since the corresponding water content and/or oxidation degree of this phase was hitherto not identified, it was generically described here as UO_{2+x}, in correspondence with similar description e.g. in [Rousseau et al., 2002] [Rousseau et al., 2006] [Rousseau et al., 2009]. Further analysis of this phase will be found in Chap. 5. To study the composition of the precipitates and their propensity propensity to thermal growth in the unconsolidated state, i.e. on just experiencing stochastic physical contact, further analysis of the precipitated was performed by applying the thermal analytical and X-ray scattering techniques like TG/DTA, HT-XRD and RT-XRD, spectroscopic techniques as XAS, NMR and IR and characterization techniques like TEM. The results are detailed and discussed in Chap. 5. The use of the method here described, was to avoid the use of foreign organics (dispersing agents, antiflocculants) in the preparation, which could disturb afterwards in the production of pellets of this material (Chap. 7).

Chapter 4

Synthesis of nc-UO_2 and nc-ThO_2 by a precursor thermal decomposition in Organic phase

4.1 Introduction and principles.

The synthesis of monodisperse nanocrystals (nc) demands a short nucleation step followed by a slower controlled growth of the formed nuclei [Murray et al., 1993]. Two different approaches can be pursued to achieve this synthesis.

One approach is the fast addition of the reactive agents into the reactor which contains the coordinating solvent at a temperature high enough to decompose them. The fast addition increases the precursor concentration over the nucleation point and after a short period of nucleation, the concentration of the species in solution falls under the critical concentration for the nucleation. So far the precursor addition rate does not go beyond the consumption rate of the reagents, no new nuclei appear and the precursor surplus just enlarges the size of the particles [Burda et al., 2005]. The final size of the particles depends on the duration between the primary nucleation step and the incubation time needed for the beginning of the particles' growth. The subsequent growth step is alike for all the particles, and therefore it does not influence the final distribution size. Therefore, a way to maintain a homogeneous final size distribution, is to induce a short nucleation step in comparison to the growth step [Murray et al., 1993] [Peng and Peng, 2001] [Qu et al., 2001] [Burda et al., 2005].

The second way to perform the synthesis (and approach used here in the synthesis of the nc-UO_2) is to mix all the reactive components at the beginning in the reactor at a temperature below which any reaction occurs, but high enough to allow a good mixing [Murray et al., 2000] [Wang et al., 2003] [Murray et al., 1993] [Peng and Peng, 2001] [Qu et al., 2001] [Burda et al., 2005]. Once a good mixture is achieved, the temperature is raised with a determinate rate to provoke the necessary supersaturation and subsequent nucleation. As in the first synthesis approach, no new nuclei will appear provided that the temperature is kept below or equal to the value where the reagents start to react more rapidly (to form new nuclei) than the consumption rate of materials to enlarge the present nuclei. Again in this case, the size distribution depends on the time between the nucleation begins and the particles growth initiation. The changes in size and shape of the crystals are achieved by playing with the composition and concentration, as well as temperature and the time of reaction [Burda et al., 2005].

Surfactants inside the reactor bind on the synthesized crystals forming an organic capping layer that protects and stabilizes the crystals against flocculation or excessive growth. Larger molecules surfactants which provide greater steric hindrance, as well as surfactants that cap stronger to the surface of the crystals, diminish the reagents incorporation rate in the nuclei and as a consequence their final size. Particles growth can be stopped (before the finishing of the reagents) by fast cooling of the reactor [Murray et al., 2000] [Wang et al., 2003] [Murray et al., 1993] [Peng and Peng, 2001] [Qu et al., 2001] [Burda et al., 2005].

To collect the particles a precipitation is induced by addition of a non-solvent which is characterized to be partially miscible with the media of the reaction but has no interaction with the capping agents. The dispersion is destabilized and the solution becomes turbid due to flocculation of the crystals. Centrifugation accelerates the process and crystals are collected on the bottom of the centrifuge tubes. Afterwards the liquid is decanted and the crystals collected. The material obtained is formed by the nc-material and the organic capping layer which permits its re-dispersion in an organic solvent [Murray et al., 2000] [Wang et al., 2003] [Murray et al., 1993] [Peng and Peng, 2001] [Qu et al., 2001] [Burda et al., 2005].

The organic solution phase decomposition route has been widely used for the synthesis of metal-oxide nanocrystals. In this project the synthesis of nc-UO_2 in organic media was developed following the second approach above described and the method reported by [Wu et al., 2006] where uranyl acetylacetonate (UAA Fig. 4.1a) is used as precursor in a mixture of long chain solvents as oleic acid (OA), oleylamine (OAM) and octadecene (ODE) which are stable at high temperatures where this kind of metal-oxide nanocrystals are normally formed [Willis et al., 2007].

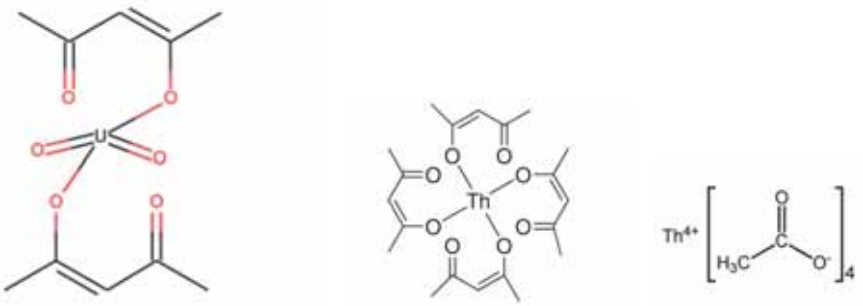

(a) UAA (b) ThAA (c) ThAc

Figure 4.1: Precursor molecular structures used in the organic synthesis.

The decomposition of the UAA precursor and the amine (OAM) is followed by a reduction of U^{VI} (UAA) to U^{IV} (UO_2) at higher temperatures. OAM might act as reducing agent [Wu, 2008]. A condensation reaction between OA and OAM occurs ending in the formation of N-(*cis*-9-octadecenyl)oleamide (OOA Fig. 4.2-*left*) and water, and is almost terminated before the beginning of the nucleation, as reported by [Wu et al., 2006]. OOA is described there as tuner of the reaction intermediate steps to form the UO_2 nanoparticles, where free UO_2 units and clusters have interaction with the amide (R-NH_3^+) and the carboxylic (R-COO^-) groups (see Fig. 4.2-*right*) [Wu, 2008].

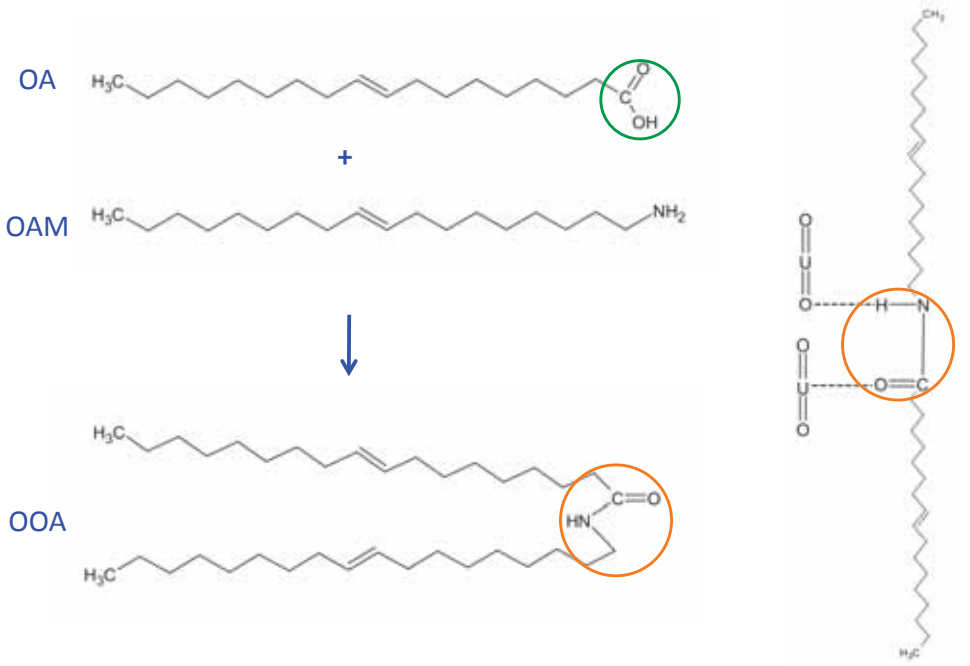

Figure 4.2: Oleic Acid (OA), Oleylamine (OAM) and N-(*cis*-9-octadecenyl)oleamide (OOA) obtained after the condensation reaction together with water [Wu et al., 2006] *(left)*. Intermediate steps of the nc-UO_2 synthesis where free UO_2 units and clusters interact with the formed OOA *(right)* [Wu, 2008].

However, no OOA but just an oleate was found bonded through chelating bidentate interaction on the surface of the nc-UO_2 [Wu et al., 2006]. A strong attraction appears between the oleate and the metal group making a very compact monolayer around the nanocrystals inhibiting their growth and protecting them against agglomeration (see Fig. 4.3).

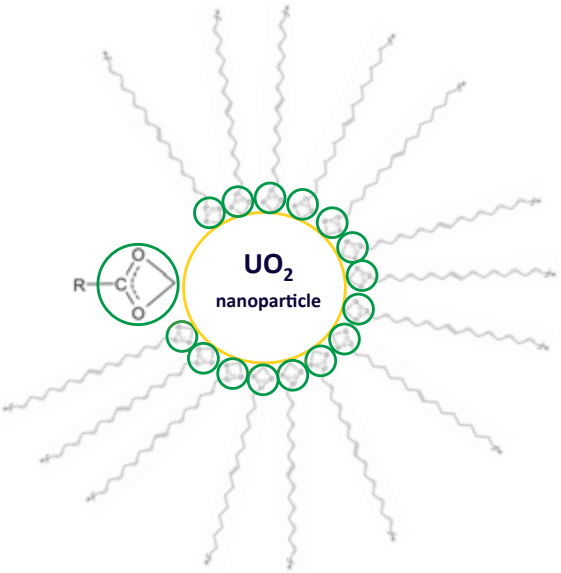

Figure 4.3: Oleate as capping ligand bonded through chelating bidentate interaction on the surface of the nc-UO_2.

4.2 Experimental.

In the present work the precursor uranyl (U^{VI})-acetylacetonate (UAA) for UO_2 nanocrystals and thorium (Th^{IV})-acetylacetonate (ThAA) or thorium (Th^{IV})-acetate (ThA) for ThO_2 nanocrystals (see Fig. 4.1), were dissolved in a solution of oleic acid (OA Fig. 4.2) and 1-octadecene (ODE) at 110°C under continuously stirring. Oleylamine (OAM Fig. 4.2) was added to the mixture and was heated at an average rate of 20°C/min until 310 to 350°C was reached (depending on the experiment). Afterwards the growth solution was aged for 1-6 h (depending on the experiment) and cooled to room temperature.

The experimental set-up involved a heater, a small-round vessel, a cooler and a continuous Ar flow. A scheme as representation of the set-up is shown in Fig. 4.4. The solution preparation as well as the reaction steps were conducted under anoxic conditions in a glove-box under N_2 atmosphere (O_2<0.5%). Posterior washing of the oxide-crystals, as well as centrifuging was performed. As a final product, nc-precipitates of UO_2 and ThO_2 redispersible in organic solvents were obtained. A picture of the different steps is shown in Fig. 4.5.

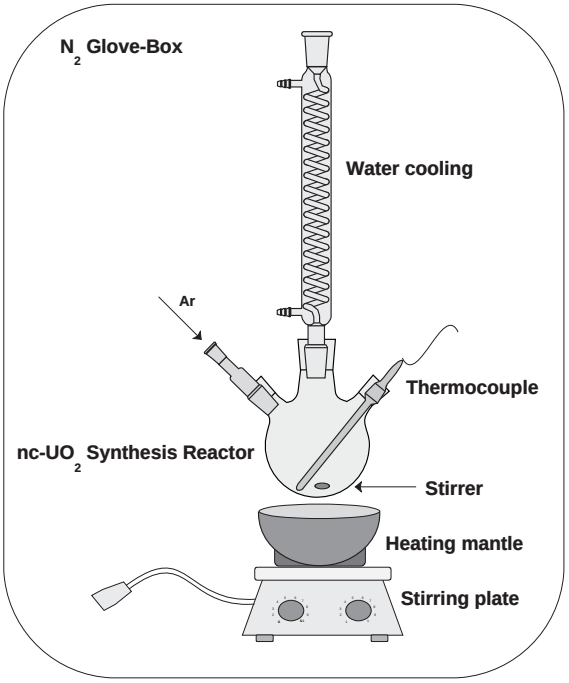

Figure 4.4: Arrangement for the organic thermal decomposition method.

Reduction of surfactant quantities with respect to the metal content in comparison with [Wu et al., 2006] was made. Posterior scale-up of the method from initial quantities of about 0.1 g of nc-UO_2 as reported by [Wu et al., 2006], to quantities of about 2 g of nc-UO_2 achieved here, was done. The same method was also extrapolated for the synthesis of nc-ThO_2.

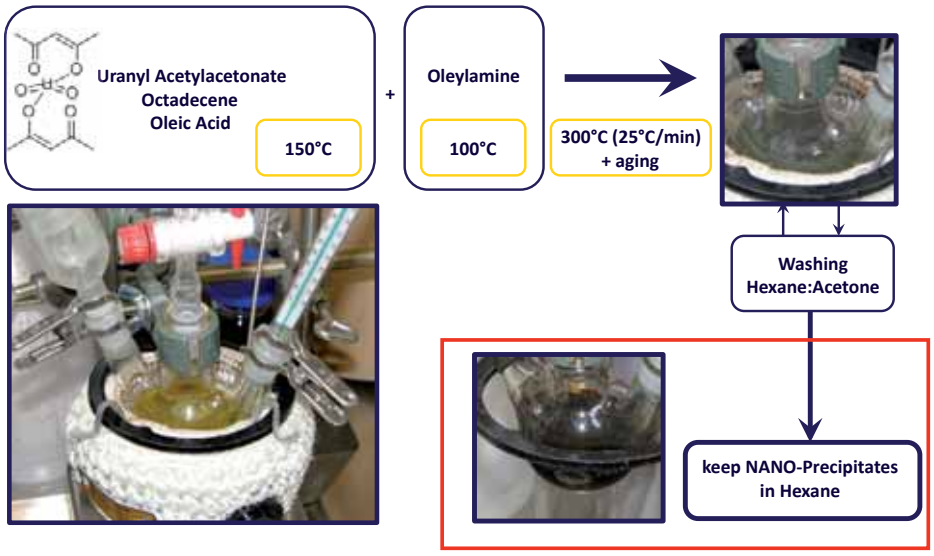

Figure 4.5: Steps in the thermal Decomposition of UAA in organic media.

4.2.1 Solution preparation.

4.2.1.1 UO_2 nanocrystals preparation.

In this method UAA ($UO_2(CH_3COCHCOCH_3)_2$ CAS: 18039-69-5 yellow orange crystals from Ibilabs based on depleted uranium ^{235}U 0.3-0.4% - ^{238}U 99.6% Fig. 4.1a) was used as a precursor. Indeed, 4 g of UAA were dissolved in a solution of 15 mL OA (9-Octadecenoic acid CAS: 112-80-1 99% from Sigma Aldrich) and 27 mL ODE (Octadecene-1 CAS: 112-88-9 90% from Sigma Aldrich) inside a 100 mL three-necked glass reactor under continuous stirring. The three necks of the vessel were occupied by an Ar flow, a condenser and a temperature sensor connected to a temperature controller. The reactor was placed on a heating mantle and the solution was slowly heated up to 150°C and maintained at this temperature during 20 min. Afterwards the solution was left to cool to room temperature and 21 mL OAM (1-Amino-9-octadecene, CAS: 112-90-3, 70%, Sigma Aldrich) were added to the mixture. The solution was then slowly at heated 100°C under continuous stirring during 15 min. During this heating the solution passed from an initial turbid yellow state to a good mixed, transparent orange state (see Fig. 4.6).

(a) (b)

Figure 4.6: (a) UAA + ODE + OA at RT (before applying any temperature). Turbid yellow solution. (b) UAA + ODE + OA + OAM at RT (after stirring at 100°C). Transparent orange solution.

As solvents ODE, OA and OAM were introduced in the reactor. The long chained alcohol (OA) was used as surfactant, and as reducing agent a long chained amine (OAM). The boiling points for the OA, OAM and ODE are 360, 364 and 315°C respectively.

4.2.1.2 ThO_2 nanocrystals preparation.

In this case ThAA ($Th(CH_3COCHCOCH_3)_4$ CAS: 17499-48-8 from Ibilabs colorless crystals Fig. 4.1b) or ThA ($Th(C_2H_3O_2)_4$ CAS: 13075-28-0 from Ibilabs colorless crystals Fig. 4.1c) were used as precursors. The steps followed for the preparation of nc-ThO_2 were similar to those used for the synthesis of nc-UO_2. In this case 0.60 g of thorium acetylacetonate (ThAA) or thorium acetate (ThA) were dissolved in a solution of 3 mL OA and 4 mL ODE inside a 50 mL three-necked glass reactor under continuous stirring. The three necks of the vessel were as before occupied by an Ar flow, a condenser and a temperature sensor connected to a temperature-controller. The reactor was placed on a heating mantle and the solution was slowly heated up to 150°C and maintained at this temperature during 20 min. Afterwards the solution was left to cool to room temperature and 4 mL OAM were added to the mixture. The solution was then slowly heated at 100°C (temperature high enough to allow a good mixing but not high enough to provoke the reaction) under continuous stirring during 15 min. The solution passed from an initial turbid-white to a good mixed transparent white solution.

4.2.2 Reaction step.

4.2.2.1 UO_2 nanocrystals production.

Once the OAM was also mixed in the solution, everything was heated with an average rate of 25°C/min until 300°C. The mixture was so progressively changing its colour from transparent orange-brown at 100°C to turbid dark brown at 190°C, to brown-black at 200°C, until finally turning to completely black at 250°C (see Fig. 4.7). Small explosions inside the reaction vessel occurred at that temperature. Once the temperature plateau at 300°C was reached, the solution was aged at this temperature for 60 min. During this ageing time, small explosions continued inside the vessel.

The solution preparation as well as the reaction steps, were conducted under anoxic conditions in a glove-box under N_2 atmosphere (O_2<0.5%). Furthermore, a continuous Ar gas flow was supplied inside the reactor vessel in order to keep an inert atmosphere. Even so, a lot of water and oxygen molecules are already inside the experimental system (UAA contains two water molecules and two oxygen atoms). The small explosions observed up to 250°C could be due to an effect of oxygen reacting with the solvents during thermal decomposition, at these temperatures.

The UAA and the OAM were thermally decomposed and subsequent reduction of the U^{VI} (UAA) to U^{IV} (UO_2) occurred using OAM as a reducing agent, as suggested by [Wu, 2008]. As a final material, nc-UO_2 were obtained. The surfactant bonded to the nanocrystals forming a lipophylic surface on them. This capping would avoid the agglomeration of the nanocrystals and would allow the post-collection of the crystals in an organic solvent. Finally the solution was left to cool to room temperature.

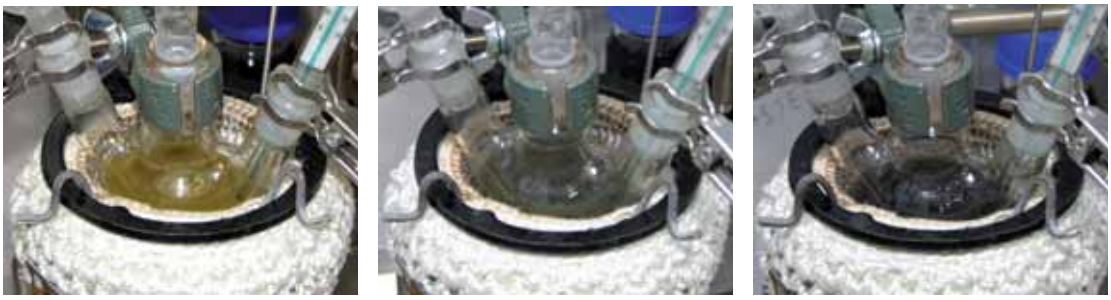

Figure 4.7: U-solution during the reaction step at different temperatures (160, 190 and 250°C).

4.2.2.2 ThO_2 nanocrystals production.

Once the OAM was added to the mixture, everything was heated at 25°C/min up to 300°C. In the experiments where higher temperatures were achieved (330°C), ODE was substituted because its boiling point at 315°C, and just OA and OAM were used as solvents for the reaction. The mixture progressively changed its colour from turbid white at 100°C to yellow transparent at 200°C, and to orange transparent during the ageing time at 300°C and to pale yellow transparent at the end of the ageing (see Fig. 4.7). No explosions occurred during any of the ThO_2-experiments. Different ageing times between 1 to 5 h were tested.

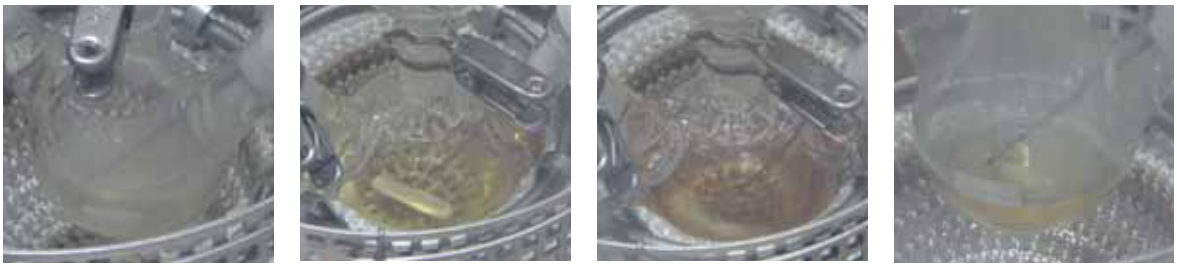

Figure 4.8: Th-solution during the reaction step at different temperatures.

4.3 Precipitation and separation of the nanocrystals.

4.3.1 UO_2 nanocrystals recovery.

The particles coated and stabilized with a non-polar layer, were therefore soluble in highly non-polar solvents such as ODE or toluene. The precipitation of the nanocrystals was induced by adding a non-solvent, a mixture of hexane/acetone (1/4) to the aged solution. The mixture was sufficiently apolar as to selectively precipitate the relatively non-polar particles without precipitating out the ODE and excess OAM and OA (which are taken by the hexane fraction). Pure acetone would be too polar to be directly miscible with ODE. Instead, the use of a mixture with a moderately non-polar solvent such as hexane permits their addition being miscible in the solution without forming a secondary immiscible liquid layer.

Figure 4.9: Typical final UO_2 solution after the reaction step and before precipitation.

Once the mixture of hexane/acetone was introduced, the dispersion was destabilized and the solution became turbid due to the flocculation of the black nc-UO_2 precipitates. The separation was forced by centrifuging the new mixture at 3500 rpm (EBA 20 centrifuge from Hettich) for 10 min. The particles accumulated at the bottom of the centrifuging tubes and the supernatant liquid containing the remaining organics (ODE, OA and OAM) was taken away. New hexane/acetone was introduced in the tubes and the centrifuging step repeated. This procedure was reiterated until the extracting liquid was clear (see Fig. 4.10). After cleaning the nanocrystals several times with the mixture hexane/acetone, the black nc-UO_2 were re-dispersed in an organic solvent such as hexane or toluene.

Figure 4.10: Precipitation, cleaning and recollection in an organic solvent (hexane) of the nanocrystals of UO_2.

4.3.2 ThO_2 nanocrystals recovery.

The ThO_2 nanocrystals where obtained in the same way, but more repeated washing and centrifuging steps were needed to obtain white ThO_2 precipitates at the end of the separation white ThO_2 precipitates. The hexane/acetone (1/4) mixture was introduced in the pale yellow reaction solution, which became white turbid. Then the crystals began to flocculate (see Fig. 4.11) and after centrifuging a pale-orange gel appeared on the bottom on the tubes. After several washing steps, however, white ThO_2 crystals were finally obtained. The ThO_2 where redispersed in an organic solvent (hexane or toluene).

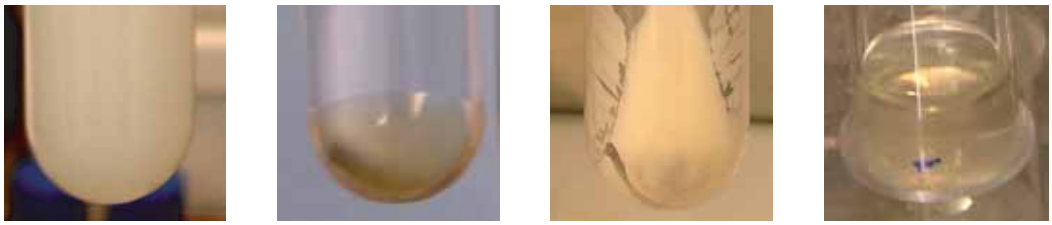

Figure 4.11: Precipitation, cleaning and recollection in an organic solvent (toluene) of the nanocrystals of ThO_2.

4.4 Characterisation of the as produced nanocrystals.

The morphology and structure of the obtained nc-UO_2 particles were characterized by means of transmission electron microscope (TEM), dynamic light scattering (DLS), and the structure confirmed by X-ray diffraction (XRD).

4.4.1 Precipitates morphology and composition.

The morphologies and dimensions of the samples were revealed by TEM. The characteristics of the instrument used, as well as the preparation of the analysed specimens are described in Sec. 2.3.2. The organic route led to high-quality monodispersed UO_2 nanocrystals and ThO_2 rod-shaped nanocrystals.

4.4.1.1 UO_2 nanocrystals morphology.

In Fig. 4.13, the TEM image of synthesised nc-UO_2 by thermal decomposition in organic phase is shown. The average precipitate size was of 4.9(3) nm, as obtained from the size distribution (Fig. 4.12).

The collected black precipitates presented the typical *fcc* fluorite structure of UO_2 and were polycrystalline, as shown by the rings of the SAED in Fig. 4.13c. The selected area electron diffraction (SAED) pattern (inset of Fig. 4.13c) revealed the polycristallinity of the material with the *fcc* structure. The calculated interference fringe spacing in the HRTEM image (Fig. 4.14) was about 0.315 nm, which was in agreement with the interplanar distance of the [111] plane in the *fcc* fluorite structure (0.3153 nm for the UO_2 standard 00-041-1422-ICCD).

Dynamic light scattering (DLS) measurements in hexane medium during 80 s of the dispersed sample of nc-UO_2 obtained by thermal decomposition in organic phase, yielded an hydrodynamic average size of 3.7(1) nm with a polydispersity index (PI) of 0.139. Characteristics of the instrument are shown in Sec. 2.2.2. The size distribution histogram is shown in Fig. 4.15). The DLS size values correspond well with the values observed by TEM.

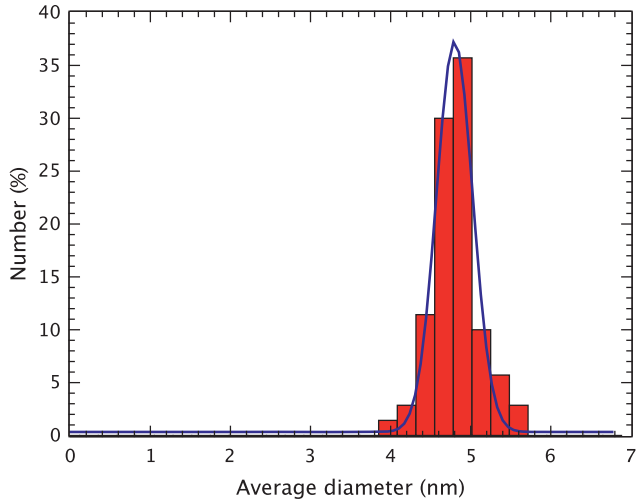

Figure 4.12: Size distribution histogram from TEM measurements of UO_2 nanoparticles synthesized by thermal decomposition of UAA in organic media. Diameter average size of 4.9(3) nm.

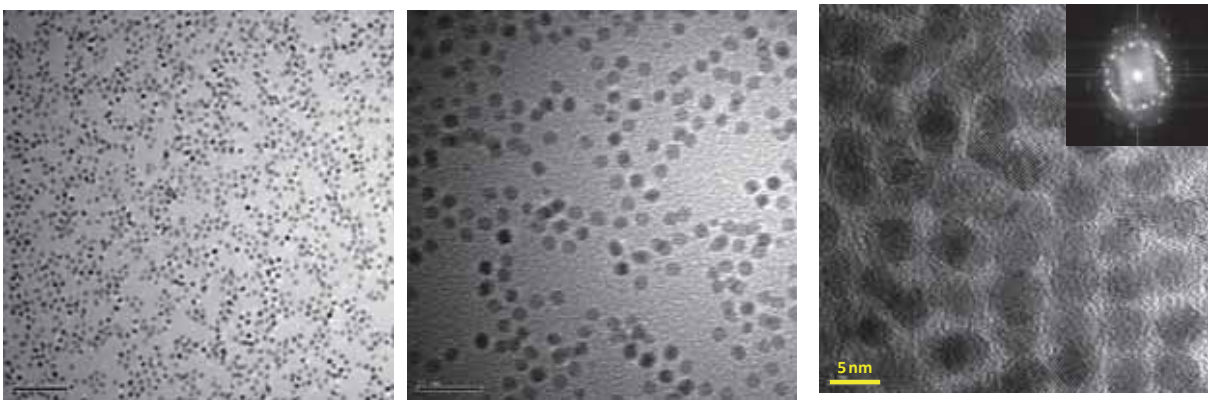

(a) The scale bar is 50 nm.

(b) The scale bar is 20 nm.

(c) The scale bar is 5 nm. The inset of the figure shows selected area electron diffraction (SAED).

Figure 4.13: TEM micrographs of UO_2 at low resolution, showing an assembly of nanocrystals, and at high resolution, revealing lattice imaging of the nanocrystals.

4.4.1.2 ThO_2 nanocrystals morphology.

In Fig. 4.13 the TEM image of synthesised nc-ThO_2 by thermal decomposition in organic phase is shown. Single crystalline 1±0.5 nm in diameter ThO_2-nanorods resulted upon precipitation. There is still not full understanding for the reason of the obtained shape. The precipitate material obtained was quite different in geometry from the one obtained from the UAA precursor, which was instead almost perfectly spherical in shape. Different ageing temperatures (290-330°C) and times (1-6 hours), as well as different precursors (ThAA and ThA) were tested, but the results gained were always ThO_2-nanorods.

The collected white precipitates presented the typical *fcc* fluorite structure of ThO_2 and were polycrystalline, as shown by the rings of the selected area electron diffraction (SAED) pattern (inset Fig. 4.16c) and the HRTEM image (inset Fig. 4.17) showing

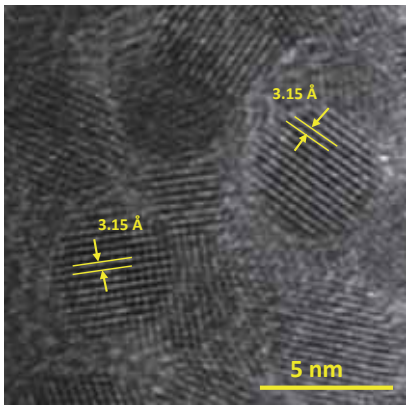

Figure 4.14: TEM micrograph of UO_2 at high resolution, revealing lattice imaging of the nanocrystals and interplanar distances.

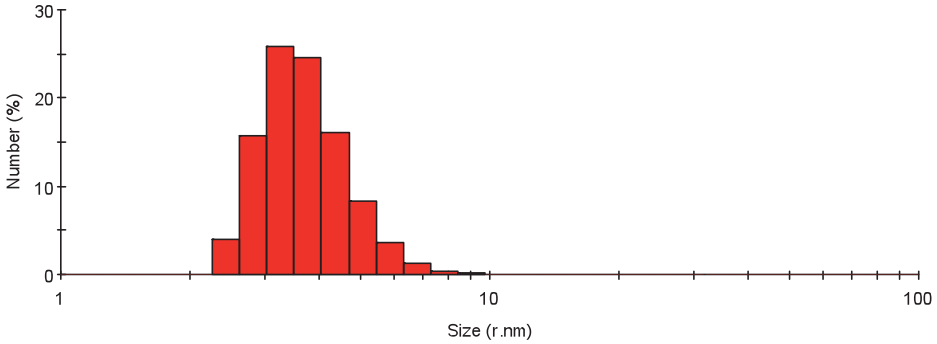

Figure 4.15: Size distribution histogram from DLS test of UO_2 nanoparticles synthesized by thermal decomposition of UAA in organic media. Hydrodynamic average size of 3.7(1) nm.

lattice spacings of an individual nanocrystal. The calculated interference fringe spacing in the HRTEM image (inset Fig. 4.17) was about 0.322 nm, which was in agreement with the interplanar distance of the [111] plane in the *fcc* fluorite structure (0.3232 nm for the ThO_2 standard 00-042-1462-ICCD).

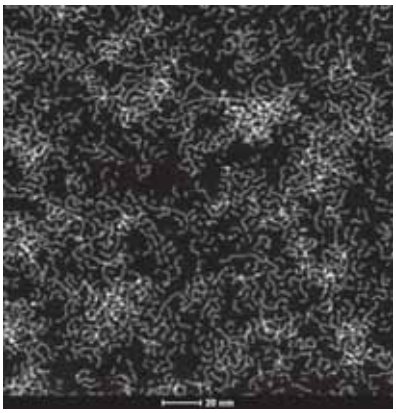

(a) HAADF STEM micrograph. The scale bar is 20 nm.

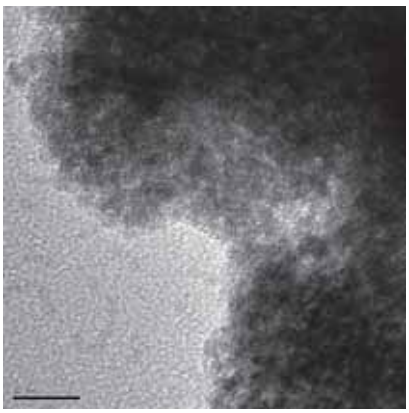

(b) The scale bar is 10 nm.

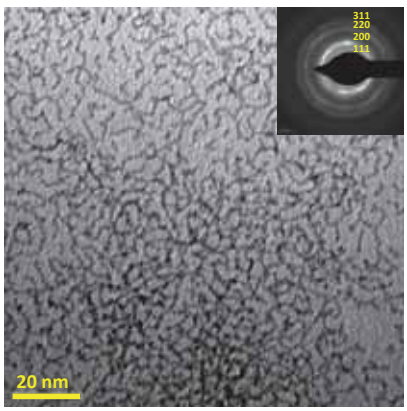

(c) The scale bar is 20 nm. The inset of the figure shows selected area electron diffraction (SAED).

Figure 4.16: STEM and TEM micrographs of ThO_2 nanorods.

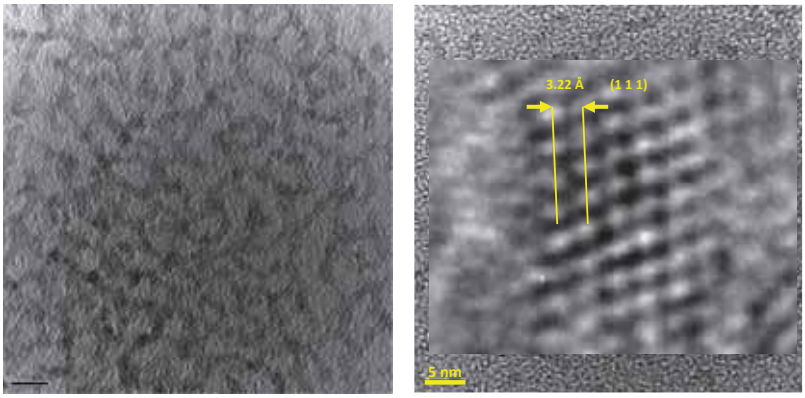

(a) The scale bar is 5 nm.

(b) High-resolution TEM image inset in the figure showing lattice spacings of an individual nanocrystal.

Figure 4.17: TEM micrographs of ThO_2 nanorods at high resolution, revealing the lattice imaging.

4.4.2 Precipitates crystal structure.

The crystal structures and crystal size of the as-synthesised nc-UO_2 particles observed in the TEM analysis were confirmed by X-ray powder diffraction (XRD). The characteristics of the instrument used are described in Sec. 2.4.1.

4.4.2.1 UO_2 nanocrystal structure.

The crystal structure of the nano-precipitates was determined by Rietveld refinement (Sec. 2.4) using bulk-UO_2 as standard. The whole diffraction pattern was taken in account. The XRD pattern of the UO_2-nanocrystalline sample (Fig. 4.18) exhibited well defined peaks (considering typical nanoparticle XRD broadness) that could be indexed to the Bragg reflections corresponding to the standard *fcc* fluorite structure (*Fm-3m* space group) of UO_2 (a=0.547 nm for the UO_2 standard 00-041-1422-ICCD). The lattice parameter was a=0.5431(0) nm, with an average crystallite size of 5.52 nm, in agreement with the average size observed by TEM of 4.9(3) nm. The overall fit quality as described by the measured R-values and the goodness of the fit (GOF) was satisfactory (R(expected)/%=4.44, R(profile)/%=4.34, GOF=1.53). All diffraction peaks showed a small shift to the higher 2θ, which suggests either a slightly higher oxidation state relative to stoichiometric UO_2, or a mechanical distortion (contraction) of the lattice due to surface stresses induced by the small particle size [Boswell, 1951] [Qi et al., 2002] [Fukuhara, 2003] [Park and Qian, 2010].

The Bragg diffraction peak positions and the relative intensities of the refined XRD pattern obtained for the as-produced UO_2-type nanocrystals is shown in Fig. 4.19. A comparison of the corresponding Bragg reflections with those of standard UO_2, U_4O_9 and U_3O_8, is also shown in Fig. 4.19. The Bragg reflections of the synthesized nanocrystals are quite distinguishable from those of the phase U_3O_8 and fully compatible with those of the phases UO_2 and U_4O_9, though more closer to the last one. All peaks showed a small shift to the right (higher diffraction angles (2θ) compared to those of the stoichiometric reference phase. This suggest

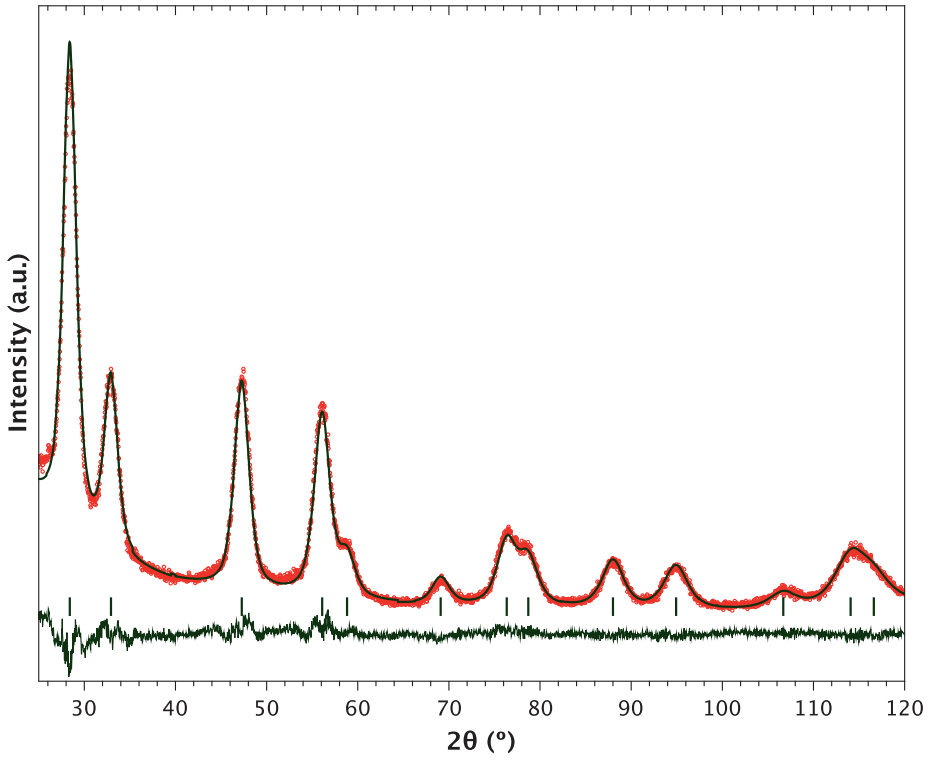

Figure 4.18: XRD pattern of nc-UO_2 (organic route) experimental data, fitted pattern, Bragg peak positions and experimental-fitted diference.

a possible higher oxidation state (perhaps even to U_4O_9 that has the same *fcc* structure).

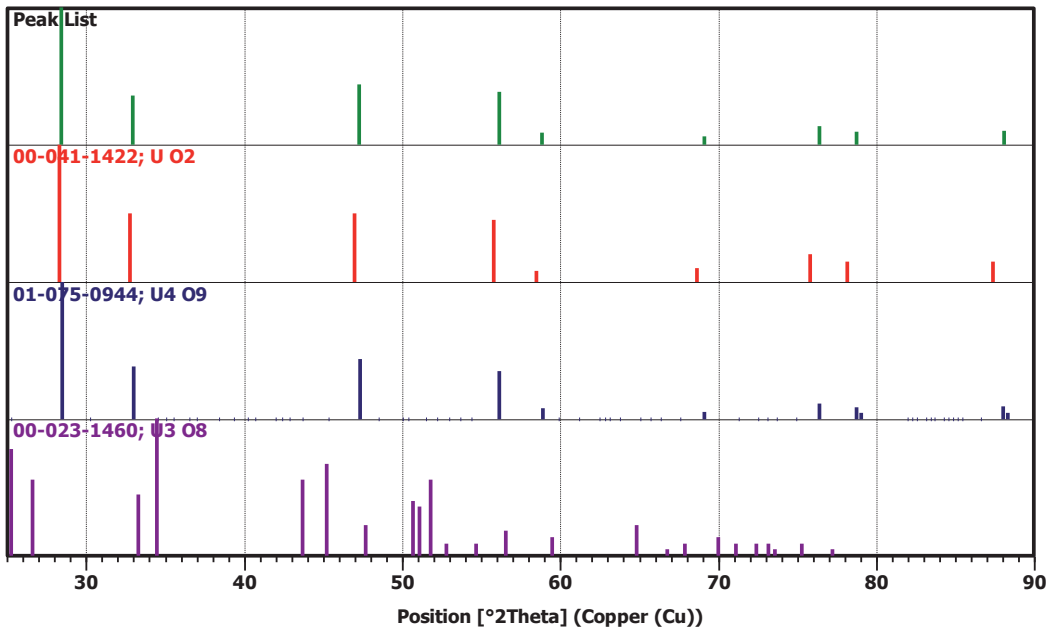

Figure 4.19: Bragg diffraction peak positions and relative intensities for the refined XRD pattern of nc-UO_2 by organic route (*green*), standard UO_2 (00-041-1422-ICCD - *red*), U_4O_9 (01-075-0944-ICCD - *blue*) and U_3O_8 (00-023-1460-ICCD - *lila*), respectively ([ICCD, 2012] database).

The interplanar distance of the [111] plane in the cubic fluorite structure was of 0.3140 nm (0.3153 nm for the UO_2 standard 00-041-1422-ICCD). Calculated interference fringe spacing for single crystals in the HRTEM image of 0.315 nm was obtained (Fig. 4.14).

4.4.2.2 ThO_2 nanocrystal structure.

The coincidence with the *fcc*-ThO_2 structure was confirmed. The very broad peaks, e.g. specially the first one which covered the width of the two first peaks for standard ThO_2 (e.g. [111] and [200], see Fig. 4.20), are a consequence of the extremely small size of the crystallites.

The XRD pattern of the nc-ThO_2 sample (Fig. 4.20) exhibited broad, but well defined peaks that could be indexed to the Bragg reflections corresponding to the standard *fcc* fluorite structure (*Fm-3m* space group) of ThO_2 (a=0.560 nm for the ThO_2 standard 00-042-1462-ICCD). The lattice constant was a=0.5579(1) nm, with an average crystallite size of 1.42 nm, as obtained by Rietveld refinement (Sec. 2.4) using bulk-UO_2 as standard. The whole diffraction pattern was taken in account. The overall fit quality as described by the measured R-values and the goodness of the fit (GOF) was, despite broadness of the peaks, satisfactory (R(expected)/%=2.30, R(profile)/%=4.04, GOF=3.08).

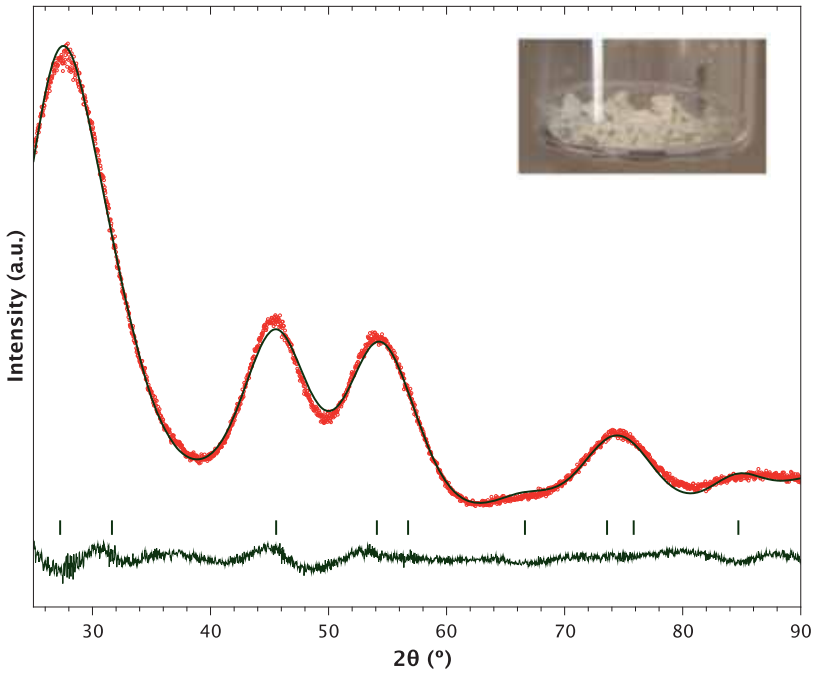

Figure 4.20: XRD pattern of nc-ThO_2 experimental data, fitted pattern, Bragg peak positions and experimental-fitted diference. *Inside picture* shows ThO_2 nanorods powder as-produced.

Moreover, this structural assignment is consistent with the HRTEM. The interplanar distance of the [111] plane in the cubic fluorite structure was of 0.3269 nm for the XRD pattern (0.3232 nm for the ThO_2 standard 00-042-1462-ICCD). Calculated interference fringe spacing for single crystals in the HRTEM image of 0.322 nm was

obtained (Fig. 4.17b).

4.5 Results and discussion.

An organic route to synthesize UO_2 nanoparticles published by [Wu et al., 2006], was here used. Reduction of surfactant quantities with respect to the metal content, as well as scale up of the method from 0.1 g of nc-UO_2 as reported by [Wu et al., 2006] to 2.3 g of nc-UO_2, was achieved. The same method was extrapolated for the synthesis of nc-ThO_2. Thermal decomposition of UAA, ThAA and ThA precursors in organic media using OAM and OA as reducing and capping agents led to high-quality monodispersed UO_2 nanocrystals and ThO_2 rod-shaped nanocrystals. These ThO_2 nanorods have been obtained. The reason for the rod-shape is unknown. More studies changing the OAM/OA ratio, decomposition and incubation temperatures and time should be done to be able to obtain nc-ThO_2 sphere shaped. Batch sizes of 0.3 g ThO_2 nanorods were obtained by this means, i.e. much lower production yield than in the case of UO_2 nanoparticles. Different conditions for the heating rate, ageing time, ageing temperature and initial precursors (ThAA and ThA) were explored for the UO_2 and ThO_2 cases. However, similar results were always found, in terms of the structure and geometry (round-shaped for nc-UO_2 and long shaped for nc-ThO_2) of the precipitates.

The structure and morphology of the obtained product, was characterized by means of TEM, HR-TEM and XRD. Perfectly crystallized solid phases, as studied by XRD, with the typical UO_2-*fcc* fluorite structure (*Fm-3m* space group), with an average crystallite size (spheres diameter) of 5.52 nm and a lattice parameter of 0.5431(0) nm were found, also in agreement with the average size observed by TEM of 4.9(3) nm. Typical ThO_2-*fcc* fluorite structure (*Fm-3m* space group), with a crystallite size (rods diameter) of 1.42 nm and a lattice parameter of 0.5579(1) nm, was found for the ThO_2 nanorods. In both cases, the precipitated nanoparticles were well protected against flocculation, since no aggregation has been observed on the TEM images. The diffractogram of the samples corresponded unmistakably to UO_2 and ThO_2, respectively.

To verify the composition of the precipitates and their propensity to thermal growth in the unconsolidated state, i.e. on just experiencing stochastic physical contact, further analysis of the precipitated material was performed by applying the thermal analytical and X-ray scattering techniques like TG/DTA, HT-XRD and RT-XRD, spectroscopic techniques as XAS, and characterization techniques like TEM. The results are detailed and discussed in Chap. 6.

Chapter 5

Crystallization and Grain Growth in f(T) for nc-UO_2 by Aqueous route

5.1 Generalities.

In this chapter the evolution of the grain size and the crystal structure as a function of temperature under inert and reducing atmosphere of nc-UO_2 precipitated from aqueous phase (see Chap. 3), have been investigated. The focusing parameters studied have been the oxidation degree (O/U ratio), the possible water content on the material, as well as lattice imperfections. Thermogravimetric analysis (TGA) of the samples provides the starting point for these investigations, enabling the identification of mass losses at given temperatures. The structure of the material as a function of temperature under inert and reducing atmosphere, has been identified mainly by X-Ray Diffraction (XRD) and high temperature X-Ray Diffraction (HT-XRD), but also by advanced methods including X-ray Absorption Near Edge Structure (XANES), Extended X-ray Absorption Fine Structure (EXAFS), Magic Angle Spinning Nuclear Magnetic Resonance spectroscopy (MAS-NMR) and Infrared spectroscopy (IR). All of these methods provide complementary information, but are also sensitive to different length scales. With XRD it is only possible to determine structural information on samples with sufficient long range periodicity, and very poorly ordered or indeed amorphous phases will not be detected at all. XANES, provides information on the oxidation state of the cation in favourable circumstances. EXAFS is a local probe detecting the cations, but samples only the order and bond lengths in the nearest and next nearest shells. MAS-NMR focuses on the oxygen, and samples doped in ^{17}O had to be prepared. Finally, IR spectroscopy, bring information on the chemical structure of the oxide system.

5.2 Thermal evolution and mass changes as probed by TGA/DTA.

Thermogravimetry analysis (TGA) and differential thermal analyses (DTA) were employed under Ar/5%H_2 gas at a heating rate of 5°C/min to determine the thermal decomposition temperature and the water content of the product. The description of the instrument is provided in Sec. 2.5.

Mass loss and crystallization for the nc-UO_2 was monitored by the TGA and

DTA signal and is shown in Fig. 5.1. Upon heating, an almost invisible endotherm with a maxima around 155°C occurs. This is accompanied by a slight weight loss of about 2.3 wt% until 207°C, which are most likely attributed to water desorption. Unfortunately, we were not in a position to identify the desorption products, as the integration of a mass spectrometer in a glove-box environment for this purpose presented too many technical difficulties (particularly subsequent maintenance) to be overcome. The mass loss continues with a further 3% until 600°C, which can be related to crystallization (perfectionism of the UO_2 *fcc*-structure). This coincides with the exothermic peak in the DTA at 280°C which reflects this heat realise due to the crystallization, on further reaction to desorb water. However, there is no reason to believe that the weight loss did not include as well some loss of oxygen due to material's reduction. A deeper analysis on the lattice parameter and crystal growth under inert and reducing atmosphere has been in the following sections performed to confirm the latest.

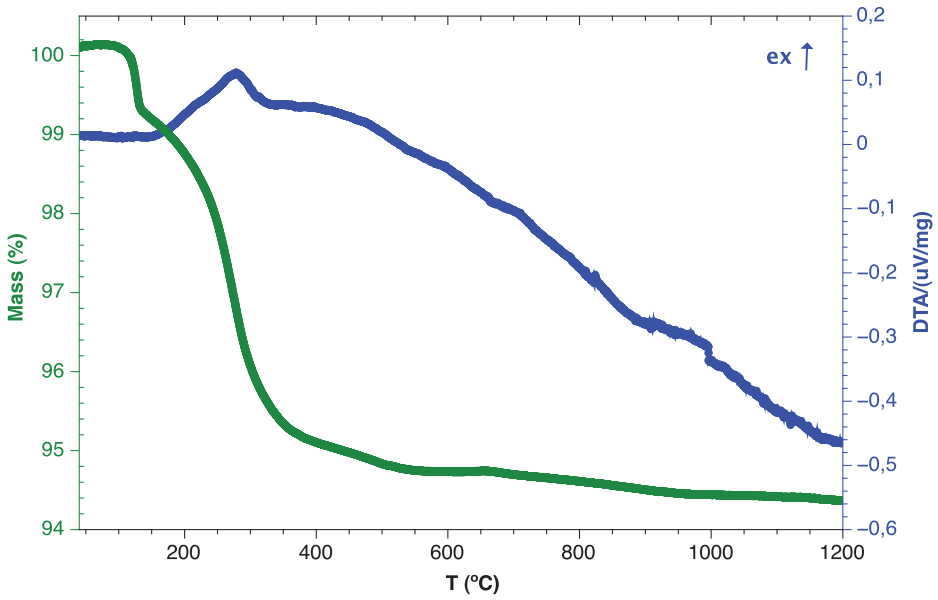

Figure 5.1: TGA and DTA signal for nc-UO_2 until 1200°C under Ar/5%H_2.

5.3 Lattice parameter and crystal growth in neutral atmosphere.

The crystal growth, lattice parameter of the nc-UO_2, has been investigated under inert conditions (static He atmosphere) using in situ HT-XRD. The effect of temperature on the crystallite size, which is a fundamental parameter in the sintering process has been analysed. The in situ HT-XRD patterns were acquired with an instrument described in 2.4.2. The temperature range explored was 30 to 1200°C at a heating rate of 5°C/min under a static He atmosphere.

The evolution with temperature of the nc-UO_2 XRD pattern is shown in Fig. 5.2 (results presented in [Jovani-Abril et al., 2011]). The observed reflections are assigned to UO_2-*fcc* phase structure and to Pt phase corresponding to the heater plate, plus an impurity peak at around $2\theta = 26°$. The pattern is similar to the one reported at room

temperature (RT) by [Rousseau et al., 2009]. They reported the impurity peak as Na polyuranate, coming from precipitation of U(VI) with NaOH. The effect of temperature on the peaks can be observed more clearly in Fig. 5.2-*right*, which displays the evolution of two main peaks (111) and (200) of the UO_2 structure. A shift in the peak position to lower angles is there observed, possibly related to a thermal lattice parameter expansion.

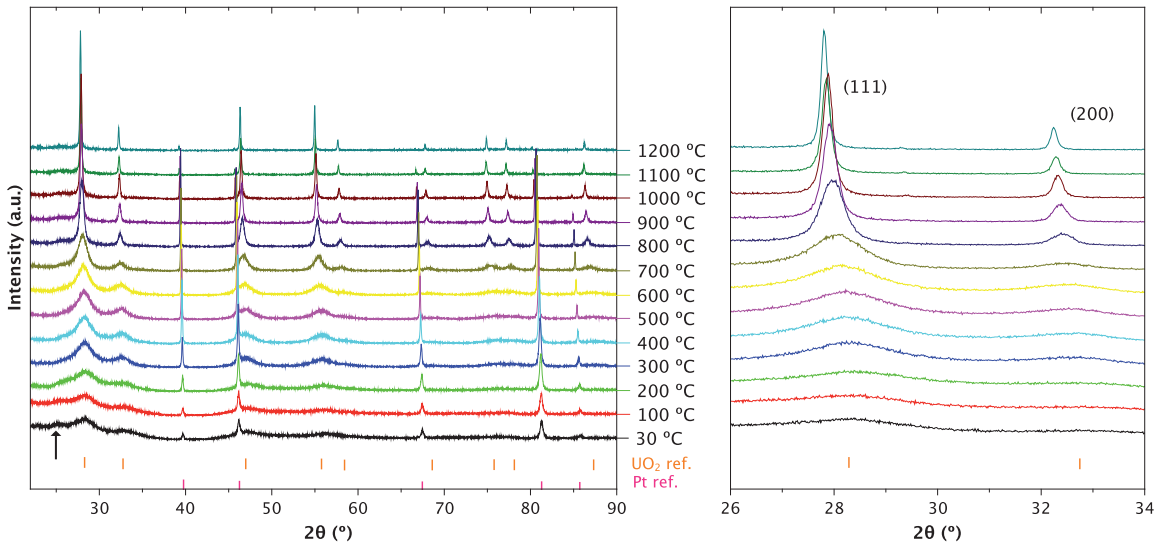

Figure 5.2: In situ HT-XRD patterns of nc-UO_2 under He *(left)*. The typical UO_2 and Pt (from the heating plate) Bragg peak positions are also marked. The arrow on down-right side of the graph shows a residual impurity which disappears with temperature. Evolution of (111) and (200) peaks of UO_2 cubic structure as a function of temperature *(right)* [Jovani-Abril et al., 2011].

An effect of the temperature is seen in the width of the peaks which decreases with increasing temperature while the intensity of the peaks increases. Since the contribution of instrumental broadening is independent of the temperature, the broadening at lower temperatures is mainly related to the crystallite size and strain present in the material, as well as increase of the structural order. Both contributions, crystal size (proportional to $cos^{-1}\theta$ Eq. 5.1) and strain (proportional to $tan\theta$ Eq. 5.2), have different angular dependences, and are so separable. A study of those influences has been in the following performed.

$$D = \frac{K\lambda}{\beta cos\theta} \tag{5.1}$$

$$e = \frac{\beta}{4 \cdot tan\theta} \tag{5.2}$$

where D is the average crystallite size, K is a constant (0.87-1) that depends upon the particle shape and the Miller-indexes (hkl), λ is the wavelength of the radiation, β is the full peak width at half maximum, θ is the Bragg angle and e is the strain.

5.3.1 Grain growth as a function of temperature under neutral atmosphere.

The effect of temperature on the crystallite size, which is a fundamental parameter in the sintering process has been here analysed. The crystallite size of the nc-UO_2 has been determined by the XRD Rietveld refinement (see Sec. 2.4) of the Bragg peaks, and used also to characterize the microstructure of the material.

From these results it is possible to generate a universal representation of the crystallite size as a function of temperature (XRD measurements done at temperature with the HT-XRD instrument under static He atmosphere) and reported in Fig. 5.3. Even though, this information is taken as universal, slight deviations from it may occur, in particular due to dwell times and temperature ramps, but more importantly due to the atmosphere of static He during thermal treatment.

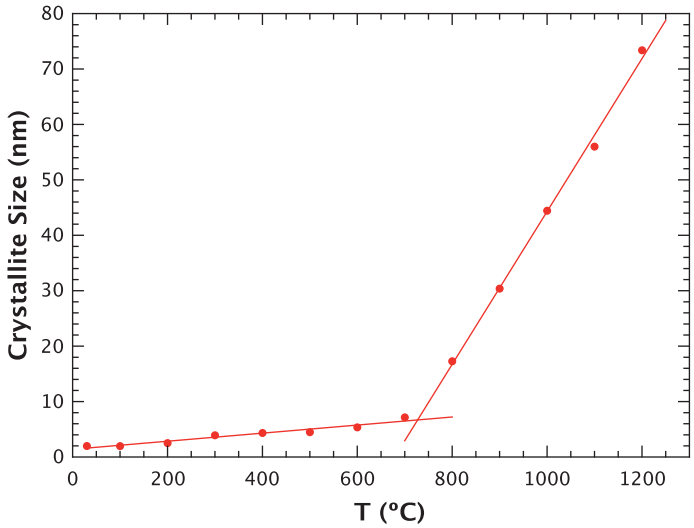

Figure 5.3: Evolution of the nc-UO_2 crystallite size in function of the temperature [Jovani-Abril et al., 2011].

At room temperature, the size of the crystallite was about 4 nm after precipitation Sec. 3.5.1, which is in agreement with previous study by [Rousseau et al., 2009]. The crystallite size change with temperature shows two domains separated at 700°C (see Fig. 5.3). Below that temperature, there was a weak influence on the crystallite size which evolved from 2 to 7 nm (measured in situ at temperature). Above 700°C, the size of the crystallite increased quasi linearly but drastically with temperature, reaching a size about 73 nm at 1200°C.

5.3.2 Lattice parameter and linear thermal expansion coefficient as a function of temperature.

The crystal growth of the sample under inert conditions (static He atmosphere) using in situ HT-XRD, have been already described. In addition, the variation of the lattice parameter versus crystal size and temperature, as well as data on the linear thermal expansion, have been reported and compared to bulk material UO_2. The crystal structure of the precipitates have been, as the crystallite size, determined by Rietveld

refinement, taking into account the whole 2θ range.

In Fig. 5.4a the lattice parameter obtained as a function of temperature (XRDs measured at temperature and under static He atmosphere) and its derivative (Fig. 5.4b), have been also determined by the XRD Rietveld refinement of the Bragg peaks, and represented together with the nc-UO_2 size evolution to observe its dependence. Also calculated lattice evolution of non-stoichiometric standard UO_{2+x} for different O/U ratios due to only thermal expansion, have been represented for comparison. The lattice parameter of a non stoichiometric UO_{2+x} is linked to the oxygen content by the relations of [Lynds et al., 1963]. Also the lattice parameter was corrected in function of temperature with the [Fink, 2000] relations reflected in Eq. 5.3.

$$\begin{aligned} 2 \leq O/U \leq 2.125 \qquad & a(nm) = 0.54705 - 0.0094 \cdot O/U \\ 2.1725 \leq O/U \leq 2.250 \quad & a(nm) = 0.54423 + 0.0029 \cdot (9 - 4 \cdot O/U) \end{aligned} \tag{5.3}$$

The main change in the lattice parameter occurs between RT and 600°C and for crystal sizes below 6 nm. The lattice parameter suffers a strong expansion increasing steeply from 0.5417(1) nm to 0.5492(1) nm at 300°C, and then decreases to 0.5485(0) nm. Above 600°C, a linear evolution of the the lattice parameter with temperature is observed.

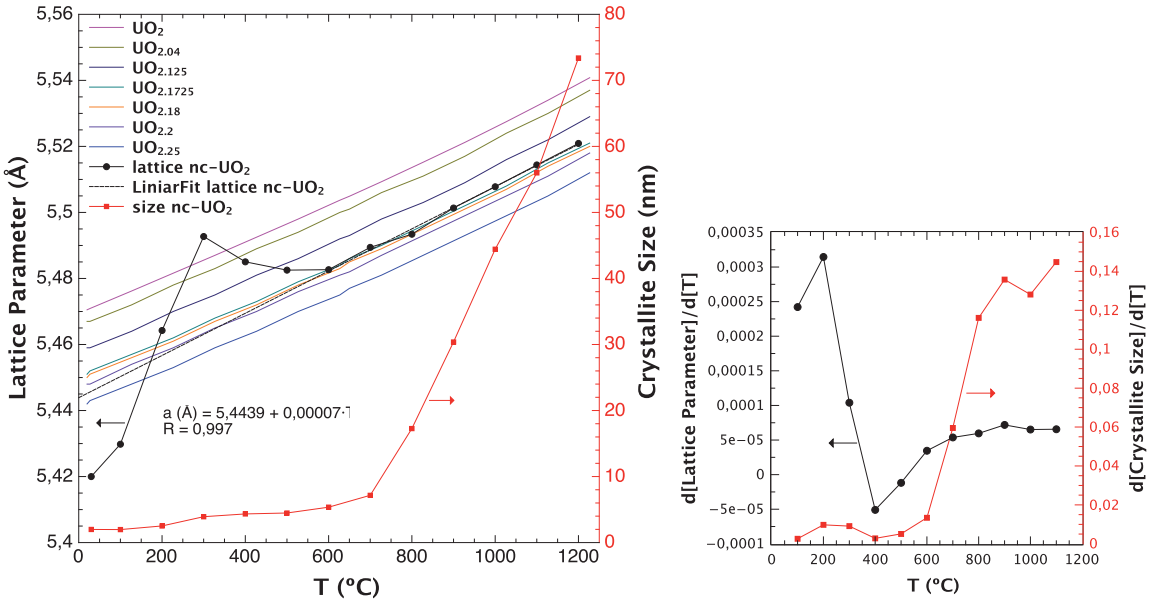

(a) (b)

Figure 5.4: a.) Lattice constant and crystallite size variation (curves only as a guide to eye) of nc-UO_2 in function of temperature, from in situ HT-XRD measurements under static He atmosphere in comparison with lattice evolution in function of temperatures of standard UO_2 for different O/U ratios obtained by the relations of [Lynds et al., 1963], due to only thermal expansion. b.) Relative crystallite size and lattice parameter vs. temperature (curves only as a guide to eye).

From, the lattice parameter curve in function of temperature, the extrapolated linear trend up to 600°C is shown by the straight dotted line and described by the following equation $a(nm) = 0.54439 - 0.00007 \cdot T$, obtaining a value of the lattice parameter at 20°C of 0.5445 nm, closer to the lattice of UO_2 bulk at RT.

Relating the lattice parameter found in this study with the [Lynds et al., 1963] relations, a stoichiometry of about $UO_{2.18}$ up to 600°C to around $UO_{2.17}$ up to 900°C has been found, which is similar to the one reported by [Rousseau et al., 2009]. So the nanocrystallites stabilize at O/U 2.17-2.18 at temperatures above 600°C, or in other words, at particles sizes higher than 6 nm. A XPS data showing a contribution of U(VI) and U(IV) in the precipitated particles was reported by [Rousseau et al., 2009]. Based on the lattice parameter determined by XRD, they concluded hence that the stoichiometry was $UO_{2.19}$, thus describing the system as nc-UO_{2+x} and is very similar to our conclusion, too. However, remark that Eq. 5.3 and other equivalent relations are valid for bulk compounds; their applicability to nanocrystals may be still open to proof.

Fig. 5.5 displays the linear thermal expansion (LTE) and the thermal expansion coefficient (LTEC) of nc-UO_2 as a function of the temperature. The LTE at temperature T was calculated using the relation:

$$LTE = \frac{(a_T - a_0) \times 100}{a_0} \tag{5.4}$$

where a_T is the lattice parameter at temperature T and a_0 is the lattice parameter at 20°C. The LTEC was calculated by differentiating the thermal expansion curve a_T versus T with respect to the temperature T:

$$LTEC = \frac{1}{a_0} \times \frac{\delta a_T}{\delta T} \tag{5.5}$$

The LTE of the nc-UO_2 is in general higher than the one for bulk-UO_2 [Martin, 1988] for all the interval of temperatures, with a jump at 300°C and a posterior stabilization above 600°C as one could already predict from the lattice parameter representation in function of temperature (see Fig. 5.4a).

The LTEC is initially higher for nc-UO_2 than for bulk-UO_2 for temperatures below 400°C and tends to stabilize above 600°C with a value of $12 \cdot 10^{-6}$ $°C^{-1}$ in agreement with the value for the LTEC of bulk-UO_2. The oscillatory trends observable for LTEC in nc-UO_2 at T <900°C can be attribute to transitory oxidation-reduction effects. At T ≥600°C it is clear that the oxygen content of the material stabilizes (at O/U 2.17-2.18) (Fig. 5.4a), at the time that the lattice expansion coefficient meets the value of the reference bulk phase (large grain) (Fig. 5.5). For crystal sizes >6 nm the nanocrystalline material meets the thermal-expansion behaviour (i.e. thermal expansion coefficient) of bulk (large-grained) UO_2. This behaviour was already observed in the representation of the relative lattice parameter (see Fig. 5.4b), and it shows once more that the ab-normal nano-effects in the material are only to be expected for particle sizes below few tens of nanometer.

If Fig. 5.6 the patterns comparison of nc-UO_2 as-produced (a = 0.5417(1) nm), nc-UO_2 at 1200°C (a = 0.5521(0) nm) and nc-UO_2 at RT after thermal treatment at 1200°C (a = 0.5473(0) nm) measured in situ in the HT-XRD instrument under static He atmosphere, is shown.

There is not explanation for the value seen for the nc-UO_2 measured at 1200°C under static He atmosphere: an O/U ratio close to $UO_{2.17}$ (see Fig. 5.4a) and the a

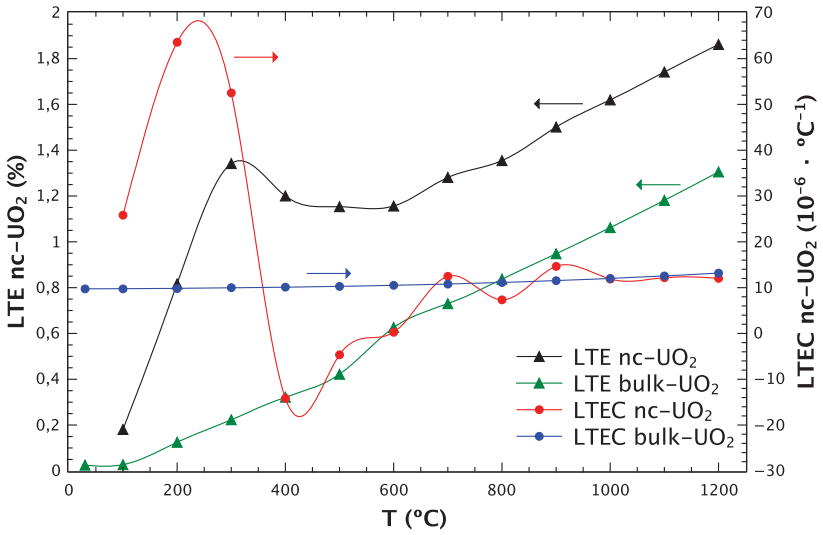

Figure 5.5: Linear thermal expansion (LTE) and linear thermal expansion coefficient (LTEC) of the nc-UO_2 (curves only as a guide to eye) in comparison with data of bulk-UO_2 from [Martin, 1988].

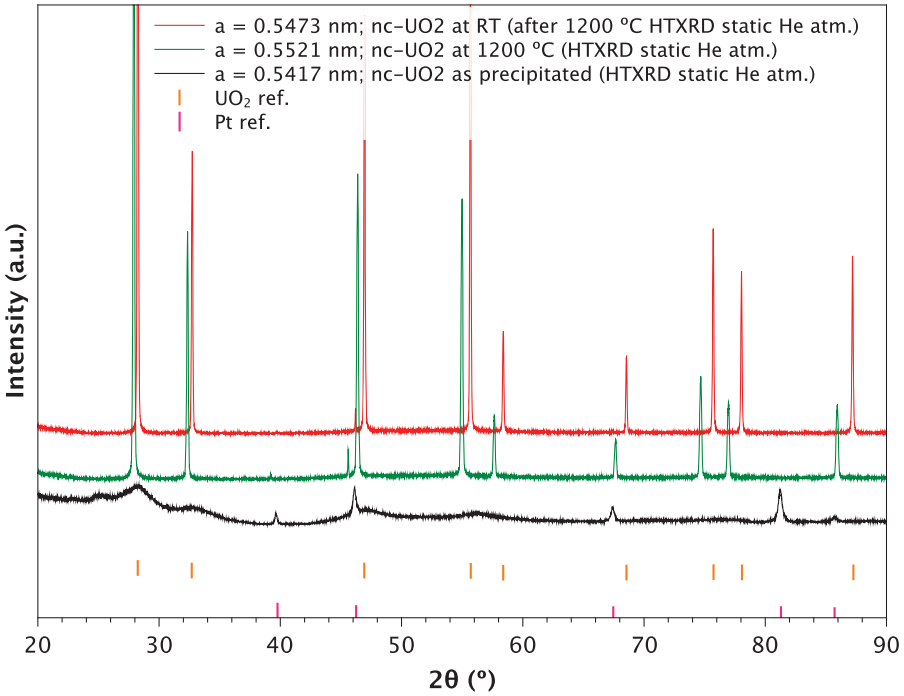

Figure 5.6: Patterns comparison of nc-UO_2 as-produced, nc-UO_2 at 1200°C and nc-UO_2 at RT after thermal treatment at 1200°C measured in situ in the HT-XRD instrument under static He atmosphere.

lattice parameter of a = 0.5521(0) nm. In contrast, the same thermal treated sample measured after cooling at RT, shows a value of 0.5473(0) nm ($UO_{2.00}$) very similar from the typical for bulk-UO_2 (0.547 nm). The peaks of the nc-UO_2 at RT after the thermal treatment at 1200°C recover the typical position for standard UO_2 (see Fig. 5.6).

So, a recovering of the crystal structure has been achieved with temperature under

static He atmosphere from the initial lattice parameter value of 0.5417(1) nm from the nc-UO_2 as-produced to 0.5473(0) nm after thermal treatment at 1200°C. It might be related to the static He atmosphere, which resulted in a thermodynamic equilibria between H_2, H_2O and O_2 in the gas phase, favouring H_2 during the cool down, thus this might be the cause.

5.3.3 Lattice strain evolution as a function of temperature.

The mean strain, e, in the material was determined by Rietveld refinement using the software [HSP-PAN, 2011] and used to characterize the deformation state of the material. The analysis of the strain by Rietveld refinement method is based on the change of the profile parameters, compared to a standard sample. Those are depending on the instrument settings used for data collection and on the profile function used for the refinement [HSP-PAN, 2011].

The crystallite size change with temperature, already shown in Sec. 5.3.1, was characterized for two steps separated at 700°C. Below that temperature, there was a weak influence on the crystallite size which evolved from 2 to 7 nm (measured in situ at temperature). Above 700°C, the size of the crystallite increased quasi linearly but drastically with temperature, reaching a size of about 73 nm at 1200°C. In the evolution of the lattice strain release with temperature, two steps can be observed (Fig. 5.7). The first step is visible at T <300°C where the strain is at its maximum, which could be related to the dehydration step (water molecules attached to the nanocrystals and to the related binding-strength) visible in the TGA/DTA (Fig. 5.1). The second step is visible in the range 300-700°C where the strain decreases, which could be related to additional loss of water and oxygen loss (O/U stabilization) and structure consolidation. Up to 700°C, the internal strain vanishes and the crystallite-size starts to grow. It is interesting to note that the complete release of the strain in the nc-UO_2 coincides with the onset of the starting of the crystallite growth. So the crystallite growth seems to be limited by the presence of the lattice strain. From RT until 700°C the thermal energy is totally used to remove the strain and up to that temperature no strain is remaining and the energy is used for the growing of the nanocrystals.

5.4 Lattice parameter and crystal growth under reducing conditions.

The local structure has been investigated for the nc-UO_2 as-produced and after thermal treatment under reduction conditions (Ar/5%H_2), by X-Ray Diffraction (XRD), MAS-NMR, IR and X-ray Absorption Spectroscopy (XAS), and compared to bulk-UO_2 as a reference. A combination of X-ray Absorption Near Edge Structure (XANES) and Extended X-ray Absorption Fine Structure (EXAFS) was used.

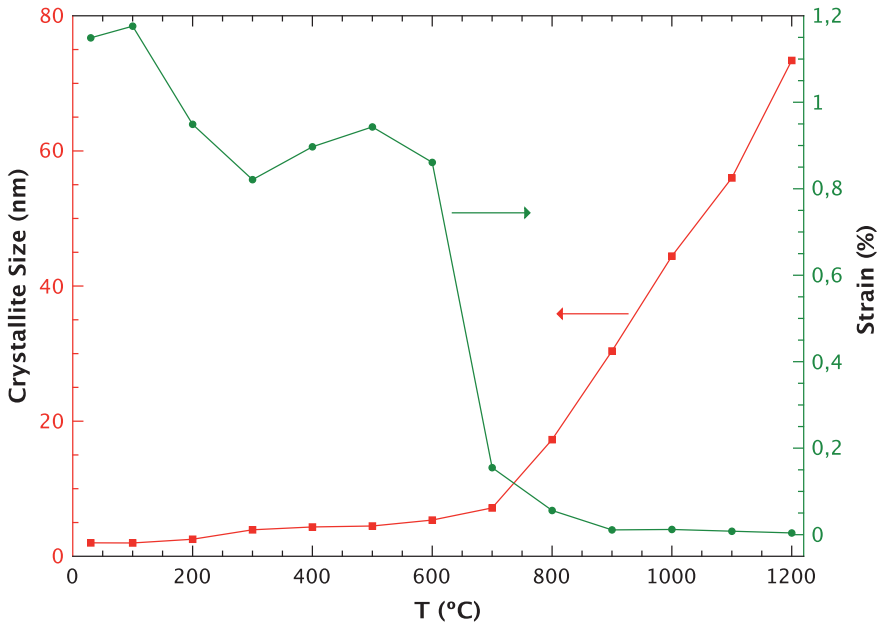

Figure 5.7: Crystallite size and strain of nc-UO_2 in function of temperature. Measurements done at temperature under static He atmosphere (curves only as a guide to eye).

5.4.1 Crystal size and lattice parameter evolution as a function of temperature as probed by XRD.

As it has been seen from the HT-XRD, the lattice constant (and crystal size) of the material in the cooled state (at RT) after reach different maximum temperatures is needed (see Fig. 5.6). This allows separation of the thermal expansion contribution in the high-temperature values to obtain cleaner curves for thermal expansion vs. temperature and lattice dimension vs. crystal size.

At the outset of this study, a higher concerning about the control of the O/U ratio, which is not simple, appeared. The structural investigations presented in the following, attempt to eliminate this issue as the samples were heated in Ar/5%H_2 to ensure that the O/U = 2.00. The impact of the heat treatment on the microstructure of nc-UO_2 at different annealing temperatures was then studied under reducing conditions (dynamic Ar/5%H_2 atmosphere). As-produced or RT, 600°C and 1200°C. The corresponding XRD data are given in Fig. 5.8. A heating rate of 5°C $\cdot$ min^{-1} under dry Ar/5%H_2 and annealing for 15 minutes were used. At 600°C the major mass loss has already occurred and no water traces should be present in the material as it has been observed in the TGA/DTA (Fig. 5.1). As a reference, a standard $UO_{2.0}$ (μm crystal size) sintered at 1600°C under Ar/5%H_2 for 6 hours and measured during the same measuring campaign, was also used.

The measurements indicated a well crystallized single cubic phase with a fluorite structure (*Fm-3m*). No evidence for orthorhombic or other phase was found. From the Rietveld refinement of the measured diffractograms, the lattice parameters as well as the size of the particles were deduced. Reduction of the nc-UO_{2+x} towards nc-UO_2 after annealing at 600°C and 1200°C was expected because the high sensitivity of the lattice parameter, a, to changes in the oxidation state of U in the hyperstoichiometric range, O/M >2. Samples treated at increasing temperature (RT, 600°C and 1200°C)

with a short isothermal hold of 15 min, exhibit an increase in the lattice constant of 1.02%. Progressing crystallization of the nc-UO_2 leaded to periodic ordering of its atom and the lattice parameter changed from 0.5417(1) nm at RT, to 0.5431(0) nm and 0.5472(0) nm at 600°C and 1200°C, respectively. The crystal-size increased from 3.79 nm ($\simeq$ 4 nm) as-prepared, to 9.3 nm ($\simeq$ 9 nm) and 82.16 nm ($\simeq$ 82 nm) following treatments at 600°C and 1200°C, respectively (Fig. 5.8).

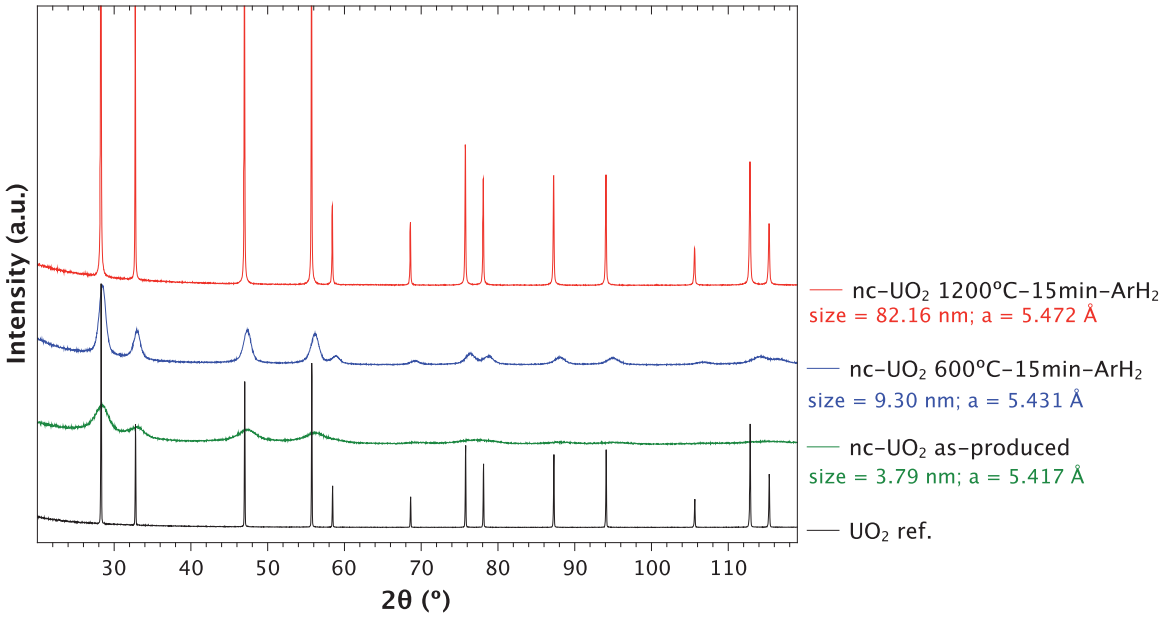

Figure 5.8: XRD patterns of reference UO_2 and aqueous route nc-UO_2 (as-produced, after thermal treatment under Ar/5%H_2 at 600°C and 1200°C)

A comparison of the crystal size and lattice parameter for the samples treated at 600°C and 1200°C under dynamic Ar/5%H_2 atmosphere (measurement after cooling) with those under static He atmosphere measured at temperature (see Fig. 5.4a), is provided in Table 5.1. No difference in the crystallite size was obtained at 600°C under either atmosphere. But a notable change is observed at 1200°C, where a crystallite size of 73.39 nm under He has been observed and a size of 82.16 nm under Ar/5%H_2. Major differences have been seen in the lattice parameters as a function of the atmosphere used without ignoring the fact that the values under He were measured at temperature. These difference in the lattice disappeared once the sample measured at temperature is measured after cooling, as it has been seen in Fig. 5.6. In the evolution of the lattice strain, e, a release was again observed with increasing temperatures. After annealing at 600°C under Ar/5%H_2, just the half of the strain was present being totally released at 1200°C, as it also happen under He atmosphere.

Fig. 5.9 shows TEM images of the nc-UO_2 (about 4 nm size) particles as-produced and after being thermal treated at 1200°C (about 120 nm size) under Ar/5%H_2. The TEM size observed after treatment is in good agreement with the average value of 82.2 nm obtained of the Rietveld refinement (Fig. 5.8).

Table 5.1: Crystal size and lattice parameter for aqueous route nc-UO_2 treated at 600°C and 1200°C under two different atmosphere (Ar/5%H_2 and He atmosphere)

	Ar/5%H_2 atm.[a]			**He atm.**[b]		
	cryst. size (nm)	**lattice param. (nm)**	**strain (%)**	**cryst. size (nm)**	**lattice param. (nm)**	**strain (%)**
nc-UO_2 RT	3.79	0.5417(1)	0.792	1.99	0.5420(10)	1.149
nc-UO_2 600°C	9.30	0.5431(0)	0.391	5.36	0.5483(5)	0.861
nc-UO_2 1200°C	82.16	0.5472(0)	0.026	73.39	0.5521(0)	0.004

a.) Measurement after cooling. b.) Measurement at temperature (HTXRD meas.).

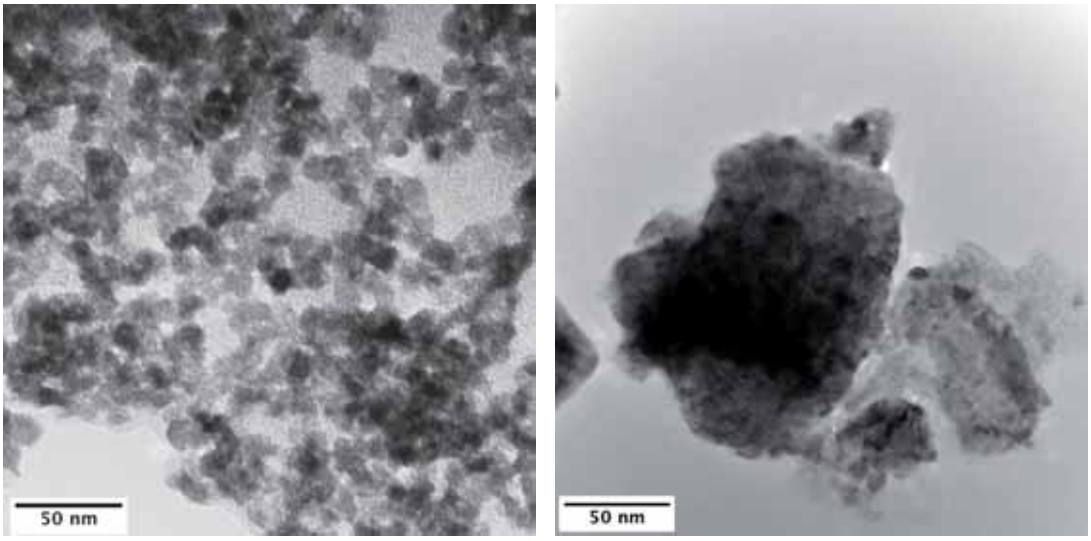

(a) nc-UO_2 as-produced. (b) nc-UO_2 after 15 min at 1200°C.

Figure 5.9: TEM images for the nc-UO_2 as-produced and after thermal treatment under Ar/5%H_2.

5.4.2 O/M ratio as a function of temperature as probed by XANES.

XANES was used to determine the oxidation state of U cations and the corresponding molar fractions and the O/U ratios were derived. The normalized XANES spectra and the first derivate at the U-L_3 absorption edge of three different heated nanocrystalline UO_2 samples (nc-UO_2 at RT, 600°C and 1200°C) are shown in Fig. 5.10, together with the reference spectra of $U^{IV}O_2$. The experimental features are specified in Sec. 2.2.3. The associated energies of the inflection point at absorption edge and of the white-line (WL), as well as the energy shift (ΔE) and the estimated oxidation states derived from this study, are given in Table 5.2.

A simple observation of the XANES spectra at the U-L_3 edge immediately shows a trend with increasing temperature and as x decreases (UO_{2+x}). The peak of the WL shifts slightly to lower energies and increases in intensity, and the within the XANES regions increase. The amplitude decrease with the increasing temperature of thermal treatment showing a higher structural order of these samples.

For the samples as-produced (RT) and at 600°C, there is a significant difference of shape compared to the $U^{IV}O_2$ reference, i.e. presence of a shoulder on the high

energy side of the edge. This feature usually indicates the presence of U^{VI}. According to [Conradson et al., 2005a], a shoulder appears on the high energy side of the main peak, ongoing from An^{IV} to An^{V} and An^{VI} (An = Actinides = Th, Pa, U, Np, Pu, Am, Cm). This is also in agreement with the observed decrease of WL amplitude with the increasing temperature. The shoulder decreases with temperature meaning that there is less U^{VI} or that the U^{IV} bulk is more visible as it size increases. A clear shift (further for the RT sample) of the absorption edge and WL-peak to higher energies, as well as a broader WL is observed. However the spectra for the $U^{IV}O_2$ reference and the annealed sample at 1200°C, are remarkably similar, indicating that the electronic structure of the 82 nm UO_2 is essentially that of the bulk $U^{IV}O_2$ at that temperature.

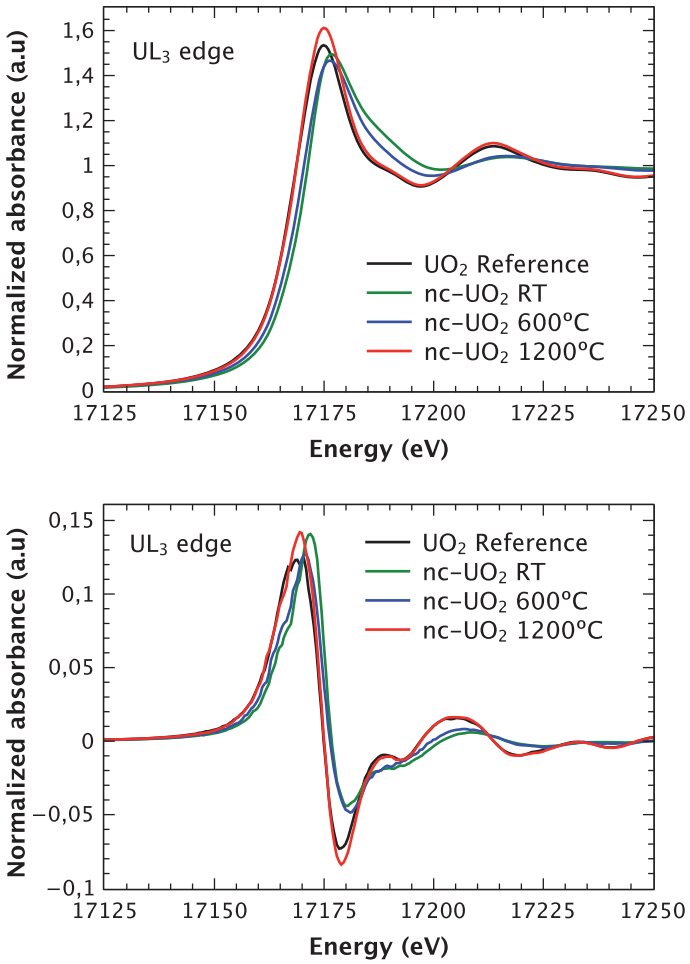

Figure 5.10: Normalized absorption XANES spectra and the first derivate at the U-L_3 edge of the three different heated nc-UO_2 samples from Aqueous route (nc-UO_2 at RT, 600°C and 1200°C), together with the reference spectra of bulk $U^{IV}O_2$.

Detailed analysis of the U-L_3 XANES spectra and of their first derivate for the RT sample, show that the energy of the WL shifts 1.8 eV (Table 5.2) to higher energies in comparison with the reference UO_2 (U^{IV}) spectrum. A shoulder on the right side of the edge for RT, is observable. It could be expected the sample is the most cluster like (smaller in size), but in addition the composition is not fully ascribed to UO_2. The shoulder could be a proof of the presence of U^{VI}. Additionally to the hyper-stoichiometry, the presence of U^{VI} suggests that water molecules and/or OH groups would be also present in the RT sample. In those nc-material, the surface is

superior to the bulk. If there is any adsorbed water molecule, the valence of U is increased and the XANES spectra is significantly different to the bulk. Molar fractions of 55% of U^{IV} and 45% of U^{VI} corresponding to a ratio O/M of 2.45 ($V_U = 4.9$) (Table 5.2), have been deduced for the RT sample according to a linear combination of UO_2 and U_3O_8, as explained in Sec. 2.2.3.

In the 600°C treated sample, the shift of the WL (1.4 eV respecting the $U^{IV}O_2$ reference; Table 5.2), as well as the shoulder (in this case less defined) are toward to the left in comparison to the RT sample. It indicates a minor presence of U^{V} and U^{VI} species but still not strictly U^{IV}. An O/M ratio of 2.30 ($V_U = 4.6$) was found for the sample treated at that temperature, with a molar fraction of 70% of U^{IV} and 30% of U^{VI} (Table 5.2).

Concerning the 1200°C treated sample, XANES analysis shows no doubt that the sample has a fluorite structure. No spectrum shift is observed and there is mainly U^{IV}, and probably some U^{V}, as there is a slight shift of the inflexion point. An O/M ratio of 2.025 ($V_U = 4.05$) was in this case found corresponding to a molar fraction of 95% of U^{IV} and 5% of U^{V} and in agreement with the lattice parameter of 0.5472 nm obtained at 1200°C by XRD. Also the U-L_3 XANES data for the reference UO_2 and nc-UO_2 treated at 1200°C samples in Fig. 5.10 are very similar to the UO_2 data reported by [Conradson et al., 2005b], [Conradson et al., 2005a]. In particular, a shoulder is identified at about 17.185 eV, which would indicate that U is stabilized in valence (IV) for the nc-UO_2 at 1200°C treated.

This result is most noteworthy, as this detailed study of bulk UO_{2+x} by [Conradson et al., 2005a] showed that the energies of these features did not change in energy as a function of stoichiometry. The results presented in Fig 5.10 clearly indicate that the 4 nm UO_2 particle even after 600°C anneal (9 nm), does not have the electronic structure of bulk UO_2. At this temperature, a reduction to U^{IV} would also be expected. XANES reflects the unoccupied electronic structure. In a molecule, these are well defined energy levels, while in a solid they are bands of a particular symmetry. One can understand the size effect if one considers this 4 nm UO_2 crystals as a cube with a side length of 4 nm, which is the same of around 7 UO_2-unit cells (lattice parameter a = 0.547 nm). This cube contains a bulk cube of around 3 nm length (5 UO_2-unit cells). Thus there are 391 unit cells in total inside the 4 nm crystal, with 241 (62%) on the surface and 150 in the interior, which one restrains from calling "bulk". For the thermal treated samples the percentage of unit cells in the surface would be 32% at 600°C (9 nm) and 4% at 1200°C (82 nm). This is a crude representation of the problem, but shows that the material is more like a large cluster in transition from a large molecule to that of the true bulk. Thus it is not surprising that the XANES depicts an electronic structure of the nc-UO_2 material unique from the bulk material.

Table 5.2: Results from the analysis of the UO_{2+x} XANES data at the U-L_3 edge.

	lattice param. (Å)[a]	**inflection point** (eV)	**energy WL** (eV)	**ΔE^b** (eV)	**U valency** (V_U)	**molar fraction** U^{IV} (%)[c]	U^{V} (%)[c]	U^{VI} (%)[c]	**O/M**
Reference:									
UO_2	5.472(0)	17168.7	17174.9	-	4.00	100	-	-	2.000
Samples:									
nc-UO_2 4 nm RT	5.417(1)	17171.8	17176.7	1.8	4.90	55	-	45	2.450
nc-UO_2 9 nm 600°C	5.431(0)	17170.7	17176.3	1.4	4.60	70	-	30	2.300
nc-UO_2 82 nm 1200°C	5.472(0)	17169.6	17174.9	0.0	4.05	95	5	-	2.025

a.) by XRD (see Fig. 5.8). b.) ($\Delta E = WL_{sample}$ - $WL_{ref.}$). c.) According to a linear combination of UO_2 (pure U^{IV}), U_4O_9 (mixture of U^{IV} and U^{V}) and U_3O_8 (mixture of U^{IV} and U^{VI}). d.) under Ar/5%H_2.

5.4.3 Order and disorder probed by local methods, as Debye-Waller EXAFS, NMR and FTIR, as a function of crystal size.

5.4.3.1 Local structures as probed by Debye-Waller EXAFS distances.

The k^3-weighted EXAFS spectra and the corresponding Fourier transforms (FT) at the U-L_3 edge for the experimental data of UO_2 nanocrystals at different temperatures annealed, and $U^{IV}O_2$-bulk reference, are shown in Fig. 5.11. The experimental features are specified in Sec. 2.2.3. The fitted k^3-weighted EXAFS spectra and their associated Fourier transforms are presented in Fig. 5.13. Also the structural parameters derived from analysis of the EXAFS data, as the coordination number (CN), interatomic distance (R), Debye-Waller (DW) factor (σ^2) and shift of the threshold energy (ΔE_0), are provided in Table 5.3.

Table 5.3: Results from the analysis of the aqueous method synthesised nc-UO_{2+x} EXAFS data at the U-L_3 edge.

	U-O_1			**U-U_1**			**U-O_2**			
	CN	R (Å)	σ^2 (Å^2)	CN	R (Å)	σ^2 (Å^2)	CN	R (Å)	σ^2 (Å^2)	R_f (%)
Reference $U^{IV}O_2$	f			f			f			
k-range = 1-15 Å^{-1}	8	2.34	0.008	12	3.85	0.005	24	4.49	0.009	2.1
R-range = 0-8 Å		(1)			(1)			(1)		
Samples nc-UO_2										
4 nm RT	f									
k-range = 3-8 Å^{-1}	8	2.26	0.027	-	-	-	-	-	-	4.7
R-range = 1-3 Å		(2)								
9 nm 600°C	f			f						
k-range = 3-9 Å^{-1}	8	2.27	0.026	12	3.82	0.014	-	-	-	4.1
R-range = 1-4.5 Å		(2)			(3)					
82 nm 1200°C	f			f			f			
k-range = 3-12 Å^{-1}	8	2.34	0.008	12	3.85	0.005	24	4.50	0.010	2.9
R-range = 1-6 Å		(1)			(1)			(1)		

Coordination number (CN), interatomic distance (R), Debye-Waller (DW) factor (σ^2), fix parameters (f), goodness of fit (R_f).

In the k^3-weighted spectra (Fig. 5.11a), the oscillations and their amplitude increases with thermal treatment. The 4 nm as-precipitated sample was very difficult to fit with a pure fluorite structure, as the fit were non stable and the data noisy. The oscillations are very quickly dampened and a small k-range = 3-8 Å^{-1} could be treated. The intensity of the FT was very low limiting the interpretation of the coordination shell to U-O_1. The FT at the U-L_3 edge for the experimental data of nc-UO_2 at different temperatures annealed and $U^{IV}O_2$ bulk reference, are shown in Fig. 5.11b. Probably several U-O distances are present in the first shell, not only corresponding to fluorite distances as the values were very low. Observing the EXAFS results in Table 5.3, the data are heavily dampened at RT where a large value for the DW factor has been found (σ^2 = 0.027 Å^2), meaning a significant static disorder (the atoms are randomly displaced from their positions) for the nc-UO_2 as-produced. Shorter distance

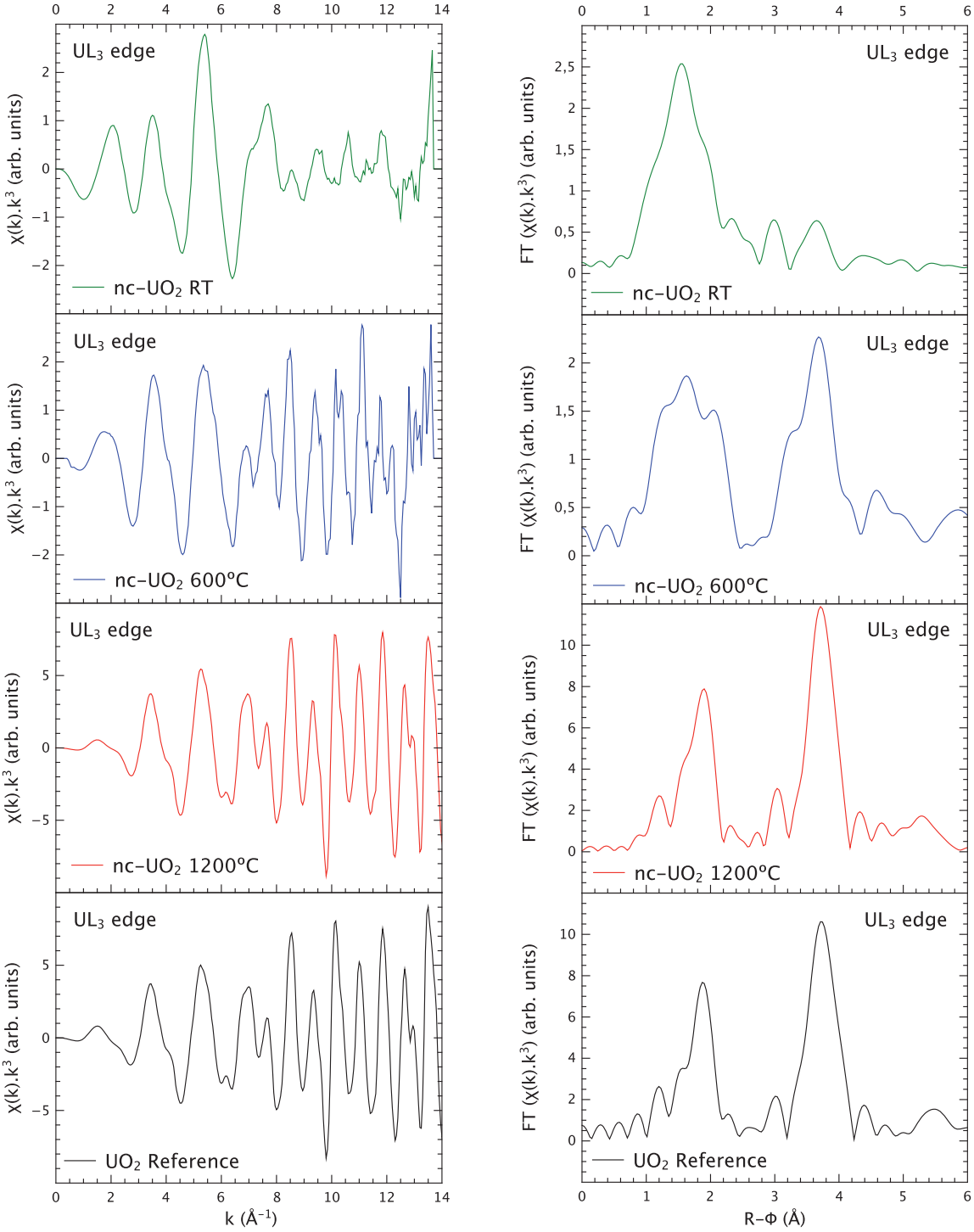

(a) Experimental k^3-weighted spectra.

(b) Experimental Fourier Transform.

Figure 5.11: a.) k^3-weighted spectra and b.) Fourier Transform at the U-L_3 edge for the experimental data of nc-UO_2 (aqueous route) at different temperatures annealed and $U^{IV}O_2$ bulk reference.

(2.26 Å) for the oxygen shell (U-O bond length) is clearly observable for the nc-UO_2 at RT which does not correspond to any U-oxide. According to the shape of the first FT peak, it looked like there were two or three U-O distances instead of one. This is consistent with the observed lattice contraction (0.5417 nm) from XRD at RT (see Table 5.2).

The 9 nm sample (600°C anneal) shows an intermediate ordering with oscillations clearly identified and extending to k = 9 $Å^{-1}$. The intensity of the FT was also low for this annealed sample, limiting the fitting and interpretation of the coordination shell to U-O_1 and U-U_1 together with UO_2 fluorite structure. Still a large value for the DW factor (σ^2 = 0.026 $Å^2$) has been found (Table 5.3). Shorter distance (2.27 Å) is also present for the oxygen shell (U-O bond length) in comparison with the reference-$U^{IV}O_2$ (2.34 Å). However the U-U_1 bond length (3.82 Å) is closer to that of the bulk-$U^{IV}O_2$ (3.85 Å), suggesting that the U-U_1 lattice is more ordered than the O anion sublattice. The U-U_1 lengths were consistent with the less lattice contraction (0.5431 nm), in comparison with the nc-UO_2 as-produced, as probed by XRD at 600°C anneal (see Table 5.2).

Ultimately, at 1200°C and 82 nm, EXAFS oscillations are similar, if not entirely matching, those of the bulk-$U^{IV}O_2$ indicating same *fcc*-structure consolidation and substantial particle growth, both observed in XRD measurements (see Fig. 5.12). Both shells were well fitted with *Fm-3m* structure for this sample (see Fig. 5.13) and very similar distances to reference $U^{IV}O_2$ structure can be observed according to the FT (k-range treated = 3-12 $Å^{-1}$). That is in agreement with the similarity for the XRD data for the annealed sample at 1200°C and the bulk-$U^{IV}O_2$ (see Fig. 5.8). Also consistent with the XANES (see Fig. 5.10) showing no different oscillation from the fluorite structure.

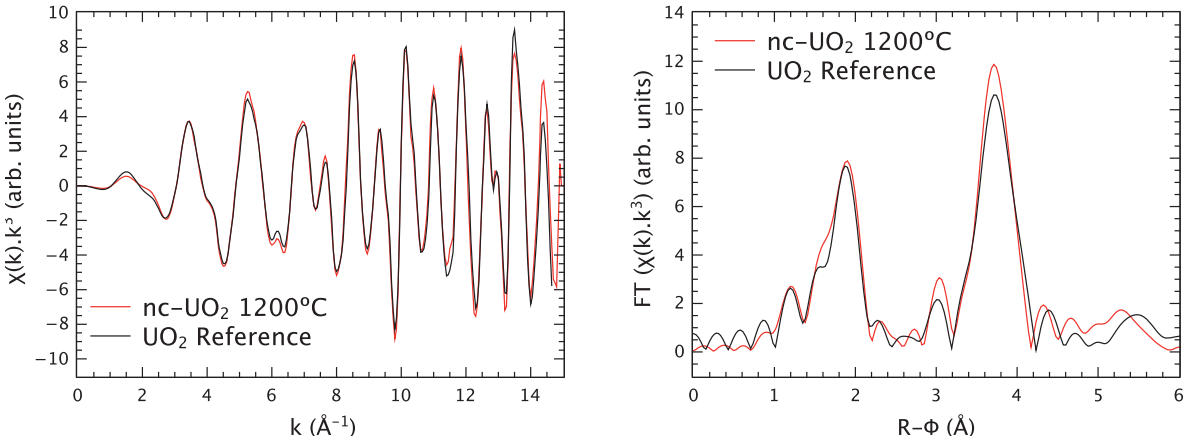

Figure 5.12: Comparison between experimental data from nc-UO_2 annealead at 1200°C and $U^{IV}O_2$ reference of *(left)* k^3-weighted spectra and *(right)* Fourier Transform at the U-L_3 edge.

In Fig. 5.14 the U-O_1 and U-U_1 bond distances have been represented in function of the annealing temperature and finale size of the nc-UO_2 sample. Both bond distances, U-O_1 and U-U_1, stay shorter and it is just first for the 82 nm and 1200°C annealed particles when they recover the typical distances of the reference $U^{IV}O_2$ (2.34 Å and 3.85 Å for U-O_1 and U-U_1, respectively) .

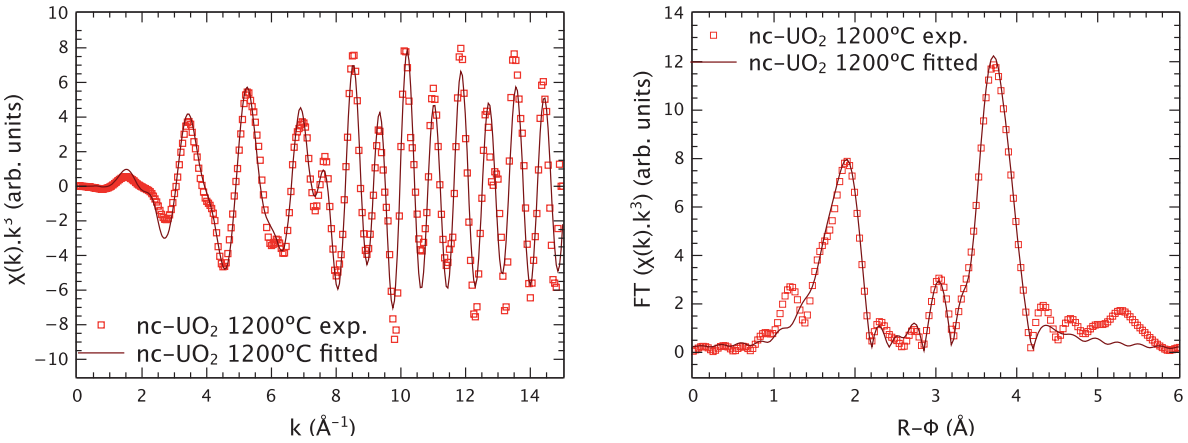

Figure 5.13: Experimental (□) and fitted data (−) for the nc-UO_2 annealead at 1200°C of *(left)* k^3-weighted spectra and *(right)* Fourier Transform at the U-L_3 edge.

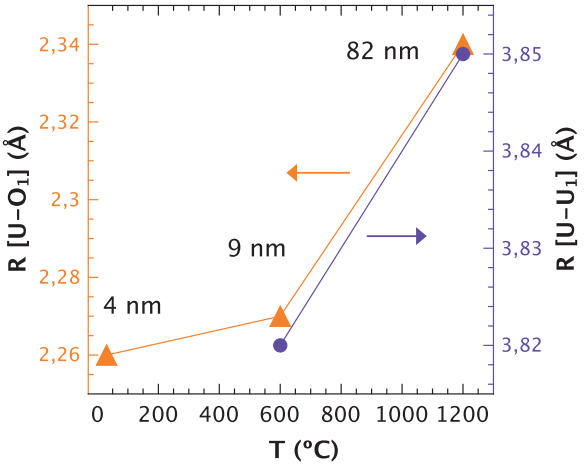

Figure 5.14: U-O_1 and U-U_1 bond distances in function of the annealing temperature (under reducing conditions) and finale size of the nc-UO_2 sample (curves only as a guide to eye).

5.4.3.2 Local structure and valence state as probed by MAS NMR.

The Hahn-echo ^{17}O MAS spectra acquired for various annealing times (600°C, 650°C, 700°C, 800°C and 1200°C) are presented in Fig. 5.15 and some fits in Fig. 5.16 and Fig. 5.17. The experimental features are specified in Sec. 2.2.4. The spectrum of the 200°C annealed sample was acquired at 10 kHz (as a 1.3 mm probe was not available at this time) therefore its analysis has to be done apart from the whole series and has been not here represented. In fact, as these compounds are paramagnetic the ^{17}O shift depends on the spinning speed which induces a slight heat of the sample. Nevertheless, another study on bulk-$U^{IV}O_2$ (done in ITU to be published) shows that the variation in the peak position is not very important between 10 kHz and 55 kHz (∼10 ppm, small compared with the peak broadening). Thus, the shift of 1075 ppm (200°C) can be compared with that extracted for these series (Fig. 5.18). At the contrary, the broadening of the peak cannot be compared with that of the others heat treatment as the Full Width at Half Maximum (FWHM) will decrease with spinning speed due to the removing of paramagnetic shift anisotropy.

For the next temperature of 600°C, a broad peak of 2478 ppm has been identified

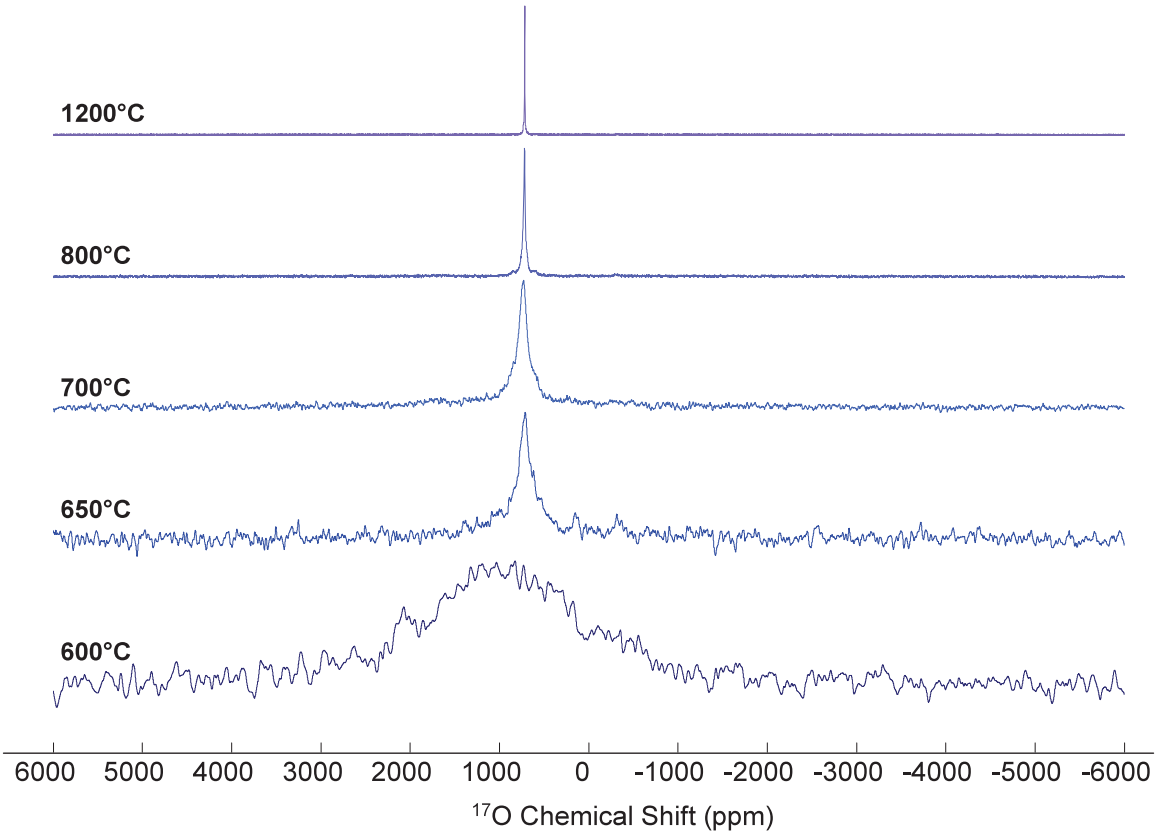

Figure 5.15: Stack of the ^{17}O MAS-NMR for nc-UO_2 annealed at five different temperatures.

at 962 ppm (Fig. 5.16a). By increasing the temperature of only 50°C (at 650°C; Fig. 5.16b), the MAS spectrum of the sample exhibits two peaks at 932 and 723 ppm. On the static spectrum acquired with more scans a third peak (not here represented) can be identified at nearly 960 ppm. The position of this peak can be relatively compared with that of the spinning spectrum while the FWHM cannot. At 700°C (Fig. 5.17a), there are still three peaks and the peaks at 732 and 738 ppm are now sharpest. For the two last heat treatments, 800°C (Fig. 5.17b) and 1200°C (Fig. 5.17c), only two peaks with very closed shifts are identified.

Two trends are observed in the plots of the shifts and the FWHM as a function of temperature presented in Fig. 5.18. Under 700°C, the shift and the FWHM decrease abruptly while above this temperature they are relatively constant. It can be noticed that the shift extracted from the spectrum acquired at 200°C is very different from that of the whole series. Due to the broadness of the peak, the presence of more than one species cannot be excluded. A similar trend was observed by XRD for the evolution of the lattice parameter as a function of temperature (Fig. 5.4). In fact, it increase steeply under 700°C, then there is only a week evolution. Therefore, it seems that under this temperature there are important changes on long and short range.

Three different oxygen environments can be identified. The first one corresponds to oxygens having a chemical shift of nearly 900 ppm (named peak *C*, green peak). These peaks have been identified up to 650°C. At 650°C, even if the peak is sharpest, the shift is very similar to that of the 600°C sample and therefore the ^{17}O will be considered as the same type of species. Due to the broadness of the peak, it is tempting to attribute this one to ^{17}O in a disordered environment. But, XRD has shown that

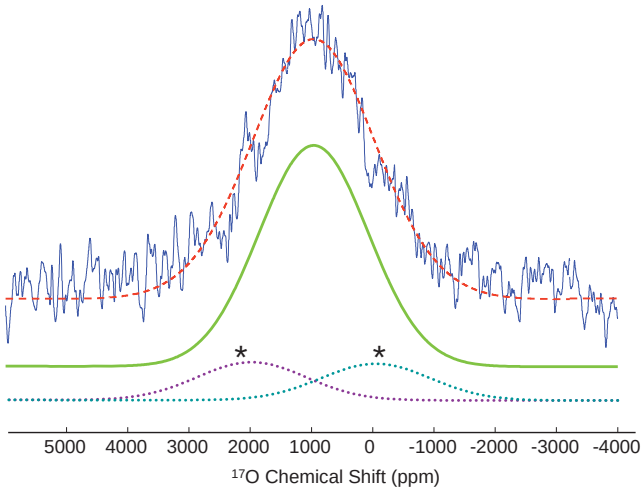

(a) 600°C

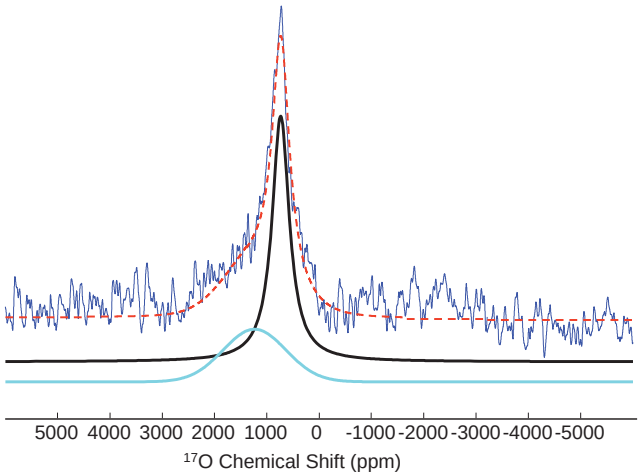

(b) 650°C

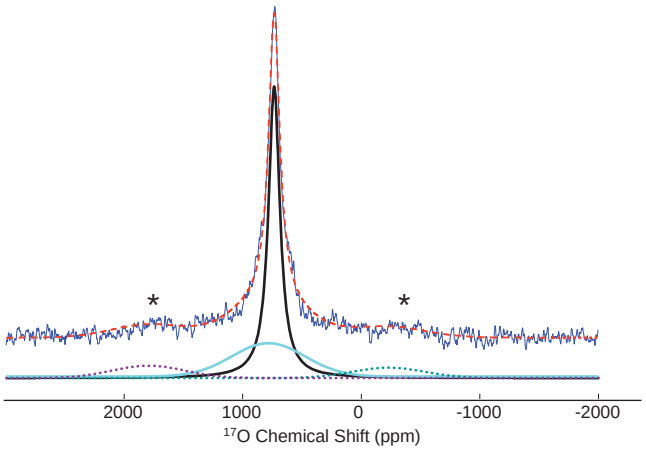

(c) 700°C

Figure 5.16: Characteristic fits for the spectra of the samples annealed at 600°C, 650°C and 700°C ($*$ = spinning sidebands; peak A = black; peak B = blue; peak C = green)

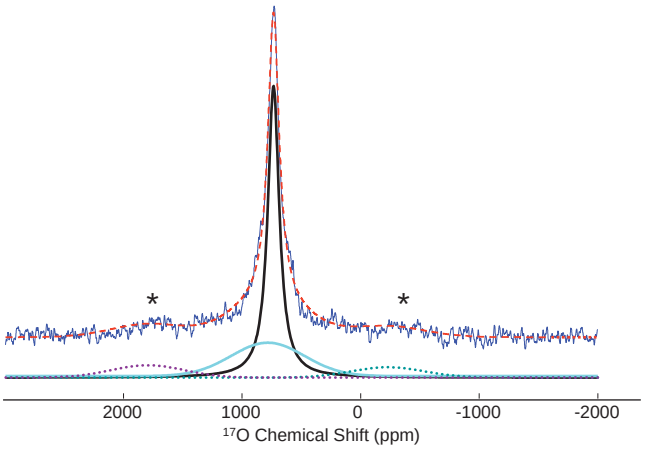

(a) 700°C

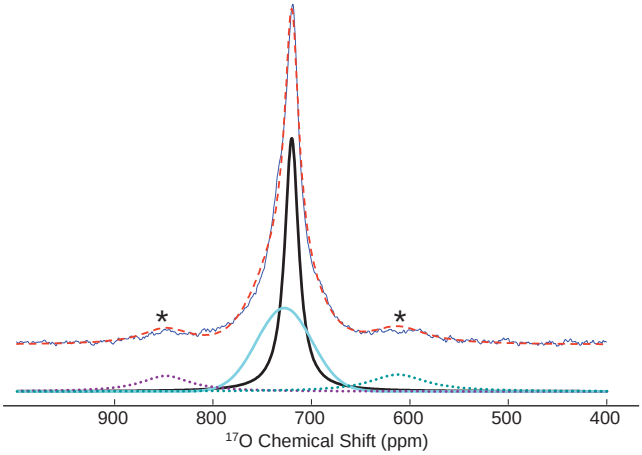

(b) 800°C

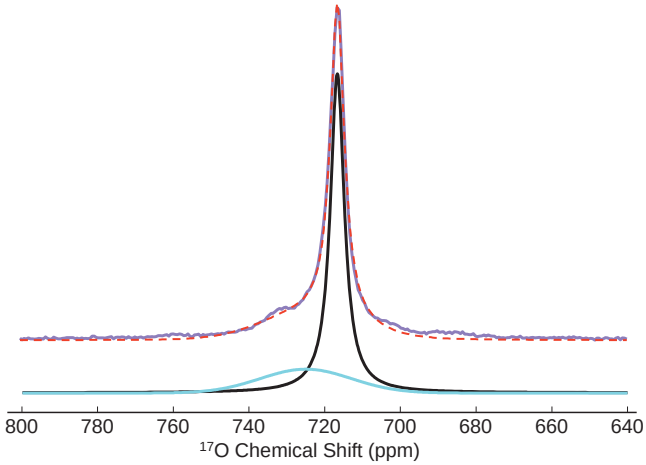

(c) 1200°C

Figure 5.17: Characteristic fits for the spectra of the samples annealed at 700°C, 800°C and 1200°C ($*$ = spinning sidebands; peak A = black; peak B = blue; peak C = green).

for this range of temperature the size of the UO_2 is around 10 nm (Fig. 5.8 under $Ar/5\%H_2$). Moreover, previous experiments done on zeolites [Zhang et al., 1999] have shown that there is an increase of the linewidth of the quadrupolar nucleus (in that case ^{27}Al) with decreasing size of nanoparticles. Indeed, according to [Casabella, 1964] for well-crystallized samples the NMR linewidth is greatly influenced by the quadrupolar coupling constant which is due to the local electric field gradients in the sample. The strong surface energy existing on the surface of the small particles will lead to more strain in the lattice, consequently causes the broadening of the main peak of the quadrupolar line. Thus, it can be proposed that this type of oxygen correspond to the ^{17}O in nanocrystals UO_2. Nevertheless, due to the broadness of the peak, presence of other ^{17}O species cannot be excluded.

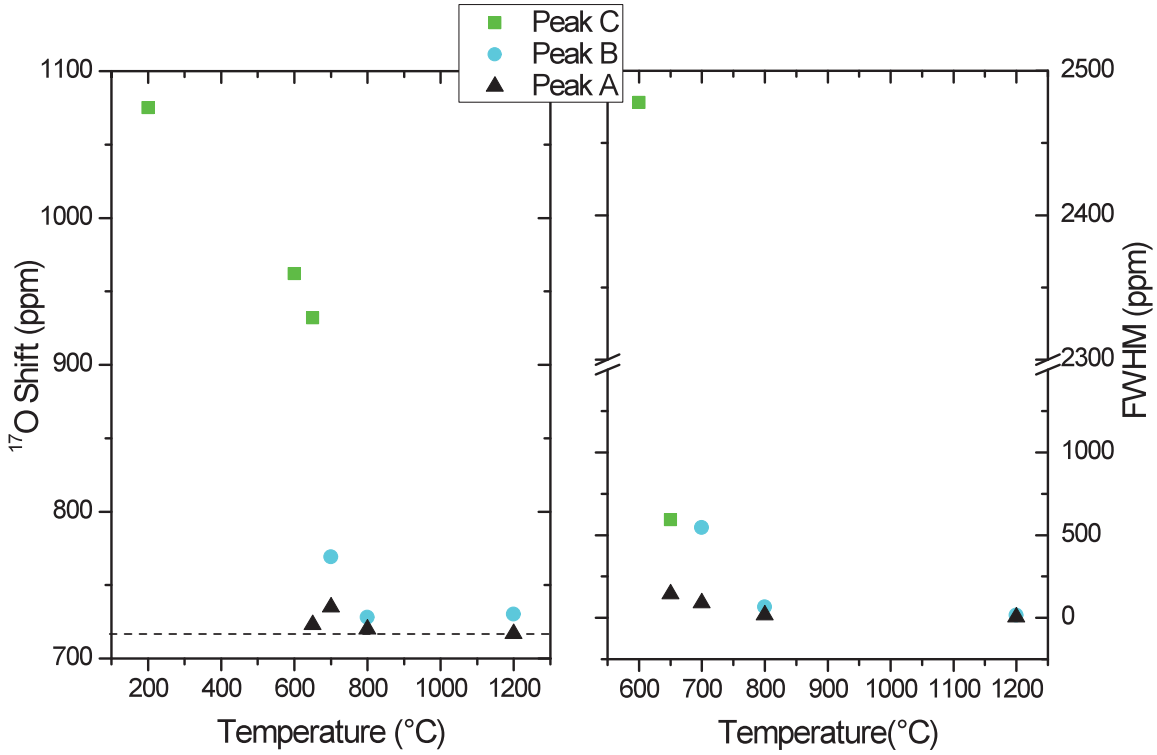

Figure 5.18: Evolution of the ^{17}O shift *(left)* and of the full width at half maximum *(right)* as a function of crystallite size for various temperatures.

The two second types of species appear clearly from 650°C (Fig. 5.18). There is one sharp and one broad (they will be named peaks A and B respectively thereafter). These peaks were fitted using a Lorentzian for A (black peak on Fig. 5.16 and Fig. 5.17) and a Gaussian for B (blue peak on Fig. 5.16 and Fig. 5.17) and could be respectively attributed to ^{17}O in a crystalline phase and in a more disordered one. It can be added that these two peaks are also observed at 1200°C meaning that even for this temperature it is not stoichiometric UO_2 contrary to that suggested by XRD (Fig. 5.8). With increasing temperature (increasing of crystallite size), the FWHM of the two peaks decrease (Fig. 5.17). As previously explained, this is the signature of such crystallite size evolution. Moreover, the shift of peak A reached a minimal value of 717 ppm at 1200°C. This one is close of the 717 ppm found for $U^{IV}O_2$-bulk. Its FWHM is of 5 ppm and corresponds to that of the crystallite having a size about 80 nm. This

value is still slightly bigger than the 3 ppm found for $U^{IV}O_2$-bulk. Hence, with the shift of peak *A* one can say that the environment around the oxygens corresponding to the biggest crystallite size (80 nm) is very close to that of $U^{IV}O_2$-bulk. Based on the FWHM, one can say that to observe the signal of crystalline UO_2 a size above 80 nm should be reached. This confirms that nc-UO_2 are obtained and this is consistent with the lattice parameter observation of 0.5472 nm (Fig. 5.8).

5.4.3.3 Local structure and valence state as probed by FTIR.

Several samples at the key temperatures were analyzed under the Fourier Transform Infrared (FTIR) spectrometer (Alpha FT-IR Spectrometer from Brucker; Sec. 2.2.5). The infrared (IR) spectra recorded for nc-UO_2 as-produced (RT), at 200°C, 600°C and 1200°C under Ar/5%H_2 annealed, as well as $U^{IV}O_2$ reference spectra, are shown in Fig. 5.19.

In the case of nc-UO_2 as-produced (RT), four peaks in the range 400-4000 cm^{-1} were observed. The absorption band for the U-O vibration in UO_2 shows up below 400 cm^{-1} which is out of the detection limit of the equipment. The peak at 1625 cm^{-1} can be assigned to the bending vibration of H-O-H bonds of the coordinated water [Fujita et al., 1956], [Sailaja et al., 2002]. This peak disappears already at 200°C. That would be in agreement with the TGA (Sec. 5.2), were nearly no loss of weight was observable after 600°C (see Fig. 5.1). Something similar occurs to the broad absorption peak at 3400 cm^{-1}, which can be ascribed to the asymmetric and symmetric stretching vibrations of the H-O-H bonds of coordinated water. However, this peak reduces for the 200°C and is nearly disappeared at 600°C annealed sample. So at 600°C all the OH would be theoretically gone taking into account the peaks at 1625 cm^{-1} and 3400 cm^{-1}. However, the peak at 880 cm^{-1} corresponding also to OH groups, stay still present at 600°C, totally disappearing at 1200°C (Fig. 5.19). The same occurred for the peak at 638 cm^{-1} corresponding to more oxidised species (UO_{2+x}) [Kim et al., 2009]. That could be an artefact due to the small size still present at 600°C (9 nm) (see Table 5.1). At 1200°C the IR spectra looks like the one for the $U^{IV}O_2$ reference and grains are about 82 nm (Table 5.1).

That is also in agreement with the results obtained by XANES where a different electronic structure at 600°C was observed, meanwhile at 1200°C a similar structure to bulk-$U^{IV}O_2$ was found (see Table 5.2). Also EXAFS is characterized for a poor ordering at 600°C but entirely matching with the bulk-$U^{IV}O_2$ oscillation pairs at 1200°C (see Table 5.3). In the NMR analysis all the additional oxygen sites disappeared once at 1200°C anneal but one which could be due to a surface effect.

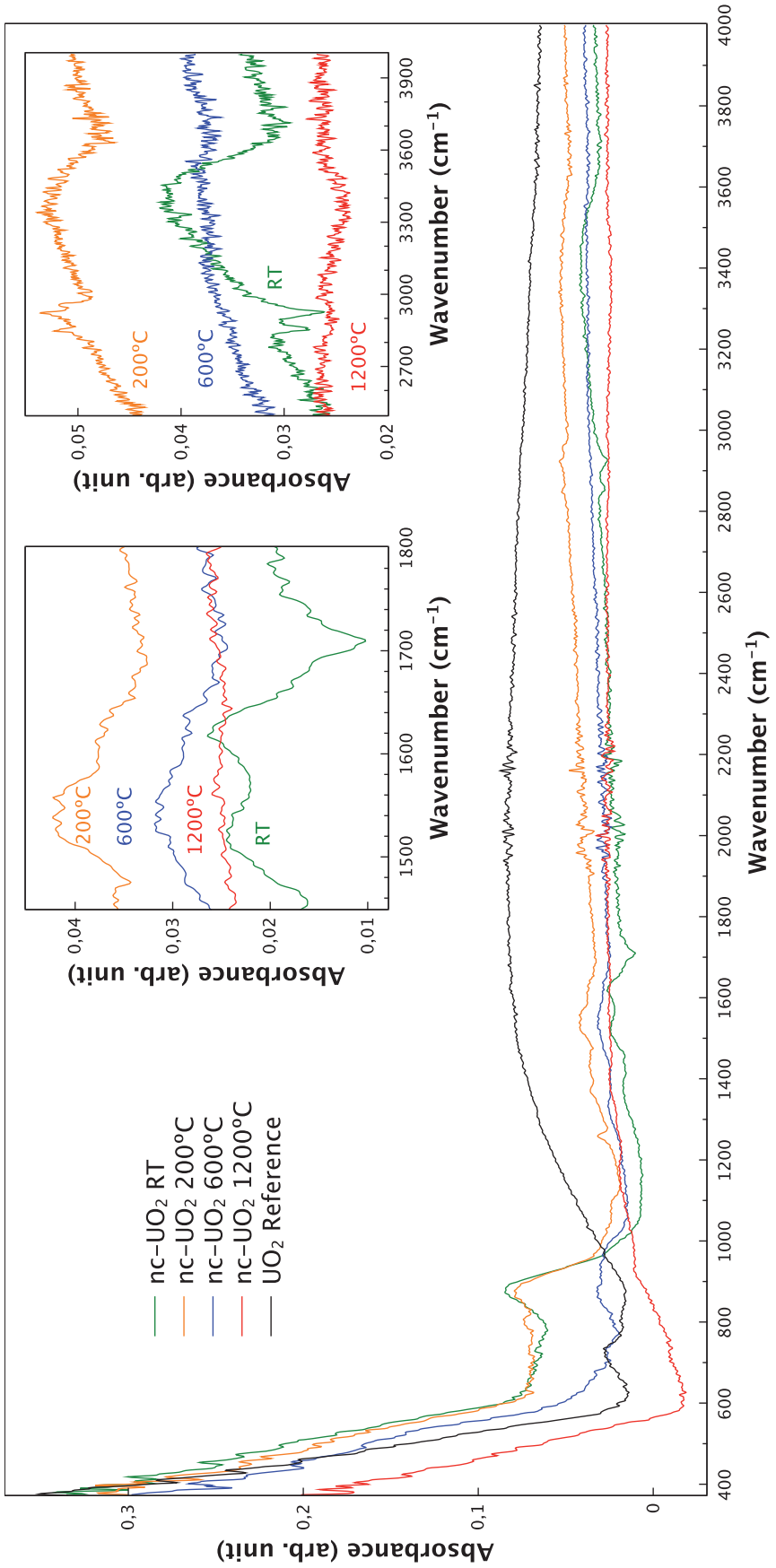

Figure 5.19: Infrared spectra recorded for nc-UO_2 as-produced (RT), at 200°C, 600°C and 1200°C under Ar/5%H_2 annealed. Reference spectra for UO_2 is also represented. Inside amplification of the infrared spectra showing the disappearing of the peaks at 1625 cm^{-1} and 3400 cm^{-1} with increasing annealing temperatures.

5.5 nc-UO_2 long-isothermal grain growth as probed by XRD under neutral and reducing conditions.

The as-produced nanocrystals presented a certain disorder and lattice strain which disappeared with the anneal of the samples, evolving to ordered crystalline structures as temperature increased. This has been proved for shorter time heat treatments under inert and reducing atmospheres (Table 5.1). Normally, ceramic heat treatments to obtain high dense monoliths finish up with grain sizes above 200 nm. Hence, isothermal grain growth kinetics at a given temperature is an essential component to determine the final grain size, and in consequence to evaluate the performance of such an innovative nuclear fuel after prolonged insertion at high temperatures. Although nuclear fuel operates at about 500°C at the periphery it can reach 1200°C at the fuel pellet centre. For that reason, it is fundamental to examine the behaviour of nano-fuel microstructure as a function of the time in a possibly wide temperature range, to ensure lack of disproportionate grain growth even at the highest temperature in play.

A study of the thermal growth of those nanocrystals over the whole range of initial microstructures from amorphous to fully nanocrystalline was performed. Based on Fig. 5.3, the critical temperatures 500°C, 700°C, 900°C and 1200°C were selected. Isothermal grain growth data at these temperatures was determined from in-situ HT-XRD measurements under static He atmosphere and annealing times from 0 to 50 h with a heating rate of 5°C/min. The data are shown in Fig. 5.20. Independent sample treatments in separate furnaces under dynamic Ar/5%H_2 for dwelling times of 50 h, 100 h and 200 h, were also performed. For each isothermal dwell temperature one new sample was chosen. Comparison of the size and lattice parameter obtained for the both routes, are shown in Table 5.5.

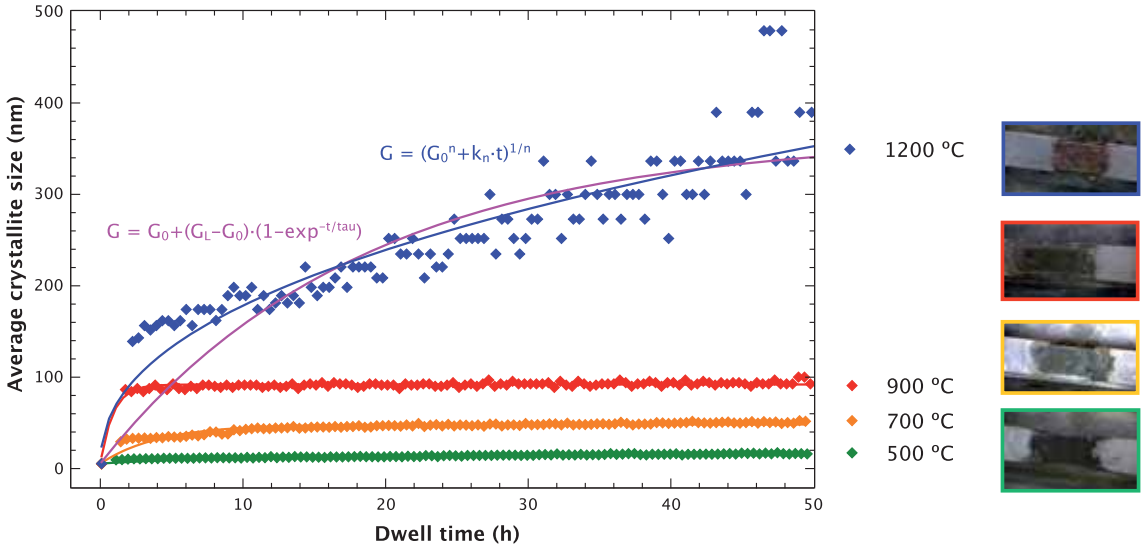

Figure 5.20: Isothermal grain growth of nc-UO_2 under He static atmosphere. For each isothermal dwell temperature one new sample was used. Measurement was done in situ in the HT-XRD device at temperature. All the curves have been fit using the Eq. 5.6. For the one at 1200°C a fit using the Eq. 5.7 was also done.

The in situ HT-XRD determination of the crystallite size was done under static He atmosphere. The experimental installation did not permit the use of Ar/5%H_2 gas in

the HT-XRD chamber, which would have been necessary to preserve the O/U ratio of the sample at a value around 2. The measurements were taken at temperature. The crystallite size was determined according to inverse of the width of the first diffraction peak [111], which was monitored during 50 h while the sample was kept at constant temperature. From these measurements information on crystal growth as a function of temperature and time was obtained (Fig. 5.20). Posterior XRD-measurement on consideration of the whole diffractogram after 50 h dwell time at temperature and once the sample was cooled down, was also done (Table 5.5). This final measurement provided data on crystal size without thermal broadening, but characteristic of the O/U final ratio that was obtained under He atmosphere. The measurement of the ex-situ annealed samples was done under a dynamic $Ar/5\%H_2$ atmosphere which ensured a final stoichiometry $UO_{2.0}$ (U^{IV}). The measurement was always done after-cooling.

Fig. 5.21 shows how grain growth takes place in the first hours of isothermal hold for the temperatures at 500°C, 700°C and 900°C until a stable average grain size below 100 nm is established at the applied temperature, at which time crystal growth ceases. This kind of self-limited grain growth was reported by [Rupp et al., 2006] and is described by the following relaxation function:

$$G - G_0 = (G_L - G_0) \cdot (1 - e^{\frac{-t}{\tau}}) \tag{5.6}$$

where G is the average grain size, G_0 is the initial grain size, G_L is the limited grain size (when the grains stop to grow) and τ is the relaxation time (time needed to reach the G_L). The values of G_L and τ obtained from the fitting described by the relaxation function Eq. 5.6, are presented in Table 5.4.

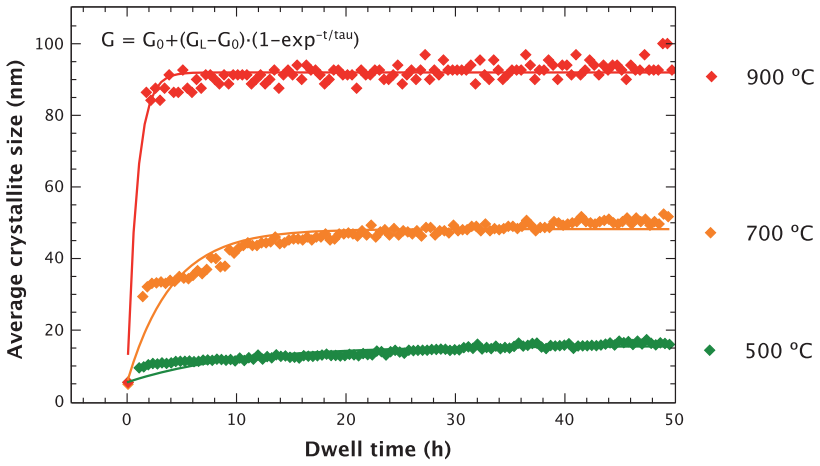

Figure 5.21: Isothermal grain growth of nc-UO_2 under He static atmosphere. For each isothermal dwell temperature one new sample was used. Measurement was done in situ in the HT-XRD device. All the curves have been fit using the Eq. 5.6.

The diffusion coefficient, D_i, have been so calculated by substitution of the values G_0, G_L and τ above determined, in the corresponding approximation by [Rupp et al., 2006] (Eq. 5.7). Afterwards, the activation energy of diffusion, Q_{diff}, has been obtained as a function of isothermal dwell temperature using the Arrhenius law dependence

[Löffler and Johnson, 2000]:

$$D_i = \frac{(G_L - G_0)^2}{4 \cdot \tau} = const \cdot e^{-\frac{Q_{diff}}{k_B T}} \tag{5.7}$$

where k_B is the Boltzmann constant ($k_B = 8.6173324 \cdot 10^{-5} eV \cdot K^{-1}$). The different parameters obtained for the fitting at each temperature, are shown in Table 5.4.

Table 5.4: Parameters obtained from the fits following the relaxation equation Eq. 5.6 for the samples annealed under He static atmosphere during 50 h.

T (°C)	G_0 (nm)	G_L (nm)	τ (h)	D_i (m^2/s)	R^2
nc-UO_2 500°C	5.41	15.51	9.65	$7.34e^{-22}$	0.72
nc-UO_2 700°C	5.41	48.21	4.10	$3.10e^{-20}$	0.87
nc-UO_2 900°C	5.41	91.99	0.90	$5.80e^{-19}$	0.90
nc-UO_2 1200°C	5.41	363.55	18.13	$4.91e^{-19}$	0.66

Starting grain size (G_0), limited grain size (G_L), relaxation time (τ), diffusion coefficient (D_i) and (R^2) correlation coefficient obtained from the fitting.

The determined kinetics parameters depend on the temperature. The D_i values increase with temperature, meanwhile the relaxation time (obtained from the fitting with Eq. 5.6) diminishes with it (Fig. 5.22). Differently, for the sample annealed at 1200°C a much higher relaxation time (see Table 5.4) has been obtained, not following the decreasing trend with temperature observed for the rest of the dwell temperatures examined (Fig. 5.22). For this sample the grains seem to continue to grow following the generalized grain growth equation (Eq. 5.8) as already observed by [Rupp et al., 2006] for temperatures above 1100°C and expressed as:

$$G^n - G_0^n = k_n \cdot t \tag{5.8}$$

where n is the growth exponent and k_n is a rate constant ($k_n = k_0 \cdot e^{-\frac{Q_{diff}}{RT}}$ with k_0= constant, Q_{diff}= activation energy of diffusion, R= gas constant and T= absolute temperature).

For the nc-UO_2 annealed at 1200°C a grain growth exponent n of 2.36 was obtained with a correlation coefficient of 0.77 using the Eq. 5.8. The fitting curve is shown in blue colour in Fig. 5.20. A final grain size of about 350 nm after 50 h is also under this mechanism obtained. This is in agreement with the range of values of traditional grain growth mechanisms (n =2-4), and in particular the parabolic grain growth mechanism (n =2.36≃2) [Rupp et al., 2006]. The fitting line shown in pink colour, with a correlation coefficient of 0.66, corresponds to the relaxation function above described (Eq. 5.6), which better fits the grain growth kinetics at the lower temperatures examined (T≤900°C).

From Fig. 5.23 an activation energy of diffusion of 0.93 eV with a correlation coefficient of 0.90 was determined for the temperature range 500-1200°C (considering

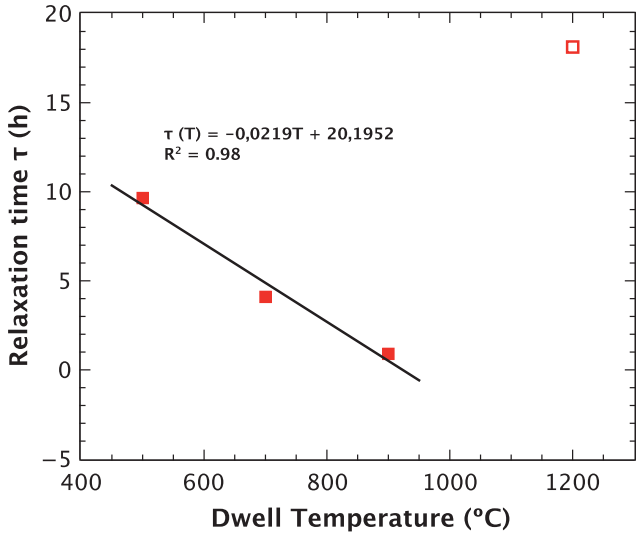

Figure 5.22: Grain growth relaxation time as a function of dwell temperature for the nc-UO_2 samples annealed under He static atmosphere during 50 h. Fit obtained excluding the value at 1200°C.

the fits following the relaxation equation Eq. 5.6). Taking away the value of D_i for the temperature of 1200°C (considering that the curve follows the generalized grain growth equation Eq. 5.8 instead of relaxation equation Eq. 5.6 as at lower temperatures), an activation energy of 1.25 eV with a correlation coefficient of 0.99 was obtained (Fig. 5.23). These low activation energies, including or not the D_i at 1200°C, could be related predominantly to grain boundary (surface and interface) diffusion, as the volume diffusion contribution appears at higher activation energies, namely above 4 eV [Sabioni et al., 1998].

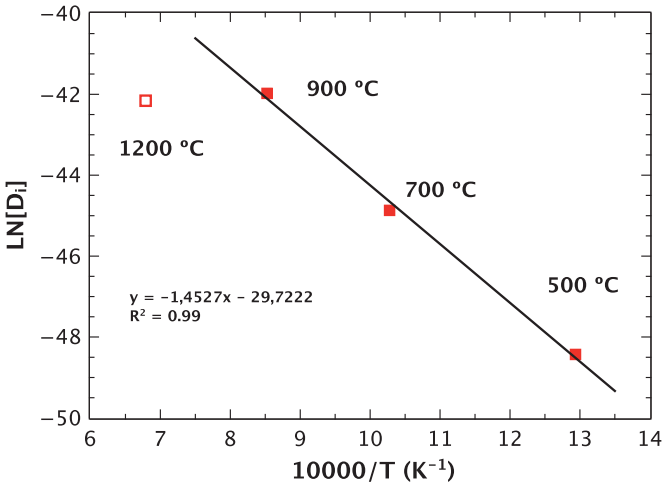

Figure 5.23: Diffusion coefficient $D_i(m^2/s)$ as a function of temperature for the nc-UO_2 samples annealed under He static atmosphere during 50 h. Fit obtained excluding the value at 1200°C.

Comparing values measured after cooling under He atmosphere and under Ar/5%H_2 atmosphere (see Table 5.5), a noticeable difference in the size of the crystals is seen for same dwelling times of 50 h being bigger for the samples heated under He environment.

This difference increased with the dwell temperature. Something interesting is that even under inert atmosphere (He), the lattice parameter increases quicker than under a reducing atmosphere (Ar/5%H_2) until 700°C. However, at 900°C the lattice parameter under Ar/5%H_2 is already the typical for bulk UO_2, while for treatments under He atmosphere that value (0.5472 nm) is reached at 1200°C. This suggests that in treatments under He environment the samples remain possibly longer time hyperstoichiometric.

Table 5.5: Crystal size and lattice parameter for samples treated at different temperatures, times and under different atmosphere.

	500°C		**700°C**		**900°C**		**1200°C**	
nc-UO_2	**size (nm)**	**lattice (nm)**	**size (nm)**	**lattice (nm)**	**size (nm)**	**lattice (nm)**	**size (nm)**	**lattice (nm)**
50 h He [a]	18	0.5457	64	0.5462	128	0.5468	322	0.5472
50 h Ar/5%H_2 [b]	6	0.5426	13	0.5442	49	0.5472	85	0.5472
100 h Ar/5%H_2 [b]	6	0.5428	13	0.5456	49	0.5472	-	-
200 h Ar/5%H_2 [b]	-	-	14	0.5456	49	0.5472	150	0.5472

All the measurements were done after cooling. a.) He static atmosphere. b.) Ar/5%H_2 dynamic atmosphere.

Generally, if UO_2 is hyperstoichiometric the self-diffusion coefficients increase steeply. The cation mobility raises due to the increase in cation vacancy concentration [Kutty et al., 2004]. In the same way, in the hyperstoichiometric range, there is a strong increase of the mass-flow, the grain-boundary motion and the grain (or crystal) growth. As example, the large-grain UO_2 pellets are produced ordinarily using slightly oxidising atmosphere (NIKUSI process [Maier et al., 1982]). This could explain the boosted crystal growth observed at 900°C and 1200°C under He atmosphere, in comparison with a nc-UO_2 sample treated Ar/5%H_2 atmosphere at the same temperature and time (50 h).

In Fig. 5.24, the Arrhenius diagram comparing the cation self-diffusion in UO_2 fluorite-structure from large-grain reported by [Matzke, 1987] and nano-grain from this study (samples annealed under He static atmosphere during 50 h), has been plotted. T_m is the melting temperature (T_{mUO_2} = 3140°K). Between 20 orders of magnitude difference at 500°C (lattice parameter =0.5457 nm; average grain size =18 nm) and 5 at 1200°C (lattice parameter =0.5472 nm; average grain size=322 nm) have been found for the diffusion coefficients between bulk-UO_2 [Matzke, 1987] and nc-UO_2 of this study (Table 5.5). Differences in the diffusivity in the grain boundaries between micro- and nano-grain have been already seen in other fluorite-structured metal oxides [Martin, 2007]. In fact, the differences in the diffusion coefficients between bulk- and nc-UO_2 are compatible with an enhancement of the diffusion processes either by grain size-effects or by oxidation (O/U>2) effects.

5.6 Results and discussion.

The synthesis of nc-UO_2 with controlled oxidation state and crystal size is essential because the chemical and physical properties depends of its adjustment just as for

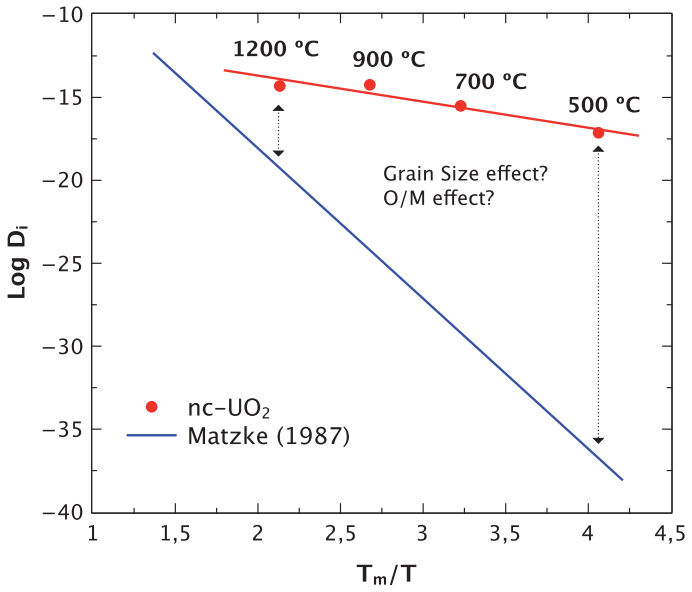

Figure 5.24: Arrhenius diagram comparing the cation self-diffusion in UO_2 fluorite-structure from large-grain ([Matzke, 1987]) and nano-grain of this study (samples annealed under He static atmosphere during 50 h). T_m is the melting point temperature ($T_{m_{UO_2}}$ =3140 °K).

other nanomaterials. To verify the composition of the precipitates and their propensity to thermal growth in the unconsolidated state, on just experiencing stochastic physical contact between particles, further analysis of the precipitated material annealed at different temperatures was then performed [Burda et al., 2005]. The evolution of the grain size and the crystal structure, which are fundamental parameters in the sintering process, as a function of temperature under inert and reducing atmosphere of nc-UO_2 precipitated from aqueous phase (see Chap. 3), was here investigated. Analysis of the precipitated material was performed by applying the thermal analytical and X-ray scattering techniques like TGA/DTA, XRD, HT-XRD, spectroscopic techniques as XAS, NMR and IR, as well as characterization techniques like TEM. The target parameters studied have been the oxidation degree (O/U ratio), the possible water content on the material, as well as the lattice imperfections as a function of the annealing temperature.

TGA and DTA were employed under inert atmosphere (Fig. 5.1). The weight loss observed was most likely attributed to water desorption and to crystallization (completion of the UO_2 *fcc*-structure). However, there was no reason to believe that the weight loss did not include as well some loss of oxygen due to reduction of the material. A deeper analysis on the lattice parameter and crystal growth under inert and reducing atmospheres was then performed to confirm the latest.

The evolution of the crystallite size, the lattice parameter, and the strain were determined from ambient temperature up to 1200°C under inert atmosphere using the in situ HT-XRD (Fig. 5.2). Below 700°C, a weak effect on the crystallite size occurred and it remained below 7 nm, while a strong expansion of the lattice parameter was measured (Fig. 5.4). A value of 0.5521 nm in the lattice parameter for the nc-UO_2 at 1200°C annealed and measured in situ in the HT-XRD instrument under static He atmosphere, was observed. The same thermal treated sample measured after cooling at RT, showed a value of 0.5473 nm ($UO_{2.00}$) very similar from the typical for bulk-UO_2 (0.547 nm) (Fig. 5.6). A recovering of the UO_2 typical crystal structure was achieved

with temperature under static He atmosphere from the initial lattice parameter value of 0.5417 nm from the nc-UO_2 as-produced to 0.5473 nm after thermal treatment at 1200°C (measurements done after cooling). It might be related to the static He atmosphere, which resulted in a thermodynamic equilibria between H_2, H_2O and O_2 in the gas phase, favouring H_2 during the cool down, thus this might be the cause.

The change in the lattice parameter with the crystallite size has been oft published [Boswell, 1951], [Fukuhara, 2003], [Boswell, 1951], [Qi et al., 2002], [Fukuhara, 2003], [Park and Qian, 2010], [Qi et al., 2002]. This effect is associated to the band structure and therefore to the physical properties changes occurring as the dimension of the system diminishes [Jovani-Abril et al., 2011]. Both, lattice expansion and contraction with the decreasing of the crystallite size have been in the literature observed. The first one has been seen mainly for transition metal oxides as α-Fe_2O_3 [Ayyub et al., 1995], CeO_{2-x} [Spanier et al., 2001] [Wu et al., 2004] [Deshpande et al., 2005] NiO [Fiévet et al., 1979], TiO_2 rutile [Li et al., 2004], and MgO [Cimino et al., 1968]. On the other side, lattice contraction at small crystallite size is mainly assigned to metals or metalloid systems like Au, Pt [Solliard and Flueli, 1985], [Vermaak and Kuhlmann-Wilsdorf, 1968], Cu [Wasserman and Vermaak, 1972], Pd, Sn, and Bi [Sun et al., 1999]. But also exceptions can be found in literature. A lattice expansion with Ni particle size decrease, despite being a metal, has been observed [Wei et al., 2007], while for the oxide TiO_2 anatase [Li et al., 2005], a lattice contraction with size decrease was noticed as the one found for the here synthesized nc-UO_2 [Jovani-Abril et al., 2011].

The LTEC (Fig. 5.5) was initially higher for nc-UO_2 than for bulk-UO_2 for temperatures below 400°C and tended to stabilize (at O/U 2.17-2.18) above 600°C (crystal sizes >6 nm), when the nanocrystalline material met the thermal-expansion behaviour (i.e. thermal expansion coefficient) of bulk (large-grained) UO_2. That showed once more that the ab-normal nano-effects in the material was only to be expected for particle sizes below few tens of nanometer. The oscillatory trends observable for LTEC in nc-UO_2 at T <900°C could be attributed to transitory oxidation-reduction effects.

The LTEC in nc-materials is one of the physical properties related to the nc-interfaces and it is subjected to anharmonic crystal lattice vibrations [Kittel, 1996]. The nc-materials are formed of a crystal core and an interface. The LTEC is enhanced relative to the coarse grained polycrystalline counterparts, due to the high density of interfaces [Sui and Lu, 1995]. Also the LTCE of the interface is related to an interfacial excess volume as demonstrated by theoretical calculations [Wagner, 1992]. This could cause this increase on reducing its grain size [Jovani-Abril et al., 2011]. In the study by [Klam et al., 1987] on the thermal expansion of Cu with different size samples, the single crystal samples presented a smaller expansion coefficient than the smaller-grained ones, theoretically due to the large anharmonic atomic vibrations in the grain boundaries. The same was found in other studies with Nb films [Banerjee et al., 2003] and nc-Fe [Zhao et al., 2001], larger lattice expansion was found for smaller-grained samples. However the contrary can also be found in literature. In the study with Zn nanowires by [Wang et al., 2007] larger lattice expansion coefficient was found for the bulk samples than the small-grained ones due to surface defects.

In the evolution of the lattice strain release with temperature, two steps were observed (Fig. 5.7). At T <300°C which could be related to the dehydration step

(water molecules attached to the nanocrystals and to the related binding-strength) also visible in the TGA/DTA. Between 300-700°C where the strain decreased, which could be related to additional loss of water and oxygen loss (O/U stabilization) and structure consolidation. The strain decreased then with temperature and was completely released at 700°C. Above this temperature, the sintering of the nanocrystallites began and reached a size of about 70 nm at 1200°C.

So, the morphology of the thermal treated nc-UO_2 differed then in form (Fig. 5.9), size and oxidation (Fig. 5.4) state from that of the original synthesized 4 nm nc-UO_2. A deeper study of the structure of the material as a function of temperature under reducing atmosphere was then also studied and compared to the reference bulk-UO_2. The lattice constant of the material in the cooled state after reach different maximum temperatures (600°C and 1200°C) was here measured. This allowed separation of the thermal expansion contribution in the high-temperature values to obtain cleaner curves for thermal expansion vs. temperature and lattice dimension vs. crystal size. The structure was identified mainly by XRD, but also by advanced methods including XANES, EXAFS, MAS-NMR, and IR. The nc-UO_2 XRD peaks under Ar/5%H_2 thermal treated, became sharper with the increase of the temperature indicating more crystalline UO_2, i.e., larger particle size (Fig. 5.8). A comparison of the crystal size and lattice parameter for the samples treated at 600°C and 1200°C under dynamic Ar/5%H_2 atmosphere (measurement after cooling) with those under static He atmosphere measured at temperature (see Fig. 5.4a), was provided in Table 5.1. No difference in the crystallite size was obtained at 600°C under either atmosphere. But a little change was observed at 1200°C, where a crystallite size of 73.39 nm under He was seen and a size of 82.16 nm under Ar/5%H_2 (by TEM corroborated Fig. 5.9). Major differences were observed in the lattice parameters as a function of the atmosphere used without ignoring the fact that the values under He were measured at temperature. These differences in the lattice disappeared once the sample measured at temperature was measured after cooling, as it was seen in Fig. 5.6. Both samples treated at 1200°C under He (0.5473 nm Fig. 5.6) or under Ar/H_2 (0.5472 nm Fig. 5.8) had a lattice parameter similar to the 0.5472 nm of bulk-UO_2.

In the lattice strain evolution the same tendency was seen under He atmosphere (Fig. 5.7) and under Ar/5%H_2 atmosphere (Table. 5.1). The complete release of the strain in the nc-UO_2 coincided with the onset of the starting of the crystallite growth. So the crystallite growth seemed to be limited by the presence of the lattice strain. From RT until 600-700°C the thermal energy was totally used to remove the strain and up to that temperature no strain was remaining and the energy was used for the growing of the nanocrystals. It has been already seen that an applied mechanical stress on crystals [Sherwood, 2001], or lattice-strains originated from defects produced during crystal formation [Wei et al., 2008], [Dong et al., 1997], would inhibit the crystal growth. If so, from the technological point of view, it would be preferable to produce nanocrystals with highest inner strain as possible (less perfect crystals), to delay as much as possible the thermal growth.

XANES was used to determine the oxidation of U cations and the corresponding molar fractions. From these, the O/U ratios were ultimately derived. The XANES spectra at the U-L_3 edge (Fig. 5.10) showed a trend with increasing temperature and as x decreased (UO_{2+x}). The samples studied were nc-UO_2 as produced and after thermal treatment at 600°C and 1200°C under Ar/5%H_2. The peak of the WL shifted

slightly to lower energies and increased in intensity, and the oscillations within the XANES regions increased. The amplitude decreased with the increasing temperature of thermal treatment showing a higher structural order of these samples. For the as-produced (RT) and at 600°C samples, there was a significant difference of shape compared to the $U^{IV}O_2$ reference, i.e. presence of a shoulder on the high energy side of the edge. This was in agreement with the observed decrease of WL amplitude with the increasing temperature. The shoulder decreased with temperature meaning that there was less U^{VI} or that the U^{IV} bulk was more visible as it size increased. A clear shift (further for the RT sample) of the absorption edge and WL-peak to higher energies, as well as a broader WL was observed. However the spectra for the $U^{IV}O_2$ reference and the annealed sample at 1200°C, were remarkably similar, indicating that the electronic structure of the 82 nm UO_2 was essentially that of the bulk $U^{IV}O_2$ at that temperature.

It could be expected the RT-sample was the most cluster like (smaller in size), but in addition the composition was not fully ascribed to UO_2. The shoulder could be a proof of the presence of U^{VI}. Additionally to the hyper-stoichiometry, the presence of U^{VI} suggested that water molecules and/or OH groups would be also present in the RT sample. In those nc-material, the surface was superior to the bulk. If there was any adsorbed water molecule, the valence of U was increased and the XANES spectra was significantly different to the bulk. A ratio O/M of 2.45 ($V_U = 4.9$) was deduced for the RT sample (Table 5.2). In the 600°C treated sample, the shift of the WL, as well as the shoulder (in this case less defined) were toward to the left in comparison to the RT sample. It indicated a minor presence of U^{V} and U^{VI} species but still not strictly U^{IV}. An O/M ratio of 2.30 ($V_U = 4.6$) was in this case found (Table 5.2). Concerning the 1200°C treated sample, XANES analysis showed no doubt that the sample had a fluorite structure. No spectrum shift was observed and there was mainly U^{IV}, and probably some U^{V}, as there was a slight shift of the inflexion point. An O/M ratio of 2.025 ($V_U = 4.05$) was in here found (Table 5.2) in agreement with the lattice parameter of 0.5472 nm obtained at 1200°C by XRD. Also the U-L_3 XANES data for the reference UO_2 and nc-UO_2 treated at 1200°C samples in Fig. 5.10 were very similar to the UO_2 data reported by [Conradson et al., 2005b], [Conradson et al., 2005a]

In the accurate XAS study of the UO_{2+x} system by [Conradson et al., 2005b], [Conradson et al., 2005a], it is shown that the U-L_3 absorption edge energy is very insensitive to the hyperstoichiometry, x, and is not a simple way to determine the oxidation state. In this study they point out that the energy of the peak increases by 0.5 eV, as x reaches 0.2. Also a possible effect on the white line due to the size of nc-UO_2 samples could be present in the obtained results. This effect cannot be quantified without a dedicated study with nano materials with the exact same stoichiometry but with different size. That was, at this moment not possible with the synthesized nc-UO_2 where just one-size samples where synthesized and different particle sizes were obtained by treatment at temperature. Under this treatment, not just a change in size occurred, but also a change in valence, even under inert atmosphere (Table 5.1). So, in principle, because of this size effect, determining the O/M from the shift is dubious. However, as this size effect was not easily to quantify, it was assumed to use the shift. Anyway, for the RT and 600°C nc-UO_2 samples, it is clear that there is U^{VI} contribution not only from the shift but also from the shoulder (which is indicative of the uranyl). For the 1200°C sample, it is unlikely that a size effect occur as 80 nm is already large.

In the k^3-weighted EXAFS spectra (Fig. 5.11a), the oscillations and their amplitude increased with thermal treatment. The 4 nm as-precipitated sample was very difficult to fit with a pure fluorite structure, as the fit were non stable and the data noisy (treated k-range = 3-8 $Å^{-1}$). The intensity of the FT (Fig. 5.11b) was very low limiting the interpretation of the coordination shell to U-O_1. Observing the EXAFS results in Table 5.3, the data were heavily dampened at RT where a large value for the DW factor was found, meaning a significant static disorder for the nc-UO_2 as-produced. Shorter distance for the oxygen shell (U-O bond length) was clearly observable for the nc-UO_2 at RT which did not correspond to any U-oxide. According to the shape of the first FT peak, it looked like there were two or three U-O distances instead of one. This was consistent with the observed lattice contraction (0.5417 nm) from XRD at RT (see Table 5.2).

The 9 nm sample (600°C anneal) showed an intermediate ordering with oscillations clearly identified and extending to k = 9 $Å^{-1}$. The intensity of the FT was also low for this annealed sample, limiting the fitting and interpretation of the coordination shell to U-O_1 and U-U_1 together with UO_2 fluorite structure. Still a large value for the DW factor was found (Table 5.3). Shorter distance was also present for the oxygen shell (U-O bond length) in comparison with the reference-$U^{IV}O_2$. However the U-U_1 bond length was closer to that of the bulk-$U^{IV}O_2$, suggesting that the U-U_1 lattice was more ordered than the O anion sublattice. The U-U_1 lengths were consistent with the less lattice contraction (0.5431 nm), in comparison with the nc-UO_2 as-produced, as probed by XRD at 600°C anneal.

Ultimately, at 1200°C and 82 nm, EXAFS oscillations were similar, if not entirely matching, those of the bulk-$U^{IV}O_2$ indicating same *fcc*-structure consolidation and substantial particle growth, both observed in XRD measurements (Fig. 5.12). Both shells were well fitted with *Fm-3m* structure for this sample (Fig. 5.13) and very similar distances to reference $U^{IV}O_2$ structure could be observed according to the FT (k-range treated = 3-12 $Å^{-1}$). That was in agreement with the similarity for the XRD data for the annealed sample at 1200°C and the bulk-$U^{IV}O_2$ (Fig. 5.8). Also consistent with the XANES (see Fig. 5.10) showing no different oscillation from the fluorite structure.

The Hahn-echo ^{17}O MAS spectra acquired for various annealing times (600°C, 650°C, 700°C, 800°C and 1200°C) were presented in Fig. 5.15 and some fits in Fig. 5.16 and Fig. 5.17. Two trends were observed in the plots of the shifts and the FWHM as a function of temperature presented in Fig. 5.18. Under 700°C, the shift and the FWHM decreased abruptly while above this temperature they were relatively constant. It can be noticed that the shift extracted from the spectrum acquired at 200°C was very different from that of the whole series. Due to the broadness of the peak, the presence of more than one species cannot be excluded, as already assumed in the EXAFS study. A similar trend was observed by XRD for the evolution of the lattice parameter as a function of temperature (Fig. 5.4). In fact, it increased steeply under 700°C, then there was only a week evolution. Therefore, it seemed that under this temperature there is important changes on long and short range.

Three different oxygen environments could be identified. The first one corresponds to oxygens having a chemical shift of nearly 900 ppm (named peak *C*, green peak). These peaks have been identified up to 650°C. Due to the broadness of the peak, it was tempting to attribute this one to ^{17}O in a disordered environment. But, XRD

has shown that for this range of temperature the size of the UO_2 was around 10 nm (Fig. 5.8 under Ar/5%H_2). The strong surface energy existing on the surface of the small particles will lead to more strain in the lattice, consequently caused the broadening of the main peak of the quadrupolar line. Thus, it could be proposed that this type of oxygen corresponded to the ^{17}O in nc-UO_2. Nevertheless, due to the broadness of the peak, presence of other ^{17}O species could not be excluded.

The two second types of species appeared clearly from 650°C (Fig. 5.18). There was one sharp and one broad (named peaks *A* and *B* respectively). These peaks could be respectively attributed to ^{17}O in a crystalline phase and in a more disordered phase. With increasing temperature (increasing of crystallite size), the FWHM of the two peaks decreased (Fig. 5.17). As previously explained, this was the signature of such crystallite size evolution. Moreover, the shift of peak *A* reached a minimal value of 717 ppm at 1200°C. This one was close of the 717 ppm found for $U^{IV}O_2$-bulk. Its FWHM was of 5 ppm and corresponded to that of the crystallite having a size about 80 nm. This value was still slightly bigger than the 3 ppm found for $U^{IV}O_2$-bulk. Hence, with the shift of peak *A* one could say that the environment around the oxygens corresponding to the biggest crystallite size (80 nm) was very close to that of $U^{IV}O_2$-bulk. Based on the FWHM, one can say that to observe the signal of crystalline UO_2 a size above 80 nm should be reached. This confirmed that nc-UO_2 were obtained being consistent with the lattice parameter observed of 0.5472 nm, as well as the O/M ratio obtained in the XANES analysis (Table 5.2).

Several samples at the key annealing temperatures were analyzed under the FTIR spectrometer. The IR spectra recorded for nc-UO_2 as-produced (RT), at 200°C, 600°C and 1200°C under Ar/5%H_2 annealed, as well as $U^{IV}O_2$ reference spectra, were shown in Fig. 5.19. In the case of nc-UO_2 as-produced (RT), four peaks in the range 400-4000 cm^{-1} could be observed. They could be assigned to the bending vibration of H-O-H of the coordinated water, and to a possible more oxidised state (UO_{2+x}). All of them diminished with annealing. The peaks assigned to the H-O-H of the coordinated water, totally disappeared at 600°C. That was in agreement with the TGA, were nearly no weight of loss was observable after 600°C (see Fig. 5.1). However two of the peaks finally disappeared at 1200°C. That could be an artefact due to the small size still present at 600°C (10 nm) (see Table 5.1). Hence, at 1200°C the IR spectra looked like the one for the $U^{IV}O_2$ reference and grains were about 80 nm (Table 5.1).

That was also in agreement with the results obtained by XANES where a different electronic structure at 600°C was seen, meanwhile at 1200°C a similar structure to bulk-$U^{IV}O_2$ was found (see Table 5.2). Also EXAFS was characterized for a poor ordering at 600°C but entirely matching with the bulk-$U^{IV}O_2$ oscillation pairs at 1200°C (see Table 5.3).

Isothermal evolution of the synthesized nc-UO_2 was then performed. Isothermal grain growth at a given temperature is an essential component to evaluate the grain growth kinetics, and in consequence the performance of such an innovative nuclear fuel. Differences in the grain growth behaviour between the micro- and nano-grain form of the same material, have been already reported [Moelle and Fecht, 1995] [Natter et al., 2000] [Natter et al., 2001] [Rupp et al., 2006]. In the first case the material follows the general growth equation, but in the nano-grain case, the grain grows until a critical time when the grain growth remains constant as described by

the relaxation function Eq. 5.6. However, when the nano-grain material is treated above a determined temperature (1100°C [Rupp et al., 2006]), the grain growth follows again the general growth equation (Eq. 5.8). This is in agreement with the results here observed. For the temperatures of 500°C, 700°C and 900°C and a static and inert atmosphere of He, the grain growth took place in the first hours of isothermal hold until a stable average grain size was established at the applied temperature, at which time crystal growth ceased (Fig. 5.21). For the isotherm at 1200°C and a static atmosphere of He, the material had a continuous growth not reaching a constant grain value in the first 50 h (Fig. 5.20).

From Fig. 5.23 an activation energy of diffusion of 0.93 eV to 1.25 eV was obtained. Diffusion can occur along the grain boundary, or it can occur intragranularly (volume diffusion), or because of grain defects. The grain boundary diffusion is always faster than the volume diffusion, meanwhile the volume diffusion occurs within a single grain and is only important at higher temperatures. In this case of nc-UO_2, the low activation energies obtained could be related predominantly to grain boundary (surface and interface) diffusion as volume diffusion contribution exhibits for higher activation energies (above 4 eV [Sabioni et al., 1998]).

A lattice of about 0.5472 nm was already found for the samples treated at 900°C after 50 h dwell time under Ar/H_2 obtaining a final size about 50 nm (Table 5.5). Therefore a temperature of 1200°C (and in consequence a final crystallite size of 80 nm) would be, in principle, not necessary to reach the typical lattice parameter of the reference large-grained UO_2 (a=0.5472 nm), as above commented.

An average grain size of 322 nm was measured after cooling for the heat treatment at 1200°C after 50 h dwell under He (Table 5.5). Taking that into account, it appears that a temperature below 1200°C would be necessary in the sintering process of of the monoliths, to avoid extreme growth of the particles (>200 nm). Nevertheless for the nc-UO_2 samples annealed at 1200°C during 50 h under Ar/H_2 dynamic atmosphere, a final grain size of 85 nm was measured after cooling. Even after 200 h dwell time at this temperature under reducing atmosphere, a final grain size of 150 nm was seen (quite far from the 322 nm observed under He atmosphere after 50 h). This difference could be due to the initial oxidation state of the nc-UO_2 samples and their evolution under a static He atmosphere.

As mentioned previously, an hyperstoichiometric UO_2 would present a stronger increase of the self-diffusion coefficients and in the same way raise the mass-flow, the grain-boundary motion and the grain (or crystal) growth will occur. In Fig. 5.24, the Arrhenius diagram comparing the cation self-diffusion in UO_2 fluorite-structure from large-grain reported by [Matzke, 1987] and nano-grain from this study (samples annealed under He static atmosphere during 50 h), has been plotted. Between 20 orders of magnitude at 500°C (lattice parameter =0.5457 nm; average grain size =18 nm) and 5 orders of magnitude at 1200°C (lattice parameter =0.5472 nm; average grain size =322 nm) have been found for the diffusion coefficients between bulk-UO_2 [Matzke, 1987] and nc-UO_2 of this study (Table 5.5). Differences in the diffusivity in the grain boundaries between micro- and nano-grain have been seen already in other fluorite structure metal oxides [Martin, 2007]. In fact the differences in the diffusion coefficient between bulk- and nc-UO_2 are compatible with an enhancement of the diffusion processes either by a diminishing of the grain size or by O/U>2 effects.

Chapter 6

Crystallization and Grain Growth in f(T) for nc-UO_2 by Organic route

6.1 Generalities.

In this chapter the evolution of the grain size and the crystal structure evolution as a function of temperature under inert and reducing atmosphere of nc-UO_2 precipitated from organic phase (see Chap. 4), have been investigated. Thermogravimetric analysis (TGA) of the samples provides the starting point for these investigations, enabling the identification of mass losses at given temperatures. The structure of the material as a function of temperature has been identified mainly by XRD and HT-XRD, but also by advanced methods including XANES and EXAFS.

6.2 Thermal evolution and mass changes as probed by TGA/DTA.

Thermogravimetry analysis (TGA) and differential thermal analyses (DTA) were employed under Ar/5%H_2 gas at a heating rate of 5°C/min to determine the thermal decomposition temperature and the water and organic content of the product (see Fig. 6.1). The description of the instrument is shown in Sec. 2.5.

Upon heating under Ar/5%H_2, a mass loss of 1 wt% is observed until 150°C together with a slight endothermic peak. This loss of weight is likely due to outgassing of residual water coming from the precursor. A second weight loss of about 3.5 wt% appears until 280°C, accompanied by an exothermic peak at 240°C. A new mass loss appears until 485°C which could be due to the residual carbon from the precursor. Between 485 and 1200°C there is no weigh loss (1 wt%) accompanied with wide exotherm probable due to the heat release because crystallization.

6.3 Lattice parameter and crystal growth in neutral atmosphere.

The crystal growth, lattice parameter of the nc-UO_2 from organic route (5.52 nm size and lattice parameter a = 0.5430(1) nm; see Sec. 4.4), has been investigated under inert

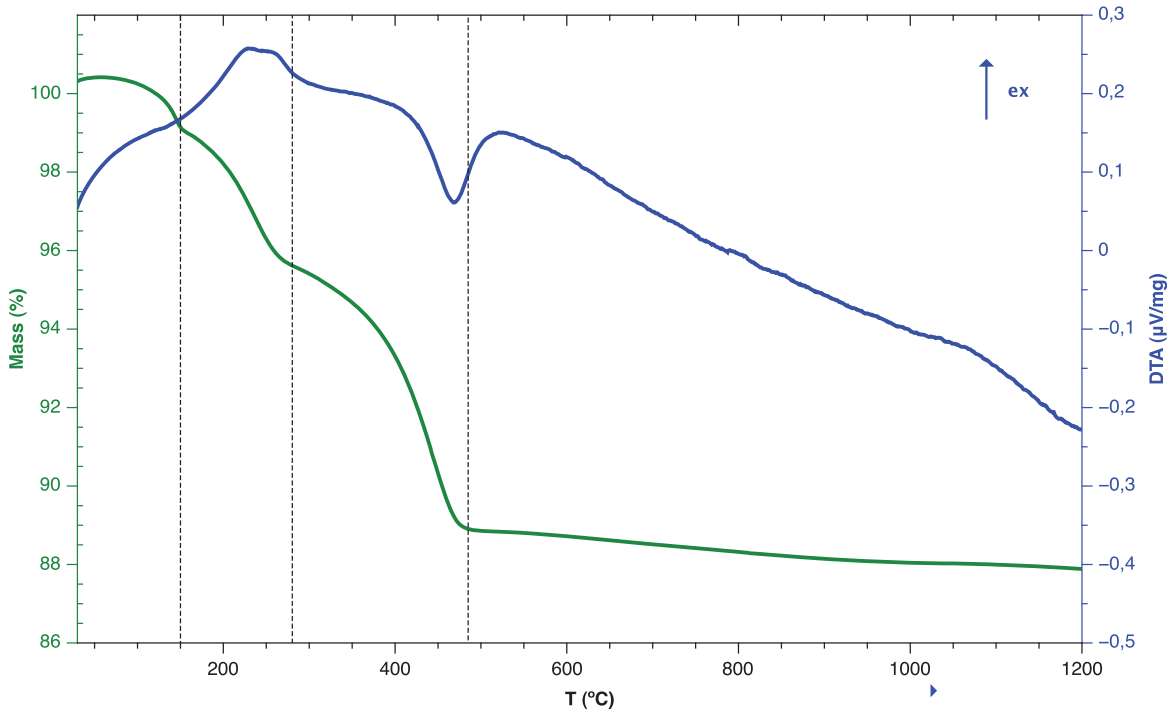

Figure 6.1: TGA and DTA signal for nc-UO_2 under Ar/5%H_2 atmosphere.

conditions (static He atmosphere) using in situ HT-XRD. The effect of temperature on the crystallite size, which is a fundamental parameter in the sintering process has been analysed. As it has been seen in Fig. 6.1, no organics loss was observed after 500°C. However, to avoid any possible decomposition of the nc-UO_2 organic layer in the static atmosphere of the HT-XRD chamber, a pretreatment under O_2 was applied (500°C during 1 h), followed by 2 h under Ar/5%H_2 to reverse the possible oxidation of the particles. After thermal pre-treatment, a size of 37 nm and lattice parameter 0.5462(0) nm, were determined. The in situ HT-XRD patterns were acquired with an instrument described in 2.4.2. The temperature range explored was 30 to 1100°C.

The evolution with temperature of the nc-UO_2 XRD pattern is shown in Fig. 6.2. The observed reflections are assigned to UO_2-*fcc* phase structure and to Pt phase corresponding to the heater plate. The effect of temperature on the peaks can be observed more clearly in Fig. 6.2-*right*, which displays the evolution of two main peaks (the (111) and (200) reflections) of the UO_2 structure. In Fig. 6.2, one observes a shift in the peak position to lower angles, possibly related to a thermal lattice parameter expansion.

An effect of the temperature is seen in the width of the peaks which decreases with increasing temperature while the intensity of the peaks increases. This width change was observed even below 700°C which was the highest pre-treatment temperature. This effect could be due to the longer times (about 10 h) at temperature used in the HT-XRD which induce to a perfectionism of the UO_2 *fcc*-structure (higher crystallization). Since the contribution of instrumental broadening is independent of the temperature, the broadening at lower temperatures is mainly related to the crystallite size and strain present in the material, as well as increase of the structural order. Both contributions, crystal size (proportional to $cos^{-1}\theta$; Eq. 5.1) and strain (proportional to $tan\theta$; Eq. 5.2), have different angular dependences, and are so separable. A study of those influences has been performed in the following.

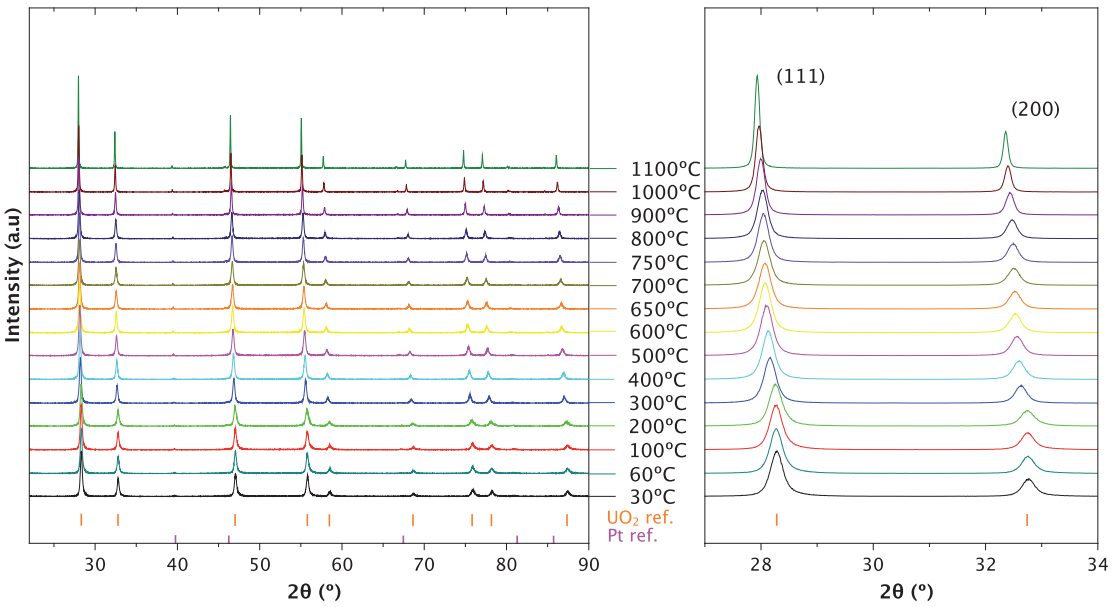

Figure 6.2: In situ HT-XRD patterns of nc-UO_2 under He *(left)*. The typical UO_2 and Pt (heating plate) Bragg peak positions are also marked. The *(right)* picture shows just the evolution of (111) and (200) peaks of UO_2 cubic structure as a function of temperature.

6.3.1 Grain growth as a function of temperature under neutral atmosphere.

The crystallite size of the nc-UO_2 has been determined by XRD Rietveld refinement (see Sec. 2.4) of the Bragg peaks (Fig. 6.2), and used also to characterize the microstructure of the material. From these results it is possible to generate a universal representation of the crystallite size as a function of temperature (XRDs measured at temperature and under static He atmosphere) and reported in Fig. 6.3. Even though, this information is taken as universal, slight deviations may occur, in particular due to dwell times and temperature ramps, but more importantly due to the atmosphere of static He during thermal treatment. Notable crystal size variations were observed above 700°C as this was the temperature already reached during the pre-treatment of the material. The crystallite size change with temperature shows a slow growth up to 700°C, and an intense growth from 37 to 150 nm at 1100°C (see Fig. 6.3).

Fig. 6.4 shows TEM images of the nc-UO_2 particles as-produced, after the pre-thermal treatment under O_2 (500°C) and Ar/H_2 (700°C) and at 1000°C. The size change corresponds to the one measured by XRD.

6.3.2 Lattice parameter and linear thermal expansion coefficient as a function of temperature.

The crystal growth of the sample under inert conditions (static He atmosphere) using in situ HT-XRD, have been already described. In addition, the variation of the lattice parameter versus crystal size and temperature, as well as data on the linear thermal expansion, are now reported and compared to bulk material UO_2. The crystal structure

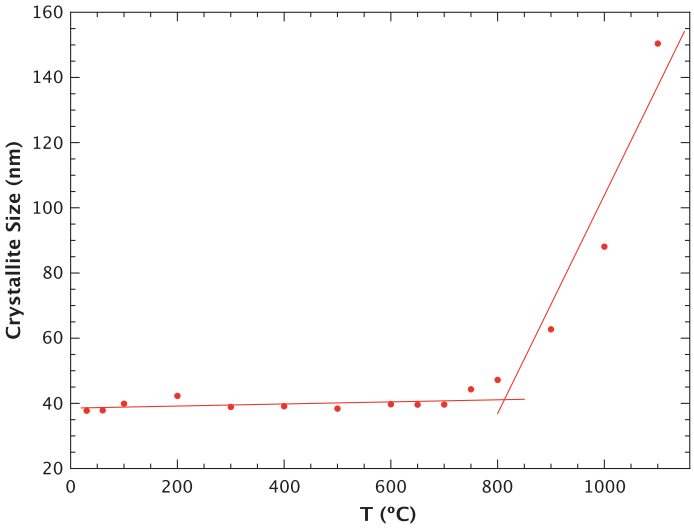

Figure 6.3: Evolution of the nc-UO_2 crystallite size in function of the temperature.

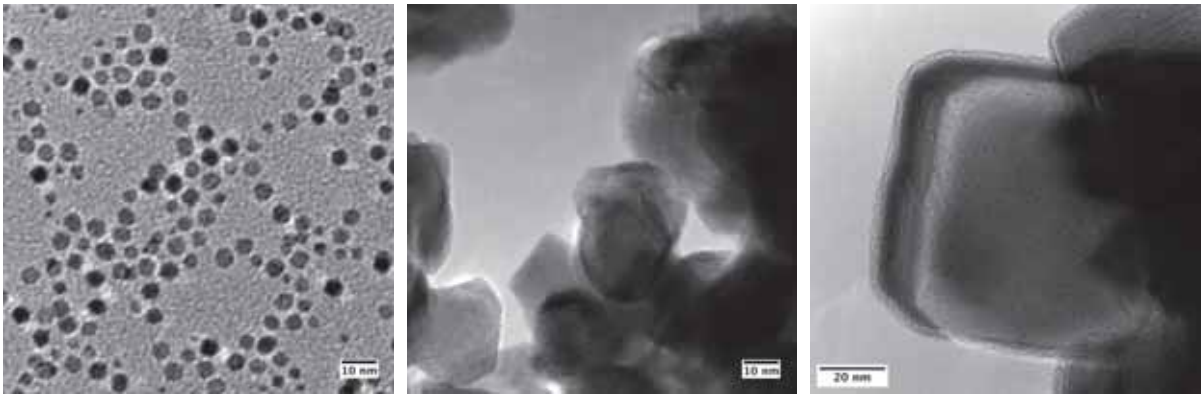

(a) 4 nm as-produced (b) 34 nm at 700°C (c) 91 nm at 1000°C

Figure 6.4: TEM images for the nc-UO_2.

of the precipitates was, as the crystallite size, determined by Rietveld refinement, taking into account the whole 2θ range.

In Fig. 6.5a the lattice parameter obtained as a function of temperature (XRDs measured at temperature and under static He atmosphere) and its derivative (Fig. 6.5b), have been also determined by the XRD Rietveld refinement of the Bragg peaks, and represented together with the nc-UO_2 size evolution to observe its dependence. Also the calculated lattice evolution of non-stoichiometric standard UO_{2+x} for different O/U ratios due to only thermal expansion, have been represented for comparison. The lattice parameter of a non stoichiometric UO_{2+x} is linked to the oxygen content by the relations of [Lynds et al., 1963]. Also the lattice parameter was corrected as a function of temperature with the [Fink, 2000] relations already reflected in Eq. 5.3.

An expansion in the lattice parameter from 0.5462(0) nm at RT (after being pretreatment) to 0.5482(0) nm at 300°C, has been determined. Above this temperature, a linear evolution of the the lattice parameter with temperature is observed. Relating the lattice parameter found in this study with the [Lynds et al., 1963] relations, a stoichiometry of $UO_{2.04}$ up to 300°C to $UO_{2.00}$ up to 750°C, has been determined. The

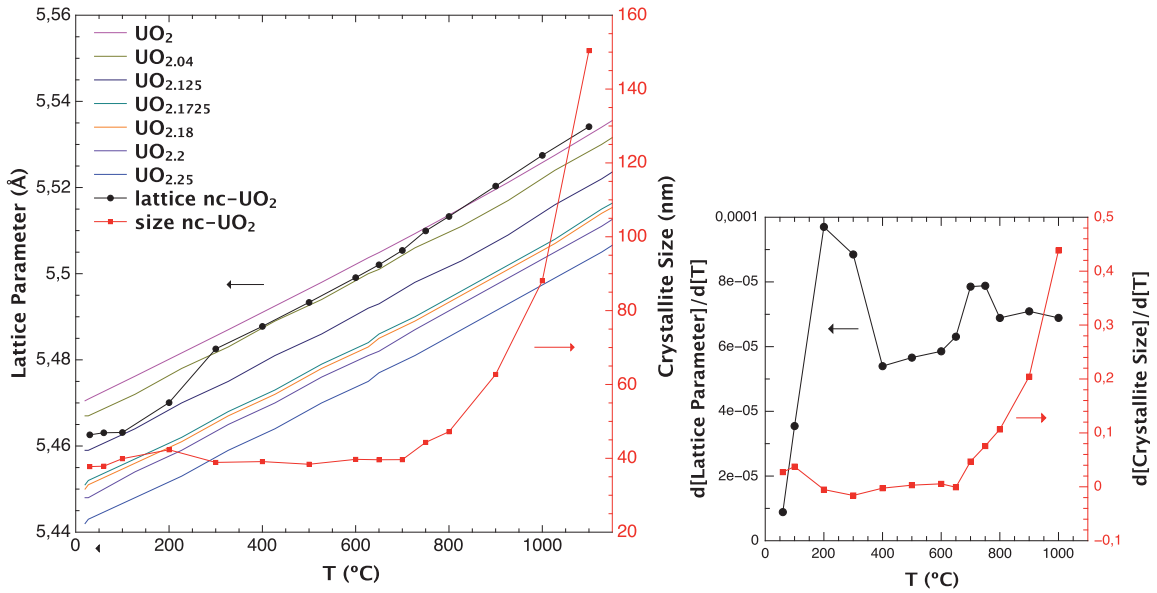

(a) (b)

Figure 6.5: a.) Lattice constant and crystallite size variation of nc-UO_2 in function of temperature (curves only as a guide to eye), from in situ HT-XRD measurements under static He atmosphere in comparison with lattice evolution in function of temperatures of standard UO_2 for different O/U ratios obtained by the relations of [Lynds et al., 1963], due to only thermal expansion. b.) Relative crystallite size and lattice parameter vs. temperature (curves only as a guide to eye).

nanocrystallites stabilize at O/U 2.0 at temperatures above 750°C, or in other words, at particles sizes >44 nm.

Fig. 6.6 displays the linear thermal expansion (LTE) and the linear thermal expansion coefficient (LTEC) of nc-UO_2 as a function of the temperature. The LTE at temperature T was calculated using the relation 5.4. The LTEC was calculated by differentiating the thermal expansion curve a_T versus T with respect to the temperature T (see Eq. 5.5).

The LTE of the nc-UO_2 is just slightly higher than the one for UO_2 bulk [Martin, 1988] for all the interval of temperatures, as one could already predict from the lattice parameter representation in function of temperature (see Fig. 6.5a). The LTEC is initially higher for nc-UO_2 than for bulk-UO_2 for temperatures below 400°C and tends to stabilize above this temperature with a value of $12 \cdot 10^{-6}$ $°C^{-1}$ in agreement with the value for the LTEC of bulk-UO_2. The oscillatory trends observable for LTEC in nc-UO_2 can be attribute to transitory oxidation-reduction effects.

If Fig. 6.7 the patterns comparison of nc-UO_2 at RT (previously treated at 500°C during 1 h and 700°C during 2 h under O_2 and Ar/5%H_2, respectively) (a = 0.5462(0) nm), nc-UO_2 at 1100°C (a = 0.5534(0) nm) and nc-UO_2 at RT after thermal treatment at 1100°C (a = 0.5472(0) nm) (all measured in situ in the HT-XRD instrument under static He atmosphere), is shown.

At 1100°C under static He atm, an O/U ratio of 2.0 (see Fig. 5.4a) and a lattice pararameter of a = 0.5534(0) nm (measured at temperature), have been observed. The same thermally treated sample measured after cooling at RT, shows a value of

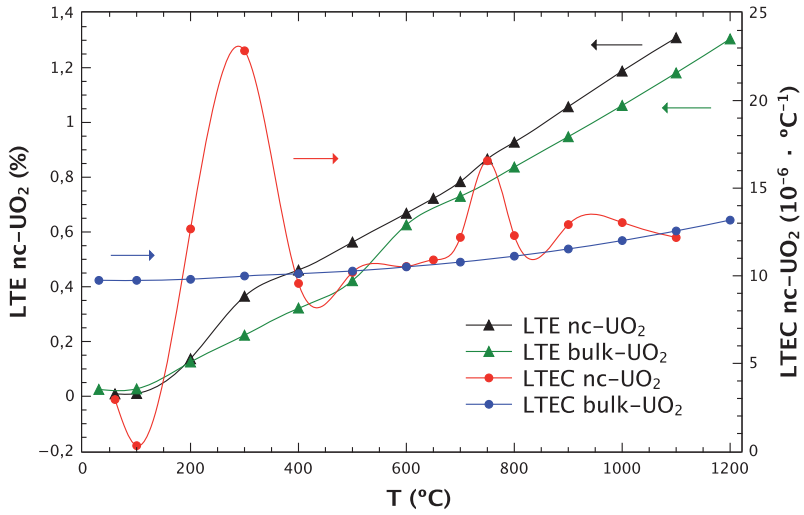

Figure 6.6: Linear thermal expansion (LTE) and linear thermal expansion coefficient (LTEC) of the nc-UO_2 in comparison with data of bulk-UO_2 from [Martin, 1988] (curves only as a guide to eye).

0.5472(0) nm very similar from the typical for bulk-UO_2 (0.547 nm). The peaks of the nc-UO_2 at RT after the thermal treatment at 1100°C recover the typical position for standard UO_2 (see Fig. 6.7).

So, a recovery of the crystal structure has been achieved with temperature under static He atmosphere from the initial lattice parameter value of a = 0.5462(0) nm from the nc-UO_2 (pre-thermal treated at 700°C) to 0.5472(1) nm after thermal treatment at 1200°C.

6.3.3 Lattice strain evolution as a function of temperature.

The mean strain e in the material was determined by Rietveld refinement using the software [HSP-PAN, 2011] and used to characterize the deformation state of the material. The crystallite size change with temperature, already shown in Sec. 6.3.1, was characterized for a quasi linearly crystal growth above the 750°C. A size of about 150 nm at 1100°C was reached.

In the evolution of the lattice strain e release with temperature, (Fig. 6.8), a first increase of the strain at 200°C is observed. Afterwards a slow and progressive decrease occurs up to 700°C with a rapid drop occurs until 1000°C when the strain of the material is totally released and a high increase in the crystallite size begins (from 88 nm at 1000°C to 150 nm at 1100°C).

6.4 Lattice parameter and crystal growth under reducing conditions.

The local structure has been investigated for the nc-UO_2 as-produced and after thermal treatment under reduction conditions (Ar/5%H_2), by X-Ray Diffraction (XRD) and

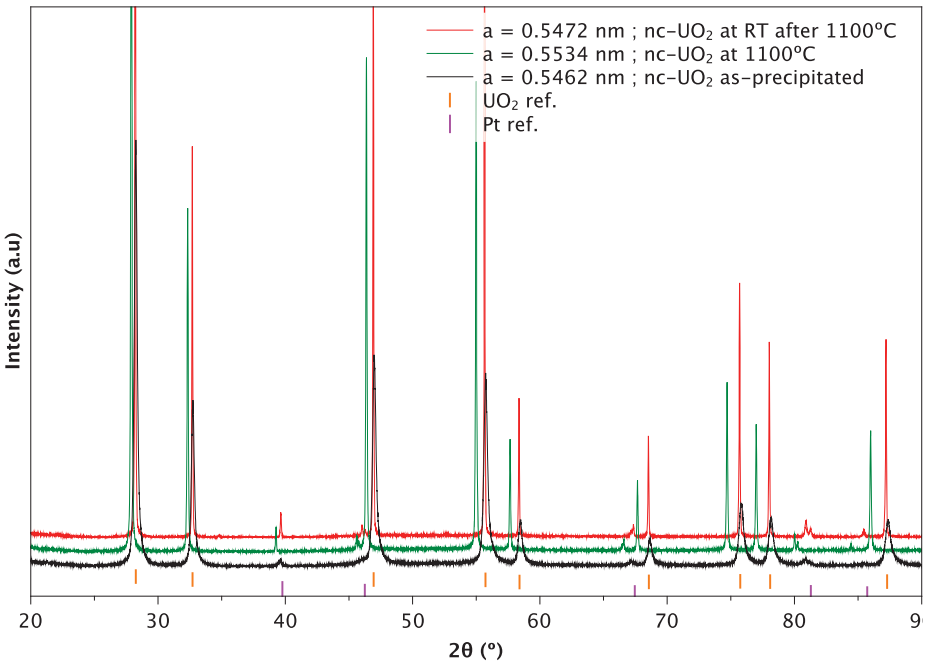

Figure 6.7: Patterns comparison of nc-UO_2 pre-thermal treated, nc-UO_2 at 1100°C and nc-UO_2 at RT after thermal treatment at 1100°C (measured in situ in the HT-XRD instrument under static He atmosphere)

X-ray Absorption Spectroscopy (XAS), and compared to bulk-UO_2 as a reference. A combination of X-ray Absorption Near Edge Structure (XANES) and Extended X-ray Absorption Fine Structure (EXAFS) was used.

6.4.1 Crystal size and lattice parameter evolution as a function of temperature as probed by XRD.

As it has been seen from the HTXRD, the lattice constant (and crystal size) of the material in the cooled state (at RT) after reach different maximum temperatures is needed (see Fig 6.7). This allows separation of the thermal expansion contribution in the high-temperature values to obtain cleaner curves for thermal expansion vs. temperature and lattice dimension vs. crystal size. Also no pre-treatment was make on the samples used here.

At the outset of this study, a high concern about the control of the O/U ratio, which is not simple, appeared. The structural investigations presented in the following, attempt to eliminate this issue as the samples were heated in Ar/5%H_2 to ensure that the O/U = 2.00. The impact of the heat treatment on the microstructure of nc-UO_2 at different annealing temperatures was then studied under reducing conditions (dynamic Ar/5%H_2 atmosphere). As-produced or room temperature (RT) (5.52 nm $\simeq$ 5 nm), 600°C (5.78 nm $\simeq$ 6 nm) and 1200°C (12.19 nm $\simeq$ 12 nm). The corresponding XRD data are given in Fig. 6.9. A heating rate of 5°C $\cdot$ min^{-1} under dry Ar/5%H_2 and annealing for 15 minutes were used. At 500°C under Ar/5%H_2 the major mass loss has already occurred, as has been observed in the TGA/DTA (Fig. 6.1). So no organics traces should be present at 600°C in the material. As a reference, a standard $UO_{2.0}$ (μm crystal size) sintered at 1600°C under Ar/5%H_2 for 6 hours and measured during

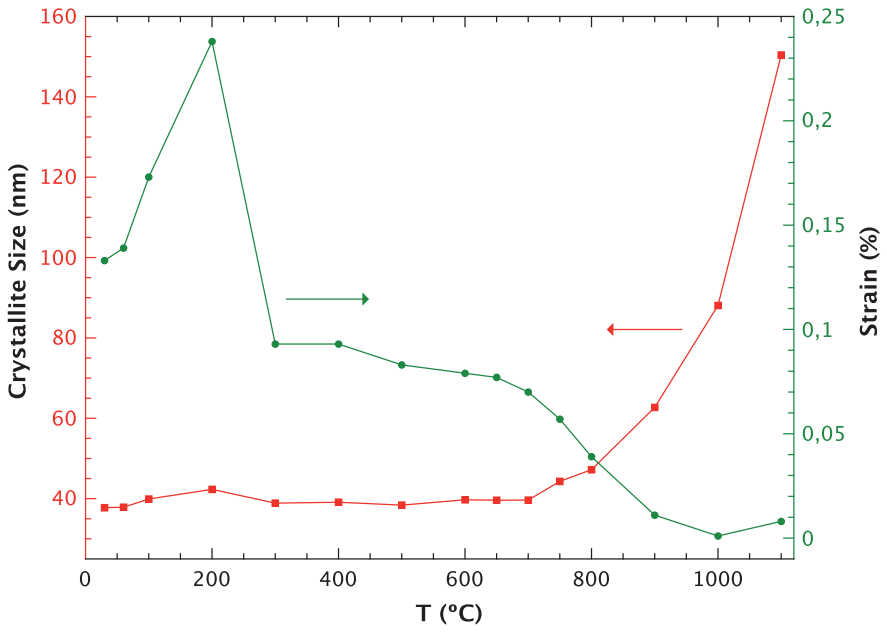

Figure 6.8: Crystallite size and strain of nc-UO_2 in function of temperature. Measurements done at temperature under static He atmosphere (curves only as a guide to eye).

the same measuring campaign, was also used.

The measurements indicated a well crystallized single cubic phase with a fluorite structure (*Fm-3m*). No evidence for orthorhombic or other phase was found. From the Rietveld refinement of the measured diffractograms, the lattice parameters as well as the size of the particles were deduced. Reduction of the nc-UO_{2+x} towards nc-UO_2 after annealing at 600°C and 1200°C, was expected because the high sensitivity of the lattice parameter (a) to changes in the oxidation state of U in the hyperstoichiometric range, O/M > 2. Samples treated at increasing temperature (RT, 600°C and 1200°C) with a short isothermal hold of 15 min, exhibit an increase in the lattice constant of 0.55%. Progressing crystallization of the nc-UO_2 leads to periodic ordering of its atom and the lattice parameter, which was shifted to higher angles, changed from 0.5430(1) nm at RT, to 0.5432 nm and 0.5461 nm at 600°C and 1200°C, respectively. The crystal-size increased from 5.5 nm as-prepared, to 5.8 nm and 12.2 nm following treatments at 600°C and 1200°C, respectively (Fig. 6.9).

A notable difference on the crystal size and lattice parameter for samples treated at 1200°C under dynamic Ar/5%H_2 atmosphere (measurement after cooling), with those at 1100°C under static He atmosphere measured at temperature (see Fig. 6.5a) is noted. The one under Ar/5%H_2 had a crystallite size around 12 nm, while the one under He atm reached a size of 150 nm. Major differences have been seen in the lattice parameters as a function of the atmosphere used without ignoring the fact that the values under He were measured at temperature. These differences in the lattice observed in the samples treated under He, disappeared once the sample measured at temperature is measured after cooling, as it has been seen in Fig. 6.7. In the evolution of the lattice strain (e), a release was observed with increasing temperatures. After annealing at 600°C under Ar/5%H_2, just little strain was released (from 0.702 to 0.664%), totally disappearing at 1200°C (0.004%), as it also happen under He atm after 1100°C.

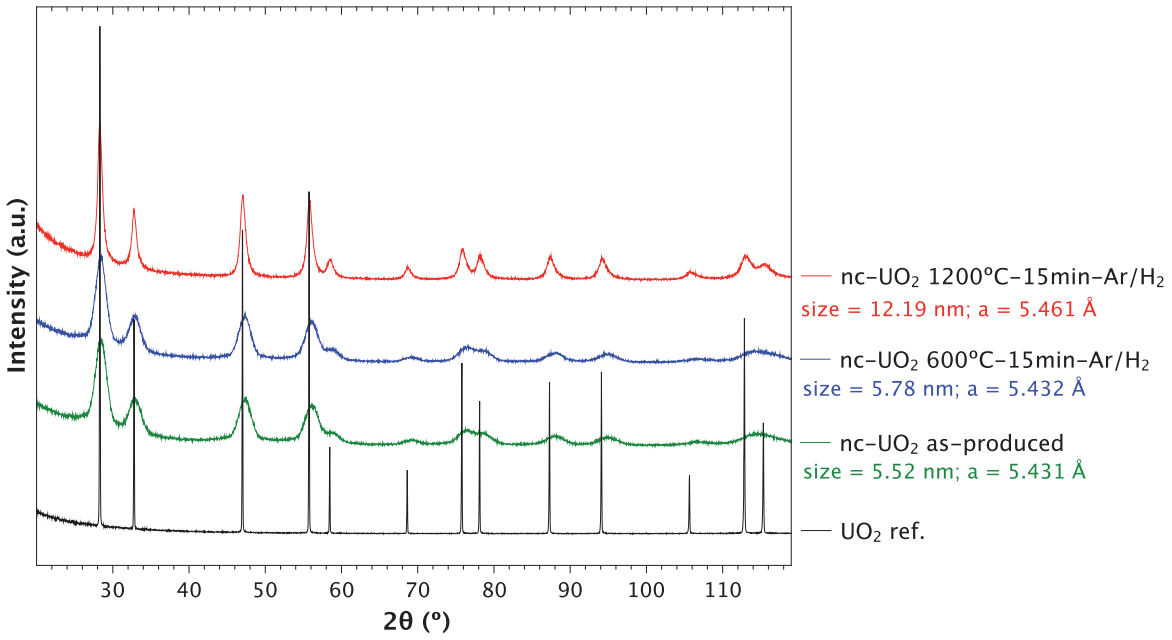

Figure 6.9: XRD patterns of reference UO_2 and organic UO_2 (as-produced, after thermal treatment under Ar/5%H_2 at 600°C and 1200°C).

6.4.2 O/M ratio as a function of temperature as probed by XANES.

XANES was used to determine the oxidation of U cations and the corresponding molar fractions. From these, the O/U ratios were ultimately derived. The normalized XANES spectra and the first derivate at the U-L_3 absorption edge of the three different heated nanocrystalline UO_2 samples (nc-UO_2 at RT, 600°C and 1200°C) are shown in Fig. 6.10, together with the reference spectra of $U^{IV}O_2$. The associated energies of the inflection point at absorption edge and of the white-line (WL), as well as the energy shift (ΔE) and the estimated oxidation states derived from this study, are given in Table 6.1

A simple observation of the XANES spectra at the U-L_3 edge immediately shows a trend with increasing temperature and as x decreases (UO_{2+x}). The peak of the WL shifts slightly to lower energies and increases in intensity, and the oscillations within the XANES regions slightly increase. The amplitude decrease with the increasing temperature of thermal treatment shows a relative higher structural order of these samples (Fig. 6.10).

For the three samples as-produced (RT), 600°C, and even at 1200°C, there is a significant difference of shape compared to the $U^{IV}O_2$ reference, i.e. presence of a shoulder on the high energy side of the edge. This feature usually indicates the presence of U^{VI}. According to [Conradson et al., 2005a], a shoulder appears on the high energy side of the main peak, ongoing from An^{IV} to An^{V} and An^{VI} (An = Actinides = Th, Pa, U, Np, Pu, Am, Cm). This is also in agreement with the observed decrease of WL amplitude with the increasing temperature. The shoulder decreases with temperature meaning that there is less U^{VI} or that the U^{IV} bulk is more visible as it size increases.

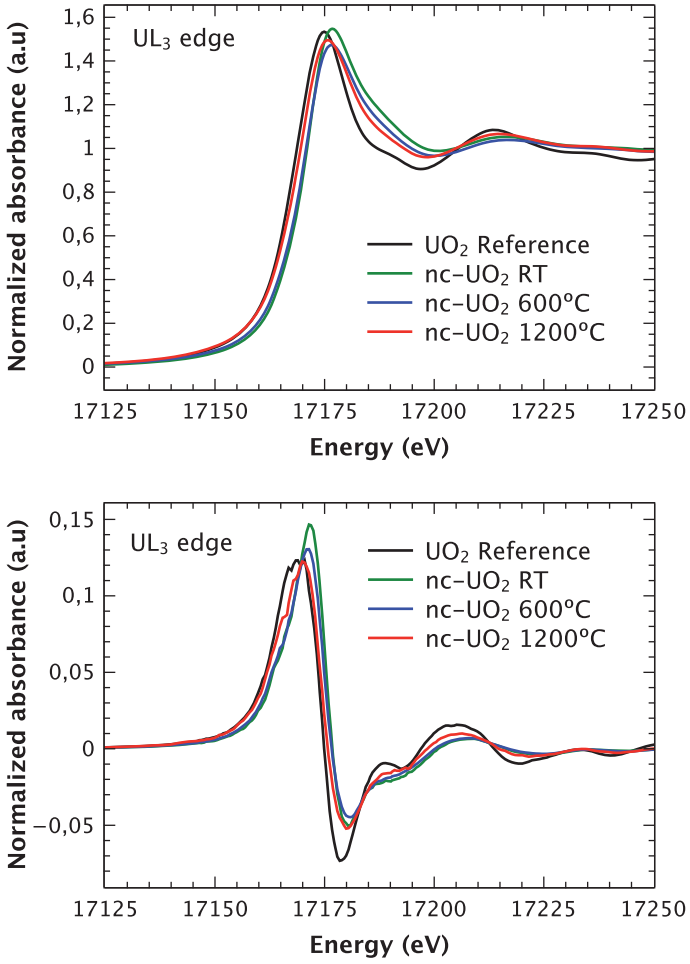

Figure 6.10: Normalized absorption XANES spectra and the first derivate at the U-L_3 edge of the three different heated nc-UO_2 samples from Organic route (nc-UO_2 at RT, 600°C and 1200°C), together with the reference spectra of bulk $U^{IV}O_2$.

A small shift of the absorption edge to higher energies (further for the RT and 600°C samples), as well as a broader WL is observed for the three nc-UO_2 samples.

Detailed analysis of the U-L_3 XANES spectra and of their first derivate for the RT sample, show that the energy of the WL shifts 1.9 eV (Table 6.1) to higher energies in comparison with the reference UO_2 (U^{IV}) spectrum. A shoulder on the right side of the edge for RT, is observable. It could be expected the sample is the most cluster like (smaller in size), but in addition the composition is not fully ascribed to UO_2. The shoulder could be a proof of the presence of U^{VI}. As explained in Sec. 2.2.3, molar fractions of 30% of U^V and 70% of U^{VI} corresponding to a ratio O/M of 2.85 ($V_U = 5.7$) (Table 6.1), have been deduced according to a linear combination of UO_2 (pure U^{IV}), U_4O_9 (mixture of U^{IV} and U^V) and U_3O_8 (mixture of U^{IV} and U^{VI}).

In the 600°C and 1200°C treated samples, the shift of the WL (1.6 eV and 0.8 eV respectively; Table 6.1), as well as the shoulder (less defined) are toward to the left in comparison to the RT sample. It indicates a minor presence of U^V and U^{VI} species but not strictly U^{IV}. Even the sample at 1200°C has not still full fluorite structure, which was also observed in the XRD measurements (5.461 nm; Fig. 6.9). An O/M ratio of 2.425 ($V_U = 4.85$) was found for the sample treated at 600°C, with a molar fraction of

40% of U^{IV}, 35% of U^{V} and 25% of U^{VI} (Table 5.2). Concerning the 1200°C treated sample an O/M ratio of 2.2 ($V_U = 4.40$) was in this case found corresponding to a molar fraction of 60% of U^{IV} and 40% of U^{V}.

The results presented in Fig. 6.10 clearly indicate that the 5 nm UO_2 particle even after 600°C anneal (6 nm) and 1200°C anneal (12 nm), does not have the electronic structure of bulk UO_2. At these temperatures, a reduction to U^{IV} would also be expected. XANES reflects the unoccupied electronic structure. In a molecule, these are well defined energy levels, while in a solid they are bands of a particular symmetry. One can understand the size effect if one considers this 5 nm UO_2 crystals as a cube with a side length of 5 nm, which is the same of around ~ 9 UO_2-unit cells (lattice parameter a = 0.547 nm). This cube contains a bulk cube of around 4 nm length (7 unit cells). Thus there are 764 unit cells in total inside the 5 nm crystal, with 400 (52%) on the surface and 364 in the interior, which one restrains from calling "bulk". For the thermal treated samples the percentage of unit cells in the surface would be 45% at 600°C (6 nm) and 25% at 1200°C (12 nm). This is a crude representation of the problem, but shows that the material is more like a large cluster in transition from a large molecule to that of the true bulk. Thus it is not surprising that the XANES depicts an electronic structure of the nc-UO_2 material unique from the bulk material.

Table 6.1: Results from the analysis of the UO_{2+x} XANES data at the U-L_3 edge.

	lattice param.	**inflection point**	**energy WL**	**ΔE^b**	**U valency**	**molar fraction**			**O/M**
	(Å)^a	(eV)	(eV)	(eV)	(V_U)	**U^{IV} (%)**^{c}	**U^V (%)**^{c}	**U^{VI} (%)**^{c}	
Reference:									
UO_2	5.472(0)	17168.7	17174.9	-	4.00	100	-	-	2.000
Samples:									
nc-UO_2 5 nm RT	5.431(0)	17171.7	17176.7	1.9	5.70	-	30	70	2.850
nc-UO_2 6 nm 600°C ^{d}	5.432(0)	17171.2	17176.5	1.6	4.85	40	35	25	2.425
nc-UO_2 12 nm 1200°C ^{d}	5.461(0)	17170.1	17175.7	0.8	4.40	60	40	-	2.200

a.) by XRD (see Fig. 6.9). b.) ($\Delta E = WL_{sample}$ - $WL_{ref.}$). c.) According to a linear combination of UO_2 (pure U^{IV}), U_4O_9 (mixture of U^{IV} and U^V) and U_3O_8 (mixture of U^{IV} and U^{VI}). d.) under Ar/5%H_2.

6.4.3 Order and disorder probed by local methods, as Debye-Waller EXAFS, as a function of crystal size.

The k^3-weighted EXAFS spectra and the corresponding Fourier transforms (FT) at the U-L_3 edge for the experimental data of UO_2 nanocrystals at different temperatures annealed, and $U^{IV}O_2$-bulk reference, are shown in Fig. 6.11. Experimental features are specified in Sec. 2.2.3.

In the k^3-weighted spectra (Fig. 6.11a), the oscillations and their amplitude increases with thermal treatment. The nc-UO_2 synthesized by organic route samples as-produced and annealed, presented a high disorder. The 5 nm as-precipitated sample was very difficult to fit with a pure fluorite structure, as the fit were non stable and the data noisy. The oscillations are very quickly dampened. The intensity of the FT was also very low. The FT at the U-L_3 edge for the experimental data of UO_2 nanocrystals at different temperatures annealed and $U^{IV}O_2$ bulk reference, are shown in Fig. 6.11b. According to the shape of the first FT peak, it looked like there were two or three U-O distances instead of one. This is consistent with the observed lattice contraction (0.5431 nm) from XRD at RT (see Table 6.1). Also samples treated at 600°C and 1200°C presented a high degree of disorder, as it was already predicted from the XANES analysis (Table 6.1). Therefore a good fit could not be achieved considering only bulk-$U^{IV}O_2$, meaning that another unidentified phase or massive disorder must be taken into account.

6.5 Results and discussion.

The evolution of the grain size and the crystal structure, which are fundamental parameters in the sintering process, as a function of temperature under inert and reducing atmosphere of nc-UO_2 precipitated from organic phase (see Chap. 4), was investigated here. Analysis of the precipitated material was performed by applying the thermal analytical and X-ray scattering techniques like TG/DTA, XRD and HT-XRD, spectroscopic techniques as XANES and IR, as well as characterization techniques like TEM. The target parameters studied have been the oxidation degree (O/U ratio), the possible organic content on the material, as well as the lattice imperfections as a function of the annealing temperature.

TGA and DTA were employed under inert atmosphere (Fig. 6.1). The weight loss observed was attribute to residual water from the precursor, but mainly to organic volatilisation and crystallization (completion of the UO_2 *fcc*-structure). However, there was no reason to believe that the weight loss did not include as well some loss of oxygen due to material's reduction. A deeper analysis on the lattice parameter and crystal growth under inert and reducing atmospheres was then performed to confirm the later.

The evolution of the crystallite size, the lattice parameter, and the strain were determined from ambient temperature up to 1100°C under inert atmosphere using the in situ HT-XRD (Fig. 6.2). As was seen in TG/DTA (Fig. 6.1), no organics presence was observed after 500°C. However, to avoid any possible decomposition of the nc-UO_2 organic layer in the static atmosphere of the HT-XRD chamber, a pretreatment under O_2 was applied (500°C during 1 h), as well, as 2 h under Ar/5%H_2 to reverse the

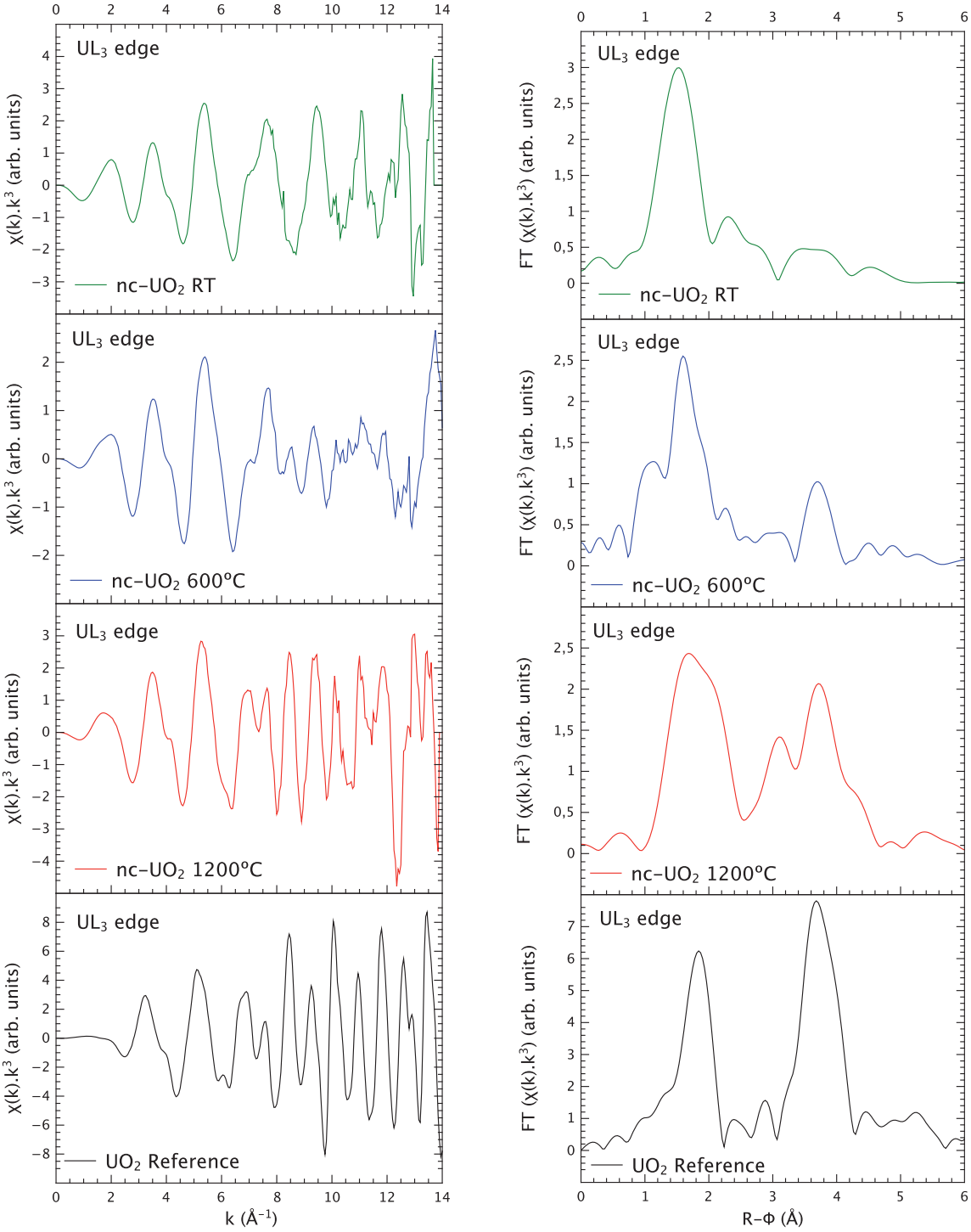

(a) Experimental k^3-weighted spectra.

(b) Experimental Fourier Transform.

Figure 6.11: a.) k^3-weighted spectra and b.) Fourier Transform at the U-L_3 edge for the experimental data of nc-UO_2 (organic route) at different temperatures annealed and $U^{IV}O_2$ bulk reference.

possible oxidation of the particles. After thermal pre-treatment, a size of 37 nm and lattice parameter 0.5462(0) nm, were determined. An effect of the temperature was seen in the width of the peaks which decreased with increasing temperature while the intensity of the peaks increased. This width change was observed even below 700°C which was the highest pre-treatment temperature. This effect could be due to the longer times (about 10 h) at temperature used in the HT-XRD which induces

a perfectionism of the UO_2 *fcc*-structure (higher crystallization). The crystallite size change with temperature showed a small growth up to 700°C, an an intense growth from 37 to 150 nm at 1100°C (see Fig. 6.3). However, slightly changes were already observable below 700°C for the lattice parameter. An expansion in the lattice parameter from 0.5462(0) nm at RT (after pre-treatment) to 0.5482(0) nm at 300°C (O/U 2.04), was determined. Above this temperature, a linear evolution of the the lattice parameter with temperature was observed. The nanocrystallites stabilized at O/U 2.0 at temperatures above 750°C, or in other words, at particles sizes >44 nm. A value of 0.5534 nm for the lattice parameter for the nc-UO_2 at 1100°C annealed and measured in situ in the HT-XRD instrument under static He atmosphere, was observed. The same thermal treated sample measured after cooling at RT, showed a value of 0.5472 nm ($UO_{2.00}$) very similar from the typical for bulk-UO_2 (0.547 nm) (Fig. 6.7). A recovering of the UO_2 typical crystal structure was achieved with temperature under static He atmosphere from the initial lattice parameter value of 0.5462 nm from the pre-treated nc-UO_2 to 0.5473 nm after thermal treatment at 1100°C (measurements done after cooling).

The LTEC (Fig. 6.5a) was initially higher for nc-UO_2 than for bulk-UO_2 for temperatures below 400°C and tends to stabilize above this temperature with a value of $12 \cdot 10^{-6}$ $°C^{-1}$ in agreement with the value for the LTEC of bulk-UO_2. The oscillatory trends observable for LTEC in nc-UO_2 might be attribute to transitory oxidation-reduction effects.

In the evolution of the lattice strain e release with temperature, (Fig. 6.8), a slowly and progressively decrease occurred up to 700°C with a rapid strain drop until 1000°C when the strain of the material is totally released and a high increase in the crystallite size began (from 88 nm at 1000°C to 150 nm at 1100°C). So the crystallite growth seemed to be limited by the presence of the lattice strain.

So, the morphology of the thermal treated nc-UO_2 differed then in form, size and oxidation state from that of the original synthesized 5 nm nc-UO_2. Furthermore, a shift in the lattice parameters was observed as a function of temperature, indicating a lattice expansion with temperature (lattice contraction with decreasing size) that extended beyond that caused by thermal effects. The origin of this size-dependent lattice expansion in the nc-UO_2 may be either the reduction of the material during thermal treatment (particle-size increase also with temperature) or the relaxation of bonding-forces at the crystal surface, which needs elucidation.

A deeper study of the structure of the material as a function of temperature under reducing atmosphere was then also studied and compared to the reference bulk-UO_2. The lattice constant of the material in the cooled state after reaching different temperatures was measured here. This allowed separation of the thermal expansion contribution in the high-temperature values to obtain cleaner curves for thermal expansion vs. temperature and lattice dimension vs. crystal size. The structure was identified mainly by XRD, but also by advanced methods including XANES, EXAFS, and Raman spectroscopy.

The nc-UO_2 XRD peaks under Ar/5%H_2 thermal treated, became sharper with the increase of the temperature indicating more crystalline UO_2, i.e., larger particle size (Fig. 6.9). A notable change in the crystallite size was observed at 1100°C, with

a size of 150 nm under He was found in contrast to 12 nm under Ar/5%H_2. However that could be due to the pre-thermal treatment (before the HT-XRD measurement under He) made under O_2 and Ar/H_2 which ended already in a size of about 37 nm at 700°C. Also differences in the lattice parameters as a function of the atmosphere, were observed. 0.5472 nm at 1100°C under He (Fig. 6.7) and 0.5461 nm at 1200°C under Ar/H_2, were measured. This difference was probably due also to the pre-thermal treatment done to the first samples where a higher consolidation of the *fcc* fluorite structure was achieved due to the longer times at temperature. A lattice parameter of 0.5462 nm was reached after 2 h under Ar/H_2 at 700°C, and 0.5472 after 1100°C under He (about 10 h at temperature).

In the evolution of the lattice strain (e) under Ar/5%H_2, a release was observed with increasing temperatures. After annealing at 600°C under Ar/5%H_2, just little strain was released (from 0.702 to 0.664%), and totally disappeared at 1200°C (0.004%), as was also observed under He atm after 1100°C.

XANES was used to determine the oxidation of U cations and the corresponding molar fractions. The O/U ratios were ultimately derived. The XANES spectra at the U-L_3 edge (Fig. 6.10) showed a trend with increasing temperature and as x decreased (UO_{2+x}). The peak of the WL shifted slightly to lower energies and increased in intensity, and the oscillations within the XANES regions slightly increased. The amplitude decreased with the increasing temperature of thermal treatment showing a relative higher structural order of these samples. However, for the three samples studied (as-produced (RT), 600°C and 1200°C), there was a significant difference of shape compared to the $U^{IV}O_2$ reference, i.e. presence of a shoulder on the high energy side of the edge. This was in agreement with the observed decrease of WL amplitude with the increasing temperature. The shoulder decreased with temperature meaning that there was less U^{VI} or that the U^{IV} bulk was more visible as it size increased. A clear shift (further for the RT sample) of the absorption edge and WL-peak to higher energies, as well as a broader WL was observed. Not even the spectra for the $U^{IV}O_2$ reference and the annealed sample at 1200°C, were similar, indicating that the electronic structure of the 12 nm UO_2 was still not $U^{IV}O_2$.

In the accurate XAS study of the UO_{2+x} system by [Conradson et al., 2005b], [Conradson et al., 2005a], it is shown that the U-L_3 absorption edge energy is relatively insensitive to the hyperstoichiometry, x, and is not a simple way to determine the oxidation state. In this study they point out that the energy of the peak increases by 0.5 eV, as x reaches 0.2. Also a possible effect on the WL due to the size of nc-UO_2 samples could be present in the obtained results. This effect could not be quantified without a dedicated study with nano materials with exactly the same stoichiometry but with different size. That was, at this moment not possible with the synthesized nc-UO_2 where just one-size samples where synthesized and different particle sizes were obtained by treatment at temperature. Under this treatment, not just a change in size occurred, but also a change in valence, even under inert atmosphere (Fig. 6.9). So, in principle, because of this size effect, determining the O/M from the shift is not straight forward but it was the only option at that time.

Another route to study this effect, could be the use of a nano-material with a unique valence state i.e. thorium dioxide (ThO_2). From the synthesized nc-ThO_2 (Sec. 4.4.1.2), different sizes could be obtained under thermal treatment without

changing the valence of the material. ThO_2 can only exist in one oxidation state, Th^{IV}, and is eliminated all discussion on the influence of the O/M ratio on the results obtained. Any changes in the XANES, would be just due to the size of the particles.

In this work, a study of the as-produced nc-ThO_2 (Chap. 4) was also done. Just one size nanoparticles (about 1 nm) was analysed because of the small quantity of material available at the time of the XAS study. The normalized XANES spectra and the first derivate at the Th-L_3 absorption edge of nc-ThO_2 at RT together with the reference spectra of $Th^{IV}O_2$ are shown in Fig. 6.12. The associated energies of the inflection point at absorption edge and of the WL, as well as the energy shift (ΔE) and the estimated oxidation states derived from this study, are given in Table 6.2. In the XANES spectra at the Th-L_3 edge, the peak of the WL corresponding to nc-ThO_2 at RT (as-produced) had an identical position and amplitude as the one for the reference spectra of $Th^{IV}O_2$-bulk. Corroboration by XRD was also obtained (lattice constant of a=0.5579(1) nm) vs. a=0.560 nm for the ThO_2 standard).

This identical behaviour suggested that the displacements observed for nc-UO_2 were not due to the size of the particles, rather the valence. Slightly less intensity for the peak of the WL was observed, as well as less oscillations for the nc-ThO_2. So for this point, one could think there might be a small size effect on the interatomic distance and ordering. The size effect observed for the nc-ThO_2 as-produced was less than that observed for nc-UO_2 (as produced, 600°C and 1200°C) with bulk-$U^{IV}O_2$. So even if there might be a small size effect, the valence might be the major cause for the differences observed with bulk-$U^{IV}O_2$, also confirmed by the lattice contraction by XRD (0.5432 nm and 0.5461 nm at 600°C and 1200°C, respectively). Having that into account, determining the O/M from the XANES shift would be justified.

Table 6.2: Results from the analysis of the ThO_2 at the Th-L_3.

	lattice param. (Å)[a]	**inflection point** (eV)	**energy WL** (eV)	**ΔE**[b] (eV)	**U valency** (V_U)	**molar fraction Th^{IV}** (%)[c]	**O/M**
Reference:							
ThO_2	5.599(0)	16295.6	16300.1	-	4.00	100	2.000
Sample:							
nc-ThO_2 1 nm RT	5.579(1)	16295.6	16300.1	-0.3	4.00	100	2.000

a.) by XRD. b.) ($\Delta E = WL_{sample}$ - $WL_{ref.}$).

In the k^3-weighted EXAFS spectra of the UO_2 samples (Fig. 6.11), the oscillations and their amplitude slightly increased with thermal treatment. The 5 nm as-precipitated sample was very difficult to fit with a pure fluorite structure, as the fit were non stable and the data noisy. The intensity of the FT (Fig. 6.11) was also very low. According to the shape of the first FT peak, it looked like there were two or three U-O distances instead of one. This is consistent with the observed lattice contraction (0.5431 nm) from XRD at RT (Table 6.1). Also samples treated at 600°C and 1200°C presented a high degree of disorder, as it was already predicted from the XANES analysis (Table 6.1). Therefore a good fit could not be achieved considering only bulk-$U^{IV}O_2$, meaning that another phase or considered disorder must be taken into account.

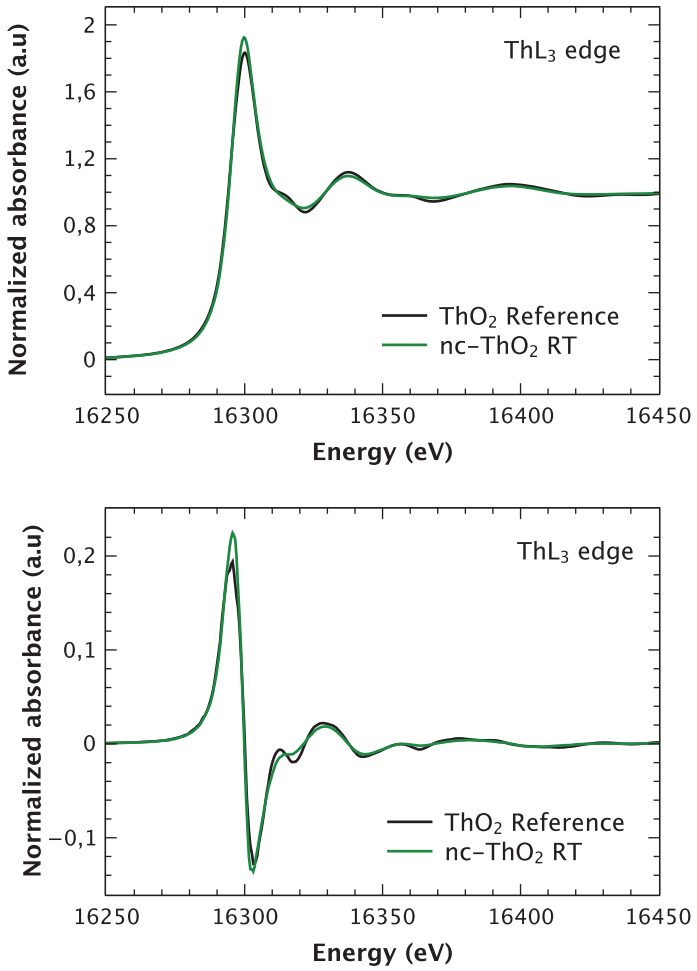

Figure 6.12: Normalized absorption XANES spectra and the first derivate at the Th-L_3 edge of nc-ThO_2 at RT together with the reference spectra of bulk $Th^{IV}O_2$.

Chapter 7

nc-UO_2 monolith consolidation and characterization

7.1 Introduction and principles.

The fabrication of dense ceramic parts with submicrometer grains and perfect microstructures is one of the most challenging objectives in modern ceramic technologies. According to novel findings, a microstructure with submicrometer grains in materials offers clear advantages over the traditional large-grain microstructure for applications under conditions of severe mechanical stress as those valid for nuclear fuel ceramic pellets in the core of a nuclear reactor (LWR). For the study and verification of such possible exceptional properties in nuclear fuel pellets the fabrication of fully dense nanostructurated ceramics and their thorough testing are hence required.

In the manufacture of the LWR-fuel pellets a standard density of 90-95% must be achieved to satisfy design requirements. The traditional way to obtain such dense ceramic bodies is conventional uniaxial pressing of the powdered raw material (e.g. using a hydraulic press), followed by high-temperature sintering. In the prior pressing step a green density of 45-55% is normally achieved. To reach the 90-95% density a posterior thermal treatment is normally carried out, where the pellet is submitted to 1600 °C during a time of up to 18 h. This procedure could not be followed in the synthesis of pellets with the nc-material because the grain size would dramatically grow whereas the objective is to produce a pellet with grain size between 100-200 nm as it appears in the rim (HBS) structure.

Therefore several routes for the consolidation and densification (sintering) into green bodies were tested. Nanocrystalline uranium oxide ceramics of high homogeneity and nearly theoretical density were prepared. The starting 4-5 nm UO_2 material was synthesized by two different methods. Controlled precipitation in aqueous media (see Chap. 3) and thermal decomposition in organic media (see Chap. 4). After consolidation of the green bodies, controlled sintering followed. The structure and properties of the final nc-UO_2-monolithic ceramic was determined by optical, mechanical and thermophysical techniques.

7.2 Compaction methods

Different alternative routes for consolidation of powder into green bodies have been tested and are briefly presented in the following sections.

7.2.1 Conventional uniaxial pressing

In conventional uniaxial pressing an axial force of up to several kN is applied onto a column of loose (as poured) powder contained in a steel-die (usually of circular section with diameter $\leq$ 1 cm) to form a pellet. The nc-UO_2 powder was first crushed by hand in a mortar for 15 min before compaction into pellets was made at different pressing forces (between 9 and 23 kN). A hard hydraulic press (PW 10 ES-Servo electro-hydraulic bi-directional press) and a steel-die with diameter of 6.5 mm were used for this purpose (Fig. 7.1). Before the pressing the nc-UO_2 monoliths, a specimen just Zn-stearate was pressed to lubricate the die-walls. No Zn-stearate was added to the nc-UO_2. The Zn-stearate is normally used as lubrication of the die-walls to avoid the breaking of the pellet during compaction.

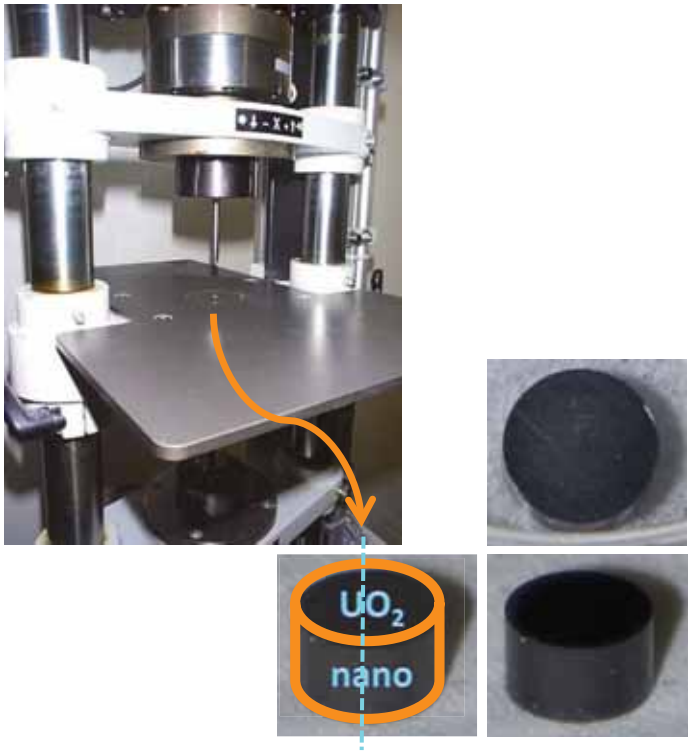

Figure 7.1: Hydraulic press (ITU) and nc-UO_2 green pressed pellet.

Monoliths between 6.24-6.33 mm in diameter and height between 1.58-3.70 mm were obtained. Their green (geometrical) densities were calculated by weighing and measuring the geometry of the pressed pellets. The theoretical densities (TD) were calculated in percentage of the bulk-UO_2 (large-grain or micron-size-grain) (TD_{UO_2}=10.96 g/cm^3). A maximal green density of 55% TD was achieved at 23 kN (see Fig. 7.2).

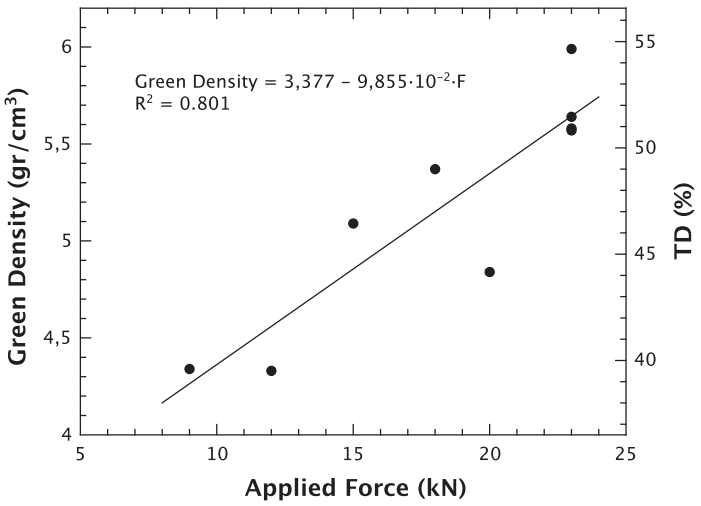

Figure 7.2: Green density and theoretical density (TD) of the nc-UO_2 pressed pellets vs. applied force.

7.2.2 Float-packing

The uniform packing of particles within green bodies of non-sintered or non-thermally treated is a critical precondition for the preparation of dense, defect-free ceramics with superior optical and mechanical properties. To reach nc-UO_2 green pellets with higher homogeneity than the pellets obtained by the traditional pressing (Sec. 7.2.1), a controlled consolidation and drying by float-packing, according to the published study of [Godlinski et al., 2002], was tested for the nc-UO_2 material from the aqueous precipitation process. For this purpose nc-UO_2 powder from the aqueous method (Chap. 3) was dispersed in bi-distilled water (solution densities ~1 g nc-UO_2/cm^3), using a high power ultrasound device (HD 3200 SONOPLUS Ultrasound-Homogenizer from Bandelin Fig. 7.3a) for 10 min with the aim to break the possible agglomerates in the solution.

The suspension was poured into moulds and the specimens were slowly dried over a period of 8 weeks. At the beginning a random distribution of stabilized nc-UO_2 particles in suspension, was present. With time, sedimentation of bigger and agglomerated particles initiated with the formation of a first layer with the bigger particles at the bottom of the mould meanwhile the small particles stayed in suspension. As water is continuous evaporating the concentration of small particles in suspension increases and their movement is limited up to a point where the compact is formed. Packing of the smallest nc-UO_2 keep on until no water is present in the mould and a thick uniform layer of fine particles is formed over the first layer of larger particles formed at the beginning of the precipitation. The process led to homogeneous green compacts that despite the low drying rates used exhibited cracks in some of the bodies formed. A scheme of the process followed in this work, as from [Godlinski et al., 2002], is shown in Fig. 7.3b.

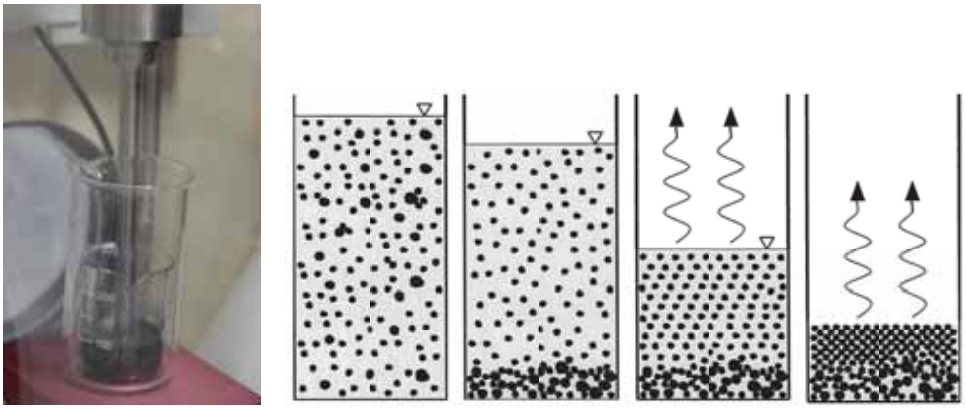

(a) (b)

Figure 7.3: a.) Dispersion of nc-UO_2 in water with homogenizer. b.) Representation of the float-packing process taken from [Godlinski et al., 2002].

7.3 Characterization of the nc-UO_2 monoliths.

The structure and morphology of the obtained products by the previous consolidation processes were characterized by means of optical microscopy (OM), X-ray diffraction (XRD) and scanning electron microscopy (SEM).

7.3.1 Green Specimens.

7.3.1.1 Conventional pressed pellets of nc-UO_2 from aqueous route. With/without thermally pre-treated powder.

The nc-UO_2 material from the aqueous precipitation route was pressed with and without thermal pre-conditioning. The pre-treatment of the powder at specific temperature was an attempt to avoid possible cracks due to the evaporation of the possible trapped water in the material during the sintering step. The nc-UO_2 powder was calcined at 400°C under Ar/5%H_2 atmosphere with heating and cooling rates of 200°C/h, while the holding-time at maximum temperature was 1.5 h (Fig. 7.10). After calcination the powder was crushed in an agate mortar to break the possible agglomerates and was further comminuted by hand for 15 min to further diminish and homogenize the particle size. A picture of a green pellet obtained by pressing from this powder is shown in Fig. 7.4. A stable structure and a smooth surface was observed. A typical microstructure of this kind of pellet is shown in Fig. 7.5.

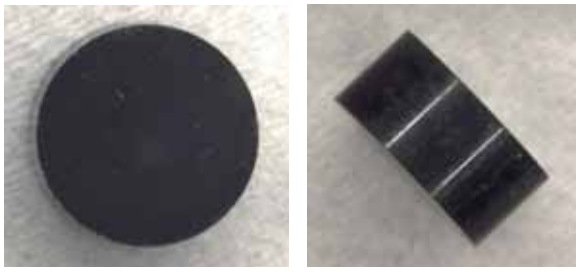

Figure 7.4: Green pellet of nc-UO_2 from aqueous route obtained by conventional uniaxial pressing.

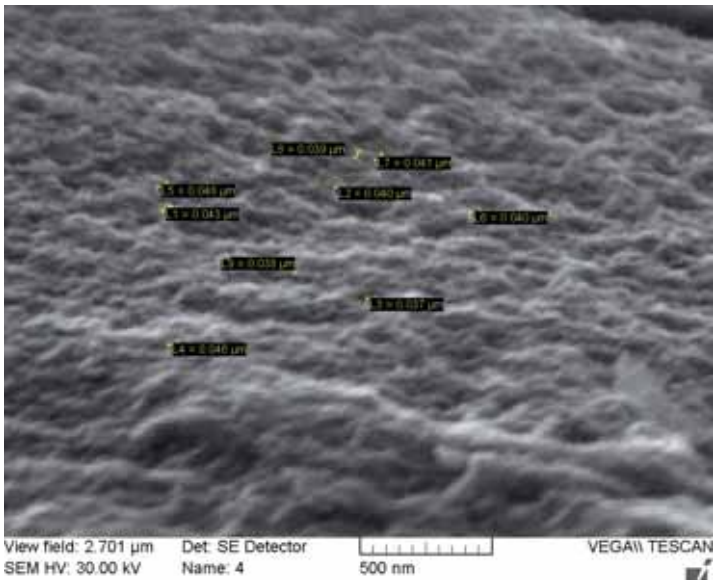

Figure 7.5: Typical microstructure of conventional pressed nc-UO_2 green pellet.

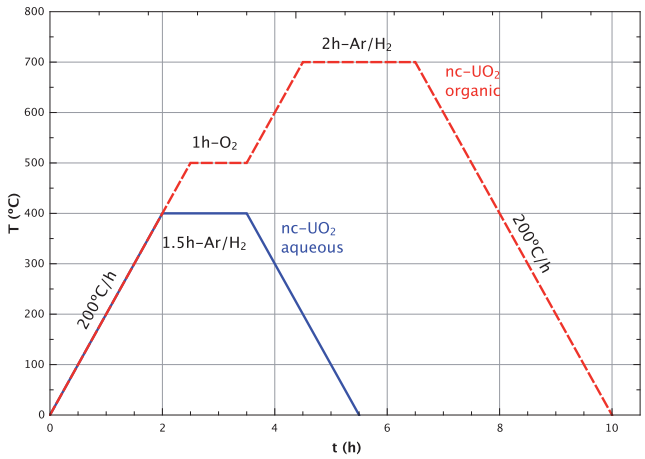

Figure 7.6: Schematic calcination steps for nc-UO_2 powders from aqueous and organic routes.

7.3.1.2 Float packing consolidation of nc-UO_2 from aqueous route in pellet form.

A picture of a green pellet of nc-UO_2 from aqueous route, consolidated by float packing as described in Sec. 7.2.2 is shown in Fig. 7.7. A smoother surface was observed in these kind of pellets. The microstructure appeared much more homogeneous than in the pellets consolidated by pressing (Sec. 7.3.1.1).

7.3.1.3 Conventional pressed pellet of nc-UO_2 from organic route. Thermally pre-treated powder.

The nc-UO_2 from organic route was pressed after thermal pre-conditioning. The treatment at temperature of the powder was aimed to make it free from possible adsorbed organic compounds from the preparation process, which could provoke cracks during their pyrolysis in the sintering step when the porosity of the ceramic becomes

Figure 7.7: Green pellet of nc-UO_2 from aqueous route obtained by float packing consolidation.

closed. The nc-UO_2 powder was calcined in two steps in an oven (Linn tube furnace). The first heating was made at 500°C under O_2 during 1 h to burn the organics. At this temperature the organics are presumable gone as the thermogravimetric graph has shown (Fig. 6.1). The second heating was made at 700°C 2 h under Ar/5%H_2 to reduce again the possible oxidated UO_2-material layer created in the first calcination step. Heating and cooling rates of 200°C/h were used (Fig. 7.6). After calcination the powder was crushed in an agate mortar (see Fig. 7.8) to break the agglomerates. The powder was ground by hand for 15 min to further reduce and homogenize the particle size. The powder was then pressed to pellet form under the conditions described in Sec. 7.2.1. A picture of a green pellet of nc-UO_2 from organic route obtained by this method is shown in Fig. 7.9. A tough structure and a smooth surface were observed.

Figure 7.8: Mortar with thermally treated nc-UO_2 powder from organic route.

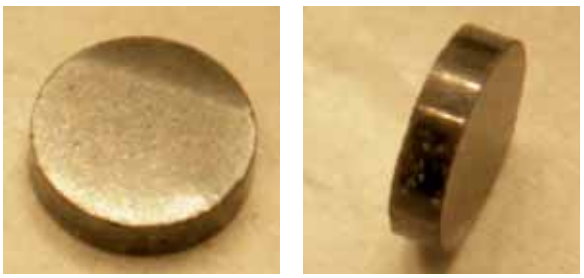

Figure 7.9: Green pellet of nc-UO_2 from organic route obtained by conventional uniaxial pressing.

7.3.2 Sintered of the nc-UO_2 green bodies.

The pellets were sintered in an oven (metal furnace from Degussa (ALD) VSL 10/18) following different thermal profiles but always reaching lower plateau temperature than

the micron-size powder in the sintering of traditional micro grain-UO_2 pellets. For the latter, a treatment at 1600°C during a time of up to 18 h under Ar/5%H_2 is applied to guarantee a high density of the final sintered pellet. These high temperatures and long times would increase tremendously the size of the nanocrystalline material. Therefore milder conditions were tested.

The nc-UO_2 green pellets from aqueous and organic routes prepared by conventional uniaxial pressing (Sec. 7.2.1) were heated for 1 h at 600°C and sintered at 1200°C during 4 h. Heating and cooling rates of 200°C/h, as well as reducing dynamic Ar/5%H_2 atmosphere (Fig. 7.10) were employed. Some pictures of nc-UO_2 pressed pellets of powders from the aqueous and organic routes are shown in Fig. 7.11 and Fig. 7.12, respectively. The pellets sintered presented a strong appearance although fine cracks were visually observable in some cases. Sintering densities between 75.5-90.5% of the theoretical density (TD_{UO_2}=10.96 g/cm^3), were obtained.

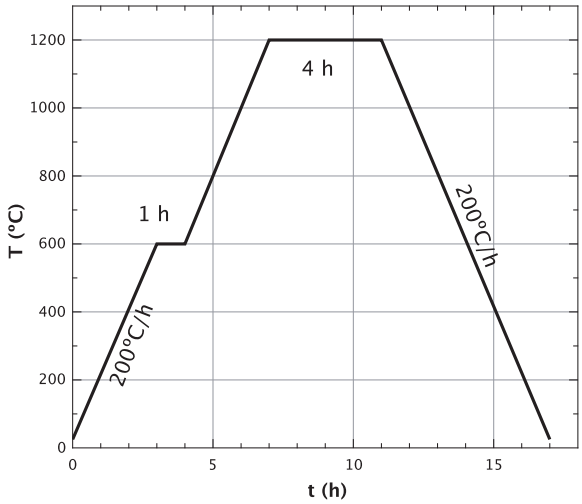

Figure 7.10: Schematic program for two-step sintering under Ar/5%H_2 atmosphere.

For the nc-UO_2 green pellets from float-packing (Sec. 7.2.2), a mild thermal treatment was used to achieve densification of the samples. In this case, no powder thermal pre-treatment was done because firmly consolidated green monoliths were already formed from the fluid by this process. Therefore a solely calcination and sintering program was applied. The monoliths were heated in various steps at different rates: namely from 20°C to 300°C with a rate of 15°C/h, then from 300°C to 600°C with a rate of 30°C/h and finally from 600°C to 1200°C with a rate of 150°C/h. The two first steps with slow heating rates were designed to smoothly release the residual water. During the last step with fast heating rate and plateau at 1200°C for 4 hours, final sintering was achieved. Cooling down from high temperature to room temperature was done in a unique step at rate 150°C/h (Fig. 7.13). Ar/5%H_2 atmosphere was used in this step. This oven heating profile with the first two slow steps had the aim to let the water still present in the monoliths to slowly evaporate, but also to avoid possible cracks which might occur by internal overpressure if faster heating ramps were applied. The heating profile used for the conventional pressed pellets (see Fig. 7.10) was also here tested, but the final macrostructure of the samples was of much poorer quality.

Complementary dilatometry (characteristics in Sec. 2.6) experiments were per-

Figure 7.11: Aqueous route nc-UO_2 sintered pellet.

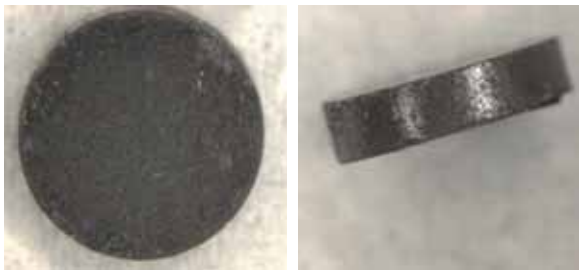

Figure 7.12: Organic route nc-UO_2 sintered pellet.

formed to compare the shrinkage of the fabricated nc-UO_2 pellet with that of bulk-UO_2 [Lahiri et al., 2006] produced by a standard fabrication process (large grain). The resulting relative linear shrinkage for the two kinds of materials as a function of temperature is represented in Fig. 7.14. The experiment was carried out using a heating rate of 0.5°C/min up to 1100°C for nc-UO_2 (1°C/min up to 1700°C for bulk-UO_2 [Lahiri et al., 2006]). In the picture it is seen that the shrinkage profile as a function of temperature for the nc-UO_2 material is shifted by 587°C towards lower temperatures compared to that of standard bulk UO_2. This describes the overwhelming sintering activity, triggered by the specific area, of the nanocrystalline oxide.

The dilatometry curves show that the nc-UO_2 starts indicating remarkable shrinkage already at very low temperatures as low as 200°C, with the maximum sintering rate being shown at around 740°C. Two sintering steps are observable. At first step up to 720°C with a weight lose of 12.3%. A second step up to 955°C with a weight lose of 9.1%(total weight lose of 21.4%). These maximum and final sintering temperatures are clearly much lower than those observed for the bulk-UO_2, which shows the sintering onset at temperatures about 900°C and the maximum sintering rate at about 1200°C. The total weight lose was here of 16.5%. Also the temperature range from onset to completion of the densification occurred at much more lower temperatures for the nc-UO_2 (200-955°C), compared to the bulk-UO_2 [Lahiri et al., 2006] (900-1540°C).

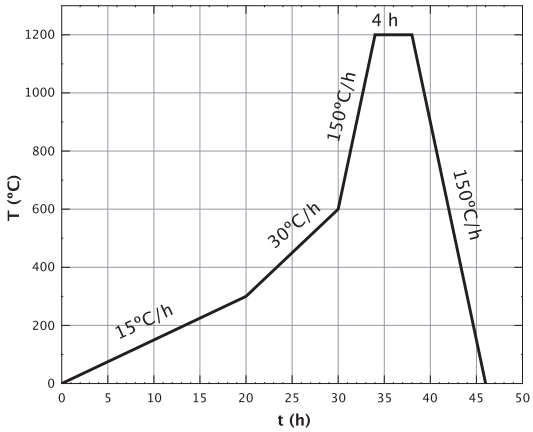

Figure 7.13: Schematic heating program for slow calcination and sintering under Ar/5%H_2 atmosphere.

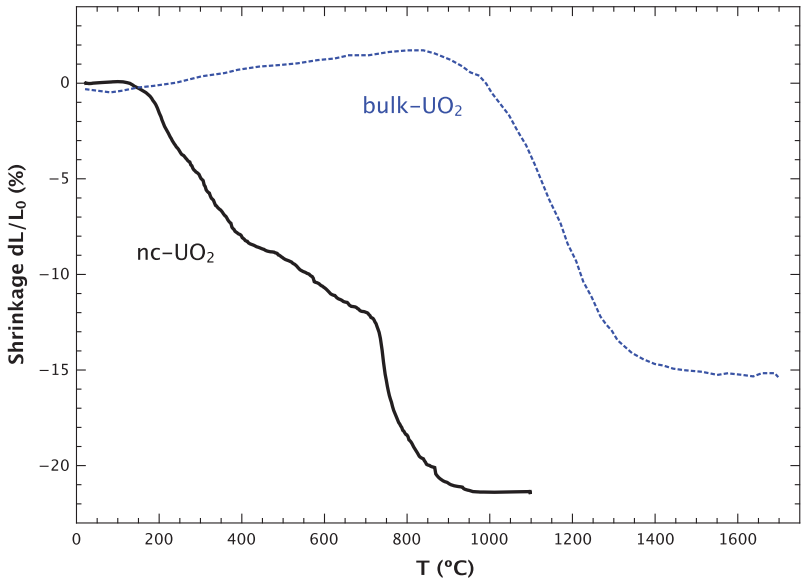

Figure 7.14: Relative linear shrinkage and its derivative of the nc-UO_2 ceramic as a function of temperature. Comparison with bulk-UO_2 taken from [Lahiri et al., 2006].

Likewise the sintering activation energy for nc-UO_2 pellet by conventional compaction method performed (Sec. 7.2.1) and sintered in oven under Ar/5%H_2, has been determined using the dilatometer data presented in Fig. 7.14. The Young and Cutler non-isothermal method [Young and Cutler, 1970] was applied according to Eq. 7.1, where n is a constant characteristic for the shrinkage mechanism, Q is the apparent activation energy for densification, $\Delta L/L_0$ is the shrinkage, R is a constant of value 8.314472 $JK^{-1}mol^{-1}$, while T in that case is a function of time $T(t)$. The Arrhenius plots obtained for the nc-UO_2 and bulk-UO_2 are presented in Fig. 7.15.

$$\frac{\Delta L/L_0}{T} = const \cdot e^{\frac{-nQ}{RT}} \tag{7.1}$$

Taking in Eq. 7.1 the value $n = 1/3$ as characteristic for the sintering step dominated by grain boundary diffusion, the sintering activation energy was determined as $Q = 171 \pm 7\ kJ/mol$ for the nc-UO_2 monolith ($Q = 287\ kJ/mol$ for bulk-UO_2 [Lahiri et al., 2006]). The characteristic temperature ranges where the densification mechanisms were activated differed considerably between nc-UO_2 and the reference bulk-UO_2. This critical temperature range is 720-740°C for nc-UO_2, as compared with that of 950-1200°C for bulk-UO_2 (Fig. 7.15).

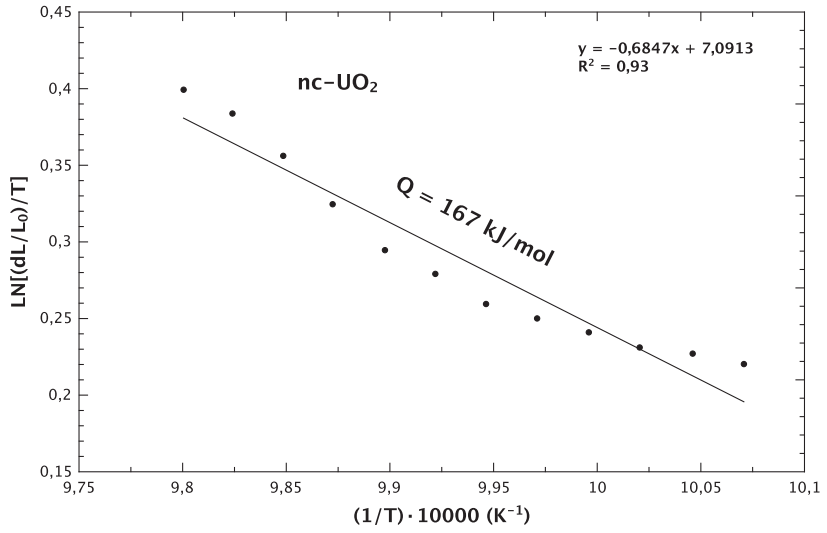

Figure 7.15: Arrhenius plot of the initial densification stages for a nc-UO_2 by conventional compaction pressed and sintered in oven under Ar/5%H_2.

The grain boundary diffusion ($n = 1/3$) is the the mostly accepted diffusion mechanism for the initial stage of densification. However, other diffusional mechanisms may be also active during this initial sintering stage, as $n = 1/2$ which takes into account the volume diffusion for the sintering activation. The energy value for this coefficient for the nc-UO_2 monolith was determined as $Q = 114 \pm 5\ kJ/mol$.

7.3.3 Macro and microstructural characterization of the nc-UO_2 monoliths.

Characterization of macrostructures by optical microscopy (OM), and microstructures by fresh-fracture observation by scanning electron microscopy (SEM), for the different samples at different magnifications are in Table 7.1 summarized and images in the following presented. The instrument used for SEM, as well as the preparation of the samples, are described in Sec. 2.3.1. A *fcc* fluorite structure (*Fm-3m* space group) with a lattice parameter of 0.5470(0) nm has been found for all nc-UO_2 monoliths.

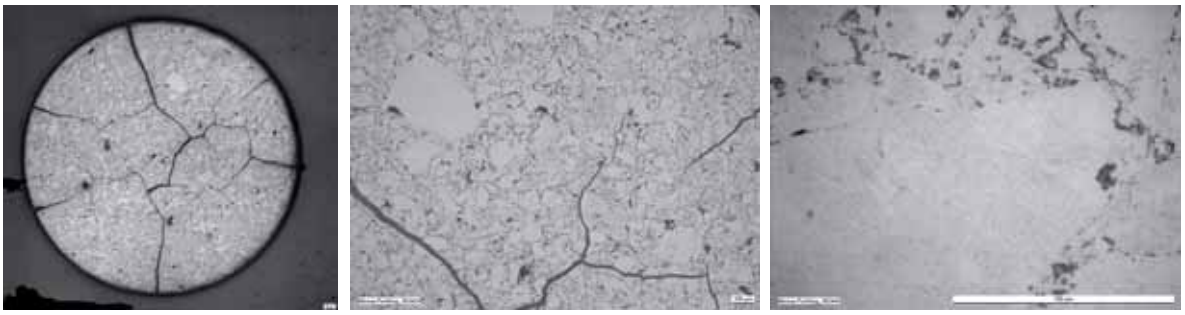

Figure 7.16: *Aqueous-Pressed*. Macrostructure of conventional-pressed and sintered (1200°C) pellet from the aqueous route nc-UO_2-powder. The scale bar is 100 μm.

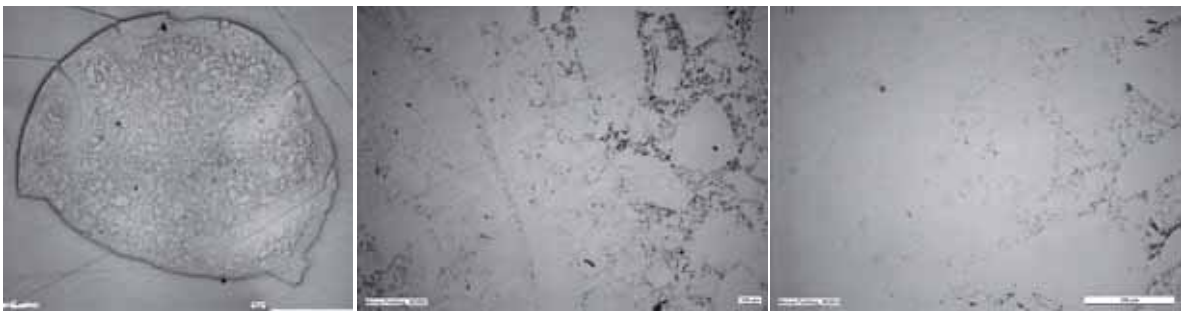

Figure 7.17: *Aqueous-Pressed-PTT*. Macrostructure of conventional-pressed and sintered (1200°C) pellet from the aqueous route nc-UO_2-powder. Previous thermal treatment for dehydration of the nc-UO_2 powder before pressing, was done. The scale bar is 100 μm.

The macrostructure-view for the four different nc-UO_2 microstructures indicates that aqueous-route-powder monoliths produced by float packing consolidation (*Aqueous-Float Packing* - Fig. 7.19) show better structure uniformity. The conventional-pressed monoliths from organic-route-powder (*Organic-Pressed-PTT* - Fig. 7.22; where *PTT* means previous Powder Thermal Treatment), show the best performance from the point of view of sintering cracks, as well as a strong structure. Looking at the quality, the conventional-pressed monoliths of pre-dehydrated powder from the aqueous route (*Aqueous-Pressed-PTT* - Fig. 7.17) present few cracks in the pellet rim, but also a strong structure. In the case of the conventional-pressed monoliths of the aqueous-route-powder without dehydrating pre-treatment (*Aqueous-Pressed* - Fig. 7.16), many of macrocracks across the whole sample are present. Similar theoretical densities were observed, being higher (about 90%) for the *Aqueous-Float Packing* and the *Organic-Pressed-PTT* (Table 7.1) pellets.

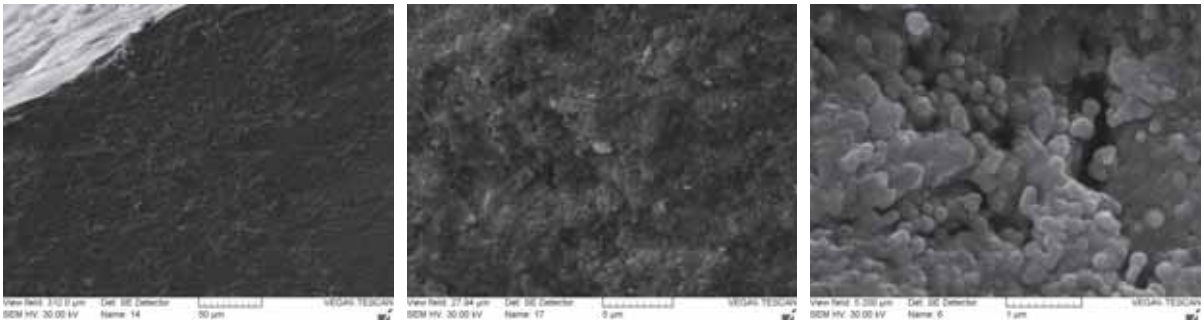

(a) The scale bar is 50 μm. (b) The scale bar is 5 μm. (c) The scale bar is 1 μm.

Figure 7.18: *Aqueous-Pressed-PTT*. Fresh-fracture microstructure of conventional-pressed and sintered (1200°C) pellet from the aqueous route nc-UO_2-powder. Previous thermal treatment for dehydration of the powder before pressing, was done.

Figure 7.19: *Aqueous-Float Packing*. Macrostructure of float packed consolidated and sintered (1200°C) pellet from the aqueous route nc-UO_2-powder. The scale bar is 100 μm.

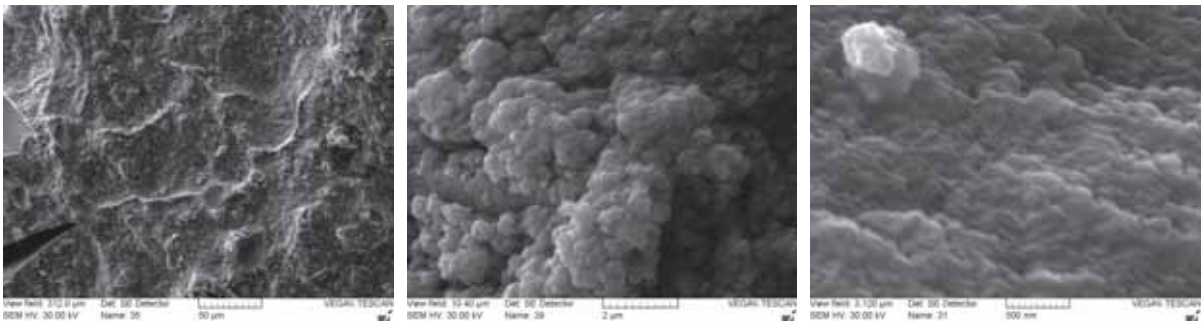

(a) The scale bar is 50 μm. (b) The scale bar is 2 μm. (c) The scale bar is 500 nm.

Figure 7.20: *Aqueous-Float Packing*. Fresh-fracture microstructure of float packed consolidated and sintered (900°C) pellet from the aqueous route nc-UO_2-powder.

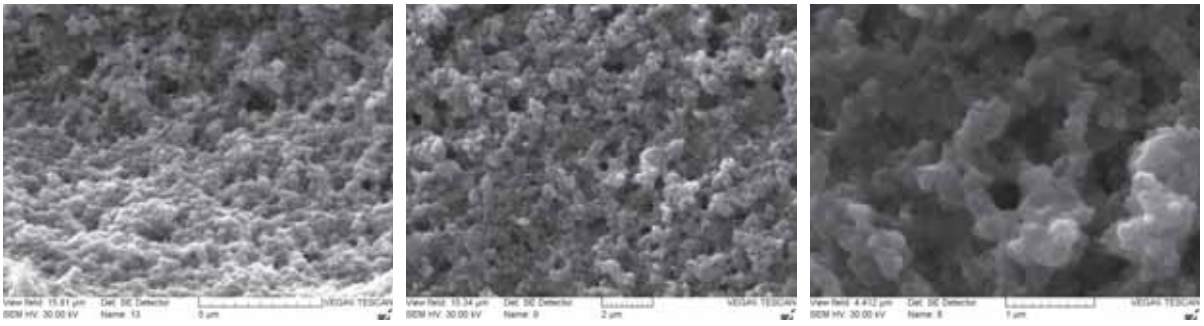

(a) The scale bar is 5 μm. (b) The scale bar is 2 μm. (c) The scale bar is 1 μm.

Figure 7.21: *Aqueous-Float Packing*. Fresh-fracture microstructure of float packed consolidated and sintered (1200°C) pellet from the aqueous route nc-UO_2-powder.

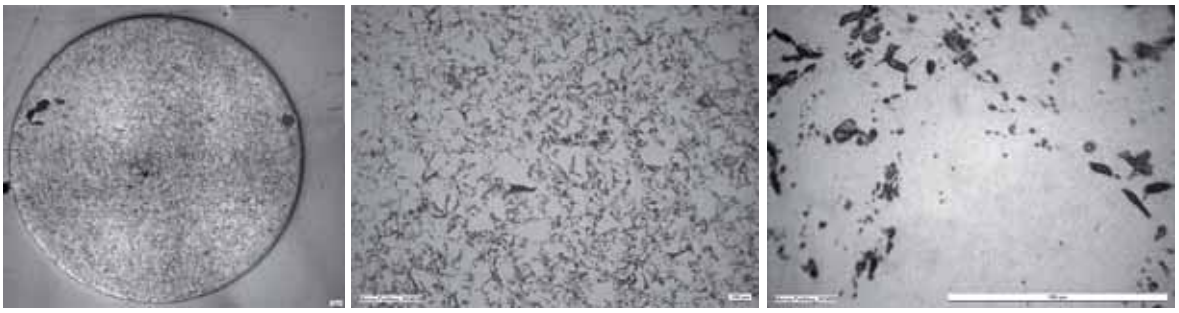

Figure 7.22: *Organic-Pressed-PTT*. Macrostructure of conventional pressed and sintered (1200°C) pellet from the organic route nc-UO_2-powder. Previous thermal treatment for burning of the capping organics before pressing, was done. The scale bar is 100 μm.

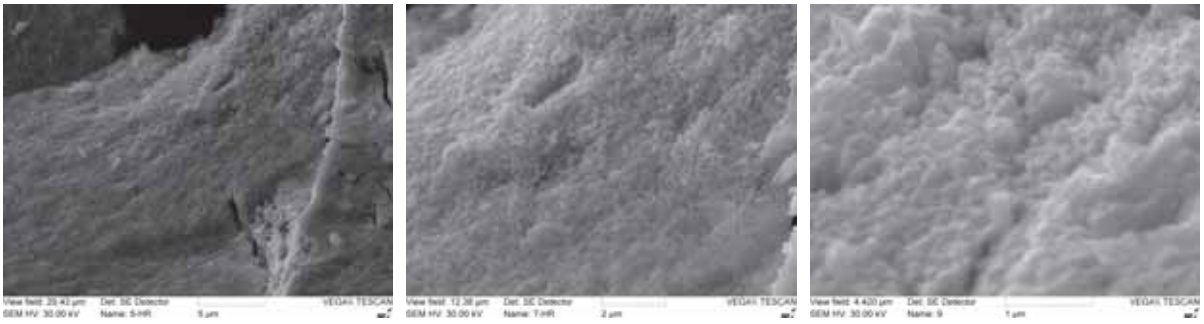

(a) The scale bar is 5 μm. (b) The scale bar is 2 μm. (c) The scale bar is 1 μm.

Figure 7.23: *Organic-Pressed-PTT*. Fresh-fracture microstructure of of conventional pressed and sintered (1200°C) pellet from the organic route nc-UO_2-powder. Previous thermal treatment for burning of the capping organics before pressing, was done.

Table 7.1: Characterization of macro- and microstructures of the different types of nc-UO_2 monoliths.

nc-UO_2 monoliths	**Powder thermal pre-treatment**[a]	**Compaction**[b] **type**	**Sintering**[c] **profile**	**TD(%)**[d]	**Macrostructure OM**	**Microstructure SEM**	**Grain Size**[e] (nm)
Aqueous[f]**-Pressed**	-	conventional (23 kN)	1200°C-4h Fig. 7.10	81	Fig. 7.16	-	-
Aqueous[f]**-Pressed-PTT**[h]	400°C-1.5h	conventional (23 kN)	1200°C-4h Fig. 7.10	87	Fig. 7.17	Fig. 7.18	212(47) nm
Aqueous[f]**-Float Packing**	-	float packing	900°C-4h Fig. 7.13	-	-	Fig. 7.20	-
Aqueous[f]**-Float Packing**	-	float packing	1200°C-4h Fig. 7.13	90	Fig. 7.19	Fig. 7.21	197(25) nm
Organic[g]**-Pressed-PTT**[h]	500°C-1h + 700°C-2h	conventional (23 kN)	1200°C-4h Fig. 7.10	91	Fig. 7.22	Fig. 7.23	202(34) nm

a.) Powder thermal pre-treatment profile in Fig. 7.6. b.) Conventional uniaxial pressing (Sec. 7.2.1), float packing (Sec. 7.2.2). c.) Different profiles were used independently of the final temperature. Sintering under Ar/5%H_2. d.) TD_{UO_2}=10.96 g/cm^3. e.) SEM pictures average grain size. f.) Powder from the aqueous route (Chap. 3). g.) Powder from the organic route (Chap. 4). h.) Previous powder thermal treatment (PTT).

All macrostructures, with exception of the *Aqueous-Float Packing* (Fig. 7.19), show non-homogeneous densification (residual porosity between densified areas). The *Aqueous-Pressed-PTT* (Fig. 7.17) pellet presents also a good quality in comparison to rest, from the point of view of the densification. This kind of pellet shows the lowest proportion of residual porosity and largest size of the dense areas (>300 μm). The structure homogeneity of the pellet *Aqueous-Float Packing* (Fig. 7.19) could help to elucidate the origin of the highly dense areas surrounded by residual porosity seen in the pressed pellets. As the *Aqueous-Float Packing* pellet was compacted without help of external pressure, we can exclude in this case the existence of pressure-induced green-density heterogeneities.

Nevertheless, the optical microscopy can only say something about the supra-micron range. It is also important to understand the highly dense and more porous regions with the study of the microstructure by SEM to see which kind of structure stays behind. Looking at the grain-structure of the fresh fracture by SEM, all samples show grains about 200 nm (100 nm to 250 nm are the typical values observed for the HBS; see Chap. 1) in the dense areas (Table 7.1). The dense areas are not single grains as it can be observed in the SEM images. The temperature was too low for that.

The SEM images from the *Aqueous-Pressed-PTT* pellet (Fig. 7.18), show a pretty homogeneous grain structure in contrast with the large inhomogeneities showed in its OM images (Fig. 7.17). The grains are acceptably small (average grain size of 212(47) nm) throughout the whole sample section. There is no indication of exaggerated grain growth, as a priori suggested from the OM-pictures (large dense islands). However, the grains do not look well joined. Micro-porosity and somewhat loose grains, separated by tiny cracks, are visible. It may be possible that the islands in the OM micrograph arose from the compaction or sintering preparation. Perhaps pull-out may have been an issue.

For the *Aqueous-Float Packing* pellet, two different sintering temperatures were analysed. In the fresh fracture SEM images of the pellets sintered at low temperature of 900°C (Fig. 7.20), not well defined grains are observable. The sinter of the crystals is still under development. For the nc-UO_2 pellet under the same method of preparation (*Aqueous-Float Packing*) and sintered at 1200°C (Fig. 7.21), the fresh fracture SEM pictures show an striking tendency to form apparently closed pores. The pores, probably steaming from still removal of water and others, are smaller than in the typical HBS, but closed likewise in this zone in irradiated pellets. An average grain size of 197(25) nm was here determined.

The fresh-fracture micostructure images from the *Organic-Pressed-PTT* pellet (Fig. 7.23), show an homogeneous grain structure. Micro-porosity as well as not well joined grains are here also observable. Grain sizes in the 200 nm range were here found (average grain size of 202(34) nm).

7.3.4 Results and discussion.

Nanocrystalline uranium oxide ceramics with nearly full density have been prepared. The starting 4-5 nm UO_2 material was synthesized by the two different methods. A controlled precipitation in aqueous media (see Chap. 3) and a thermal decomposition in organic media (see Chap. 4). All materials had narrow particle-size distribution.

Different alternative routes for consolidation (e.g. conventional uniaxial pressing, float packing) into green bodies have been tried (Sec. 7.2). Afterwards the green bodies were sintered at temperatures between 900°C and 1200°C (Sec. 7.3.2).

Complementary dilatometry experiments were performed to compare the shrinkage of the fabricated nc-UO_2 pellet with that of bulk-UO_2 produced by a standard fabrication process (large grain). The temperature range from onset to completion of the densification occurred at much more lower temperatures (Fig. 7.14) for the nc-UO_2 (200-955°C, with a maximum sintering rate at 740°C), compared to the bulk-UO_2 [Lahiri et al., 2006] (900-1540°C, with a maximum sintering at 1200°C). The reason of that might be the higher surface present in the nc-UO_2 compared with the bulk-UO_2 material, rendering the sintering to become more effective (at lower temperatures).

Likewise the sintering activation energy for nc-UO_2 pellet by conventional compaction method performed (Sec. 7.2.1) and sintered in oven under Ar/5%H_2, has been determined using the dilatometer data presented. The sintering activation energy was determined as $Q = 171 \pm 7\ kJ/mol$ for the nc-UO_2 monolith ($Q = 287\ kJ/mol$ for bulk-UO_2 [Lahiri et al., 2006]). The grain boundary diffusion ($n = 1/3$), used for the calculation, is the mostly accepted diffusion mechanism for the initial stage of densification. However, other diffusional mechanisms may be also active during this initial sintering stage, as $n = 1/2$ which takes into account the volume diffusion for the sintering activation. The energy value for this coefficient for the nc-UO_2 monolith was determined as $Q = 114 \pm 5\ kJ/mol$.

Characterization of macrostructures by OM, and microstructures by the fresh-fracture observation by SEM, for different samples at different magnifications, was performed. In the *Aqueous-Pressed* monoliths (Fig. 7.16), many of macrocracks across the whole sample were present. The case of *Aqueous-Pressed-PTT* monoliths (Fig. 7.17) presented few cracks in the pellet rim. The risk to create fractures during the sintering of compacted nano-powders because of the rapid closure of the channels and the hindered gas-exhaust, is very common. This tends to occur for green bulks produced from uniaxial pressing of dried particles. However, no macrocracks have been observed on the *Organic-Pressed-PTT* monoliths (Fig. 7.22). All macrostructures, with exception of the *Aqueous-Float Packing* pellet (Fig. 7.19), showed non-homogeneous densification (residual porosity between densified areas). The *Aqueous-Pressed-PTT* pellet (Fig. 7.17) presented also a good quality in comparison to rest, from the point of view of the densification.

The highly dense areas surrounded by residual porosity seen in the conventional pressed pellets after sintering (see *Aqueous-Pressed-PTT*-(Fig. 7.17) and *Organic-Pressed-PTT*-Fig. 7.22), independently of the material used, look similar to the microstructure heterogeneities shown by [Yongvanich et al., 2010]. In that publication a preparation using a similar route (dry pressing and pressureless sintering of calcined nanopowders from precipitation process), was performed. The dense islands seem to arise from the initial steps of the process (e.g. nanopowder conditioning, drying/pre-calcination). It could be that if the raw material is not well dispersed, the agglomerates could affect the sintering or pre-sintering steps.

Looking at the fresh-fracture surfaces, the microstructure of the *Aqueous-Float Packing* pellet sintered at 1200°C under Ar/5%H_2 (Fig. 7.21), was the closest approxi-

mation to the HBS material until now obtained. But also the microstrucutres observed conventional-pressed pellets, *Aqueous-Pressed-PTT* (Fig. 7.18) and *Organic-Pressed-PTT* (Fig. 7.23), could be a suitable option.

The average grain size in the different pellet samples was in the 170-250 nm range. Here a major success of this work was achieved. Also a striking tendency to form closed nanopores from still removal of water or organics (depending on the sample) with size <200 nm, was observable. The pores-size was smaller than the one observed for the HBS ($\sim$1 μm), but likewise in this zone in irradiated pellets, closed. Nanopores can inhibit grain-growth (or pore-drag). Pore-drag is mainly effective for pores with dimension comparable or smaller than the grain size (boundary control). So, an increasing of the pore size should be achieved. However, because of the closed pores, the chances that in such a material under irradiation the fission-gas gets swept and stored into them, are high. That should be proved in-pile experiments.

7.4 Mechanical properties of nc-UO_2.

The mechanical response of final sintered pieces of nc-UO_2 ceramics, was studied via indentation. The expected behaviour was an increase of the mechanical properties of the nc-structure in comparison to larger grain sized monoliths of same composition due to grain size effects, as well as due to the better densification of the nc-pellets. The porosity in the material has an enormous influence in its mechanical properties due the zero participation of the voids to the load-bearing capacity of the material. The estimation of the mechanical properties of a material as e.g. Young's modulus (E) is achievable by different prediction models. These empirical, mechanistic and microstructure-geometry dependent models, are based on supposed ideal structures. Hence, real experimental data obtained from close to ideal and well characterised microstructures are fundamental to validate the assumed suppositions. Mechanical properties as Vickers Hardness (H_V), Knoop Hardness (H_K) and Young's modulus (E) were measured and calculated from Vickers and Knoop indentation for sintered nc-UO_2 pellets obtained by different methods (*Aqueous-Pressed*, *Aqueous-Float Packing* and *Organic-Pressed*). Micro- and macro-structure characterization of these pellets have been described in Sec. 7.3.3. Also scanning acoustic microscopy (SAM) has been used in some of the samples for the estimation and comparison of the Young's E-modulus obtained by indentation. Finally a study by in-situ high pressure X-ray diffraction (HP-XRD) has been performed for the study of a possible bulk modulus dependence of the crystal size dependence in nc-UO_2.

7.4.1 Hardness and Young's modulus of nc-UO_2 monoliths as probed by Vickers and Knoop indentation.

The microindentations were performed as described in Sec. 2.7.1. The evaluation of the indentations was made by optical microscopy. Representative pictures for each load applied of the indentation prints on different nc-UO_2 pellets (*Aqueous-Pressed*, *Aqueous-Float Packing* and *Organic-Pressed*), are shown in Fig. 7.25 and Fig. 7.26 for the Vickers case, and Fig. 7.27 for the Knoop case. Vickers Hardness (H_V) and Knoop Hardness (H_K) (dimensionless) numbers were calculated by Eq. 7.2 and Eq. 7.3,

respectively.

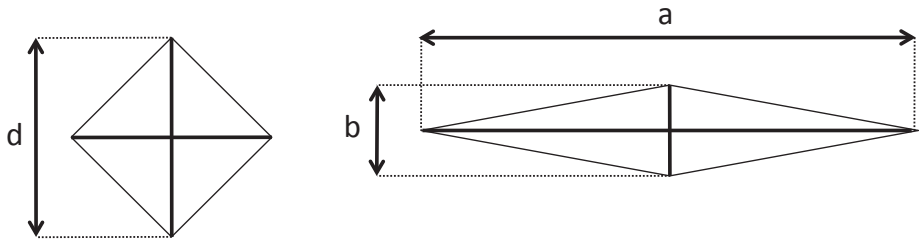

Figure 7.24: Typical Vickers (*left*) and Knoop (*right*) indentations.

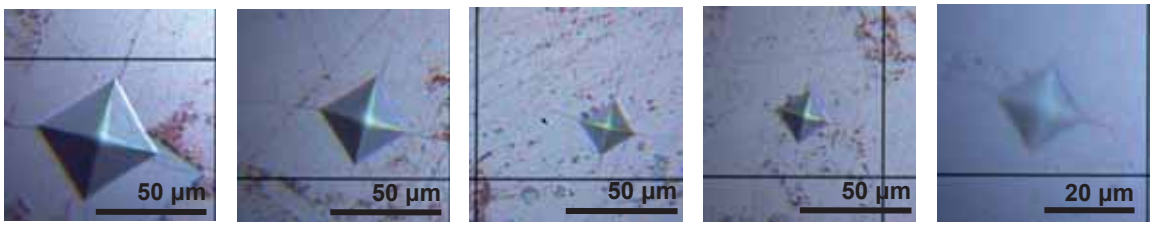

(a) 9.8 N (b) 4.9 N (c) 1.96 N (d) 0.98 N (e) 0.49 N.

Figure 7.25: Vickers indentations at different loads for the nc-UO_2 *Aqueous-Pressed* pellet (Fig. 7.17). Indentations performed with the instrumented indentor.

$$H_V = 0.102 \cdot 1.8544 \cdot \frac{F}{d^2} \tag{7.2}$$

with F (load in N) and d (average diagonal in mm).

$$H_K = 0.102 \cdot 14.229 \cdot \frac{F}{a^2} \tag{7.3}$$

with F (load in N) and a (long diagonal in mm).

The calculated values for H_V (-) and H_K (-) numbers at 9.8 N load, are shown in Table 7.2. Also the average H_V (-) as a function of the different loads used for each kind of monolith, has been represented in Fig. 7.28.

The indentation tests have been used to evaluate the Young's modulus or E-modulus (E) of materials based on the demonstration of [Lawn and Howes, 1981]. The extent of the elastic recovery during unloading after indentation is proportional to the $\left(\frac{H}{E}\right)_K$ ratio of the material, where H is the corresponding Knoop hardness.

For the asymmetric Knoop pyramid indenter (see Fig. 7.24), where a = long diagonal, b = short diagonal and $a = 7.11 \cdot b$, the relation 7.4 has been verified (with $\frac{b'}{a'}$ = ratio of the remaining imprint diagonals and $\alpha = constant$) [Marshall et al., 1982].

$$\frac{b'}{a'} = \frac{b}{a} - \alpha \cdot \left(\frac{H}{E}\right)_K \tag{7.4}$$

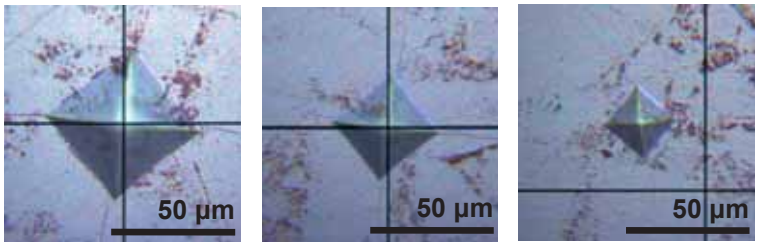

(a) Aqu.-Press. 9.8 N (b) Aqu.-Press. 4.9 N (c) Aqu.-Press. 1.96 N

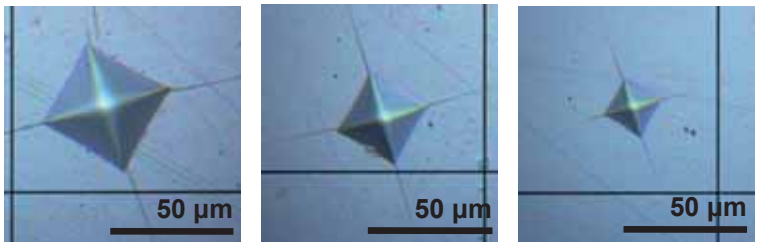

(d) Aqu.-F.Pack. 9.8 N (e) Aqu.-F.Pack. 4.9 N (f) Aqu.-F.Pack. 1.96 N

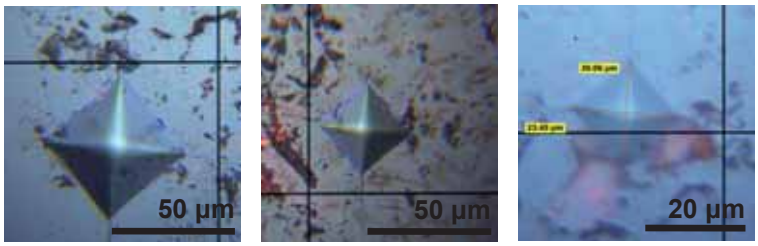

(g) Org.-Press. 9.8 N (h) Org.-Press. 4.9 N (i) Org.-Press. 1.96 N

Figure 7.26: Vickers indentations at different loads for three kind of nc-UO_2 pellets (Table 7.1): *Aqueous-Pressed* (Fig. 7.17), *Aqueous-Float Packing* (Fig 7.19) and *Organic-Pressed* (Fig 7.22). Indentations performed with the manual mictroindentor.

(a) Aqueous-Pressed (Macrostruct. Fig. 7.17)

(b) Aqueous-Float Packing (Macrostruct. Fig. 7.19)

(c) Organic-Pressed (Macrostruct. Fig. 7.22)

Figure 7.27: Micrographs of Knoop indented nc-UO_2 pellets.

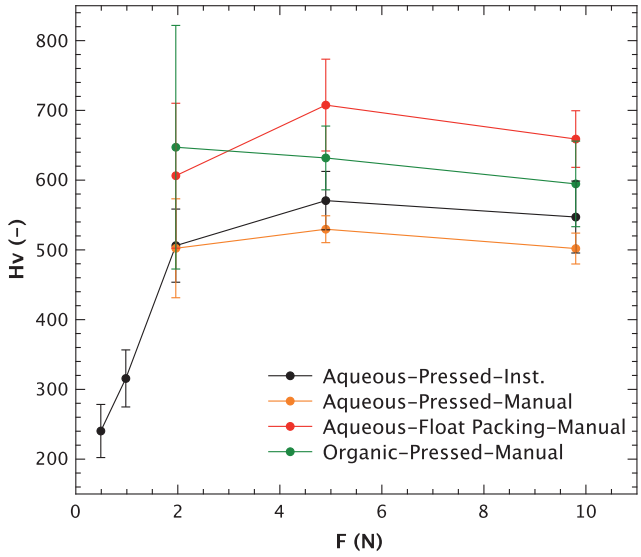

Figure 7.28: Average H_V (-) obtained for the different loads used for each kind of monolith.

With a calibration curve available for a wide range of well characterised materials, the $\frac{H_V}{E}$ ratio of a given brittle material can be estimated via its measured $\frac{b'}{a'}$ = ratio with an error <10% [Marshall et al., 1982].

For this study, the calibration curve $\frac{b'}{a'}$ vs. $\left(\frac{H}{E}\right)_K$ (Eq. 7.5) was used as determined by [Marshall et al., 1982] and [Pujol et al., 2004] as:

$$\frac{b'}{a'} = 0.143 - 0.497 \cdot \left(\frac{H}{E}\right)_K \tag{7.5}$$

Average $\frac{b'}{a'}$ ratios of the nc-samples were determined using an indentation load of 9.8 N for the Knoop indentation. The corresponding $\left(\frac{H}{E}\right)_K$ value was derived by the calibration curve determined by [Pujol et al., 2004] (Eq. 7.5). The representation of the curve with the values of $\left(\frac{H}{E}\right)_K$ for the different nc-UO_2 monoliths obtained is shown in Fig. 7.29 together with other reference materials.

Finally, E was from the Eq. 7.6 calculated, taking into account the H_V values determined by Vickers indentation likewise at 9.8 N load. The H_V in GPa was determined by the Eq. 7.7 [Spino et al., 2003].

$$E = \frac{H_V}{\left(\frac{H}{E}\right)_K} \tag{7.6}$$

where H_V is the hardness given in GPa units, F is the indentation load in N (9.8 N), and d is the average Vickers imprint diagonal in mm.

$$H_V = 0.0018544 \cdot \frac{F}{d^2} \quad (GPa) \tag{7.7}$$

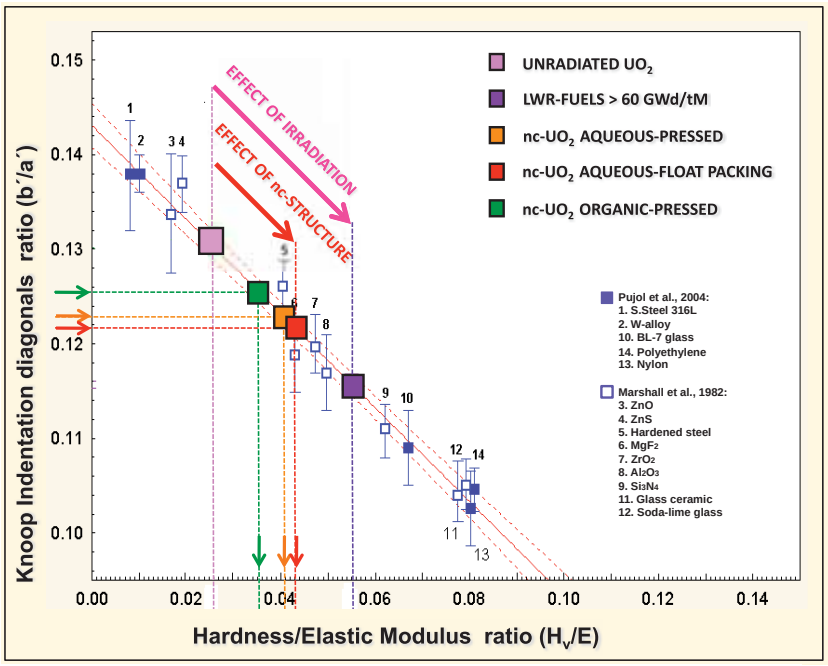

Figure 7.29: Calibration curve $\frac{b'}{a'}$ vs. $\left(\frac{H}{E}\right)_K$ determined by [Pujol et al., 2004] (Eq. 7.5). Representation of values for $\left(\frac{H}{E}\right)_K$ for the different nc-UO_2 monoliths obtained by the calibration curve together with other reference materials from [Marshall et al., 1982] and [Pujol et al., 2004].

Obtained parameters for Vickers and Knoop indentation of the different pellets, are detailed in Table 7.2.

7.4.2 Young's modulus as probed by scanning acoustic microscopy (SAM).

The high-frequency acoustic microscopy is a non-destructive and non-invasive method, very sensible to structural defects. It can reveal cracks at and underneath the surface, therefore is more more powerful than optical microscopy to appreciate cracks. These cracks affect the values of Young's modulus (E) and naturally thermal conductivity too, in the same way as porosity and other structure-obstacles do (property deterioration). The characteristics of the acoustic microscope used, as well as the preparation of the setup, are described in Sec. 2.7.3. The results here obtained are just an approximation to compare and support the E measurements by indentation.

For embedded samples, just one surface was available. Therefore no echographic analysis could be applied. However the measurement of the Rayleigh wave velocity (V_R) could be achieved just with one surface, and the E-modulus could be then only with the V_R and using the relations described by [Laux et al., 2012] determined. Measurements with a V_R of 2300(30) m/s^{-1} were carried out on a sample from the float-packing consolidation method and powder of the aqueous-synthesis (*Aqueous-Float Packing*; mactrostructure in Fig. 7.19). A Poissson's ratio (υ) about 0.3 for the UO_2 was assumed. With this value and based on calibration laws performed on standard UO_2 making the assumption of lenticular pores [Laux et al., 2012], it lead to a porosity of 10(2)% ($\sim$ 90(2)% density) for the nc-UO_2 sample. A Young's modulus of to 155(5) GPa

Table 7.2: Obtained average parameters for Vickers and Knoop indentation for the different nc-UO_2 pellets.

nc-UO_2 Monoliths	${H_V}^{a,b}$	${H_K}^{a,c}$	$\frac{b'}{a'}$ ^{d}	$\left(\frac{H}{E}\right)_K$ ^{e}	${H_V}^{f}$	E ^{g}
	(-)	(-)	(-)	(-)	(GPa)	(GPa)
Aqueous-Pressed (instrumented) Macrostr. Fig. 7.17	547(52)		0.123(3)	0.041	5.4(5)	132(12)
Aqueous-Pressed (manual) Macrostr. Fig. 7.17	502(22)	466(28)	0.123(3)	0.041	4.9(2)	121(5)
Aqueous-Float Packing (manual) Macrostr. Fig. 7.19	659(41)	579(15)	0.122(2)	0.043	6.5(4)	150(9)
Organic-Pressed (manual) Macrostr. Fig. 7.22	595(61)	545(65)	0.126(5)	0.035	5.8(6)	166(17)

a.) For 9.8 N load. b.) From Eq. 7.2. c.) From Eq. 7.3. d.) Ratio of the remaining imprint diagonals of the Knoop-pyramid indenter. e.) From the calibrated curve Eq. 7.5 [Pujol et al., 2004]. f.) From Eq. 7.7. g.) From Eq. 7.6.

was determined using the following equation:

$$E = \rho V_T^2 \frac{3V_L^2 - 4V_T^2}{V_L^2 - V_T^2} \tag{7.8}$$

where the transverse velocity (V_T) and the longitudinal (V_L) could be calculated by the relations described in [Laux et al., 2012]. An acoustical image of a nc-UO_2 sample from *Aqueous-Float Packing* is shown in Fig. 7.30. No sub-surface microcracks were observable in the area studied. Vickers and Knoop indentations previous done on some parts of the surface are visible on the figure.

Figure 7.30: Acoustical image of a nc-UO_2 sample from *Aqueous-Float Packing*.

7.4.3 Bulk and Young's modulus of nc-UO_2 as a function of the crystal size by high pressure XRD.

A decrease of the Young's modulus (E) for the nc-UO_2 ~150 GPa for the nc-UO_2 (from aqueous-float packing Table 7.2) vs. 220 GPa for standard UO_2 pellets have been observed as probed by indentation. The interest of a high pressure XRD (HP-XRD) measurement is to elucidate if the decrease of Young's modulus (E) observed in the nc-UO_2 monoliths could have a dependence on the particle size. The Young modulus

has two components (see Eq. 7.9). The compressibility of the lattice or compressibility modulus B_0 and the Poisson's ratio. The structural defects, porosity and cracks make the value of B_0 to decrease, but also the crystallite size can induce a variation in the B_0 [Wang et al., 2001], [He et al., 2005].

$$E = 3B_0(1 - 2\upsilon) \tag{7.9}$$

The crystal size dependence of the bulk modulus of nc-UO_2 have been investigated by means of in-situ high pressure X-ray diffraction (HP-XRD). Characteristics of the device are shown in Sec. 2.7.2. Three different nc-UO_2 sizes (4(0.5) nm, 6(0.5) nm and 34(0.5) nm), obtained by heating the as-produced nc-UO_2 under Ar/5%H_2 and measured by high resolution TEM (see Fig. 7.31), have been studied. The XRD at ambient conditions showed that the three nc-UO_2 samples crystallised with a cubic structure (*Fm-3m* space group No. 225) and a cell parameter of a_0=5.46 Å, which is in good agreement with the literature values [Idiri et al., 2004], [Zvoriste-Walters et al., 2013].

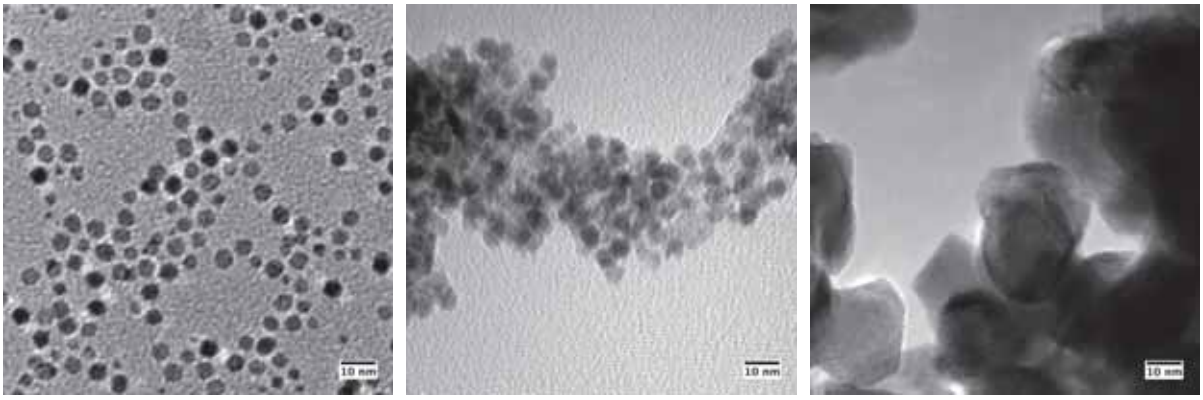

(a) 4 nm (scale bar of 10 nm) (b) 6 nm (scale bar of 10 nm) (c) 34 nm (scale bar of 10 nm)

Figure 7.31: TEM micrographs of UO_2 at high resolution for the three different sizes [Zvoriste-Walters et al., 2013].

The variation of the unit cell volumes with increasing pressure was measured with the aim to study the compressibility behaviour of nc-UO_2 as a function of the size. Some of the high pressure X-ray diffraction (HP-XRD) patterns measured in-situ for the three nc-UO_2 sizes are shown in Fig. 7.32 and where already published in [Zvoriste-Walters et al., 2013]. The nc-UO_2 was compressed up to 23 GPa (for the nc-UO_2 4 nm sample), 21 GPa (6 nm), and 34 GPa (34 nm). The $P(V)$ compression data for the three nc-UO_2 sizes are shown in Fig. 7.33 [Zvoriste-Walters et al., 2013]. One expected problem was that the Bragg peaks of the nanomaterial were too wide (short order range), which could mask the peak shift on applying pressure. But even using an x-ray source in house, the three UO_2-sized samples showed a strong scattering activity (Fig. 7.32).

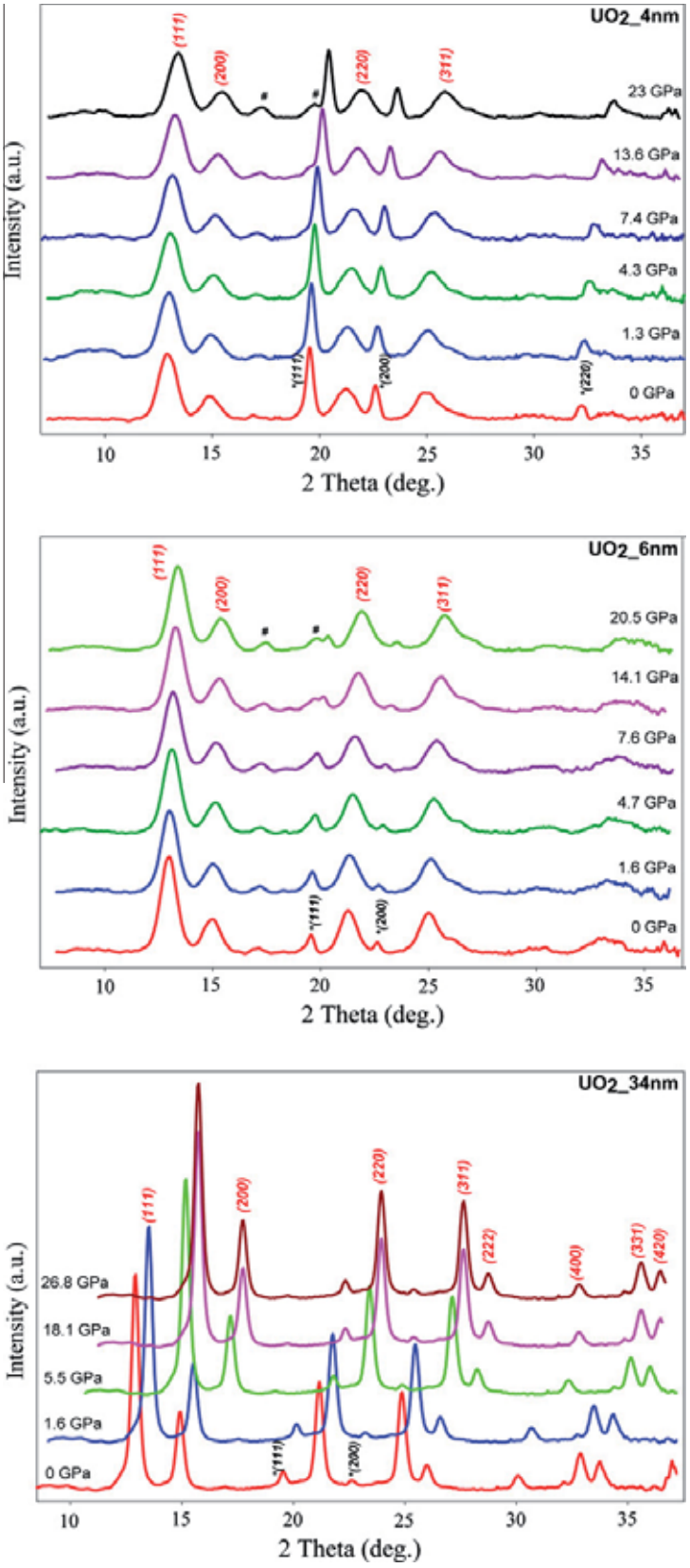

Figure 7.32: In-situ HP-XRD pattern of nc-UO_2 for the three different sizes [Zvoriste-Walters et al., 2013].

Table 7.3: Calculated bulk moduli (B_0) and their first pressure derivative (B_0') for the three nc-UO_2 samples using different EOS, as well as bulk moduli values for UO_2-bulk [Zvoriste-Walters et al., 2013].

Sample	*BM, P(V)*				*F(f)*		*V*			
	LP		*HP*		*HP*		*LP*		*HP*	
	B_0	B_0'	B_0	B_0'	B_0	B_0'	B_0	B_0'	B_0	B_0'
4 nm	122(5)	8(2)	101(6)	18(2)	113	13	**122(5)**	**8(2)**	106(5)	14(1)
6 nm	148(7)	9(3)	146(5)	12(1)	144	12	**148(7)**	**9(2)**	148(4)	11(1)
34 nm	168(4)	20(2)	182(2)	14(1)	175	15	171(4)	17(1)	**186(2)**	**11(1)**
Bulk	198(4) 6.5(6)[a] 207(2), 4.5(4)[b]				–		198(4), 6.6(6)[a]			

Low pressure range (LP); high pressure range (HP); pressure-volume data fitted with the BM-EOS ($BM, P(V)$) with $P = 3/2 \cdot B_0 \cdot f(1+2f)^{5/2} \cdot [1+3/2(B_0^{'}-4)f]$ and $f = [(V/V_0)^{-2/3}-1]/2$ [Birch, 1947]; normalised pressure vs. Eurelian finite strain plot ($F(f)$) with $F = P/[3f(1+2f)^{5/2}]$ and $f = [(V/V_0)^{-2/3}-1]/2$; Vinet EOS (V) with $P = 3B_0(1-f_V)/f_V^2 \cdot exp[3/2(B_0^{'}-1)(1-f_V)]$ and $f_V = (V/V_0)^{1/3}$ [Vinet et al., 1989]. a). [Pujol et al., 2004] b). [Idiri et al., 2004]

The experimental data were fitted to different equations of state an the bulk modulus (B_0) and its pressure derivative (B_0') were determined. The data for the three samples with the least-squares fit of the 3^{rd} order Birch-Murnaghan equation of state (BM-EOS) are shown in Fig. 7.33. The 3^{rd} order BM-EOS is one of the most used in material science and geophysics [Birch, 1947]. For clarity and due to the good agreement in pressure measurement for the Cu equation of state (Cu-EOS) as internal standard and the ruby scale [Piermarini et al., 1975], the x axis is defined just from the pressures from the ruby scale. The bulk moduli obtained are reflected in Table 7.3 [Zvoriste-Walters et al., 2013]. Bulk moduli values for UO_2-bulk [Pujol et al., 2004] and [Idiri et al., 2004] are also detailed. Because of the low pressure range in which silicone oil has a quasi-hydrostatic sample environment [Meresse et al., 2000], only the experimental data up to 10 GPa (were silicon used to solidify) was used (inset Fig. 7.33).

Another representation of the finite strain BM-EOS in terms of the normalised pressure and the Eulerian finite strain which is more sensitive to experimental uncertainties [Birch, 1978], was also done. The compression data obtained with this method are shown in Fig. 7.34 and the bulk moduli obtained are detailed in Table 7.3. As an alternative approach to the BM-EOS, the Vinet EOS [Vinet et al., 1989] was also used in order to determine the bulk moduli for the three nc-UO_2 samples. The bulk moduli obtained with this equation are reflected in Table 7.3.

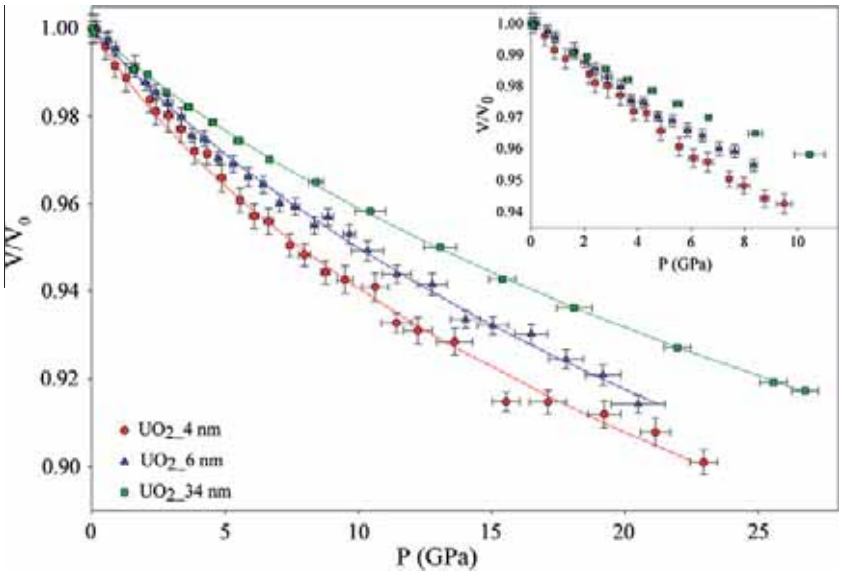

Figure 7.33: Relative volumes vs. pressure. The lines represent the least-square fit of the 3^{rd} order BM-EOS to the experimental data. *Insert Fig.:* compression data from the three nc-UO_2 samples plotted in the low pressure (LP) range (LP up to around 10 GPa) [Zvoriste-Walters et al., 2013].

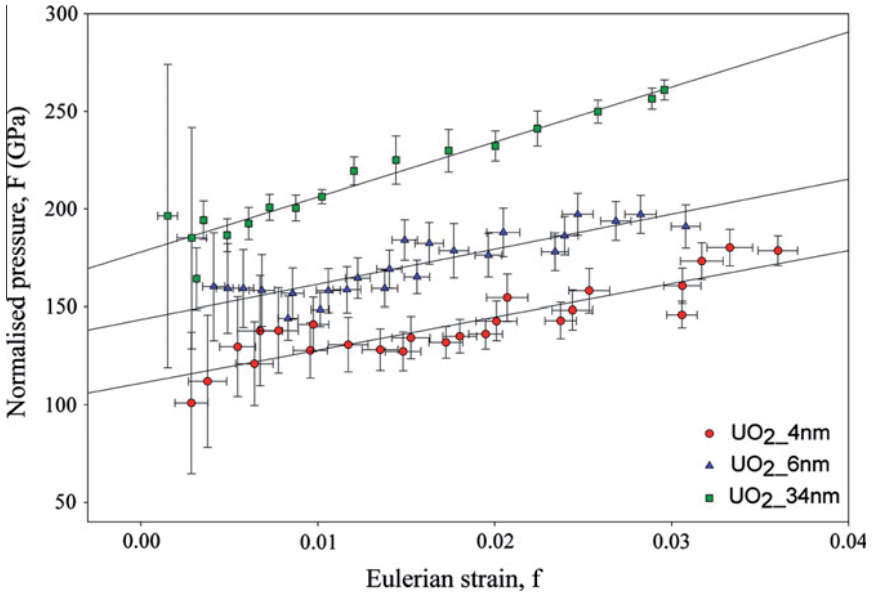

Figure 7.34: Normalised pressure as a function of the Eulerian strain for the three nc-UO_2 samples. The solid lines represent a linear fit to the experimental data. In the $F(f)$ linear plot the bulk modulus is obtained from the intercept on the F axis and the $B_0^{'}$ from the gradient $F = B_0 + (3B_0(B_0^{'} - 4)f)/2$ [Zvoriste-Walters et al., 2013].

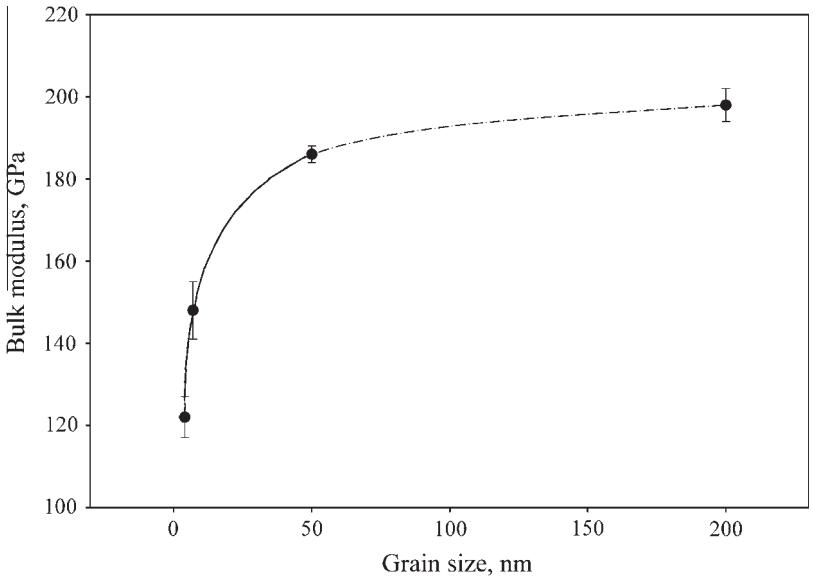

Figure 7.35: The bulk modulus plotted as a function of three crystal size samples (4 nm, 6 nm and 34 nm). A size approximation for the micro-sized bulk modulus UO_2 from [Pujol et al., 2004] to 200 nm has been done [Zvoriste-Walters et al., 2013].

7.4.4 Results and discussion.

Mechanical properties as Vickers Hardness (H_V), Knoop Hardness (H_K) and Young's modulus (E) were determined for sintered nc-UO_2 pellets obtained by different methods (*Aqueous-Pressed*, *Aqueous-Float Packing* and *Organic-Pressed*). Micro- and macro-structure characterization of these pellets have been described in Sec. 7.3.3. Also scanning acoustic microscopy (SAM) has been used in some of the samples for the estimation and comparison of the Young's E-modulus obtained by indentation. Finally

a study by in-situ high pressure X-ray diffraction (HP-XRD) has been performed for the study of a possible bulk modulus dependence of the crystal size dependence in nc-UO_2.

In the indentation study, an increase in hardness (H_V) of the nc-UO_2 material for the *Organic-Pressed* pellet, and more pronounced for the *Aqueous-Float Packing* pellet, have been obtained (Table 7.2) in comparison with bulk-UO_2 ($H_{V_{(UO_2)}} = 5.72\ GPa$). A tendency of decreased values for the different nc-UO_2 pellets in $\frac{b'}{a'}$, and therefore increased values in $\left(\frac{H}{E}\right)_K$, has been observed in comparison with the typical values for unradiated standard-UO_2 ($\left(\frac{H}{E}\right)_{K(UO_2)} = 0.026$). As a consequence (see Eq. 7.6), and despite as formerly said that the H_V values of the nc-UO_2 material appeared increased with respect to standard-UO_2, rather low values for E (Table. 7.2) for all nc-UO_2 monoliths have been observed in comparison with standard-UO_2 ($E_{UO_2} = 220\ GPa$). The smaller E-modulus was seen for the *Aqueous-Float Packing* sample (150(9) GPa), which was about 30% lower than for bulk-UO_2.

This difference observed with respect to bulk-UO_2 pellets, could be influenced by microstructure imperfections (nanocavities at triple-grain junctions, pores, cracks, etc.). That could be possible in the case of *Aqueous-Pressed* pellet, as it has been seen in the macrostructure images (Fig. 7.17). However, the drop is still too large to be attributed only to the presence of cavities. It would be equivalent to 30% porosity, not agreeing with the apparent density of about 90% measured at least for the nc-UO_2 *Aqueous-Float-Packing* pellet and the *Organic-Pressed* pellet (Table 7.1). Therefore, it is believed that the effect observed is predominantly due to the presence of the nanostructure, as trends of this type (i.e. increase of H_V values and decrease of E-modulus values) have been confirmed repeatedly in nanostructured materials. The grain size observed on the fresh fracture pictures was about 200 nm for all the different kind of pellets (Table 7.1). Hence, the difference of 30-40 GPa observed between the E-modulus from the *Aqueous-Pressed* pellet and the *Organic-Pressed* and *Aqueous-Float Packing* monoliths could be due to a better colloidal compaction of the last ones (higher E values) and apparently indicating a better structural quality.

In contrast, the same type of tendency observed in the nc-UO_2 specimens, i.e. with increase of H_V values and decrease of the E-modulus values, has been found before in irradiated standard-UO_2 fuel at high burn-ups (see Fig. 7.36 and Fig. 7.37). In this case also the E-modulus decrease could not be fully attributed to a porosity increase and was to contradict the effect of the fission products dissolution, which causes in reality an increase of the material's stiffness. Since with the increase of burn-up the irradiated nuclear fuels transforms into a nano-recrystallized structure [Spino et al., 2012], the effects of H_V-increase and E-modulus decrease in the present work observed, were attributed to the nanostructure. Just in the case of the *Aqueous-Pressed* pellet, an H_V-decrease is observed which could be due, as above mentioned, to the structural imperfections.

In agreement with the above, measured reduction of the E-modulus in the nc-UO_2 samples is perfectly matching the results of acoustic and Knoop indentation tests in irradiated fuels with burn-up 80 GWd/tM (see Fig. 7.37), for which a fully developed nanostructure (HBS) has been found in post-irradiation examinations [Spino et al., 2012]. In contrast, the increase of hardness (H_V) matches well the values of irradiated fuels and seems to respond to the Hall-Petch effect, which describes the

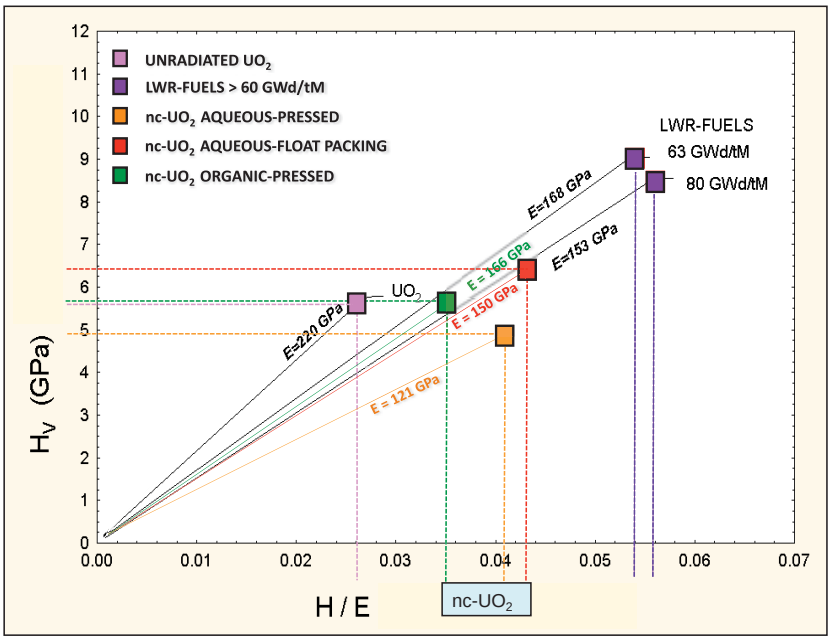

Figure 7.36: Differences in the H_V vs. $\left(\frac{H}{E}\right)_K$ behaviour of irradiated and non-irradiated UO_2.

increase of the strength of the material according to the inverse of the square root of its grain size.

The acoustic microscope was also tested on the nc-UO_2 sample from aqueous-float packing. The estimated results for the E-modulus (155(5) GPa) were found to be in agreement with those obtained by indentation (150(9) GPa Table. 7.2) where the measurements of compressibility indicated also that the nc-UO_2 sample exhibited an E-modulus below that of standard UO_2 (220 GPa).

Finally, the crystal size dependence of the bulk modulus of nc-UO_2 have been investigated by means of in-situ HP-XRD and the different B_0 and $B_0^{'}$ values were summarized in Table 7.3. Three different nc-UO_2 sizes (4 nm, 6 nm and 34 nm), obtained by heating the as-produced nc-UO_2 under $Ar/5\%H_2$, were studied up to 27) GPa. The fits for the experimental data were done in a low pressure range (LP) up to around 10 GPa (where solidification of the silicone oil occurs [Meresse et al., 2000]) and a high pressure range (HP) (up to the maximum pressure achieved in this run of experiments). The three fitting procedures used (3^{rd} order BM-EOS ($P(V)$ and $F(f)$ plots) and V-EOS) suggested a size dependence of the bulk modulus which drastically decrease with the particle size. The best fit to all the compression data was obtained with the V-EOS (see Table 7.3) and its bulk moduli were represented in Fig. 7.35 as a function of the particle size. The B_0 values with this fit obtained were of B_0(4nm)=122(5), $B_0^{'}$(4nm)=8(2), B_0(6nm)=148(7), $B_0^{'}$(6nm)=9(2) and B_0(34nm)=186(1), $B_0^{'}$(34nm)=11(1). A size approximation for the micro-sized bulk modulus UO_2 from [Pujol et al., 2004] to 200 nm has been done [Zvoriste-Walters et al., 2013]. A decrease in the bulk moduli of about 60%, 25% and 14% (for the 4 nm, 6 nm and 34 nm samples, respectively) have been identified in comparison with the reported standard bulk-UO_2. Similar bulk moduli values were obtained from the $F(f)$ and $P(V)$. The small difference observed between them (smaller values for the normalized pressure $F(f)$) might be because of its expected more sensitivity to the experimental uncertainties [Birch, 1978].

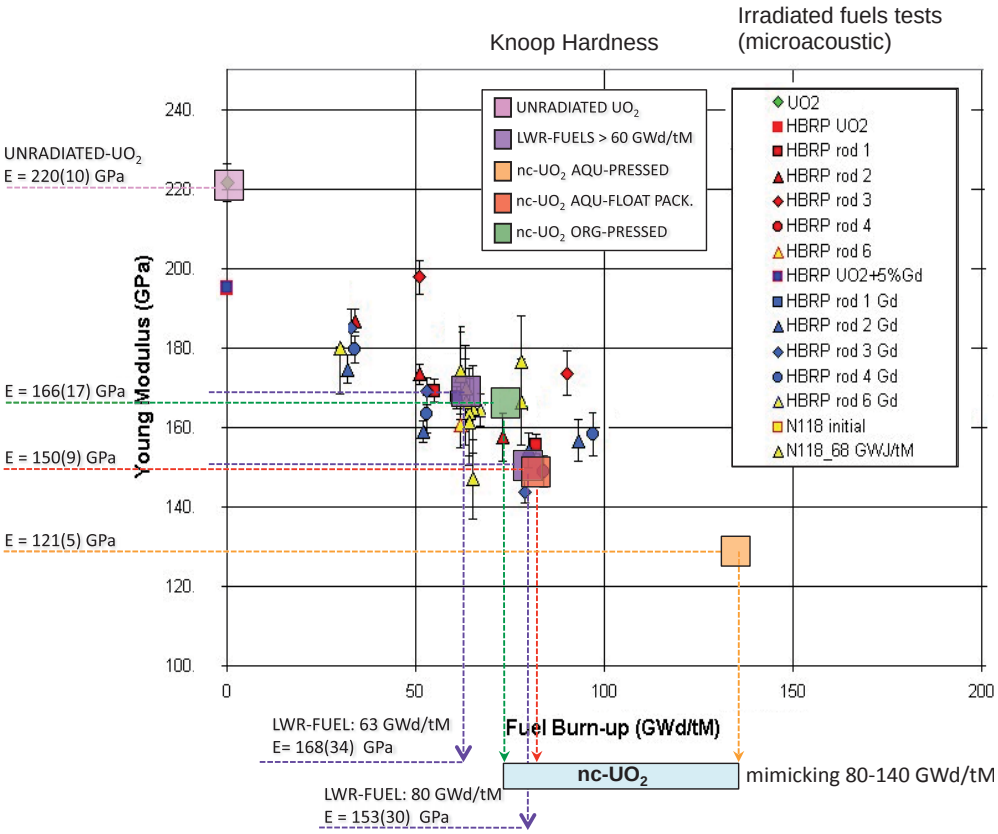

Figure 7.37: E values from microacoustic tests and Knoop indentation from irradiated fuels [Baron et al., 2005] and nc-UO_2 (this work).

Different works can be found in literature indicating contrary conclusions about the variation of the compressibility modulus or bulk-modulus (B_0) with the crystallite size. Some of these studies indicate no variation of B_0 with the size of the particles in materials such as Fe, CuO [Chen et al., 2001], [Wang et al., 2002]. Some others indicate an upward variation respecting their respective bulk materials [Tolbert and Alivisatos, 1995] and [Qadri et al., 1996], for materials such as CdSe, CdS and PbS. And most of them indicate an downward variation respecting their respective bulk materials, for materials such as CeO_2, SnO_2 [Wang et al., 2001], [He et al., 2005]. A difference of only 7% and only for grains <3 nm have been observed for nc-Ni by [Zhao et al., 2006], [Zhang et al., 2007] because a higher compressibility of the surface shell. Meanwhile a large large variation of bulk modulus with the crystallite size (from 150 GPa at 5 nm to 240 GPa at 70 nm) has been seen for nc-Al_2O_3 [Chen et al., 2002]. In other studies, a complex two-phase structure (core-surface shell system) in nanocrystals has been described, making difficult the determination of an only bulk modulus value under pressure [Palosz et al., 2004]. Also the influence of the crystallite size on the pressure inducing phase transition, has been for different materials reported. An increase of the transition pressure in nanocrystals in comparison to the bulk has been shown in [Qadri et al., 1996], [Tolbert et al., 1996] [He et al., 2005]. Also, phase transitions at much lower pressures relative to the bulk has been observed for other nano systems [Olsen et al., 1999], [Rekhi et al., 2001].

Elastic moduli of a material is commonly dependent of microscopic interatomic interactions. Particularly, the bulk modulus is directly dependent on the valence electron density [Haines et al., 2001], [Brazhkin et al., 2002]. As a consequence, the

variation of the valence electron shells by modifying the surface to volume ratio (change in crystal size), has also a variation in the bulk modulus values. For lots of materials a value of 4 for $B_0^{'}$ has been found using the third order Eulerian finite strain equation, in agreement with other works where the interatomic potentials for fixed structures was studied. Most of these materials where NaCl-type and the upper limit for $B_0^{'}$ was depending on the size of the attractive potential relative to the repulsive one. Values for $B_0^{'}$ about 6 for neutral solids or incompressible materials, or about 8 for ionic or soft solids, like NaCl, were observed [Hofmeister, 1993]. Taking that in account, the value of 20 for the $B_0^{'}$ obtained for the 34 nm sample with the BM-EOS fit would not have physical meaning. However, for some materials with values of $B_0^{'}$ of 7 to 23, just the V-EOS was valid, giving $B_0^{'}$ values nearer to physically realistic potentials [Hofmeister, 1993].

Also different observations could be done in the compression of the nc-UO_2. In the curves of the 4 and 6 nm samples, two minor discontinuities appear shifted one relative to the other towards bigger strains with decreasing particle's size (see Fig. 7.33 and Fig. 7.34). The better fit was obtained for the 34 nm which had a more linear compression curve. In this sample just a small discontinuity can be seen in the pressure range 6.66 to 13.07 GPa (f=10.2e^{-3}-17.2e^{-3}). The discontinuity at around 10 GPa in all the compression data might be due to the influence of non-hydrostatic stress in the sample chamber. The discontinuity at higher pressures is similar to the one observed for other materials as for $AuIn_2$ and $Cd_{0.8}Hg_{0.2}$ because of electronic topological transitions [Godwal et al., 2010]. More studies should be done for nc-UO_2 to clarify these deviations. Also some differences have been seen for the B_0 and $B_0^{'}$ values between the 34 nm UO_2 sample in comparison with the 4 and 6 nm ones. Higher values in B_0 at LP than at HP have been seen for the smaller size samples. But smaller values for at LP than at HP have been seen for the 34 nm UO_2 sample. Also the $B_0^{'}$, given by the slope of the curves, changes different for the 34 nm sample. That could be due to the minor number of experimental points taken at LP for this sample. A good agreement was found between the values obtained with the BM-EOS and the V-EOS, but lower values for $B_0^{'}$ have been seen with the last one for the 34 nm UO_2 sample. These differences identified between the smaller-size samples and the bigger one, could be due to critical particle size which could characterize the material with different properties [Zvoriste-Walters et al., 2013].

7.5 Thermophysical properties of nc-UO_2 monoliths.

The determination of elastic properties of UO_2 is relevant particularly to reactor-transients where a pellet cladding mechanical interaction (PCMI) and possibly cladding failure is willing to occur. The level of stress in the UO_2-pellets can be then elucidated by means of the elastic properties and thermal expansion.

However, worsening of the thermophysical properties due to the nano-size of the particles could be a possible disadvantage for licensing purposes. Temperature diminution when melting point depression occurs, and thermal conductivity decrease, have been observed for nanosized-grains respect to large-grains (10 μm). The latter is due to the increase of grain boundaries and therefore increase of thermal boundary resistance

(Kapitza resistance) [Spino et al., 2012].

7.5.1 Thermal Diffusivity in nc-UO_2 monoliths.

The nc-UO_2 with grain size about 200 nm (217(47) nm determined by SEM) sample (0.65 mm^3 in diameter) was heated up to the temperature of measurement in a high frequency furnace under Ar-atmosphere of 10^{-2} mbar. Several test points within the temperature range 527°K to 1438°K (254°C to 1165°C) were taken. Experimental characteristics are described in Sec. 2.8.1.

Fig. 7.38 shows the thermal diffusivity in function of temperature curves for nc-UO_2 (∼200 nm) considering 90% density (determined by SAM in Sec. 7.4.2), as determined by the laser-flash device (LAF I) (Sec. 2.8.1). Backward measurements with decreasing temperature show quasi no modification. This indicates that the microstructure of the specimens remained unaltered during the high temperature measurements (i.e., at $T \leq T_{sintering}$=1200°C). The data obtained for the nc-UO_2 monolith have been extrapolated to 95% density to make the comparison with the 95% density bulk-UO_2 from [Fink, 2000].

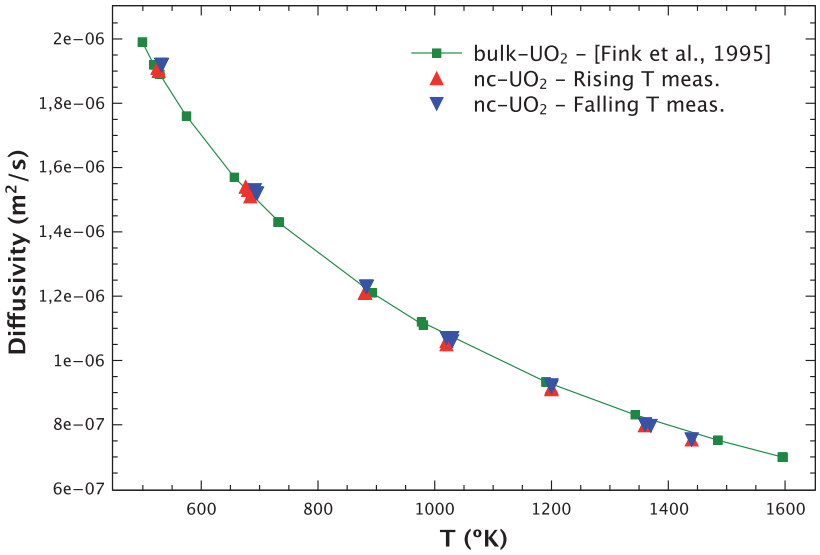

Figure 7.38: Thermal diffusivity of nc-UO_2 (200 nm - 90% density) specimen upon temperature, extrapolated at 95% density for comparison with bulk-UO_2 (large-grain) (95% density) from [Fink, 2000]; *red symbols*: measurements at rising temperature, *blue symbols*: measurements at falling temperature levels.

7.5.2 Melting Point Depression in nc-UO_2 monoliths.

The sub-second laser heating coupled with pyrometry has been already in ITU proved with success in multiple occasions for bulk refractory oxides [Ronchi and Hiernaut, 1996] [Manara et al., 2005] [Manara et al., 2008] [Böhler et al., 2012] [Manara et al., 2012]. However first tests with nano actinide oxides have been just in [Cappia et al., 2013] tested. Determination of the melting point depression for the nc-UO_2 monolith in function of the size was done by observing the break point on the upward slope and was compared with the one for bulk-UO_2

(large-grain). Characteristics of the melting point setup used are described in Sec. 2.8.2. nc-UO_2 samples 3 mm thick and 5 mm in diameter were used in the measurement. Two different nano-grain sizes were tested (about 10(0.5) nm determined by TEM and 217(47) nm determined by SEM). The laser penetration depth was of a few micrometers, and according to the power some tens micrometers of material could be melt. The grain growth was tried to be limited using a fast ramp. A post SEM determination in the region close the molten surface was done for the 10 nm pellet (Fig. 7.41, 7.42).

In Fig. 7.39 the measurement done for the 10 nm-UO_2 (a=0.5438 nm) at 600 bar He, is shown. A melting point depression of about 150°K with respect to the normal value of bulk-UO_2 (large-grain) (3140°K), was found.

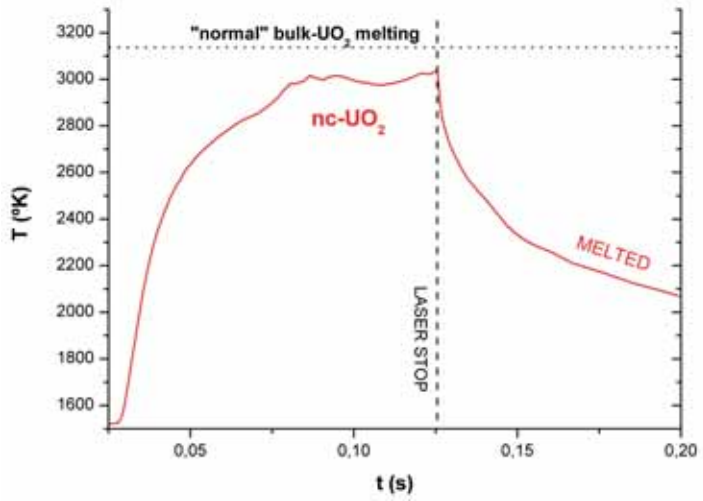

Figure 7.39: Melting point measurement for 10 nm-UO_2 sample.

In Fig. 7.40 the measurement done for the 200 nm-UO_2 (a=0.5470 nm) at 600 bar He, is shown. The melting point was observed at a similar temperature as for bulk-UO_2 (3140°K).

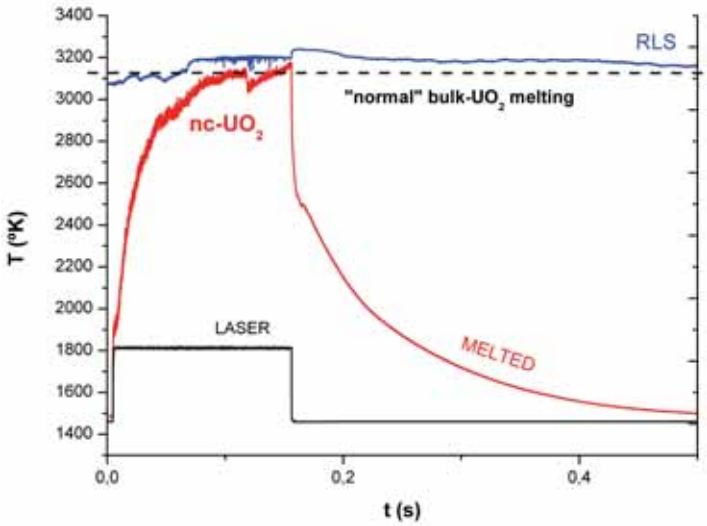

Figure 7.40: Melting point measurement for ∼200 nm-UO_2 sample.

In Fig. 7.41, the SEM images of the fresh fracture of melted nc-UO_2 samples, are shown. Thee grain growth was dramatically at these higher temperatures. Three differentiated grain size areas were clearly observable (Fig. 7.41b). First area, from the melted surface until ∼40 μm depth (Fig. 7.42a, 7.42b, 7.42c) with columnar growth (typical from melting). Second area, from the melted surface until ∼115 μm depth (Fig. 7.42d, 7.42e, 7.42f) with non columnar growth. These first and second areas corresponded to the molten and refrozen zone. Third area appeared above the 115 μm from surface and corresponded to the unmolten zone (Fig. 7.42g, 7.42h, 7.42i). However here a grain-growth was also observed with an average size of 241(70) nm, due to the higher temperatures reached at that distance from the surface.

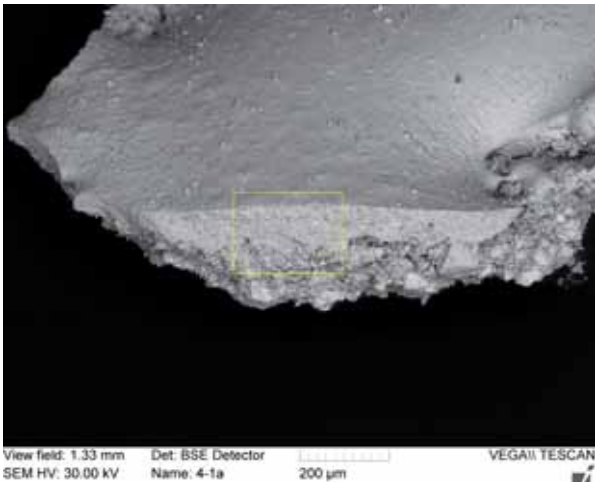

(a) The scale bar is 200 μm.

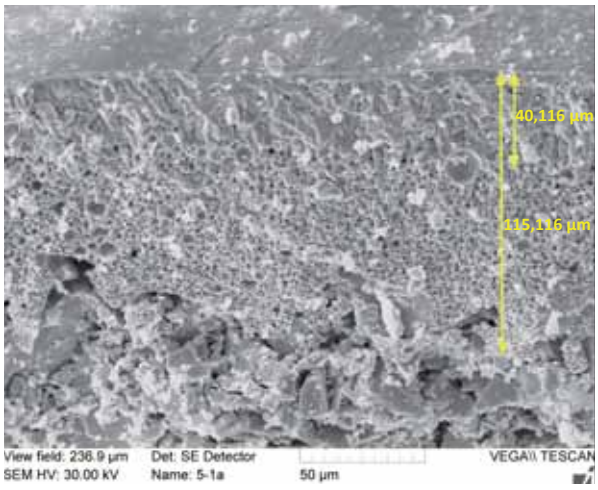

(b) The scale bar is 50 μm.

Figure 7.41: SEM images of the fresh fracture of surface-melted nc-UO_2 sample. Three different size areas (from surface to 40 μm depth, 40 μm to 115 μm and 115 μm to the opposite surface) are distinguishable.

7.5.3 Results and discussion.

The thermal diffusivity for nc-UO_2 (∼200 nm and a 90% density), was determined between 254°C to 1165°C. Extrapolation to 95% density was done and same thermal diffusivity as standard bulk-UO_2 pellet with 95% density was found. Some studies confirmed already that the effect of the grain size in the thermal conductivity is not that accused up to a determined size, as initially though.

Determination of the melting point by laser-heating and pyrometric temperature detection has been performed for compacted nc-UO_2 with two different nano-grain sizes (about 10 nm and 200 nm) and their variation with respect to bulk-UO_2 (large-grain), assessed. A melting point depression of about 150°K with respect to the normal value of bulk-UO_2 was found for the 10 nm-size nc-UO_2 sample (Fig. 7.39). This reduction would be a priori due to the nano-size grains. That has been already reported by [Lai et al., 1996], [Lai et al., 1998], [Guisbiers, 2012]. However, the measured lattice constant of the sample before melting (a=0.5438 nm) was below the value of bulk-UO_2 (a=0.547 nm) and indicated in reality a hyperstoichiometric oxide, which would also cause a melting point decrease. To corroborate the measured tendency with the grain-size reduction, a strictly stoichiometric nc-UO_2 sample would be needed.

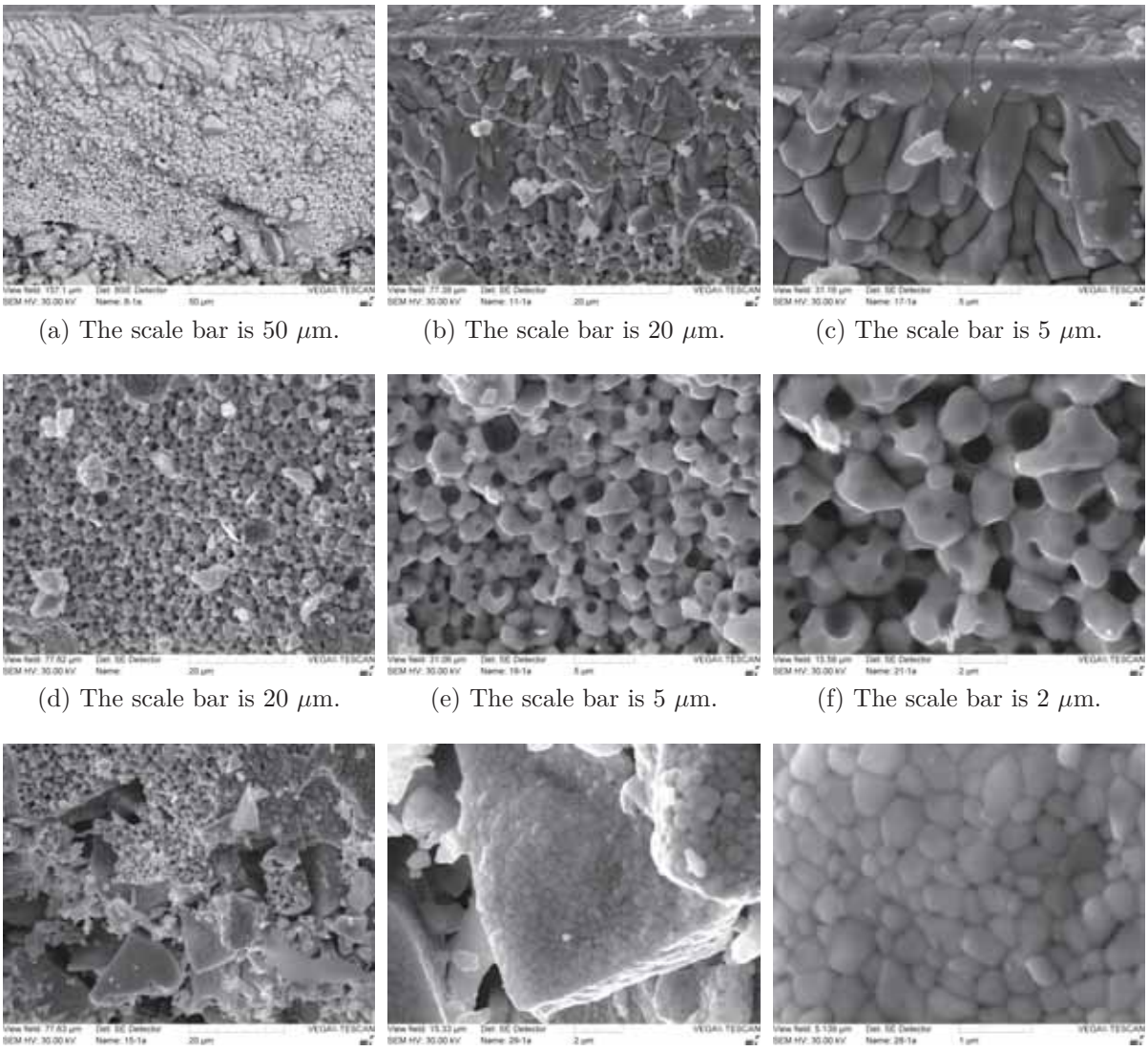

(a) The scale bar is 50 μm. (b) The scale bar is 20 μm. (c) The scale bar is 5 μm.

(d) The scale bar is 20 μm. (e) The scale bar is 5 μm. (f) The scale bar is 2 μm.

(g) The scale bar is 20 μm. (h) The scale bar is 2 μm. (i) The scale bar is 1 μm.

Figure 7.42: SEM images of the three different size regions formed after surface melting of the nc-UO_2 sample. *(First line of images):* surface-40 μm, molten zone and columnar growth. *(Second line):* 40 μm-115 μm, molten zone and non columnar growth. *(Third line):* 115 μm-opposite surface, unmolten zone, grain growth (241(70) nm)

However, an identical melting point as for bulk-UO_2, was found for the 200 nm-sample (Fig. 7.40) for which a stoichiometry of O/M=2.00 was confirmed from the lattice constant measurement before melting.

7.6 Results and discussion.

Conversion of nanoparticle systems into dense nanostructured monoliths has been achieved. The purpose was the synthesizing UO_2-nuclear fuels mimicking the HBS of LWR-fuels (nanostructured), for which improved properties are expected compared to standard fuel [Spino et al., 2012]. Monoliths with the two kind of nc-UO_2 obtained by the precipitation in aqueous media (Chap. 3) and in organic media (Chap. 4), were performed.

Different alternative routes for consolidation (e.g. conventional uniaxial pressing, float packing, etc.) into green bodies (Fig. 7.4) have been tried (Sec. 7.2). Afterwards the green bodies were sintered at temperatures between 900°C and 1200°C under Ar/H_2 atmosphere. The optimum sintering conditions were deduced from the long-isothermal crystallite growth studies under He and Ar/H_2 atmosphere (Table. 5.5). This ensured lack of disproportionate grain growth risks even at the highest temperature used of 1200°C. The nc-UO_2 material from the aqueous precipitation route was pressed with and without thermal pre-conditioning. The pre-treatment of the powder at specific temperature was an attempt to avoid possible cracks due to the evaporation of the possible trapped water in the material during the sintering step. The nc-UO_2 from organic route was pressed after thermal pre-conditioning. The treatment at temperature of the powder was aimed to make it free from possible adsorbed organic compounds from the preparation process, which could provoke cracks during their pyrolysis in the sintering step when the porosity of the ceramic becomes closed. The pellets were after sintered in an oven following different thermal profiles but always reaching lower plateau temperature than the micron-size powder in the sintering of traditional micro grain-UO_2 pellets. For the nc-UO_2 green pellets from float-packing, a mild thermal treatment was used to achieve densification of the samples. In this case, no powder thermal pre-treatment was done because firmly consolidated green monoliths were already formed from the fluid by this process. Therefore a solely calcination and sintering program was applied. The slow steps took in this last oven profile had the aim to let the water still present in the monoliths to slowly evaporate, but also to avoid possible cracks which might occur by internal overpressure if faster heating ramps were applied. The pellets sintered presented a strong appearance although fine cracks were visually observable in some cases (Fig. 7.11 and 7.12). Sintering densities between 75.5-90.5% of the theoretical density (TD_{UO_2}=10.96 g/cm^3), were obtained (Table. 7.1). An average grain size of ∼200 nm, replicating the HBS, was obtained for all the different sintered nc-UO_2 pellets.

Additional dilatometry experiments were performed to compare the shrinkage of the fabricated nc-UO_2 pellet with that of bulk-UO_2 (large-grain) produced by a standard fabrication process. The temperature range from onset to completion of the densification occurred at much more lower temperatures (Fig. 7.14) for the nc-UO_2 (200-955°C, with a maximum sintering rate at 740°C), compared to the bulk-UO_2 [Lahiri et al., 2006] (900-1540°C, with a maximum sintering rate at 1200°C). The reason of that might be the higher surface present in the nc-UO_2 compared with the bulk-UO_2 material, rendering the sintering to become more effective (at lower

temperatures). The sintering activation energy was determined as $Q = 171 \pm 7\ kJ/mol$ assuming surface diffusion and $Q = 114 \pm 5\ kJ/mol$ assuming volume diffusion for the nc-UO_2 monolith, compared to $Q = 287\ kJ/mol$ determined for bulk-UO_2 in the literature [Lahiri et al., 2006]). Both diffusion mechanisms showed low values of the sintering activation energies as typical for nanopowders. That means a clear technological advantage in the fabrication of nc-UO_2 monoliths due to its high densification capacity at low temperatures. Furthermore, the nc-UO_2 offered the possibility of adjusting the grain size at will by varying sintering temperatures and times. Maintaining an acceptably low temperature range, will diminish the costs and simplify the manufacturing technology.

Characterization of macrostructures by optical microscopy (OM), and microstructures by fresh-fracture observation by SEM, for different samples at different magnifications, was performed. Not well defined grains were observable in the fresh-fracture SEM images of the pellets sintered at low temperature of 900°C (Fig. 7.20). The sinter of the crystals was still under development, therefore sintering temperatures of 1200°C were used afterwards. Macrocracks across different samples were observed. In the conventional-pressed monoliths from aqueous-route-powder and not dehydrating pre-treatment (*Aqueous-Pressed* - Fig. 7.16), many of macrocracks across the whole sample were present. The case of the conventional-pressed monoliths of pre-dehydrated powder from aqueous-route (*Aqueous-Pressed-PTT* - Fig. 7.17) presented few cracks in the pellet rim. No macrocracks have been observed on the conventional-pressed monoliths from organic-route and powder pre-thermal treatment (*Organic-Pressed-PTT* - Fig. 7.22) and the aqueous-route-powder sample by float-packing (*Aqueous-Float Packing* - Fig. 7.19). All macrostructures, with exception of the last one (*Aqueous-Float Packing* - Fig. 7.19), showed non-homogeneous densification (residual porosity between densified areas). Also the *Aqueous-Pressed-PTT* (Fig. 7.17) showed a good quality in comparison to the rest, from the point of view of the densification. However, improvements in the performance of the monoliths would be necessary to avoid the problem of cracks in the sintered pellets (and therefore the diminishing material's properties).

Looking at the fresh fracture surfaces, the microstructure of the *Aqueous-Float Packing* pellet and sintered at 1200°C, was the closest approximation to the HBS material obtained until now. The average grain size for the different monoliths was in the 170 nm to 250 nm range. So a success was found out meeting one goal: high density and low grain size (Table 7.1).

Mechanical properties as Vickers Hardness (H_V), Knoop Hardness (H_K) and Young's modulus (E) were determined for sintered nc-UO_2 pellets. An increase in hardness (H_V) and low values for E-modulus (up to 30%) were in general seen for the different nc-UO_2 monoliths (Table 7.2) in comparison with bulk-UO_2. Also scanning acoustic microscopy (SAM) was used for the estimation and comparison of the Young's E-modulus obtained by indentation. The results by SAM (E=150 GPa) matched the ones derived from microindentation (E=155 GPa).

This difference observed with respect to bulk-UO_2 pellets (220 GPa), could be influenced by microstructure imperfections (nanocavities at triple-grain junctions, pores, cracks, etc.). However, the drop was still too large to be attributed only to the presence of cavities. The same type of tendency observed in the nc-UO_2 specimens, i.e.

with increase of H_V values and decrease of the E-modulus values, has been found before in irradiated standard-UO_2 fuel at high burn-ups. In this case also the E-modulus decrease could not be fully attributed to a porosity increase and was to contradict the effect of the fission products dissolution, which causes in reality an increase of the material's stiffness. Thus, since with the increase of burn-up the irradiated nuclear fuels transform into a nano-recrystallized structure [Spino et al., 2012], the effects of H_V-increase and E-modulus decrease, likewise the particularities here found, was attributed to the nanostructure.

Taking the value of Young's modulus obtained by Knoop indentation (E=150 GPa) as an indicative of the lattice compressibility, and assuming a Poisson's ration of 0.31, a compressibility modulus B_0=131.6 GPa (Eq. 7.9). This indicates a more compressible lattice, i.e, a larger lattice-volume decrease with pressure, compared to bulk-UO_2 (B_0=198 GPa [Pujol et al., 2004]). So the compressibility of nc-UO_2 was in fact to be larger than that of standard-UO_2. As the product between compressibility and thermal expansion is constant in the Grüneisen relation ($\gamma = \alpha K_T V/C_v = \alpha K_S V/C_p$, where α=thermal expansion, K_S=adiabatic bulk-modulus, K_T=isothermal bulk-modulus, C_v=heat capacity at constant volume, C_p=heat capacity at constant pressure, V=molar volume and γ=Grüneisen constant) [Grüneisen, 1912],a larger compressibility (i.e. lower bulk modulus) will imply larger thermal expansion, as well as a lower compressibility (i.e. higher bulk modulus) will imply lower thermal expansion. A size-dependency of the physical-chemical properties of nc-UO_2 was confirmed. The thermal expansion increased with the size-decrease (see Fig. 5.5 and Fig. 6.6), at the time that the bulk modulus decreased. This is compatible with the Grüneisen relationship and the bulk modulus measurements as probed after by HP-XRD. However, verification of the trend in Cp is still lacking, which is indeed needed to complete the Grüneisen-relationship analysis.

A totally opposite behaviour was seen for UO_2-SF (SIMFUEL or simulated nuclear fuel) where a lower thermal (less compressibility) expansion and a higher bulk modulus, than for standard bulk-UO_2, were found. This increase in the bond strength of the fuel with the BU, would traduced in a higher rigidity of the lattice against temperature variations [Pujol et al., 2004]. However, measured reduction of the E-modulus in the nc-UO_2 samples was perfectly matching the results of acoustic and Knoop indentation tests in irradiated fuels with burn-up 80 GWd/tM, for which a fully developed nanostructure (HBS) has been found in post-irradiation examinations [Spino et al., 2012].

In-situ high pressure x-ray diffraction (HP-XRD) has been performed for the study of a possible bulk modulus dependence of the crystal size dependence in nc-UO_2. Three different nc-UO_2 sizes (4 nm, 6 nm and 34 nm) were studied up to 27 GPa. The different B_0 and B_0' values obtained are summarized in Table 7.3. The bulk modulus of UO_2 suffered an extreme decrease in the nano-size particle range. For the 4 nm nc-UO_2 a B_0 of around 40% lower than the one for bulk-UO_2 [Pujol et al., 2004], has been observed. The Vinet equation of state showed the best fit to all the compression data. Discontinuities were identified in the plot of normalized pressure vs. finite strain. A shift to higher strains with decreasing particle's size was observable which could indicate the presence of different electronic properties for the smaller particle's sizes of UO_2 [Zvoriste-Walters et al., 2013]. This confirmed the dependence of the bulk modulus with the crystallite size. However, studies with bigger particle sizes as

the ones here studied (>34 nm) would be necessary to guarantee that the tendency observed in the monoliths (decrease of E-modulus), is due to the size of the grains and not just because of imperfections and porosity possibly present in the samples.

The results of thermal diffusivity tests of the compacted nc-UO_2-material showed similar behaviour as that of standard nuclear grade UO_2 (bulk). The thermal diffusivity for sintered nc-UO_2 (∼200 nm, 90% density), was determined between 254°C to 1165°C. Extrapolation to 95% density was done and same thermal diffusivity as standard bulk-UO_2 pellet [Fink, 2000] with 95% density was found. Some studies confirmed already that the effect of the grain size in the thermal conductivity is not that accused up to a determined size, as initially though. In this published study [Raghavan et al., 1998], almost no effect in the thermal conductivity has been seen between a grain size from 70 nm to 400 nm, but because the porosity of the monoliths.

Regarding the feared worsening of the thermal conductivity of the HBS material due to grain-size effect (Kapitza resistance), it has been here shown that no thermal properties deterioration has to be expected for the 200 nm-UO_2 pellet material mimicking the HBS.

Determination of the melting point by laser-heating and pyrometric temperature detection has been performed for compacted nc-UO_2 with two different nano-grain sizes (about 10 nm and 200 nm) and their variation with respect to bulk-UO_2 (large-grain), assessed. A melting point depression of about 150°K with respect to the normal value of bulk-UO_2 was found for the 10 nm-size nc-UO_2 sample (Fig. 7.39). This reduction would be a priori due to the nano-size grains. That has been already reported by [Lai et al., 1996], [Lai et al., 1998], [Guisbiers, 2012]. However, the measured lattice constant of the sample before melting (a=0.5438 nm) was below the value of bulk-UO_2 (a=0.547 nm) and indicated in reality a hyperstoichiometric oxide, which would also cause a melting point decrease. To corroborate the measured tendency with the grain-size reduction, a strictly stoichiometric nc-UO_2 sample would be needed. However, an identical melting point as for bulk-UO_2, was found for the 200 nm-sample (Fig. 7.40) for which a stoichiometry of O/M=2.00 was confirmed from the lattice constant measurement before melting. This is an important technological result for the use of nc-UO_2 ceramics as nuclear fuel. Indeed, a lower melting point would suppose a problem for the licensing of the monoliths as a fuel for the reactor. Fortunately the possibility of a lower melting point disappears for the 200 nm-UO_2 samples, as it would occur for the HBS material in the reactor, too.

Chapter 8

Overall Discussion and Conclusions

The final goal of this work was to develop an accessible route to perform scale defect-free nc-UO_2-based monolithic ceramic specimens with tailored grain/pore microstructure. The creation of the latest novel microstructure has been achieved by passing through very different study steps. From the material synthesis to the fuel pellet manufacture, many individual process stages, previously unknown or unexplored, had to be specifically developed and optimized.

8.1 Synthesis of nc-UO_2 and nc-ThO_2.

Hence, regarding the initial nc-powder needed to perform the described monoliths, considerable work was devoted to the development of two different chemical synthesis routes leading to deflocculated nc-UO_2 and nc-ThO_2 precipitates. A controlled precipitation method that uses an electrolytically reduced aqueous solution of uranyl nitrate as precursor and dropped NaOH-solution as alkalinisation agent to trigger the precipitation of the nc-UO_2 is described in Chap. 3. In Chap. 4 another method based in a thermal decomposition to induce the precipitation of the nc-UO_2 in an organic phase using UAA as precursor, was reported. The same method was also extrapolated for the synthesis of nc-ThO_2 using in this case ThAA or ThA as precursors. To obtain larger amounts of nc-UO_2 as required, both methods were adapted, developed and scaled-up according to the aim needs. The material in the as-produced condition was studied by TEM and XRD.

For the method described in Chap. 3, an intensive study of the range of U-concentration and acidity for nc-UO_{2+x} precipitation from electrolytically reduced uranyl nitrate solutions was endeavoured, using higher concentration (10^{-1} M) ranges as the observed in literature (10^{-2} M), and therefore lower pH ranges, following the solubility line of U^{IV}. In light of this study, the conditions for the electrochemical reduction of these species could be defined. Precipitation from the electrochemically reduced U^{IV}-solution was achieved by gradual alkalinisation of the solution following as close as possible the theoretical solubility limit line of U^{IV} species in aqueous media. As a final result, 10 g of nc-UO_{2+x} per batch were obtained. The solid phase, as studied by XRD, was found to crystallize with the typical UO_2-*fcc* fluorite structure (*Fm-3m* space group), with a lattice parameter a=0.5417(1) nm and average crystallite size of 3.79 nm, also in agreement with an average size observed by TEM of 3.9(8) nm (Fig. 3.21). The predominant diffractogram of the samples corresponded unmistakably to UO_2, but in a slightly oxidized state. The latter was manifested

through a lattice contraction of about 0.9% of the precipitated phase (a=0.5417(1) nm) with respect to the values of stoichiometric UO_2 (a=0.547 nm), an effect which could be also caused by surface stresses induced by the small particle size, as frequently observed in nanoparticles. Further studies were undertaken in Chap. 5 to clarify this influence. Since the corresponding water content and/or oxidation degree of this phase was hitherto not identified, it was generically described here as UO_{2+x}, in correspondence with similar description e.g. in [Rousseau et al., 2002] [Rousseau et al., 2006] [Rousseau et al., 2009]. Further analysis of this phase is found in Chap. 5.

For the method described in Chap. 4, thermal decomposition of UAA, ThAA and ThA precursors in organic media using OAM and OA as reducing and capping agents led to high-quality monodispersed UO_2 nanocrystals and ThO_2 rod-shaped nanocrystals. Reduction of surfactant quantities with respect to the metal content, as well as scale up of the method from 0.1 g of nc-UO_2 as reported by [Wu et al., 2006] to 2.3 g of nc-UO_2, was achieved. The same method was extrapolated for the synthesis of nc-ThO_2 and ThO_2 nanorods have been obtained. The reason for the rod-shape is unknown. due to hitherto unknown reasons. Batch sizes of 0.3 g ThO_2 nanorods were obtained by this means, i.e. much lower production yield than in the case of UO_2 nanoparticles. Different conditions for the heating rate, ageing time, ageing temperature and initial precursors (ThAA and ThA) were explored for the UO_2 and ThO_2 cases. However, similar results were always found, in terms of the structure and geometry (round-shaped for nc-UO_2 and rod-shaped for nc-ThO_2) of the precipitates. Perfectly crystallized solid phases, as studied by XRD, with the typical UO_2-*fcc* fluorite structure (*Fm-3m* space group), with an average crystallite size (spheres diameter) of 5.52 nm and a lattice parameter of 0.5431(0) nm were found for the UO_2 case, also in agreement with the average size observed by TEM (4.9(3) nm) (Fig. 4.13 and 4.15) and DLS (3.7(1) nm). Typical ThO_2-*fcc* fluorite structure (*Fm-3m* space group), with a crystallite size (rods diameter) of 1.42 nm and a lattice parameter of 0.5579(1) nm, was found for the ThO_2 nanorods (Fig. 4.16 and 4.17). In both cases, the precipitated nanoparticles were well protected against flocculation, since no aggregation has been observed on the TEM images.

Regarding the advantages and disadvantages of the two types of nanoparticles synthesis methods (in aqueous or in organic media) in this work, different aspects can be considered. In terms of production yields, 2.3 g nc-UO_2 per batch were obtained by thermal decomposition of UAA in organic phase (Chap. 4). This is considered a real improvement vis a vis the original results by this method (0.1 g/UO_2 per batch) obtained in literature [Wu et al., 2006]. Nevertheless this material output was considerably lower compared with that achieved with the precipitation method in aqueous media (10 g UO_2 per batch) described in Chap. 3.

Another advantage of the aqueous controlled precipitation respect the organic thermal decomposition, could be also the avoidance of organics in the system which on larger scale can be a safety factor, as well as economic. These foreign organics capping nanoparticles could have detrimental effects during the sintering of the compacted pellets and the properties obtained afterwards. With the increase of temperature, these organics, convert to volatile gases on burning, would be released from the material, leading to impurities, and to possible internal fractures and to reduction of the final material strength.

A disadvantage of the aqueous method is the more difficult dispersability of the raw material, which could affect the microstructure uniformity and could induce possible abnormal grain growth during the pre-sintering and sintering steps, if a memory effect of the agglomerates shape is retained during these stages. The thermal decomposition in organic media had the peculiarity that nanoparticles with very narrow (monomodal) size distribution are obtained, which for some applications (e.g. markers in solution, etc) would be very convenient. However, it must be proved by tests whether this characteristic of the powder would represent a real advantage (or perhaps otherwise a disadvantage) for producing sintered pellets, since in the production of bulk materials by powder technology, practice shows that maximum green compact densities and maximum sintered densities are obtained using multi-modal powder size distributions.

ThO_2-nanofibers or nanorods instead of spherical nanoparticles were rendered by the method of thermal decomposition of ThAA (or ThA). More studies should be done to obtain similar spherical shaped nanoparticles, as obtained with UO_2.

Finally, in terms of possible improvements of both type of methods tested in Chap. 3 and Chap. 4, various possibilities could be considered. The first would be to try to change the precipitation media in the organic method. This would have the aim to lower the precipitation temperature, trying to avoid the use of the cracking agent oleylamine (OAM), which induces the decomposition of the precursor metal-acetylacetonate (UAA). In this case, this expensive and only limitedly available precursor could be replaced by a more accessible U-salt. The use of oleic acid as dispersing agent, which helps to keep small the size of the precipitated nanoparticles by acting on the surface tension, will still be needed.

Another possible improvement of the organic method to be analysed would be the possible change of the precipitation media, with the aim of reducing the acceleration needed for solid separation by centrifugation, which would imply a technical simplification. Also, the addition of certain amount of acetone to the organic media could be analysed, to enhance the particle's precipitation, which could eliminate the use of centrifugation in particle's separation and the use of filters. In all these, however, care is to be taken that particle's aggregation is not induced.

With regard to the aqueous precipitation method, the possibility of eliminating the electrolytic reduction step could be analysed, by just inducing the precipitation in the U^{+6} state instead of in the U^{+4} state reducing the material in the posterior thermal treatments. Here it is to be considered that possibly the precipitation in the U^{+6} state might not lead to incipient nanosized precipitates but to larger particles. Also the possibility of obtaining abnormal particle (or grain) growth during the powder conditioning (reduction) and sintering treatments need to be analysed.

8.2 Crystallization and Grain Growth in f(T) for nc-UO_2.

To study the composition of the precipitates obtained by the both methods described in Chap. 3 and Chap. 4 and their propensity to thermal growth in the unconsolidated state, further analysis of the precipitated material annealed at different temperatures

was performed by applying the thermal analytical and X-ray scattering techniques like TGA/DTA, XRD and HT-XRD, spectroscopic techniques such as XAS, NMR and IR and characterization techniques like TEM. The results were detailed and discussed in Chap. 5 and Chap. 6.

TGA and DTA were employed under inert atmosphere. The weight loss observed for the material synthesized in aqueous media (Fig. 5.1) was most likely attributed to water desorption and to crystallization (completion of the UO_2 *fcc*-structure). The weight loss observed for material synthesized in organic media, was attribute to residual water from the precursor, but mainly to organic volatilisation and crystallization. However, in both cases there was no reason to believe that the weight loss did not include as well some loss of oxygen due to reduction of the material. A deeper analysis on the lattice parameter and crystal growth under inert and reducing atmospheres was then performed to confirm the latter.

The evolution of the crystallite size, the lattice parameter, and the strain were determined from ambient temperature up to 1200°C under inert atmosphere. For the aqueous precipitated nc a weak effect on the crystallite size occurred below 700°C and it remained below 7 nm (Fig. 5.2), while a strong expansion of the lattice parameter was measured (Fig. 5.4). Above 700°C, the size of the crystallite increased quasi linearly but drastically with temperature, reaching a size about 73 nm at 1200°C. A recovery of the UO_2 typical crystal structure was achieved with temperature under static He atmosphere from the initial lattice parameter value of 0.5417 nm from the nc-UO_2 as-produced to 0.5473 nm after thermal treatment at 1200°C (measurements done after cooling). For the organic precipitated nc, a pre-thermal treatment was done to avoid any possible decomposition of the nc-UO_2 organic layer in the static atmosphere of the HT-XRD chamber. The crystallite size change with temperature showed a small growth up to 700°C, an intense growth from 37 to 150 nm at 1100°C (see Fig. 6.3). The nanocrystallites stabilized at O/U 2.0 at temperatures above 750°C (particles sizes >44 nm).

The linear thermal expansion coefficient (LTEC) was initially higher for nc-UO_2 from the aqueous method than for bulk-UO_2 for temperatures below 400°C and tended to stabilize (at O/U 2.17-2.18) above 600°C (crystal sizes >6 nm), when the nanocrystalline material met the thermal-expansion behaviour (i.e. thermal expansion coefficient) of bulk (large-grained) UO_2 (Fig. 5.5). This showed once more that the ab-normal nano-effects in the material was only observed for particle sizes below a few tens of a nanometer. Similar behaviour was observed for the nc-UO_2 from the organic method.

The strain decreased with temperature and was completely released at 700°C for the aqueous method material (Fig. 5.7). Above this temperature, the sintering of the nanocrystallites began and reached a size of about 73 nm at 1200°C. In the organic case, the strain was totally released at 1000°C when a high increase in the crystallite size began (from 88 nm at 1000°C to 150 nm at 1100°C). So the crystallite growth seemed to be limited by the presence of the lattice strain.

8.3 Structure and oxygen-stoichiometry studies by XRD, XANES, EXAFS, NMR AND FTIR.

The evolution of the crystallite size, the lattice parameter, and the strain under reducing atmosphere was also studied and compared to the reference bulk-$U^{IV}O_2$. The lattice constant of the material in the cooled state after reach different maximum temperatures (600°C and 1200°C) was measured. This allowed separation of the thermal expansion contribution in the high-temperature values to obtain cleaner curves for thermal expansion vs. temperature and lattice dimension vs. crystal size. No big differences in size, lattice and strain, were observed between inert and reducing atmospheres (measurement after cooling) for the material obtained with the aqueous method (Table 5.1). However, a notable change in the crystallite size was observed for the material obtained with the organic method at 1100°C, with a size of 150 nm under He and a size of 12 nm under Ar/5%H_2. Also differences in the lattice parameters as a function of the atmosphere in the organic case, were observed. A value of 0.5472 nm at 1100°C under He (Fig. 6.7) and 0.5461 nm at 1200°C under Ar/H_2, were measured. However these difference were probably due to the pre-thermal treatment (before the HT-XRD measurement under He) done under O_2 and Ar/H_2 which ended already in a size of about 37 nm and a lattice parameter of of 0.5462 nm at 700°C. In the evolution of the lattice strain (e), a release was observed with increasing temperatures. After annealing at 600°C under Ar/5%H_2, just little strain was released (from 0.702 to 0.664%), and totally disappeared at 1200°C (0.004%), as was also observed under He atm after 1100°C. Comparing the aqueous and organic produced material under reducing atmosphere (without pre-thermal treatment), no big change was observed until 600°C anneal, but at 1200°C. A size of 82 nm for the aqueous method material vs. 12 nm for the organic method at the last temperature under Ar/5%H_2, were measured. That could be ascribed to the organic layer protecting the organic precipitated nanoparticles.

XANES was used to determine the oxidation state of U cations and the corresponding molar fractions and the O/U ratios were derived. The XANES spectra at the U-L_3 edge for the aqueous method material (Fig. 5.10) and for the organic method material (Fig. 6.10), showed similar trend with increasing temperature and as the stoichiometry shift (x) decreased (UO_{2+x}). The samples studied were nc-UO_2 as produced and after thermal treatment at 600°C and 1200°C under Ar/5%H_2. The peak of the WL shifted slightly to lower energies and increased in intensity, and the oscillations within the XANES regions increased. The amplitude decreased with the increasing temperature of thermal treatment showing a higher structural order of these samples. For the as-produced (RT) and at 600°C samples, there was a significant difference of shape compared to the $U^{IV}O_2$ reference, i.e. presence of a shoulder on the high energy side of the edge. This was in agreement with the observed decrease of WL amplitude with the increasing temperature. The shoulder decreased with temperature meaning that there was less U^{VI} or that the U^{IV} bulk was more visible as it size increased. A clear shift (further for the RT sample) of the absorption edge and WL-peak to higher energies, as well as a broader WL was observed. In the aqueous method material the spectra for the $U^{IV}O_2$ reference and the annealed sample at 1200°C, were remarkably similar, indicating that the electronic structure of the 82 nm UO_2 was essentially that of the bulk $U^{IV}O_2$ at that temperature. However, for the organic method material, the spectra for the annealed sample at 1200°C was still following the same tendency as the other samples at RT and 600°C, indicating that the electronic structure of the 12 nm UO_2 was still not $U^{IV}O_2$.

These effects on the WL could be due to the size of nc-UO_2 samples, but also to the stoichiometry shift of the synthesised material. To quantify these effects a dedicated study with UO_2 nano materials with exactly same stoichiometry, possibly at the exact stoichiometry (U^{IV}), but with different crystal sizes, would have been necessary. That was, at this moment not possible with the synthesized nc-UO_2 where just one-size samples where synthesized and different particle sizes were obtained by thermal treatment. Under this treatment, not just a change in size occurred, but also a change in valence, even under inert atmosphere (Fig. 6.9). So, in principle, because of this size effect, determining the O/M from the shift is dubious but it was the only option at that time. Anyway, for the RT, 600°C samples (aqueous route) and for the RT, 600°C and 1200°C samples (organic route), it was clear that there was U^{VI} contribution not only from the shift but also from the shoulder (which was indicative of the uranyl).

A beautiful way to study the size effect, could be the use of a nano-material with a unique valence state i.e. thorium dioxide (ThO_2). From the synthesized nc-ThO_2 (Sec. 4.4.1.2), different sizes could be obtained under thermal treatment without changing the valence of the material. ThO_2 can only exist in one oxidation state, Th^{IV}, and is eliminated all discussion on the influence of the O/M ratio on the results obtained. Any changes in the XANES, would be just do to the size of the particles.

In Chap. 6, a study of the as-produced nc-ThO_2 (Chap. 4) was also done. In the XANES spectra (Fig. 6.12) at the Th-L_3 edge, the peak of the WL corresponding to nc-ThO_2 at RT (as-produced) had an identical position and amplitude as the one for the reference spectra of $Th^{IV}O_2$-bulk. Corroboration by XRD was also obtained (lattice constant of a=0.5579(1) nm) vs. a=0.560 nm for the ThO_2 standard). This identical behaviour suggested that the displacements observed for nc-UO_2 were not due to the size of the particles, rather the valence. Slightly less intensity for the peak of the WL was observed, as well as less oscillations for the nc-ThO_2. So for this point, one could think there might be a small size effect on the interatomic distance and ordering. The size effect observed for the nc-ThO_2 as-produced was less than that observed for nc-UO_2 (as produced, 600°C and 1200°C) with bulk-$U^{IV}O_2$. So even if there might be a small size effect, the valence might be the major cause for the differences observed with bulk-$U^{IV}O_2$, also confirmed by the lattice contraction by XRD. Having that in account, determining the O/M from the XANES shift would be justified.

In the k^3-weighted EXAFS spectra for the aqueous method particles (Fig. 5.11a), the oscillations and their amplitude increased with thermal treatment. The 4 nm as-precipitated sample was very difficult to fit with a pure fluorite structure, as the fit were non stable and the data noisy. A significant static disorder was found and a shorter distance for the oxygen shell (U-O bond length) was clearly observable for the nc-UO_2 at RT which did not correspond to any U-oxide. The intensity of the FT was very low limiting the interpretation of the coordination shell to U-O_1. Observing the EXAFS results in Table 5.3, the data were heavily dampened at RT where a large value for the DW factor was found, meaning a significant static disorder for the nc-UO_2 as-produced. Shorter distance for the oxygen shell (U-O bond length) was clearly observable for the nc-UO_2 at RT which did not correspond to any U-oxide. According to the shape of the first FT peak, it looked like there were two or three U-O distances instead of one. This was consistent with the observed lattice contraction (0.5417 nm)

from XRD at RT (see Table 5.2).

The 9 nm sample (600°C anneal) showed an intermediate ordering with oscillations clearly identified and extending to k = 9 $Å^{-1}$. The intensity of the FT was also low for this annealed sample, limiting the fitting and interpretation of the coordination shell to U-O_1 and U-U_1 together with UO_2 fluorite structure. Still a large value for the DW factor was found (Table 5.3). Shorter distance was also present for the oxygen shell (U-O bond length) in comparison with the reference-$U^{IV}O_2$. However the U-U_1 bond length was closer to that of the bulk-$U^{IV}O_2$, suggesting that the U-U_1 lattice was more ordered than the O anion sublattice. The U-U_1 lengths were consistent with the less lattice contraction (0.5431 nm), in comparison with the nc-UO_2 as-produced, as probed by XRD at 600°C anneal.

Ultimately, at 1200°C and 82 nm, EXAFS oscillations were similar, if not entirely matching, those of the bulk-$U^{IV}O_2$ indicating same *fcc*-structure consolidation and substantial particle growth, both observed in XRD measurements (Fig. 5.12). Both shells were well fitted with *Fm-3m* structure for this sample (Fig. 5.13) and very similar distances to reference $U^{IV}O_2$ structure could be observed according to the FT (k-range treated = 3-12 $Å^{-1}$). That was in agreement with the similarity for the XRD data for the annealed sample at 1200°C and the bulk-$U^{IV}O_2$ (Fig. 5.8). Also consistent with the XANES (see Fig. 5.10) showing no different oscillation from the fluorite structure.

In the k^3-weighted EXAFS spectra for the organic particles (Fig. 6.11), the oscillations and their amplitude slightly increased with thermal treatment, also. The 5 nm as-precipitated sample was very difficult to fit with a pure fluorite structure, as the fit were non stable and the data noisy. Nevertheless, also the samples treated at 600°C and 1200°C presented a high degree disorder, as it was already predicted from the XANES analysis (Table 6.1). Therefore a good fit could not be achieved considering only bulk-$U^{IV}O_2$, meaning that another unidentified phase must be taken into account.

NMR Hahn-echo ^{17}O MAS spectra could be acquired for samples prepared by the aqueous method after annealing at different temperatures (Fig. 5.15) under reducing atmosphere (Ar/5%H_2). Three different oxygen environments could be identified (Fig. 5.18) from the fitting of the chemical-shift signatures of these samples, i.e., the records of the ^{17}O-resonance-frequency peak displacement with respect to that of a reference specimen, expressed in relative units (ppm). In the present case, the ^{17}O-resonance of a ^{17}O-doped H_2O sample was taken as reference, and defined as 0 ppm. The first identification corresponded to oxygen species having a chemical shift of nearly 900 ppm and was found for samples annealed up to 650°C. The two other types of oxygen species identified appeared clearly in the temperature range 650°C-1200°C. These new species, i.e., one showing a sharp and the other a broad ^{17}O-peak, could be respectively attributed to ^{17}O in a well crystalline environment and in a more disordered one; the last due to the larger peak broadening. Both peaks diminished strongly their chemical shifts and half-maximum widths in the temperature range 650°C-800°C, to converge rapidly at temperatures above 800°C to values near those of the sample annealed at 1200°C, i.e., respectively, 717 ppm (chemical shift) and 5 ppm (FWHM), which due to very small peak broadening (FWHM) indicated a very well crystallized environment. This last was still slightly bigger than the 3 ppm found for $U^{IV}O_2$-bulk. Despite this, the chemical shift (717 ppm) was the same as that found

for $U^{IV}O_2$-bulk. Hence, one can say that the environment around the oxygen lattice positions in the case of the sample with the biggest crystallite size (∼80 nm) was very close to that of $U^{IV}O_2$-bulk. Based on the FWHM, one can say that to observe the signal of crystalline UO_2 a crystallite size above 80 nm should be reached. This is in line with the observation by XRD of an UO_2-*fcc* structure with lattice parameter 0.5472 nm in this case (Fig. 5.8).

Several samples from the aqueous method at key annealing temperatures were also analysed under the FTIR spectrometer (Fig. 5.19). In the case of nc-UO_2 as-produced (RT), four peaks in the range 400-4000 cm^{-1} could be observed. They could be assigned to the bending vibration of H-O-H of the coordinated water, and to a possible more oxidised state (UO_{2+x}). All these peaks diminished in intensity with annealing temperature. The peaks assigned to the H-O-H of the coordinated water, totally disappeared at 600°C. That was in agreement with the TGA, were nearly no weight of loss was observable after 600°C (see Fig. 5.1). However two of the peaks finally disappeared at 1200°C. That could be an artefact due to the small size still present at 600°C (10 nm). Hence, at 1200°C the IR spectra looked like the one for the $U^{IV}O_2$ reference and grains were about 80 nm. That was also in agreement with the results above commented by XANES where a different electronic structure at 600°C was seen, meanwhile at 1200°C a similar structure to bulk-$U^{IV}O_2$ was found (see Table 5.2). Also EXAFS was characterized for a poor ordering at 600°C but entirely matching with the bulk-$U^{IV}O_2$ oscillation pairs at 1200°C (see Table 5.3).

Isothermal grain-growth study of the synthesized nc-UO_2 was then performed. For the annealing temperatures of 500°C, 700°C and 900°C and a static and inert atmosphere of He, the grain growth took place in the first hours of isothermal hold until a stable average crystal size was established at the applied temperature, at which time grain growth ceased (Fig. 5.21). For the isotherm at 1200°C and a static atmosphere of He, the material had a continuous growth not reaching a constant grain value in the first 50 h (Fig. 5.20). An activation energy of diffusion of 0.93 eV to 1.25 eV was obtained (Fig. 5.23). Diffusion can occur along the grain boundary, or it can occur intragranularly (volume diffusion), or because of grain defects. The grain boundary diffusion is always faster than the volume diffusion, meanwhile the volume diffusion occurs within a single grain and is only important at higher temperatures. In this case of nc-UO_2, the low activation energies obtained could be then related predominantly to grain boundary (surface and interface) diffusion.

A lattice of about 0.5472 nm was already found for the samples treated at 900°C after 50 h dwell time under Ar/H_2 obtaining a final size about 50 nm (Table 5.5). Therefore a temperature of 1200°C (and in consequence a final crystallite size of 80 nm) would be, in principle, not necessary to reach the typical lattice parameter of the reference large-grained UO_2 (a=0.5472 nm), as above commented.

An average crystal size of 322 nm was measured after cooling for the heat treatment at 1200°C after 50 h dwell time under He (Table 5.5). Taking that into account, it appears that a temperature below 1200°C would be necessary in the sintering process of the monoliths to avoid extreme growth of the particles (>200 nm). Nevertheless for the nc-UO_2 samples annealed at 1200°C during 50 h under Ar/H_2 dynamic atmosphere, a final crystal size of 85 nm was measured after cooling. Even after 200 h dwell time at this temperature under reducing atmosphere, a final crystal size of 150 nm was seen (quite far from the 322 nm observed under He atmosphere after 50 h). This

difference could be due to the initial oxidation state of the nc-UO_2 samples and their evolution under a static He atmosphere. An hyperstoichiometric UO_2 would present a stronger increase of the self-diffusion coefficients and in the same way raise the mass-flow, for which enhanced grain-boundary motion and grain (or crystal) growth will occur Fig. 5.24. Differences in the diffusivity in the grain boundaries between micro- and nano-grain have been seen already in other fluorite structure metal oxides [Martin, 2007]. In fact the differences in the diffusion coefficient between bulk-large-grain-UO_2 and nc-UO_2 are compatible with an enhancement of the diffusion processes either by a diminishing of the grain size or by O/U>2 effects.

8.4 nc-UO_2 monolith consolidation and characterization.

Conversion of nanoparticle systems into dense nanostructured monoliths has been achieved. The purpose was the synthesizing UO_2-nuclear fuels mimicking the high burn-up structure (HBS) of LWR-fuels (nanostructured), for which improved properties are expected compared to standard fuel [Spino et al., 2012]. Monoliths with the two kind of nc-UO_2 obtained by the precipitation in aqueous media (Chap. 3) and in organic media (Chap. 4), were produced.

Different alternative routes for consolidation (e.g. conventional uniaxial pressing, float packing, etc.) into green bodies (Fig. 7.4) have been tested (Sec. 7.2). Afterwards the green bodies were sintered at temperatures between 900°C and 1200°C under Ar/H_2 atmosphere. The optimum sintering conditions were deduced from the long-isothermal crystallite growth studies under He and Ar/H_2 atmosphere (Table. 5.5). This ensured lack of disproportionate grain growth risks even at the highest temperature used of 1200°C. Also thermal pre-conditioning of the powder before pressing was in some cases done to avoid cracks during the sintering step due to the presence of water or organics (depending on the case) in the material. Therefore the organics presence did not have a detrimental effect during the sintering of the compacted pellet when the porosity of the ceramic becomes closed. The pellets sintered presented a strong appearance although fine cracks were visually observable in some cases (Fig. 7.11 and 7.12). Sintering densities between 75.5-90.5% of the theoretical density (TD_{UO_2}=10.96 g/cm^3), were obtained (Table. 7.1). An average grain size of ∼200 nm, replicating the HBS, was obtained for all the different sintered nc-UO_2 pellets.

Complementary dilatometry experiments were performed to compare the shrinkage of the fabricated nc-UO_2 pellet with that of bulk-UO_2 (large grain) produced by a standard fabrication process. Enhanced sinter activities of the nanocrystalline materials compared to microcrystalline UO_2 were found at lower temperatures. The temperature range from onset to completion of the densification occurred at much more lower temperatures (Fig. 7.14) for the nc-UO_2 (200-955°C, with a maximum sintering rate at 740°C), compared to the bulk-UO_2 [Lahiri et al., 2006] (900-1540°C, with a maximum sintering rate at 1200°C). The reason of that might be the higher surface present in the nc-UO_2 compared with the bulk-UO_2 material, rendering the sintering to become more effective (at lower temperatures). The sintering activation energy was determined as $Q = 171 \pm 7\ kJ/mol$ assuming surface diffusion and $Q = 114 \pm 5\ kJ/mol$ assuming volume diffusion for the nc-UO_2 monolith, compared to

$Q = 287\ kJ/mol$ determined for bulk-UO_2 in the literature [Lahiri et al., 2006]). Both diffusion mechanisms showed low values of the sintering activation energies as typical for nanopowders. The obtained sinter activities at much lower temperatures that the typical temperatures used in the sintering of standard UO_2 monoliths would represent an important technological advantage by energy saving.

Characterization of macrostructures by optical microscopy (OM), and microstructures by fresh-fracture observation by SEM, for different samples at different magnifications, was performed. Not well defined grains were observable in the fresh-fracture SEM images of the pellets sintered at low temperature of 900°C (Fig. 7.20). The sinter of the crystals was still under development, therefore sintering temperatures of 1200°C were used afterwards. Macrocracks across different samples were observed, but not for the monoliths from nc-UO_2 synthesized by the organic-route with powder thermal pre-treatment (*Organic-Pressed-PTT* - Fig. 7.22), and not for the monoliths from the float-packing consolidation method and powder of the aqueous-synthesis (*Aqueous-Float Packing* - Fig. 7.19). All macrostructures, with exception of the last one (*Aqueous-Float Packing* - Fig. 7.19), showed non-homogeneous densification (residual porosity between densified areas). Also the conventional pressed sample of pre-dehydrated powder from aqueous route (*Aqueous-Pressed-PTT* - Fig. 7.17) showed a good quality in comparison to the rest, from the point of view of the densification. However, improvements in the performance of the monoliths would be necessary to avoid the problem of cracks in the sintered pellets (and therefore the diminishing material's properties).

Looking at the fresh fracture surfaces, the microstructure of the aqueous-route-powder pellet produced by float packing consolidation ((*Aqueous-Float Packing*)) and sintering at 1200°C, was the closest approximation to the HBS material obtained until now (Fig. 7.21b). The average grain size for the different monoliths was in the 170 nm to 250 nm range. Here a major success of this work was achieved.

Mechanical properties as Vickers Hardness (H_V), Knoop Hardness (H_K) and Young's modulus (E) were determined for sintered nc-UO_2 pellets. An increase in hardness (H_V) and low values for E-modulus (up to 30%) were in general seen for the different nc-UO_2 monoliths (Table 7.2) in comparison with bulk-UO_2. Also scanning acoustic microscopy (SAM) was used for the estimation and comparison of the Young's E-modulus obtained by indentation. The results by SAM (E=150 GPa) matched the ones derived from microindentation (E=155 GPa). This difference observed with respect to bulk-UO_2 pellets (220 GPa), could be influenced by microstructure imperfections (nanocavities at triple-grain junctions, pores, cracks, etc.). However, the drop was still too large to be attributed only to the presence of cavities. The same type of tendency observed in the nc-UO_2 specimens, i.e. with increase of H_V values and decrease of the E-modulus values, has been found before in irradiated standard-UO_2 fuel at high burn-ups. In this case also the E-modulus decrease could not be fully attributed to a porosity increase and was to contradict the effect of the fission products dissolution, which causes in reality an increase of the material's stiffness. Since with the increase of BU the irradiated nuclear fuels transform into a nano-recrystallized structure [Spino et al., 2012], the effects of (partial) H_V-increase (fission products dissolution causes as well hardening) and additional E-modulus decrease (beside that caused by porosity) like the effects observed in the present work could be attributed in high BU fuels due to the nanostructure.

The confirmation of the size-dependent physical-chemical properties of nc-UO_2 has been successfully accomplished. So the compressibility of nc-UO_2 was proved in fact to be larger than that of standard-UO_2. A size-dependence of the thermal expansion properties of nc-UO_2 was also confirmed. The thermal expansion was shown to increase with the size-decrease (see Fig. 5.5 and Fig. 6.6), at the time that the bulk modulus decreased. This is compatible with the Grüneisen relationship showing a constant product between the thermal conductivity and the bulk modulus. However, verification of the trend in the specific heat (Cp) is still lacking, which is indeed neeeded to complete the Grüneisen-relationship analysis.

Regarding the material's compressibility, in-situ high pressure X-ray diffraction (HP-XRD) has been performed for the study of the bulk modulus dependence on the crystal size in nc-UO_2. Three different nc-UO_2 sizes (4 nm, 6 nm and 34 nm) were studied up to a pressure of 27 GPa and the corresponding compressibility constants B_0 and $B_0^{'}$ determined are summarized in Table 7.3. The bulk modulus of UO_2 suffered an extreme decrease in the nano-size particle range. For the 4 nm-size nc-UO_2-particles, a bulk modulus (B_0) around 40% lower than the one measured for bulk-UO_2 (micron-size grains) [Pujol et al., 2004], has been observed. The Vinet equation of state showed the best fit to all the compression data. Discontinuities were identified in the plot of normalized pressure vs. finite strain. A shift to higher strains with decreasing particle's size was observable which could indicate the presence of different electronic properties for the smaller particle's sizes of UO_2 [Zvoriste-Walters et al., 2013]. This confirmed the dependence of the bulk modulus with the crystallite size. However, studies with bigger particle sizes as the ones here studied (>34 nm) would be necessary to guarantee that the tendency observed in the monoliths (decrease of E-modulus), is due to the size of the grains and not just because of imperfections and porosity possibly present in the samples.

The results of thermal diffusivity tests of the compacted nc-UO_2-material showed similar behaviour as that of standard, nuclear grade UO_2 (bulk). The thermal diffusivity for sintered nc-UO_2 (∼200 nm, 90% density), was determined between 254°C to 1165°C. Extrapolation to 95% density was done and same thermal diffusivity as standard bulk-UO_2 pellet [Fink, 2000] with 95% density was found. Regarding the feared worsening of the thermal conductivity of the HBS material due to grain-size effect (Kapitza resistance), it has been here shown that no thermal properties deterioration has to be expected for the 200 nm-UO_2 pellet material mimicking the HBS.

Determination of the melting point by laser-heating and pyrometric temperature detection has been performed for compacted nc-UO_2 with two different nano-grain sizes (about 10 nm and 200 nm) and their variation with respect to bulk-UO_2 (large-grain), assessed. A melting point depression of about 150°K with respect to the normal value of bulk-UO_2 was found for the 10 nm-size nc-UO_2 sample (Fig. 7.39). This reduction would be a priori due to the nano-size grains. However, the measured lattice constant of the sample before melting (a=0.5438 nm) was below the value of bulk-UO_2 (a=0.547 nm) and indicated in reality a hyperstoichiometric oxide, which would also cause a melting point decrease. To corroborate the measured tendency with the grain-size reduction, a strictly stoichiometric nc-UO_2 sample would be needed. However, an identical melting point as for bulk-UO_2, was found for the 200 nm-sample (Fig. 7.40) for which a stoichiometry of O/M=2.00 was confirmed from the lattice

constant measurement before melting. This result is important for the use of nc-UO_2 ceramics as nuclear fuel. Indeed, a lower melting point would pose a problem for the licensing of the monoliths as a fuel for the reactor. Fortunately the possibility of a lower melting point disappears for the 200 nm-UO_2 samples, as it would occur for the HBS material in the reactor, too. Again this is an important technological result of this work.

So, postulated nano-effects such as diminution of the thermal conductivity and the melting point could be here excluded as weak points for the use of nc-UO_2 as a nuclear fuel. These effects might be relevant for very low crystal/grain sizes ($\sim$10 nm) but they disappear for grain sizes of $\sim$ 200 nm, where, conveniently, the sought advantageous properties of the nano-structure (super-plasticity, low swelling under Xe-bombardment [Spino et al., 2012], self-limiting grain growth, etc.), still remain. This anticipates the lack of property loss of the developed nc-UO_2 monoliths for technical applications in this size range.

Chapter 9

Future Recommendations

9.1 Synthesis of the nanoparticles.

9.1.1 Synthesis of ThO_2 nanoparticles to study a unique valence system.

The major problem found by the study of the UO_2 system was the presence of two variables, namely the size of the particles and the U-valence. Studies on the ThO_2 system would facilitate steadfast conclusions due to its unique valence (IV). The organic route has been already tested but more data is needed. Also, not nanoparticles rather nanorods were obtained. Synthesis by the aqueous method of ThO_2 nanoparticles would be another option. In this case, no electroreduction steps would be needed.

9.1.2 Synthesis of PuO_2 nanoparticles and ^{238}Pu doping to enable damage in the nc-UO_2.

Preliminary test with ^{239}Pu have been performed using the aqueous route method. This system has the inconvenience of its multiple valences (III, IV and V) but luckily the IV valence state is the most stable. Further (U, $^{238}Pu)O_2$ nanoparticles would permit damage studies and simulate what occurs in the reactor.

9.1.3 Synthesis of nanoparticles of different controlled sizes.

The pressing and sintering of pellets from monosized UO_2 nanoparticles with respectively different sizes. Ultimately to compare their mechanical properties in dependence on the patricle's size. This could be achieved by precipitating the particles in small pH intervals for the aqueous route and to collect separately the particles obtained at each interval. For the organic route, parameters playing a role in the growth of the nanoparticles are heating rates, ageing temperature and time, precursor concentration, surfactants ratio, types of solvent, etc.

9.1.4 Use of ThO_2 nanorods as reinforcement in the the nc-monoliths to increase strength.

The ThO_2 nanofibers were obtained by the organic route (Fig. 4.16) and they could have a potential use to induce material reinforcement, i.e. to increase the strength

of the sintered nc-bulk, for instance by producing mixtures of nc-UO_2 and nc-ThO_2 (nano compounds) [Wan et al., 2006a], [Wan et al., 2006b], [Mazaheri et al., 2010], [Mazaheri et al., 2011]. SiC (or Mo) nanorods (or nanofibers) for nc-UO_2 bulk reinforcement, would substantially increase its thermal conductivity [Patzke et al., 2002], which would improve its operating safety.

9.2 Basic science of nc-actinide oxides.

First tests to determine magnetic properties of nc-samples were performed with the Actinides Research department in ITU. The main conclusion was the observation of a remaining signature of the magnetic order similar to the single crystal even at the lowest size (about 31°K), further a clear decrease of the susceptibility with decreasing size was observed (see Fig. 9.1 and Fig. 9.2). This can be explained by a reduction of the magnetic moment on U. New test are are planned. This is an untested domain, and is relevant as computational methods are today based in nanoscale clusters.

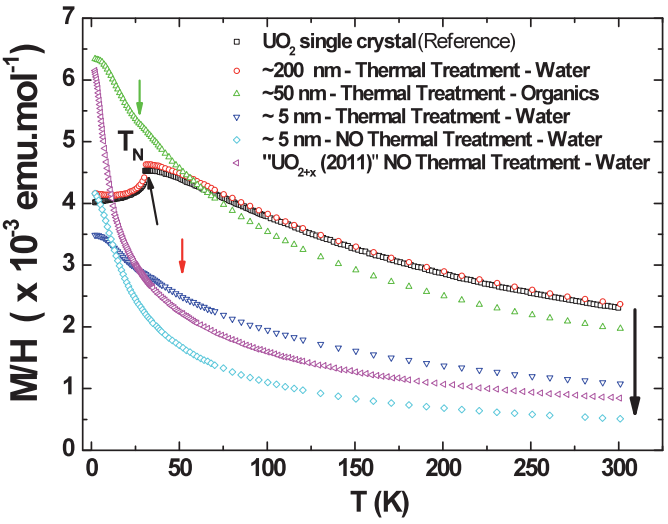

Figure 9.1: Magnetic susceptibility at 70 KOe for nano materials and 10 KOe for single crystal.

9.3 Alternative monolith compaction and sintering methods.

9.3.1 Sintering of commercial nc-Y-ZrO_2 by spark plasma sintering (SPS), as substitute of nc-UO_2.

During this thesis another sintering process, spark plasma sintering (SPS), was tested. Using alternating current, the device applies a pressing force at high temperatures (but much lower that the 1600°C used in a conventional sintering process) for a shorter period of time. nc-UO_2 compaction by SPS was not possible as the device was not implanted in a radiological facility. Instead commercial partially stabilized nc-Y_2O_3-doped tetragonal zirconia (4 mol% $Y_2O_3ZrO_2$ or nc-Y-ZrO_2) was utilized. This material was used already in a previous work performed at ITU

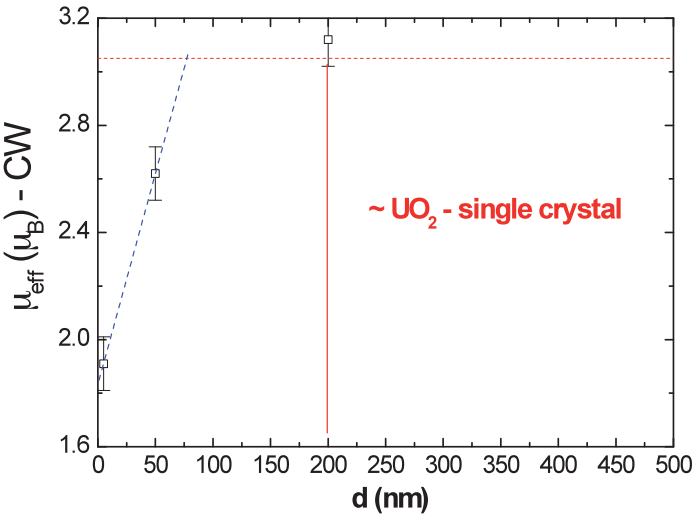

Figure 9.2: Effective magnetic moment extracted from the Curie Weiss law Model (CW) for the different size of nano materials.

[Santa-Cruz, 2009]). Nc-Y-ZrO_2 was used then to simulate the HBS-material due to its similarities (mechanical strength, slow creep and radiation resistance) of nc-Y-ZrO_2 with UO_2 [Spino et al., 2012]. However, possible discrepancies in the behaviour of the respective nano-phases (nc-Y-ZrO_2 vs. nc-UO_2) due to differences in the crystal structure (tetragonal vs. cubic) and reduction/oxidation behaviour (hypostoichiometric nc-Y-ZrO_{2-x} vs. hyperstoichiometric UO_{2+x}), were not contemplated.

Tests were performed at different temperatures. Increasing densities (measured by Archimedes principle) with increasing sintering temperatures were obtained (Table 9.1). The sintered pellets were about 19.80 mm in diameter and 4.78 mm high. A picture of a nc-Y-ZrO_2 pellet after SPS preparations is shown in Fig. 9.3. The black colour of the pellet is due to the SPS graphite matrix.

Table 9.1: Densities obtained for the nc-Y-ZrO_2 samples after SPS treatment at different temperatures.

T (°C)	**green density** (g/cm^3)	**TD (%)**[a]
nc-Y-ZrO_2 1250 °C	5.7146	93.68
nc-Y-ZrO_2 1300 °C	5.7735	94.65
nc-Y-ZrO_2 1400 °C	5.9960	98.30

Heating rates of 100°C/min under vacuum, applied pressure of 16 kN (50 Mpa) and dwellings of 5 min.
a.) TD_{Y-ZrO_2}=6.1 g/cm^3.

An examination of the macrostructure and microstructure of SPS produced pellets is shown in Fig. 9.4. The particles remeinded about 100 nm showing that this method bodes well for the future. SPS has two great advantages, namely lower temperatures and short time both of these inhibit grain growth.

Figure 9.3: Spark Plasma Sintering pellet of nc-Y-ZrO_2.

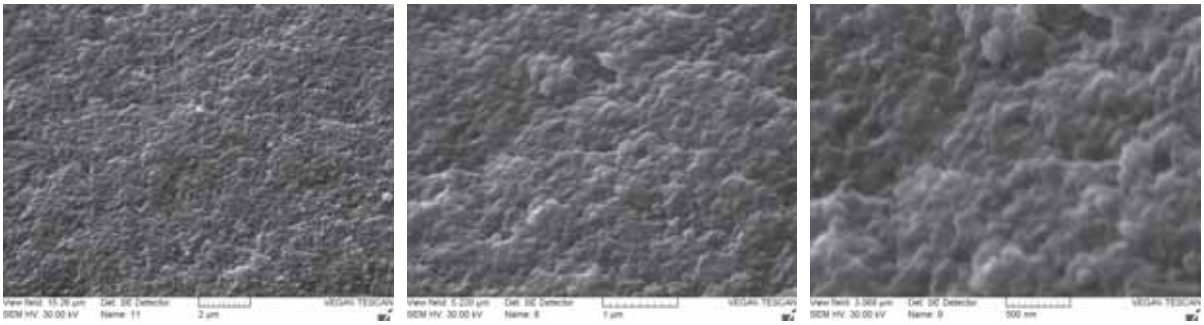

(a) The scale bar is 2 μm. (b) The scale bar is 1 μm. (c) The scale bar is 500 nm.

Figure 9.4: Microstructure of fresh fracture of nc-Y-ZrO_2 pellet by SPS.

9.3.2 Centrifugal casting

A centrifugal casting of an electrostatically stabilized colloidal nc-UO_2 precipitates solution could be another option for green compaction. The material in solution is then introduced in a tube and after being submitted under forces of 480.000 g, it stacks at the bottom of the tube as a pellet. The objective, is to obtain a high green density that would allow lower sintering temperatures. An ultracentrifuge (SORVALL® TH-660 Swinging Bucket Ultraspeed Centrifuge Rotor from Thermo Scientific), is already disposable in ITU to test this method further.

9.4 nc-UO_2 in extreme conditions.

The licensing of nuclear fuel is made on basis of its safety performance not just only under normal operation conditions, but also when a temperature rise occurs in the fuel. This could be caused in a Loss of Coolant Accident (LOCA) or in a Reactivity Initiated accident (RIA). Under such extreme conditions fuel fragmentation could occur. During this thesis, one attempt was made to mimic such an accident in an out of pile experiment using nc-Y-ZrO_2 as a sample instead of nc-UO_2. This test was made in a facility at ITU known as POLARIS, which permits very rapid laser heating of the sample. The ZrO_2 pellets used were sintered by SPS (see Sec. 9.3.1). The black colour of the pellet is due to the SPS graphite matrix.

The picture in Fig. 9.5 shows the pellet (produced by SPS) before and after the laser shot on the surface. The white area corresponds to the laser heated area. The temper-

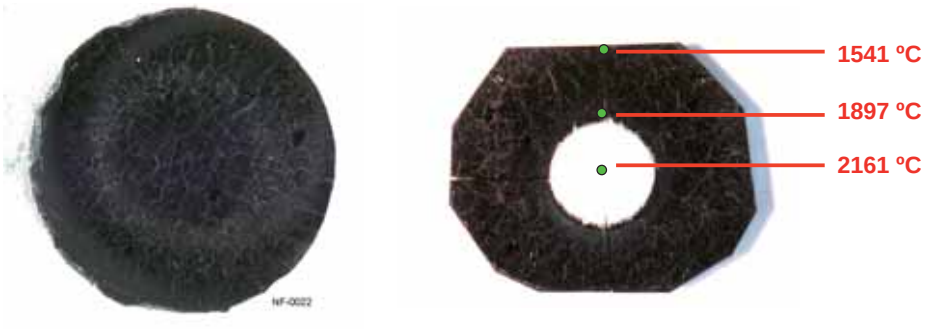

Figure 9.5: Spark Plasma Sintering pellet of nc-Y-ZrO_2 *(left)*. Optical microscopy of the fresh fracture for the thermal treated sample. The temperature gradients measured on the sample surfaced are also indicated *(right)*.

atures reached at the different areas are also shown. The duration of the test was about 20 minutes. Fresh fracture of the sample is shown in Fig. 9.6, while SEM measurements are presented in Fig. 9.7 which shows the evolution of the grain size on a fracture surface.

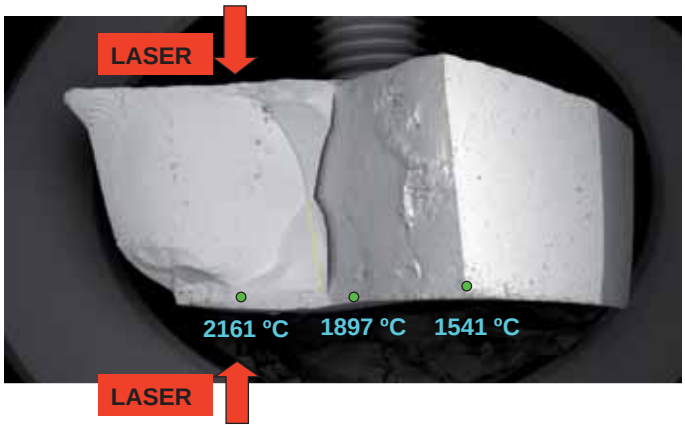

Figure 9.6: Fresh fracture of the thermal treated sample. Thermal distribution measured in the POLARIS facility. The temperatures were measured on the surface.

The initial material tested in POLARIS was pore free and its surface was flat. The laser treatment showed that a local swelling occurred through formation of porosity (see Fig. 9.7). This experiment was not perfectly well controlled, but it is likely that the observed swelling was due to CO or CO_2 gas generated when the carbon impurity in the material reacted with oxygen from the atmosphere, which caused pore formation, in a process similar to the production of foamed glass. A particularly interesting result of the test is that the formed pores were closed and astonishingly similar to those of the HBS-zone in high burn-up fuels. Chances appear therefore that during such kind of postulated fuel melting accident, at least part of the fission gas could be trapped in potentially forming closed pores, as it occurs in the HBS material at low temperatures. Although these experiments are preliminary they suggest a promising novel method to test the gas retention capability of the nc-UO_2 fuel under accident conditions.

Finally, another important method to understand the resistance of nc-materials to irradiation can be provided by ion beam irradiation tests. This can be done at facilities like the ANL (Argonne National Laboratory) IVEM-Tandem facility in Chicago, where

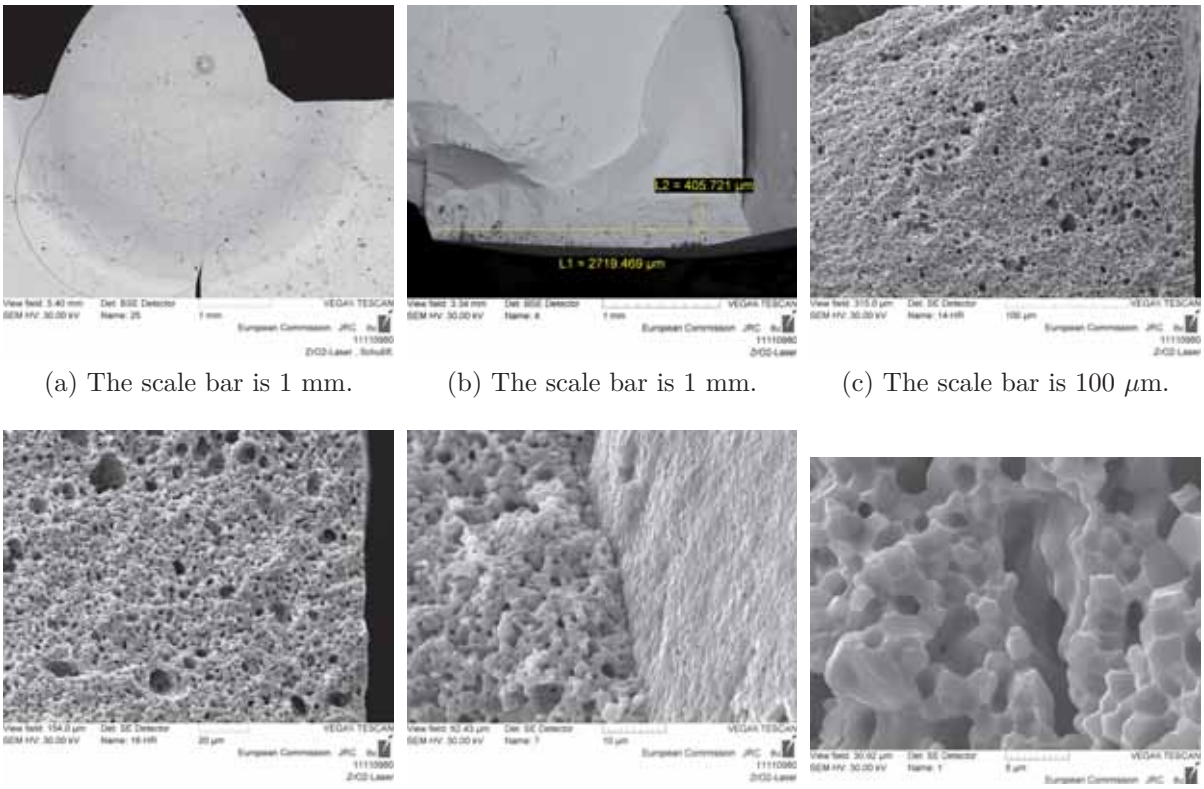

(a) The scale bar is 1 mm. (b) The scale bar is 1 mm. (c) The scale bar is 100 μm.

(d) The scale bar is 20 μm. (e) The scale bar is 10 μm. (f) The scale bar is 5 μm.

Figure 9.7: Micro- and macro-structure of nc-Y-ZrO_2 bulk specimens subjected to POLARIS heating experiments to simulate a Large LOCA event.

irradiation with inert gas ions (He or Xe) with on-line TEM observation provides a very useful way to implant the gas atoms and to evaluate how they behave in the matrix, e.g. dissolution therein, formation of bubbles, transport of bubbles along grain boundaries, etc.

Concluding Remarks.

Successful consolidation of the synthesized nanocrystalline UO_2 nanopowders into dense pellets mimicking of the High Burn-up Structure (HBS) as ideal system has been achieved. From the different synthesized nc-UO_2 powders (4-5 nm size) to the nc-UO_2 compacted monoliths with 200 nm average grain size and about 90% density were achieved. Stability of the structure after ageing and self limiting grain growth kinetics up to temperatures of 1200°C, were shown. The out-of-pile mechanical properties of sintered pellets (in terms of hardness and elastic modulus) were confirmed to closely resemble those of the HBS-material in-pile. Beneficial properties found, like stability of the structure, enhanced mechanical properties and self-limiting grain growth, strongly encourage the performance of irradiation tests to verify the in-reactor behaviour. As determined previously in out-of-pile tests of monoliths of the brother system of nanocrystalline nc-Y-ZrO_2 [Spino et al., 2012], a strong reduction of the gas bubble swelling, long term thermal stability of the pore-grain configuration, and striking superplastic behaviour and accelerated creep, would be expected as well for the developed nc-UO_2. Confirmation of anomalies in the physical properties of the material for grain sizes in the absolute nanorange (<30 nm), consistent with observations in

other nc-systems was also achieved. These pernicious nano-effects, as diminution of the thermal conductivity and the melting point, which could be a weak point for the use of nc-UO_2 as a fuel, were found, however, to become relevant only at very low crystal/grain sizes (<30 nm) and to disappear for grain sizes of $\sim$ 200 nm, where, suitably, the other searched beneficial properties of this nanostructure super-plasticity, low gas-bubble swelling, self-limiting grain growth, etc., remain. This anticipates the lack of property loss of the developed nc-UO_2 monoliths for technical applications in this size range. This has been a very rewarding work, with a number of breakthroughs achieved. Much has been learned, but more needs to be done to determine the true potential of this intriguing material.

Institute for Transuranium Elements (ITU)

"The mission of ITU is to provide the scientific foundation for the protection of the European citizen against risks associated with the handling and storage of highly radioactive material. ITU's prime objectives are to serve as a reference centre for basic actinide research, to contribute to an effective safety and safeguards system for the nuclear fuel cycle, and to study technological and medical applications of radionuclides/actinides."

"ITU works very closely with national and international bodies in the nuclear field, both within the EU and beyond, as well as with the nuclear industry. In addition to playing a key role in EU policy on nuclear waste management and the safety of nuclear installations, ITU is also heavily involved in efforts to combat illicit trafficking of nuclear materials, and in developing and operating advanced detection tools to uncover clandestine nuclear activities. ITU provides the expertise and access to the necessary special handling facilities for the study of the actinide elements, which is of relevance for the issues related to nuclear power generation and the radioactive waste treatment and disposal, but also for the advancement of science in general. Another key role is in the study and production of radionuclides used in the treatment of cancer."

Laboratories in ITU *(left)* and typical glove-box of N_2 atmosphere (oxygen<0.5%) *(right)*.

"The JRC-ITU is comprised of seven scientific and one support departments, based in Karlsruhe (Germany, 330 staff) and Ispra (Italy, 70 staff). In total the Institute has a multidisciplinary team of more than 400 academic, technical and support staff. Its specialists have access to an extensive range of advanced facilities, many unavailable elsewhere in Europe. The Institute itself has more than 45 years of experience in the nuclear field. To foster the transfer of knowledge, the Institute encourages outside

scientists to join its work through secondment and grants. Within the Commission, ITU provides vital support to policy makers, particularly in the areas of environment and energy. It also works in the fields of EU enlargement and external relations, addressing safety and security concerns with nuclear installations in Central and Eastern Europe. In the safeguards and non-proliferation area, it works closely with the Commission Directorate General Energy and Transport, operating on site laboratories in Sellafield (UK) and La Hague (France). In the field of nuclear inspection, it supports the International Atomic Energy Agency (IAEA), and the External Relations Directorate General." [JRC-ITU, 2013]

Contamination measuring monitors *(left)* and personal dosimetry *(right)*.

List of Tables

5.1 Crystal size and lattice parameter for aqueous route nc-UO_2 treated at 600°C and 1200°C under two different atmosphere (Ar/5%H_2 and He atmosphere) . . . 83
5.2 Results from the analysis of the UO_{2+x} XANES data at the U-L_3 edge. . . . 86
5.3 Results from the analysis of the aqueous method synthesised nc-UO_{2+x} EXAFS data at the U-L_3 edge. . . . 88
5.4 Parameters obtained from the fits following the relaxation equation Eq. 5.6 for the samples annealed under He static atmosphere during 50 h. . . . 101
5.5 Crystal size and lattice parameter for samples treated at different temperatures, times and under different atmosphere. . . . 103

6.1 Results from the analysis of the UO_{2+x} XANES data at the U-L_3 edge. . . . 123
6.2 Results from the analysis of the ThO_2 at the Th-L_3. . . . 128

7.1 Characterization of macro- and microstructures of the different types of nc-UO_2 monoliths. 144
7.2 Obtained average parameters for Vickers and Knoop indentation for the different nc-UO_2 pellets. . . . 153
7.3 Calculated bulk moduli (B_0) and their first pressure derivative (B_0') for the three nc-UO_2 samples using different EOS, as well as bulk moduli values for UO_2-bulk [Zvoriste-Walters et al., 2013]. . . . 156

9.1 Densities obtained for the nc-Y-ZrO_2 samples after SPS treatment at different temperatures. . . . 186

List of Figures

1.1 Light Water Reactor [The energy net, 2012] [U.S.NRC, 2012]. . . . 2
1.2 A typical temperature profile of a LWR fuel as a function of the fuel pin radius [Konings et al., 2011]. . . . 3
1.3 Micrograph of a fuel pellet after irradiation showing the typical radial cracks *(left)*. Pellet inside the pin illustrating the swelling with the irradiation time *(right)*. [Bailly et al., 1996]. . . . 4
1.4 Micrographs at different pellet radius areas [Spino and Papaioannou, 2008]. High burn-up structure (HBS or rim-structure) transformation [The energy net, 2012]. . . . 5
1.5 Coordination state change in the transformation to the HBS (or rim-structure). . . . 6
1.6 SEM micrographs of a fuel pellet at high-BU from the outer radius or rim (HBS in the first micrograph) to inner radial positions from [Manzel and Walker, 2002]. . . . 7
1.7 A novel fuel microstructure: nc-UO_2 [The energy net, 2012]. . . . 9

2.1 Cyclic voltammetry experimental arrangement. . . . 13
2.2 Overview of the acoustic microscope (in ITU developed) device showing acoustic sensors, coupling liquid holder, sample platform and translation stages. . . . 21
2.3 Laser heating experimental set-up [Cappia et al., 2013]. . . . 23
2.4 Sample melting point setup. In the yellow area, the nc-UO_2 pellet hold with three screws is observable. . . . 24

3.1 Theoretical solubility limits of U^{IV} and U^{VI} species in aqueous solutions [Fanghänel, Th. and Neck, 2002] [Neck and Kim, 2001] and experimental determinations for U-sulphate [Gil et al., 2010] and U-chloride solutions [Rousseau et al., 2002] [Opel et al., 2007]. Compounds shown beside each equilibrium line show the precipitated solid phase when these conditions are exceeded. . . . 31
3.2 General set-up for reduction and controlled precipitation in a aqueous media method. . 31
3.3 Controlled massive precipitation in aqueous phase steps. . . . 32
3.4 Uranyl Nitrate molecular structure. . . . 32
3.5 Cyclic voltammetry set-up. . . . 32
3.6 Cyclic voltammogram 0.1 M U and pH 0.5. $UO_2(NO_3)_2$ solution in NaCl 1 M scanned between -0.4 and +1.4 V vs. Ag/AgCl saturated at a scan rate of 0.1 V/s. . . . 33
3.7 Influence of the frit on the system. Cyclic voltammogram 0.02 M U and pH=3. $UO_2(NO_3)_2$ solution in NaCl 1 M scanned between -1.0 and +1.2 V vs. Ag/AgCl saturated at a scan rate of 0.1 V/s. . . . 34
3.8 Influence of the concentration on the system. Cyclic voltammogram 0.02 M, 0.04 M and 0.06 M U and pH∼3. $UO_2(NO_3)_2$ solution in NaCl 1 M scanned between -1.0 and +1.2 V vs. Ag/AgCl saturated at a scan rate of 0.1 V/s. . . . 35
3.9 Influence of the acidity and scan rate on the system. Cyclic voltammogram 0.02 M U at different pH (1.1, 1.6, 1.8 and 2.2) and rates (0.01, 0.02, 0.05 and 0.1 V/s). $UO_2(NO_3)_2$ solution in NaCl 1 M scanned between -1.0 and +1.2 V vs. Ag/AgCl saturated. . . . 36
3.10 Electrochemical reduction set-up. . . . 38
3.11 Cyclic voltammogram 0.1 M U and pH<1. $UO_2(NO_3)_2$ solution in HCl 0.33 M scanned between -0.4 and +1.4 V vs. Ag/AgCl (saturated) at a scan rate of 0.1 V/s. The theoretical reduction rate of the ion UO_2^{2+} at each moment was calculated with Eq. 2.7. 40
3.12 Change in visible absorption spectra for the reduction of 0.1 M U and initial pH<1. $UO_2(NO_3)_2$ solution in HCl 0.33 M. The theoretical reduction rate of the ion UO_2^{2+} at each moment was calculated with Eq. 2.7. . . . 41
3.13 U-solution at different steps during electrochemical reduction . . . 42

3.14 Intensity peak decrease by both CV (e.g. UO_2^{2+}/U^{+4} cathodic peak, Fig. 3.11) and UV-spectrophotometry (e.g. UO_2^{2+} absorption peak at 412.43 nm, Fig. 3.12) as a function of the percentage of $UO_2(NO_3)_2$ electrochemical conversion. . . . 42
3.15 Precipitation of nc-UO_2 set-up. . . . 44
3.16 Controlled nc-UO_2 precipitation from a electrochemically reduced U^{IV}-solution 0.5 M U in HCl 1M. pH monitoring vs. NaOH addition and time. . . . 45
3.17 Change in visible absorption spectra of the typical U^{IV} band between 630 and 665 nm, of a controlled nc-UO_2 precipitation from a electrochemically reduced U^{IV}-solution 0.1 M U in HCl 1 M and pH<1 *(left)*. Diminishing of intensity with increasing of the pH because the precipitation of the U^{+4} in solution as nc-UO_2 *(right)*. . . . 49
3.18 U-solution before and after the precipitation. . . . 50
3.19 Uranium Speciation at different acidic media and solubility lines for UO_2 (c) and $UO_2 \cdot xH_2O$ (am) represented with the constants data by [Guillaumont et al., 2003]. *Yellow circles* represent experimental points. *Yellow line* represents the piece of solubility line followed during precipitation. . . . 50
3.20 Size distribution histogram from TEM measurements of nc-UO_2 synthesized by precipitation in aqueous media. Diameter average size of 3.9(8) nm diameter average size. . . . 51
3.21 TEM micrographs of UO_2 at low resolution, showing an assembly of nanocrystals, and at high resolution, revealing lattice imaging of the nanocrystals. . . . 51
3.22 XRD pattern of nc-UO_2 experimental data, fitted pattern, Bragg peak positions and experimental-fitted difference. . . . 52
3.23 Bragg diffraction peak positions and relative intensities for the refined XRD pattern of nc-UO_2 by aqueous route (*green*), standard UO_2 (00-041-1422-ICCD - *red*)), U_4O_9 (01-075-0944-ICCD - *blue*)) and U_3O_8 (00-023-1460-ICCD - *lila*)), respectively ([ICCD, 2012] database). . . . 53

4.1 Precursor molecular structures used in the organic synthesis. . . . 56
4.2 Oleic Acid (OA), Oleylamine (OAM) and N-(*cis*-9-octadecenyl)oleamide (OOA) obtained after the condensation reaction together with water [Wu et al., 2006] *(left)*. Intermediate steps of the nc-UO_2 synthesis where free UO_2 units and clusters interact with the formed OOA *(right)* [Wu, 2008]. . . . 57
4.3 Oleate as capping ligand bonded through chelating bidentate interaction on the surface of the nc-UO_2. . . . 57
4.4 Arrangement for the organic thermal decomposition method. . . . 57
4.5 Steps in the thermal Decomposition of UAA in organic media. . . . 58
4.6 (a) UAA + ODE + OA at RT (before applying any temperature). Turbid yellow solution. (b) UAA + ODE + OA + OAM at RT (after stirring at 100°C). Transparent orange solution. . . . 59
4.7 U-solution during the reaction step at different temperatures (160, 190 and 250°C). . . . 60
4.8 Th-solution during the reaction step at different temperatures. . . . 61
4.9 Typical final UO_2 solution after the reaction step and before precipitation. . . . 62
4.10 Precipitation, cleaning and recollection in an organic solvent (hexane) of the nanocrystals of UO_2. . . . 63
4.11 Precipitation, cleaning and recollection in an organic solvent (toluene) of the nanocrystals of ThO_2. . . . 63
4.12 Size distribution histogram from TEM measurements of UO_2 nanoparticles synthesized by thermal decomposition of UAA in organic media. Diameter average size of 4.9(3) nm. 65
4.13 TEM micrographs of UO_2 at low resolution, showing an assembly of nanocrystals, and at high resolution, revealing lattice imaging of the nanocrystals. . . . 65
4.14 TEM micrograph of UO_2 at high resolution, revealing lattice imaging of the nanocrystals and interplanar distances. . . . 66
4.15 Size distribution histogram from DLS test of UO_2 nanoparticles synthesized by thermal decomposition of UAA in organic media. Hydrodynamic average size of 3.7(1) nm. . . . 66
4.16 STEM and TEM micrographs of ThO_2 nanorods. . . . 67
4.17 TEM micrographs of ThO_2 nanorods at high resolution, revealing the lattice imaging. . 67
4.18 XRD pattern of nc-UO_2 (organic route) experimental data, fitted pattern, Bragg peak positions and experimental-fitted diference. . . . 68
4.19 Bragg diffraction peak positions and relative intensities for the refined XRD pattern of nc-UO_2 by organic route (*green*), standard UO_2 (00-041-1422-ICCD - *red*), U_4O_9 (01-075-0944-ICCD - *blue*) and U_3O_8 (00-023-1460-ICCD - *lila*), respectively ([ICCD, 2012] database). . . . 69

4.20 XRD pattern of nc-ThO_2 experimental data, fitted pattern, Bragg peak positions and experimental-fitted diference. *Inside picture* shows ThO_2 nanorods powder as-produced. 70

5.1 TGA and DTA signal for nc-UO_2 until 1200°C under Ar/5%H_2. 74
5.2 In situ HT-XRD patterns of nc-UO_2 under He *(left)*. The typical UO_2 and Pt (from the heating plate) Bragg peak positions are also marked. The arrow on down-right side of the graph shows a residual impurity which disappears with temperature. Evolution of (111) and (200) peaks of UO_2 cubic structure as a function of temperature *(right)* [Jovani-Abril et al., 2011]. 75
5.3 Evolution of the nc-UO_2 crystallite size in function of the temperature [Jovani-Abril et al., 2011]. 76
5.4 a.) Lattice constant and crystallite size variation (curves only as a guide to eye) of nc-UO_2 in function of temperature, from in situ HT-XRD measurements under static He atmosphere in comparison with lattice evolution in function of temperatures of standard UO_2 for different O/U ratios obtained by the relations of [Lynds et al., 1963], due to only thermal expansion. b.) Relative crystallite size and lattice parameter vs. temperature (curves only as a guide to eye). 78
5.5 Linear thermal expansion (LTE) and linear thermal expansion coefficient (LTEC) of the nc-UO_2 (curves only as a guide to eye) in comparison with data of bulk-UO_2 from [Martin, 1988]. 79
5.6 Patterns comparison of nc-UO_2 as-produced, nc-UO_2 at 1200°C and nc-UO_2 at RT after thermal treatment at 1200°C measured in situ in the HT-XRD instrument under static He atmosphere. 79
5.7 Crystallite size and strain of nc-UO_2 in function of temperature. Measurements done at temperature under static He atmosphere (curves only as a guide to eye). 81
5.8 XRD patterns of reference UO_2 and aqueous route nc-UO_2 (as-produced, after thermal treatment under Ar/5%H_2 at 600°C and 1200°C) 82
5.9 TEM images for the nc-UO_2 as-produced and after thermal treatment under Ar/5%H_2. 83
5.10 Normalized absorption XANES spectra and the first derivate at the U-L_3 edge of the three different heated nc-UO_2 samples from Aqueous route (nc-UO_2 at RT, 600°C and 1200°C), together with the reference spectra of bulk $U^{IV}O_2$. 84
5.11 a.) k^3-weighted spectra and b.) Fourier Transform at the U-L_3 edge for the experimental data of nc-UO_2 (aqueous route) at different temperatures annealed and $U^{IV}O_2$ bulk reference. 87
5.12 Comparison between experimental data from nc-UO_2 annealead at 1200°C and $U^{IV}O_2$ reference of *(left)* k^3-weighted spectra and *(right)* Fourier Transform at the U-L_3 edge. . 89
5.13 Experimental (□) and fitted data (−) for the nc-UO_2 annealead at 1200°C of *(left)* k^3-weighted spectra and *(right)* Fourier Transform at the U-L_3 edge. 89
5.14 U-O_1 and U-U_1 bond distances in function of the annealing temperature (under reducing conditions) and finale size of the nc-UO_2 sample (curves only as a guide to eye). 90
5.15 Stack of the ^{17}O MAS-NMR for nc-UO_2 annealed at five different temperatures. 91
5.16 Characteristic fits for the spectra of the samples annealed at 600°C, 650°C and 700°C ($*$ = spinning sidebands; peak A = black; peak B = blue; peak C = green) 92
5.17 Characteristic fits for the spectra of the samples annealed at 700°C, 800°C and 1200°C ($*$ = spinning sidebands; peak A = black; peak B = blue; peak C = green). 93
5.18 Evolution of the ^{17}O shift *(left)* and of the full width at half maximum *(right)* as a function of crystallite size for various temperatures. 95
5.19 Infrared spectra recorded for nc-UO_2 as-produced (RT), at 200°C, 600°C and 1200°C under Ar/5%H_2 annealed. Reference spectra for UO_2 is also represented. Inside amplification of the infrared spectra showing the disappearing of the peaks at 1625 cm^{-1} and 3400 cm^{-1} with increasing annealing temperatures. 97
5.20 Isothermal grain growth of nc-UO_2 under He static atmosphere. For each isothermal dwell temperature one new sample was used. Measurement was done in situ in the HT-XRD device at temperature. All the curves have been fit using the Eq. 5.6. For the one at 1200°C a fit using the Eq. 5.7 was also done. 99
5.21 Isothermal grain growth of nc-UO_2 under He static atmosphere. For each isothermal dwell temperature one new sample was used. Measurement was done in situ in the HT-XRD device. All the curves have been fit using the Eq. 5.6. 100
5.22 Grain growth relaxation time as a function of dwell temperature for the nc-UO_2 samples annealed under He static atmosphere during 50 h. Fit obtained excluding the value at 1200°C. 101

5.23 Diffusion coefficient $D_i(m^2/s)$ as a function of temperature for the nc-UO_2 samples annealed under He static atmosphere during 50 h. Fit obtained excluding the value at 1200°C. . . . 102
5.24 Arrhenius diagram comparing the cation self-diffusion in UO_2 fluorite-structure from large-grain ([Matzke, 1987]) and nano-grain of this study (samples annealed under He static atmosphere during 50 h). T_m is the melting point temperature ($T_{m_{UO_2}}$ =3140 °K). 104

6.1 TGA and DTA signal for nc-UO_2 under Ar/5%H_2 atmosphere. . . . 112
6.2 In situ HT-XRD patterns of nc-UO_2 under He *(left)*. The typical UO_2 and Pt (heating plate) Bragg peak positions are also marked. The *(right)* picture shows just the evolution of (111) and (200) peaks of UO_2 cubic structure as a function of temperature. . . . 113
6.3 Evolution of the nc-UO_2 crystallite size in function of the temperature. . . . 114
6.4 TEM images for the nc-UO_2. . . . 114
6.5 a.) Lattice constant and crystallite size variation of nc-UO_2 in function of temperature (curves only as a guide to eye), from in situ HT-XRD measurements under static He atmosphere in comparison with lattice evolution in function of temperatures of standard UO_2 for different O/U ratios obtained by the relations of [Lynds et al., 1963], due to only thermal expansion. b.) Relative crystallite size and lattice parameter vs. temperature (curves only as a guide to eye). . . . 115
6.6 Linear thermal expansion (LTE) and linear thermal expansion coefficient (LTEC) of the nc-UO_2 in comparison with data of bulk-UO_2 from [Martin, 1988] (curves only as a guide to eye). . . . 116
6.7 Patterns comparison of nc-UO_2 pre-thermal treated, nc-UO_2 at 1100°C and nc-UO_2 at RT after thermal treatment at 1100°C (measured in situ in the HT-XRD instrument under static He atmosphere) . . . 117
6.8 Crystallite size and strain of nc-UO_2 in function of temperature. Measurements done at temperature under static He atmosphere (curves only as a guide to eye). . . . 118
6.9 XRD patterns of reference UO_2 and organic UO_2 (as-produced, after thermal treatment under Ar/5%H_2 at 600°C and 1200°C). . . . 120
6.10 Normalized absorption XANES spectra and the first derivate at the U-L_3 edge of the three different heated nc-UO_2 samples from Organic route (nc-UO_2 at RT, 600°C and 1200°C), together with the reference spectra of bulk $U^{IV}O_2$. . . . 121
6.11 a.) k^3-weighted spectra and b.) Fourier Transform at the U-L_3 edge for the experimental data of nc-UO_2 (organic route) at different temperatures annealed and $U^{IV}O_2$ bulk reference. . . . 124
6.12 Normalized absorption XANES spectra and the first derivate at the Th-L_3 edge of nc-ThO_2 at RT together with the reference spectra of bulk $Th^{IV}O_2$. . . . 128

7.1 Hydraulic press (ITU) and nc-UO_2 green pressed pellet. . . . 130
7.2 Green density and theoretical density (TD) of the nc-UO_2 pressed pellets vs. applied force. . . . 131
7.3 a.) Dispersion of nc-UO_2 in water with homogenizer. b.) Representation of the float-packing process taken from [Godlinski et al., 2002]. . . . 132
7.4 Green pellet of nc-UO_2 from aqueous route obtained by conventional uniaxial pressing. . . 132
7.5 Typical microstructure of conventional pressed nc-UO_2 green pellet. . . . 133
7.6 Schematic calcination steps for nc-UO_2 powders from aqueous and organic routes. . . . 133
7.7 Green pellet of nc-UO_2 from aqueous route obtained by float packing consolidation. . . . 133
7.8 Mortar with thermally treated nc-UO_2 powder from organic route. . . . 134
7.9 Green pellet of nc-UO_2 from organic route obtained by conventional uniaxial pressing. . . 134
7.10 Schematic program for two-step sintering under Ar/5%H_2 atmosphere. . . . 135
7.11 Aqueous route nc-UO_2 sintered pellet. . . . 135
7.12 Organic route nc-UO_2 sintered pellet. . . . 136
7.13 Schematic heating program for slow calcination and sintering under Ar/5%H_2 atmosphere. 137
7.14 Relative linear shrinkage and its derivative of the nc-UO_2 ceramic as a function of temperature. Comparison with bulk-UO_2 taken from [Lahiri et al., 2006]. . . . 137
7.15 Arrhenius plot of the initial densification stages for a nc-UO_2 by conventional compaction pressed and sintered in oven under Ar/5%H_2. . . . 139
7.16 *Aqueous-Pressed*. Macrostructure of conventional-pressed and sintered (1200°C) pellet from the aqueous route nc-UO_2-powder. The scale bar is 100 μm. . . . 140

7.17 *Aqueous-Pressed-PTT*. Macrostructure of conventional-pressed and sintered (1200°C) pellet from the aqueous route nc-UO_2-powder. Previous thermal treatment for dehydration of the nc-UO_2 powder before pressing, was done. The scale bar is 100 μm. . . . 141
7.18 *Aqueous-Pressed-PTT*. Fresh-fracture microstructure of conventional-pressed and sintered (1200°C) pellet from the aqueous route nc-UO_2-powder. Previous thermal treatment for dehydration of the powder before pressing, was done. . . . 141
7.19 *Aqueous-Float Packing*. Macrostructure of float packed consolidated and sintered (1200°C) pellet from the aqueous route nc-UO_2-powder. The scale bar is 100 μm. . . . 142
7.20 *Aqueous-Float Packing*. Fresh-fracture microstructure of float packed consolidated and sintered (900°C) pellet from the aqueous route nc-UO_2-powder. . . . 142
7.21 *Aqueous-Float Packing*. Fresh-fracture microstructure of float packed consolidated and sintered (1200°C) pellet from the aqueous route nc-UO_2-powder. . . . 142
7.22 *Organic-Pressed-PTT*. Macrostructure of conventional pressed and sintered (1200°C) pellet from the organic route nc-UO_2-powder. Previous thermal treatment for burning of the capping organics before pressing, was done. The scale bar is 100 μm. . . . 143
7.23 *Organic-Pressed-PTT*. Fresh-fracture microstructure of of conventional pressed and sintered (1200°C) pellet from the organic route nc-UO_2-powder. Previous thermal treatment for burning of the capping organics before pressing, was done. . . . 143
7.24 Typical Vickers (*left*) and Knoop (*right*) indentations. . . . 148
7.25 Vickers indentations at different loads for the nc-UO_2 *Aqueous-Pressed* pellet (Fig. 7.17). Indentations performed with the instrumented indentor. . . . 148
7.26 Vickers indentations at different loads for three kind of nc-UO_2 pellets (Table 7.1): *Aqueous-Pressed* (Fig. 7.17), *Aqueous-Float Packing* (Fig 7.19) and *Organic-Pressed* (Fig 7.22). Indentations performed with the manual mictroindentor. . . . 149
7.27 Micrographs of Knoop indented nc-UO_2 pellets. . . . 150
7.28 Average H_V (-) obtained for the different loads used for each kind of monolith. . . . 151
7.29 Calibration curve $\frac{b'}{a'}$ vs. $\left(\frac{H}{E}\right)_K$ determined by [Pujol et al., 2004] (Eq. 7.5). Representation of values for $\left(\frac{H}{E}\right)_K$ for the different nc-UO_2 monoliths obtained by the calibration curve together with other reference materials from [Marshall et al., 1982] and [Pujol et al., 2004]. . . . 152
7.30 Acoustical image of a nc-UO_2 sample from *Aqueous-Float Packing*. . . . 153
7.31 TEM micrographs of UO_2 at high resolution for the three different sizes [Zvoriste-Walters et al., 2013]. . . . 154
7.32 In-situ HP-XRD pattern of nc-UO_2 for the three different sizes [Zvoriste-Walters et al., 2013]. . . . 155
7.33 Relative volumes vs. pressure. The lines represent the least-square fit of the 3^{rd} order BM-EOS to the experimental data. *Insert Fig.:* compression data from the three nc-UO_2 samples plotted in the low pressure (LP) range (LP up to around 10 GPa) [Zvoriste-Walters et al., 2013]. . . . 157
7.34 Normalised pressure as a function of the Eulerian strain for the three nc-UO_2 samples. The solid lines represent a linear fit to the experimental data. In the $F(f)$ linear plot the bulk modulus is obtained from the intercept on the F axis and the $B_0^{'}$ from the gradient $F = B_0 + (3B_0(B_0^{'} - 4)f)/2$ [Zvoriste-Walters et al., 2013]. . . . 158
7.35 The bulk modulus plotted as a function of three crystal size samples (4 nm, 6 nm and 34 nm). A size approximation for the micro-sized bulk modulus UO_2 from [Pujol et al., 2004] to 200 nm has been done [Zvoriste-Walters et al., 2013]. . . . 159
7.36 Differences in the H_V vs. $\left(\frac{H}{E}\right)_K$ behaviour of irradiated and non-irradiated UO_2. . . . 160
7.37 E values from microacoustic tests and Knoop indentation from irradiated fuels [Baron et al., 2005] and nc-UO_2 (this work). . . . 160
7.38 Thermal diffusivity of nc-UO_2 (200 nm - 90% density) specimen upon temperature, extrapolated at 95% density for comparison with bulk-UO_2 (large-grain) (95% density) from [Fink, 2000]; *red symbols*: measurements at rising temperature, *blue symbols*: measurements at falling temperature levels. . . . 163
7.39 Melting point measurement for 10 nm-UO_2 sample. . . . 164
7.40 Melting point measurement for ∼200 nm-UO_2 sample. . . . 165
7.41 SEM images of the fresh fracture of surface-melted nc-UO_2 sample. Three different size areas (from surface to 40 μm depth, 40 μm to 115 μm and 115 μm to the opposite surface) are distinguishable. . . . 165

7.42 SEM images of the three different size regions formed after surface melting of the nc-UO_2 sample. *(First line of images):* surface-40 μm, molten zone and columnar growth. *(Second line):* 40 μm-115 μm, molten zone and non columnar growth. *(Third line):* 115 μm-opposite surface, unmolten zone, grain growth (241(70) nm) 166

9.1 Magnetic susceptibility at 70 KOe for nano materials and 10 KOe for single crystal. . . 184
9.2 Effective magnetic moment extracted from the Curie Weiss law Model (CW) for the different size of nano materials. 185
9.3 Spark Plasma Sintering pellet of nc-Y-ZrO_2. 186
9.4 Microstructure of fresh fracture of nc-Y-ZrO_2 pellet by SPS. 186
9.5 Spark Plasma Sintering pellet of nc-Y-ZrO_2 *(left)*. Optical microscopy of the fresh fracture for the thermal treated sample. The temperature gradients measured on the sample surfaced are also indicated *(right)*. 187
9.6 Fresh fracture of the thermal treated sample. Thermal distribution measured in the POLARIS facility. The temperatures were measured on the surface. 188
9.7 Micro- and macro-structure of nc-Y-ZrO_2 bulk specimens subjected to POLARIS heating experiments to simulate a Large LOCA event. 188

Bibliography

[Ayyub et al., 1995] Ayyub, P., Palkar, V. R., Chattopadhyay, S., and Multani, M. (1995). Effect of crystal size reduction on lattice symmetry and cooperative properties. *Physical Review B*, 51(9):6135–6138.

[Bailly et al., 1996] Bailly, H., D. Ménessier, and Prunier, C. (1996). *Le Combustible nucléaire des réacteurs à eau sous pression et des réacteurs à neutrons rapides: Conception et comportement*, volume Série Synthèses.

[Banerjee et al., 2003] Banerjee, R., Sperling, E. A., Thompson, G. B., Fraser, H. L., Bose, S., and Ayyub, P. (2003). Lattice expansion in nanocrystalline niobium thin films. *Applied Physics Letters*, 82(24):4250–4252.

[Baron et al., 2005] Baron, D., Masson, R., Gatt, J.-M., Spino, J., and Laux, D. (2005). Evolution of the Fuel Mechanical Properties with Burn-up, an Extensive European Experimental Program. In *Water Reactor Fuel Performance JNS-ENS-ANS meeting.*, Kyoto, Japan.

[Birch, 1947] Birch, F. (1947). Finite Elastic Strain of Cubic Crystals. *Physical Review*, 71(11):809–824.

[Birch, 1978] Birch, F. (1978). Finite strain isotherm and velocities for single-crystal and polycrystalline NaCl at high pressures and 300°K. *Journal of Geophysical Research: Solid Earth*, 83(B3):1257–1268.

[Böhler et al., 2012] Böhler, R., Welland, M. J., Bruycker, F. D., Boboridis, K., Janssen, A., Eloirdi, R., Konings, R. J. M., and Manara, D. (2012). Revisiting the melting temperature of NpO_2 and the challenges associated with high temperature actinide compound measurements. *Journal of Applied Physics*, 111(11):–.

[Boswell, 1951] Boswell, F. W. C. (1951). Precise Determination of Lattice Constants by Electron Diffraction and Variations in the Lattice Constants of Very Small Crystallites. *Proceedings of the Physical Society. Section A*, 64(5):465.

[Brazhkin et al., 2002] Brazhkin, V. V., Lyapin, A. G., and Hemley, R. J. (2002). Harder than diamond: Dreams and reality. *Philosophical Magazine A*, 82(2):231–253.

[Brendebach et al., 2007] Brendebach, B., Dardenne, K., Denecke, M., Rothe, J., and Vitova, T. (2007). New developments at the INE-Beamline for actinide research at ANKA. Nuclear Instruments and Methods in Physics Research Section A: Accelerators, Spectrometers, Detectors and Associated Equipment. 582:80–81.

[Bristow et al., 2001] Bristow, S., Shekunov, T., Shekunov, B. Y., and York, P. (2001). Analysis of the supersaturation and precipitation process with supercritical CO_2. *The Journal of Supercritical Fluids*, 21(3):257–271.

[Burda et al., 2005] Burda, C., Chen, X., Narayanan, R., and El-Sayed, M. A. (2005). Chemistry and Properties of Nanocrystals of Different Shapes. *ChemInform*, 36(27).

[Cappia et al., 2013] Cappia, F., Jovani-Abril, R., Spino, J., Luzzi, L., Janßen, A., and Manara, D. (2013). Laser melting of nano-crystalline uranium dioxide. *Progress in Nuclear Energy*, (0):–.

[Carbol et al., 2009] Carbol, P., Fors, P., Winckel, S. V., and Spahiu, K. (2009). Corrosion of irradiated MOX fuel in presence of dissolved H_2. *Journal of Nuclear Materials*, 392(1):45 – 54.

[Casabella, 1964] Casabella, P. A. (1964). Determination of Nuclear Quadrupole Coupling Constants from Nuclear Magnetic Resonances in Polycrystalline Solids. *The Journal of Chemical Physics*, 40(1):149–152.

[Chen et al., 2002] Chen, B., Penwell, D., Benedetti, L. R., Jeanloz, R., and Kruger, M. B. (2002). Particle-size effect on the compressibility of nanocrystalline alumina. *Physical Review B*, 66(14):144101–.

[Chen et al., 2001] Chen, B., Penwell, D., Kruger, M. B., Yue, A. F., and Fultz, B. (2001). Nanocrystalline iron at high pressure. *Journal of Applied Physics*, 89(9):4794–4796.

[Chung and Davies, 1979] Chung, T. and Davies, T. (1979). The superplastic creep of uranium dioxide. *Journal of Nuclear Materials*, 79(1):143 – 153.

[Cimino et al., 1968] Cimino, A., Jacono, M. L., Porta, P., and Valigi, M. (1968). Structural and Magnetic Investigations of Oxide Solid Solution. *Zeitschrift für Physikalische Chemie*, 59(1_4):134–150.

[Claassen and Sandenbergh, 2006] Claassen, J. O. and Sandenbergh, R. F. (2006). Particle growth parameters in the precipitation of metastable iron phases from zinc-rich solutions. *Hydrometallurgy*, 84(3–4):165–174.

[Conradson et al., 2005a] Conradson, S. D., Begg, B. D., Clark, D. L., den Auwer, C., Ding, M., Dorhout, P. K., Espinosa-Faller, F. J., Gordon, P. L., Haire, R. G., Hess, N. J., Hess, R. F., Webster Keogh, D., Lander, G. H., Manara, D., Morales, L. A., Neu, M. P., Paviet-Hartmann, P., Rebizant, J., Rondinella, V. V., Runde, W., Drew Tait, C., Kirk Veirs, D., Villella, P. M., and Wastin, F. (2005a). Charge distribution and local structure and speciation in the UO_{2+x} and PuO_{2+x} binary oxides for $x \leqslant 0.25$. *Journal of Solid State Chemistry*, 178(2):521–535.

[Conradson et al., 2005b] Conradson, S. D., Manara, D., Wastin, F., Clark, D. L., Lander, G. H., Morales, L. A., Rebizant, J., and Rondinella, V. V. (2005b). Local Structure and Charge Distribution in the UO_2-U_4O_9 System. *ChemInform*, 36(1):no–no.

[Deshpande et al., 2005] Deshpande, S., Patil, S., Kuchibhatla, S. V., and Seal, S. (2005). Size dependency variation in lattice parameter and valency states in nanocrystalline cerium oxide. *Applied Physics Letters*, 87(13):133113–3.

[Dong et al., 1997] Dong, X., Hong, G., Yu, D., and Yu, D. (1997). Synthesis and Properties of Cerium Oxide Nanometer Powders by Pyrolysis of Amorphous Citrate. *J. Mater. Sci. Technol.*, 13:113.

[Ekeroth et al., 2009] Ekeroth, E., Low, J., Zwicky, H.-U., and Spahiu, K. (2009). Corrosion studies with high burn-up LWR fuel in simulated groundwaters. volume 1224, page 123. Material Research Society Proceedings.

[Fanghänel, Th. and Neck, 2002] Fanghänel, Th. and Neck, V. (2002). Aquatic chemistry and solubility phenomena of actinide oxi-des/hydroxides. *Pure Appl. Chem.*, 74(10):1895 – 1907.

[Fiévet et al., 1979] Fiévet, F., Germi, P., de Bergevin, F., and Figlarz, M. (1979). Lattice parameter, microstrains and non-stoichiometry in NiO. Comparison between mosaic microcrystals and quasi-perfect single microcrystals. *Journal of Applied Crystallography*, 12(4):387–394.

[Fink, 2000] Fink, J. K. (2000). Thermophysical properties of uranium dioxide. *Journal of Nuclear Materials*, 279(1):1–18.

[Fujita et al., 1956] Fujita, J., Nakamoto, K., and Kobayashi, M. (1956). Infrared Spectra of Metallic Complexes. II. The Absorption Bands of Coördinated Water in Aquo Complexes. *Journal of the American Chemical Society*, 78(16):3963–3965.

[Fujiwara et al., 2005] Fujiwara, K., Yamana, H., Fujii, T., Kawamoto, K., Sasaki, T., and Moriyama, H. (2005). Solubility product of hexavalent uranium hydrous oxide. *Journal of Nuclear Science and Technology*, 42(3):289–294.

[Fujiwara et al., 2003] Fujiwara, K., Yamana, H., Fujii, T., and Moriyama, H. (2003). Determination of uranium(IV) hydrolysis constants and solubility product of $UO_2 \cdot xH_2O$. *Radiochimica Acta*, 91(6-2003):345–350.

[Fuketa et al., 2006] Fuketa, T., Sugiyama, T., and Nagase, F. (2006). Behaviour of 60 to 78 MWd/kgU PWR fuels under reactivity initiated accidents conditions. *Journal of Nuclear Science and Technology*, 43(9):1080–1088.

[Fukuhara, 2003] Fukuhara, M. (2003). Lattice expansion of nanoscale compound particles. *Physics Letters A*, 313(5–6):427–430.

[Garzarolli et al., 1979] Garzarolli, F., von Jan, R., and Stehle, H. (1979). The Main Causes of Fuel Failure in Water Cooled Power Reactors. *Atomic Energy Review*, 17(1):31–128.

[Gil et al., 2010] Gil, D., Malmbeck, R., Spino, J., Fanghänel, Th., and Dinnebier, R. E. (2010). Nanoscale UO_2 and novel complex U(IV)-sulphate phase formation from electrolytically reduced uranyl sulphate solutions. *Radiochimica Acta*, 98(2):77–89.

[Godlinski et al., 2002] Godlinski, D., Kuntz, M., and Grathwohl, G. (2002). Transparent alumina with submicrometer grains by float packing and sintering. *Journal of the American Ceramic Society*, 85(10):2449–2456.

[Godwal et al., 2010] Godwal, B. K., Speziale, S., Clark, S. M., Yan, J., and Jeanloz, R. (2010). High pressure equation of state studies using methanol–ethanol–water and argon as pressure media. *Journal of Physics and Chemistry of Solids*, 71(8):1059–1064.

[Grüneisen, 1912] Grüneisen, E. (1912). Theorie des festen Zustandes einatomiger Elemente. *Annalen der Physik*, 344(12):257–306.

[Guillaumont et al., 2003] Guillaumont, R., Fanghänel, Th, Fuger, J., and Grenthe, I. (2003). *Update on the Chemical Thermodynamics of Uranium, Neptunium, Plutonium, Americium and Technetium*, volume 5 of *Chemical Thermodynamics*. Elsevier Science Ltd.

[Guisbiers, 2012] Guisbiers, G. (2012). Review on the analytical models describing melting at the nanoscale. *J. Nanosci. Lett.*, 2(8).

[Haines et al., 2001] Haines, J., Léger, J., and Bocquillon, G. (2001). Synthesis and design of superhard materials. *Annual Review of Materials Research*, 31(1):1–23.

[He et al., 2005] He, Y., Liu, J. F., Chen, W., Wang, Y., Wang, H., Zeng, Y. W., Zhang, G. Q., Wang, L. N., Liu, J., Hu, T. D., Hahn, H., Gleiter, H., and Jiang, J. Z. (2005). High-pressure behavior of SnO_2 nanocrystals. *Physical Review B*, 72(21):212102–.

[Hennig et al., 2007] Hennig, C., Schmeide, K., Brendler, V., Moll, H., Tsushima, S., and Scheinost, A. C. (2007). EXAFS Investigation of U(VI), U(IV), and Th(IV) Sulfato Complexes in Aqueous Solution. *ChemInform*, 38(38).

[Hennig et al., 2005] Hennig, C., Tutschku, J., Rossberg, A., Bernhard, G., and Scheinost, A. C. (2005). Comparative EXAFS Investigation of Uranium(VI) and -(IV) Aquo Chloro Complexes in Solution Using a Newly Developed Spectroelectrochemical Cell. *Inorganic Chemistry*, 44(19):6655–6661.

[Hiernaut et al., 2008] Hiernaut, J.-P., Wiss, T., Colle, J.-Y., Thiele, H., Walker, C., Goll, W., and Konings, R. (2008). Fission product release and microstructure changes during laboratory annealing of a very high burn-up fuel specimen. *Journal of Nuclear Materials*, 377(2):313 – 324.

[Hofmeister, 1993] Hofmeister, A. M. (1993). Interatomic potentials calculated from equations of state: Limitation of finite strain to moderate K'. *Geophysical Research Letters*, 20(7):635–638.

[HSP-PAN, 2011] HSP-PAN (2011). *HighScore Plus*. PANalytical B.V., Almelo, The Netherlands, version: 3.0d (3.0.4) edition.

[ICCD, 2012] ICCD (2012). The International Centre for Diffraction Data, www.icdd.com.

[Idiri et al., 2004] Idiri, M., Le Bihan, T., Heathman, S., and Rebizant, J. (2004). Behavior of actinide dioxides under pressure: UO_2 and ThO_2. *Physical Review B*, 70(1):014113–.

[Jovani-Abril et al., 2011] Jovani-Abril, R., Eloirdi, R., Bouëxière, D., Malmbeck, R., and Spino, J. (2011). In situ high temperature X-ray diffraction study of UO_2 nanoparticles. *Journal of Materials Science*, pages 1–6.

[JRC-ITU, 2013] JRC-ITU (2013). Joint Research Centre - Institute for Transuranium Elements. *http://itu.jrc.ec.europa.eu/index.php?id=11type=0*.

[Kim et al., 2009] Kim, J.-G., Park, Y.-S., Ha, Y.-K., and Song, K. (2009). Infrared Spectra of Uranium Oxides Measured by ATR-FTIR. *Journal of Nuclear Science and Technology*, 46(12):1188–1192.

[Kittel, 1996] Kittel, C. (1996). *Introduction to solid state physics*. Wiley, New York.

[Klam et al., 1987] Klam, H. J., Hahn, H., and Gleiter, H. (1987). The thermal expansion of grain boundaries. *Acta Metallurgica*, 35(8):2101–2104.

[Kleykamp, 1979] Kleykamp, H. (1979). The chemical state of LWR high-power rods under irradiation. *Journal of Nuclear Materials*, 84(1–2):109–117.

[Konings et al., 2011] Konings, R. J. M., Wiss, T., and Guéneau, C. (2011). Nuclear Fuels. In Morss, L. R., Edelstein, N. M., and Fuger, J., editors, *The Chemistry of the Actinide and Transactinide Elements*, page 3720. Springer Netherlands.

[Kulisch et al., 2009] Kulisch, W., Freudenstein, R., Ruiz, A., Valsesia, A., Sirghi, L., Ponti, J., Colpo, P., and Rossi, F. (2009). Nanostructured Materials For Advanced Technological Applications: A Brief Introduction. NATO Science for Peace and Security Series B: Physics and Biophysics, pages 3–34. Springer Netherlands.

[Kutty et al., 2004] Kutty, T., Hegde, P., Khan, K., Jarvis, T., Sengupta, A., Majumdar, S., and Kamath, H. (2004). Characterization and densification studies on ThO_2–UO_2 pellets derived from ThO_2 and U_3O_8 powders. *Journal of Nuclear Materials*, 335(3):462 – 470.

[Lahiri et al., 2006] Lahiri, D., Rao, S. V. R., Rao, G. V. S. H., and Srivastava, R. K. (2006). Study on sintering kinetics and activation energy of UO_2 pellets using three different methods. *Journal of Nuclear Materials*, 357(1–3):88–96.

[Lai et al., 1998] Lai, S. L., Carlsson, J. R. A., and Allen, L. H. (1998). Melting point depression of Al clusters generated during the early stages of film growth: Nanocalorimetry measurements. *Applied Physics Letters*, 72(9):1098–1100.

[Lai et al., 1996] Lai, S. L., Guo, J. Y., Petrova, V., Ramanath, G., and Allen, L. H. (1996). Size-Dependent Melting Properties of Small Tin Particles: Nanocalorimetric Measurements. *Physical Review Letters*, 77(1):99–102.

[Laux et al., 2012] Laux, D., Baron, D., Despaux, G., Kellerbauer, A. I., and Kinoshita, M. (2012). Determination of high burn-up nuclear fuel elastic properties with acoustic microscopy. *Journal of Nuclear Materials*, 420(1–3):94–100.

[Lawn and Howes, 1981] Lawn, B. R. and Howes, V. R. (1981). Elastic recovery at hardness indentations. *Journal of Materials Science*, 16:2745–2752.

[Li et al., 2004] Li, G., Boerio-Goates, J., Woodfield, B. F., and Li, L. (2004). Evidence of linear lattice expansion and covalency enhancement in rutile TiO_2 nanocrystals. *Applied Physics Letters*, 85(11):2059–2061.

[Li et al., 2005] Li, G., Li, L., Boerio-Goates, J., and Woodfield, B. F. (2005). High Purity Anatase TiO_2 Nanocrystals: Near Room-Temperature Synthesis, Grain Growth Kinetics, and Surface Hydration Chemistry. *Journal of the American Chemical Society*, 127(24):8659–8666.

[Lifshitz and Slyozov, 1961] Lifshitz, I. M. and Slyozov, V. V. (1961). The kinetics of precipitation from supersaturated solid solutions. *Journal of Physics and Chemistry of Solids*, 19(1–2):35–50.

[Ling et al., 2008] Ling, T., Yu, H., Shen, Z., Wang, H., and Zhu, J. (2008). Virus-mediated FCC iron nanoparticle induced synthesis of uranium dioxide nanocrystals. *Nanotechnology*, 19(11):115608.

[Löffler and Johnson, 2000] Löffler, J. F. and Johnson, W. L. (2000). Model for decomposition and nanocrystallization of deeply undercooled $Zr_{41.2}Ti_{13.8}Cu_{12.5}Ni_{10}Be_{22.5}$. $AppliedPhysicsLetters$, 76(23) : 3394 − −3396.

[Lovley and Phillips, 1992] Lovley, D. R. and Phillips, E. J. (1992). Reduction of uranium by Desulfovibrio desulfuricans. *Applied and Environmental Microbiology*, 58(3):850–856.

[Lynds et al., 1963] Lynds, L., Young, W. A., Mohl, J. S., and Libowitz, G. G. (1963). X-ray and density study of nonstoichiometry in uranium oxides. page 58.

[Maeda et al., 2009] Maeda, K., Yamamoto, Y., Asakuma, Y., and Fukui, K. (2009). Determination of crystal nucleus size of potassium chloride from ethanol solution caused by ultrasonic irradiation. *Chemical Engineering and Processing: Process Intensification*, 48(4):902–906.

[Maier et al., 1982] Maier, G., Assmann, H., Dorr, W., Manzel, R., and Peehs, M. (1982). Jahrestagung Kerntechnik. page 485, Bonn.

[Manara et al., 2012] Manara, D., Böhler, R., Boboridis, K., Capriotti, L., Quaini, A., Luzzi, L., De Bruycker, F., Guéneau, C., Dupin, N., and Konings, R. (2012). The Melting Behaviour of Oxide Nuclear Fuels: Effects of the Oxygen Potential Studied by Laser Heating. *Procedia Chemistry*, 7(0):505–512.

[Manara et al., 2005] Manara, D., Ronchi, C., Sheindlin, M., Lewis, M., and Brykin, M. (2005). Melting of stoichiometric and hyperstoichiometric uranium dioxide. *Journal of Nuclear Materials*, 342(1–3):148–163.

[Manara et al., 2008] Manara, D., Sheindlin, M., Heinz, W., and Ronchi, C. (2008). New techniques for high-temperature melting measurements in volatile refractory materials via laser surface heating. *Review of Scientific Instruments*, 79(11):–.

[Manzel and Walker, 2002] Manzel, R. and Walker, C. (2002). EPMA and SEM of fuel samples from PWR rods with an average burn-up of around 100 MWd/kgHM. *Journal of Nuclear Materials*, 301(2–3):170 – 182.

[Marshall et al., 1982] Marshall, D. B., Noma, T., and Evans, A. G. (1982). A Simple Method for Determining Elastic-Modulus-to-Hardness Ratios using Knoop Indentation Measurements. *Journal of the American Ceramic Society*, 65(10):c175–c176.

[Martin, 1988] Martin, D. G. (1988). The thermal expansion of solid UO_2 and (U, Pu) mixed oxides- a review and recommendations. *Journal of Nuclear Materials*, 152(2–3):94–101.

[Martin, 2007] Martin, M. (2007). Oxygen and Cation Diffusion Processes in Oxygen Ion Conductors. *Diffusion Fundamentals*, 39.1(6).

[Mathur and Singh, 2009] Mathur, S. and Singh, M., editors (2009). *Nanostructured Materials and Nanotechnology II - A Collection of Papers Presented at the 32nd International Conference on Advanced Ceramics and Composites*, volume 29.

[Matzke, 1987] Matzke, H. (1987). Atomic transport properties in UO_2 and mixed oxides (U, Pu)O_2. *J. Chem. Soc., Faraday Trans. 2*, 83:1121–1142.

[Matzke, 1992] Matzke, H. (1992). On the rim effect in high burnup UO_2LWR fuels. *Journal of Nuclear Materials*, 189(1):141 – 148.

[Matzke and Spino, 1997] Matzke, H. and Spino, J. (1997). Formation of the rim structure in high burnup fuel. *Journal of Nuclear Materials*, 248(0):170–179.

[Mazaheri et al., 2011] Mazaheri, M., Mari, D., Hesabi, Z. R., Schaller, R., and Fantozzi, G. (2011). Multi-walled carbon nanotube/nanostructured zirconia composites: Outstanding mechanical properties in a wide range of temperature. *Composites Science And Technology*, 71:939–945.

[Mazaheri et al., 2010] Mazaheri, M., Mari, D., and Schaller, R. (2010). High temperature mechanical spectroscopy of yttria stabilized zirconia reinforced with carbon nanotubes. *physica status solidi (a)*, 207(11):2456–2460.

[Mennecart et al., 2004] Mennecart, T., Grambow, B., Fattahi, M., and Andriambololona, Z. (2004). Effect of alpha radiolysis on doped UO_2 dissolution under reducing conditions. *Radiochimica Acta*, 92(9-11-2004):611–615.

[Meresse et al., 2000] Meresse, Y., Heathman, S., Le Bihan, T., Rebizant, J., Brooks, M. S. S., and Ahuja, R. (2000). X-ray diffraction studies of AuCu3-type neptunium compounds under pressure. *Journal of Alloys and Compounds*, 296(1):27–32.

[Mikeev, 1989] Mikeev, N. B. (1989). Die stellung der lanthaniden und actiniden im periodensystem des mendeleev. *Naturwissenschaften*, 76:107–113. 10.1007/BF00366600.

[Moelle and Fecht, 1995] Moelle, C. and Fecht, H. (1995). Thermal stability of nanocrystalline iron prepared by mechanical attrition. *Nanostructured Materials*, 6(1–4):421 – 424.

[Mogensen et al., 1999] Mogensen, M., Pearce, J., and Walker, C. (1999). Behaviour of fission gas in the rim region of high burn-up UO_2 fuel pellets with particular reference to results from an XRF investigation. *Journal of Nuclear Materials*, 264(1–2):99 – 112.

[Murray et al., 2000] Murray, C. B., Kagan, C. R., and Bawendi, M. G. (2000). Synthesis and characterization of monodisperse nanocrystals and close-packed nanocrystal assemblies. *Annual Review of Materials Science*, 30(1).

[Murray et al., 1993] Murray, C. B., Norris, D. J., and Bawendi, M. G. (1993). Synthesis and characterization of nearly monodisperse CdE (E = sulfur, selenium, tellurium) semiconductor nanocrystallites. *Journal of the American Chemical Society*, 115(19):8706–8715.

[Natter et al., 2001] Natter, H., Löffler, M.-S., Krill, C., and Hempelmann, R. (2001). Crystallite growth of nanocrystalline transition metals studied in situ by high temperature synchrotron X-ray diffraction. *Scripta Materialia*, 44(8–9):2321 – 2325.

[Natter et al., 2000] Natter, H., Schmelzer, M., Löffler, M.-S., Krill, C. E., Fitch, A., and Hempelmann, R. (2000). Grain-Growth Kinetics of Nanocrystalline Iron Studied In Situ by Synchrotron Real-Time X-ray Diffraction. *The Journal of Physical Chemistry B*, 104(11):2467–2476.

[Neck and Kim, 2001] Neck, V. and Kim, J. I. (2001). Solubility and hydrolysis of tetravalent actinides. *Radiochimica Acta*, 89.

[Newville, 2001] Newville, M. (2001). IFFEFFIT: interactive XAFS analysis and FEFF fitting. *J. Synchrotron Radiat.*, 8:322–324.

[Nita et al., 2005] Nita, N., Schaeublin, R., Victoria, M., and Valiev, R. Z. (2005). Effects of irradiation on the microstructure and mechanical properties of nanostructured materials. *Philosophical Magazine*, 85(4-7):723–735. Sp. Iss. SI.

[Nogita and Une, 1994] Nogita, K. and Une, K. (1994). Radiation-induced microstructural change in high burnup UO_2 fuel pellets. *Nuclear Instruments and Methods in Physics Research Section B: Beam Interactions with Materials and Atoms*, 91(1-4):301 – 306.

[Noirot et al., 2008] Noirot, J., Desgranges, L., and Lamontagne, J. (2008). Detailed characterisations of high burn-up structures in oxide fuels. *Journal of Nuclear Materials*, 372(2–3):318–339.

[O'Loughlin et al., 2003] O'Loughlin, E. J., Kelly, S. D., Cook, R. E., Csencsits, R., and Kemner, K. M. (2003). Reduction of Uranium(VI) by Mixed Iron(II)/Iron(III) Hydroxide (Green Rust): Formation of UO_2 Nanoparticles. *Environmental Science & Technology*, 37(4):721–727. PMID: 12636270.

[Olsen et al., 1999] Olsen, J. S., Gerward, L., and Jiang, J. Z. (1999). On the rutile/α-PbO_2-type phase boundary of TiO_2. *Journal of Physics and Chemistry of Solids*, 60(2):229–233.

[Opel et al., 2007] Opel, K., Weiß, S., Hübener, S., Zänker, H., and Bernhard, G. (2007). Study of the solubility of amorphous and crystalline uranium dioxide by combined spectroscopic methods. *Radiochimica Acta*, 95(3):143–149.

[Packter, 1958] Packter, A. (1958). Precipitation from Supersaturated Solutions of Insoluble and Sparingly Soluble Metal Salts. Part I. The Particle Size of Crystalline Precipitates. *The Journal of Physical Chemistry*, 62(9):1025–1029.

[Palosz et al., 2004] Palosz, B., Stel'makh, S., Grzanka, E., Gierlotka, S., Pielaszek, R., Bismayer, U., Werner, S., and Palosz, W. (2004). High pressure x-ray diffraction studies on nanocrystalline materials. *Journal of Physics: Condensed Matter*, 16(5):S353.

[Park and Qian, 2010] Park, H. S. and Qian, X. (2010). Surface-Stress-Driven Lattice Contraction Effects on the Extinction Spectra of Ultrasmall Silver Nanowires. *The Journal of Physical Chemistry C*, 114(19):8741–8748.

[Patzke et al., 2002] Patzke, G. R., Krumeich, F., and Nesper, R. (2002). Oxidic Nanotubes and Nanorods—Anisotropic Modules for a Future Nanotechnology. *Angewandte Chemie International Edition*, 41(14):2446–2461.

[Peng and Peng, 2001] Peng, Z. A. and Peng, X. (2001). Mechanisms of the Shape Evolution of CdSe Nanocrystals. *Journal of the American Chemical Society*, 123(7):1389–1395.

[Piermarini et al., 1975] Piermarini, G. J., Block, S., Barnett, J. D., and Forman, R. A. (1975). Calibration of the pressure dependence of the R_1 ruby fluorescence line to 195 kbar. *Journal of Applied Physics*, 46(6):2774–2780.

[Pujol et al., 2004] Pujol, M. C., Idiri, M., Havela, L., Heathman, S., and Spino, J. (2004). Bulk and Young's modulus of doped UO_2 by synchrotron diffraction under high pressure and Knoop indentation. *Journal of Nuclear Materials*, 324(2-3):189 – 197.

[Qadri et al., 1996] Qadri, S. B., Yang, J., Ratna, B. R., Skelton, E. F., and Hu, J. Z. (1996). Pressure induced structural transitions in nanometer size particles of pbs. *Applied Physics Letters*, 69(15):2205–2207.

[Qi et al., 2002] Qi, W. H., Wang, M. P., and Su, Y. C. (2002). Size effect on the lattice parameters of nanoparticles. *Journal of Materials Science Letters*, 21:877–878. 10.1023/A:1015778729898.

[Qu et al., 2001] Qu, L., Peng, Z. A., and Peng, X. (2001). Alternative Routes toward High Quality CdSe Nanocrystals. *Nano Letters*, 1(6):333–337.

[Raghavan et al., 1998] Raghavan, S., Wang, H., Dinwiddie, R. B., Porter, W. D., and Mayo, M. J. (1998). The effect of grain size, porosity and yttria content on the thermal conductivity of nanocrystalline zirconia. *Scripta Materialia*, 39(8):1119–1125.

[Rai et al., 2003] Rai, D., Yui, M., and Moore, D. A. (2003). Solubility and Solubility Product at 22 °C of UO_2(c) Precipitated from Aqueous U(IV) Solutions. *Journal of Solution Chemistry*, 32:1–17.

[Ravel and Newville, 2005] Ravel, B. and Newville, M. (2005). ATHENA, ARTEMIS, HEPHAESTUS: data analysis for X-ray absorption spectroscopy using IFEFFIT. *J. Synchrotron Radiat.*, 12:537–541.

[Rehr et al., 1998] Rehr, J. J., Ankudinov, A., and Zabinsky, S. I. (1998). New developments in NEXAFS/EXAFS theory. *Catalysis Today*, 39(4):263–269.

[Rekhi et al., 2001] Rekhi, S., Saxena, S. K., and Lazor, P. (2001). High-pressure Raman study on nanocrystalline CeO_2. *Journal of Applied Physics*, 89(5):2968–2971.

[Rodríguez-Carvajal, 1993] Rodríguez-Carvajal, J. (1993). Recent advances in magnetic structure determination by neutron powder diffraction. *Physica B: Condensed Matter*, 192(1–2):55–69.

[Ronchi et al., 1999] Ronchi, C., Heinz, W., Musella, M., Selfslag, R., and Sheindlin, M. (1999). A Universal Laser-Pulse Apparatus for Thermophysical Measurements in Refractory Materials at Very High Temperatures. *International Journal of Thermophysics*, 20(3):987–996.

[Ronchi and Hiernaut, 1996] Ronchi, C. and Hiernaut, J. P. (1996). Experimental measurement of pre-melting and melting of thorium dioxide. *Journal of Alloys and Compounds*, 240(1–2):179–185.

[Ronchi et al., 2004] Ronchi, C., Sheindlin, M., Staicu, D., and Kinoshita, M. (2004). Effect of burn-up on the thermal conductivity of uranium dioxide up to 100.000 $MWdt^{-1}$. *Journal of Nuclear Materials*, 327(1):58 – 76.

[Rondinella and Wiss, 2010] Rondinella, V. V. and Wiss, T. (2010). The high burn-up structure in nuclear fuel. *Mater. Today*, (13):24–32.

[Rothe et al., 2012] Rothe, J., Butorin, S., Dardenne, K., Denecke, M. A., Kienzler, B., Loble, M., Metz, V., Seibert, A., Steppert, M., Vitova, T., Walther, C., and Geckeis, H. (2012). The INE-Beamline for actinide science at ANKA. *Review of Scientific Instruments*, 83(4):043105.

[Rousseau et al., 2002] Rousseau, G., Fattahi, M., Grambow, B., Boucher, F., and Ouvrard, G. (2002). Coprecipitation of thorium with UO_2. *Radiochimica Acta*, 90(9-11_2002):523–527.

[Rousseau et al., 2006] Rousseau, G., Fattahi, M., Grambow, B., Boucher, F., and Ouvrard, G. (2006). Coprecipitation of thorium and lanthanum with $UO_{2+x(s)}$ as host phase. *Radiochimica Acta*, 94(9-11):517–522.

[Rousseau et al., 2009] Rousseau, G., Fattahi, M., Grambow, B., Desgranges, L., Boucher, F., Ouvrard, G., Millot, N., and Nièpce, J. (2009). Synthesis and characterization of nanometric powders of UO_{2+x}, $(Th,U)O_{2+x}$ and $(La,U)O_{2+x}$. *Journal of Solid State Chemistry*, 182(10):2591 – 2597.

[Rupp et al., 2006] Rupp, J. L. M., Infortuna, A., and Gauckler, L. J. (2006). Microstrain and self-limited grain growth in nanocrystalline ceria ceramics. *Acta Materialia*, 54(7):1721–1730.

[Ryan and Rai, 1983] Ryan, J. L. and Rai, D. (1983). The solubility of uranium(IV) hydrous oxide in sodium hydroxide solutions under reducing conditions. *Polyhedron*, 2(9):947 – 952.

[Sabioni et al., 1998] Sabioni, A. C. S., Ferraz, W. B., and Millot, F. (1998). First study of uranium self-diffusion in UO_2 by SIMS. *Journal of Nuclear Materials*, 257(2):180–184.

[Sailaja et al., 2002] Sailaja, B. B. V., Kebede, T., Raju, G. S., and Rao, M. S. P. (2002). Thermal decomposition of ammonium dioxodiaquaperoxyoxalatouranate(VI) hydrate. *Thermochimica Acta*, 386(1):51–57.

[Santa-Cruz, 2009] Santa-Cruz, H. (2009). *Processing and Properties of Macroporous Nanocrystalline Yttria-Stabilised Zirconia Ceramics*. PhD thesis, UNIVERSITÄT BREMEN.

[Sarig et al., 1978] Sarig, S., Eidelman, N., Glasner, A., and Epstein, J. A. (1978). The effect of supersaturation on the crystal characteristics of potassium chloride. *Journal of Chemical Technology and Biotechnology*, 28(10):663–667.

[Sasajima et al., 2010] Sasajima, H., Sugiyama, T., Chuto, T., Nagase, F., Nakamura, T., and Fuketa, T. (2010). Identification of radial position of fission gas release in high burn-up fuel pellets under RIA conditions. *Journal of Nuclear Science and Technology*, 47(2):202 – 210.

[Sherwood, 2001] Sherwood, J. N. (2001). Influence of mechanical stress on the growth of crystals. pages 9–17.

[Solliard and Flueli, 1985] Solliard, C. and Flueli, M. (1985). Surface stress and size effect on the lattice parameter in small particles of gold and platinum. *Surface Science*, 156, Part 1(0):487–494.

[Sonoda et al., 2002] Sonoda, T., Kinoshita, M., Ray, I., Wiss, T., Thiele, H., Pellottiero, D., Rondinella, V., and Matzke, H. (2002). Transmission electron microscopy observation on irradiation-induced microstructural evolution in high burn-up UO_2 disk fuel. *Nuclear Instruments and Methods in Physics Research Section B: Beam Interactions with Materials and Atoms*, 191(1–4):622–628.

[Spanier et al., 2001] Spanier, J. E., Robinson, R. D., Zhang, F., Chan, S.-W., and Herman, I. P. (2001). Size-dependent properties of CeO_{2-y} nanoparticles as studied by Raman scattering. *Physical Review B*, 64(24):245407.

[Spino et al., 2003] Spino, J., Cobos-Sabate, J., and Rousseau, F. (2003). Room-temperature microindentation behaviour of LWR-fuels, part 1: fuel microhardness. *Journal of Nuclear Materials*, 322(2-3):204 – 216.

[Spino et al., 2008] Spino, J., Cruz, H. S., Birtcher, R., Ferrero, C., Pierritz, R., and Fernández, A. (Sept. 2008). Developments at ITU towards a high-performance, gas-retentive and PCI-resistant nanocrystalline UO_2-fuel. In *Workshop on Radiation Stability of Complex Microstructures. Santa Fe, USA*.

[Spino and Papaioannou, 2000] Spino, J. and Papaioannou, D. (2000). Lattice parameter changes associated with the rim-structure formation in high burn-up UO_2 fuels by micro X-ray diffraction. *Journal of Nuclear Materials*, 281(2-3):146 – 162.

[Spino and Papaioannou, 2008] Spino, J. and Papaioannou, D. (2008). Lattice contraction in the rim zone as controlled by recrystallization: Additional evidence. *Journal of Nuclear Materials*, 372(2–3):416–420.

[Spino et al., 2004] Spino, J., Papaioannou, D., and Glatz, J.-P. (2004). Comments on the threshold porosity for fission gas release in high burn-up fuels. *Journal of Nuclear Materials*, 328(1):67 – 70.

[Spino et al., 2012] Spino, J., Santa-Cruz, H., Jovani-Abril, R., Birtcher, R., and Ferrero, C. (2012). Bulk-nanocrystalline oxide nuclear fuels - an innovative material option for increasing fission gas retention, plasticity and radiation-tolerance. *Journal of Nuclear Materials*, 422(1–3):27 – 44.

[Spino et al., 1996] Spino, J., Vennix, K., and Coquerelle, M. (1996). Detailed characterisation of the rim microstructure in PWR fuels in the burn-up range 40-67 GWd/tM. *Journal of Nuclear Materials*, 231(3):179 – 190.

[Staicu, 2007] Staicu, D. (2007). Thermal diffusivity of irradiated MATINA inert matrices (MgO, Al_2O_3 and $MgAl_2O_4$). *Joint Research Centre, Institute for Transuranium Elements, Materials Research Unit*, JRC-ITU-TPW-2007/10.

[Stehle et al., 1975] Stehle, H., Assmann, H., and Wunderlich, F. (1975). Uranium dioxide properties for LWR fuel rods. *Nuclear Engineering and Design*, 33(2):230–260.

[Sui and Lu, 1995] Sui, M. L. and Lu, K. (1995). Thermal expansion behavior of nanocrystalline Ni-P alloys of different grain sizes. *Nanostructured Materials*, 6(5–8):651–654.

[Sun et al., 1999] Sun, C. Q., Sun, X. W., Gong, H. Q., Huang, H., Ye, H., Jin, D., and Hing, P. (1999). Frequency shift in the photoluminescence of nanometric SiO_x: surface bond contraction and oxidation. *Journal of Physics: Condensed Matter*, 11(48):L547.

[Suzuki et al., 2006] Suzuki, T., Abdelouas, A., Grambow, B., Mennecart, T., and Blondiaux, G. (2006). Oxidation and dissolution rates of UO_2(s) in carbonate-rich solutions under external alpha irradiation and initially reducing conditions. *Radiochimica Acta*, 94(9-11):567–573.

[Suzuki et al., 2002] Suzuki, Y., Kelly, S. D., Kemner, K. M., and Banfield, J. F. (2002). Radionuclide contamination: Nanometre-size products of uranium bioreduction. *Nature*, 419(6903):134–134.

[Swam, 1997] Swam, L. F. P. V. (Nov. 1997). Nuclear fuel pellet. *US Patent 5991354*.

[The energy net, 2012] The energy net (2012). The Nuclear Fuel Cycle. *http://www.energy-net.org/01NUKE/NUKE-14.HTM*.

[Tolbert and Alivisatos, 1995] Tolbert, S. H. and Alivisatos, A. P. (1995). High-Pressure Structural Transformations in Semiconductor Nanocrystals. *Annual Review of Physical Chemistry*, 46(1):595–626.

[Tolbert et al., 1996] Tolbert, S. H., Herhold, A. B., Brus, L. E., and Alivisatos, A. P. (1996). Pressure-Induced Structural Transformations in Si Nanocrystals: Surface and Shape Effects. *Physical Review Letters*, 76(23):4384–4387.

[Tulenko and Wang, 2008] Tulenko, J. S. and Wang, J. (2008). Improved nuclear fuel pellet design to eliminate the rim effect. *Societe Francaise d'Energie Nuclaire – International Congress on Advances in Nuclear Power Plants – ICA PP 2007. "The Nuclear Renaissance at work"*, 2:1004.

[U.S.NRC, 2012] U.S.NRC (2012). United States Nuclear Regulatory Commission. Boiling Water Reactor (BWR). *http://www.nrc.gov/reading-rm/basic-ref/students/reactors.html*.

[Vermaak and Kuhlmann-Wilsdorf, 1968] Vermaak, J. S. and Kuhlmann-Wilsdorf, D. (1968). Measurement of the average surface stress of gold as a function of temperature in the temperature range 50-985.deg. *The Journal of Physical Chemistry*, 72(12):4150–4154.

[Villegas and Shaw, 2009] Villegas, J. and Shaw, L. (2009). Nanocrystallization process and mechanism in a nickel alloy subjected to surface severe plastic deformation. *Acta Materialia*, 57(19):5782 – 5795.

[Vinet et al., 1989] Vinet, P., Rose, J. H., Ferrante, J., and Smith, J. R. (1989). Universal features of the equation of state of solids. *Journal of Physics: Condensed Matter*, 1(11):1941.

[Wagner, 1992] Wagner, M. (1992). Structure and thermodynamic properties of nanocrystalline metals. *Physical Review B*, 45(2):635–639.

[Wan et al., 2006a] Wan, J., Duan, R.-G., Gasch, M. J., and Mukherjee, A. K. (2006a). Highly Creep-Resistant Silicon Nitride/Silicon Carbide Nano–Nano Composites. *Journal of the American Ceramic Society*, 89(1):274–280.

[Wan et al., 2006b] Wan, J., Duan, R.-G., Gasch, M. J., and Mukherjee, A. K. (2006b). Methods of processing Si_3N_4/SiC nano-nano composites from polymer precursor. *Materials Science and Engineering: A*, 424(1–2):105–116.

[Wang et al., 2008] Wang, Q., Li, G.-D., Xu, S., Li, J.-X., and Chen, J.-S. (2008). Synthesis of uranium oxide nanoparticles and their catalytic performance for benzyl alcohol conversion to benzaldehyde. *J. Mater. Chem.*, 18:1146–1152.

[Wang et al., 2007] Wang, Y., Mei, Z. X., Yuan, H. T., Du, X. L., Zou, J., Jia, J. F., Xue, Q. K., and Zhang, Z. (2007). Effect of MgO in ZnO films grown on nitrided sapphires. *Journal of Crystal Growth*, 305(1):74–77.

[Wang et al., 2003] Wang, Z., Liu, Y., and Zhang, Z. (2003). *Handbook of Nanophase and Nanostructured Materials.* Number p.59. Kluwer Academic.

[Wang et al., 2002] Wang, Z., Pischedda, V., Saxena, S. K., and Lazor, P. (2002). X-ray diffraction and Raman spectroscopic study of nanocrystalline CuO under pressures. *Solid State Communications*, 121(5):275–279.

[Wang et al., 2001] Wang, Z., Saxena, S. K., Pischedda, V., Liermann, H. P., and Zha, C. S. (2001). In situ x-ray diffraction study of the pressure-induced phase transformation in nanocrystalline CeO2. *Physical Review B*, 64(1):012102–.

[Wasserman and Vermaak, 1972] Wasserman, H. J. and Vermaak, J. S. (1972). On the determination of the surface stress of copper and platinum. *Surface Science*, 32(1):168–174.

[Watteau et al., 2001] Watteau, M., Estève, B., Güldner, R., and Hoffman., R. (2001). Framatome ANP Extended Burnup Experience and Views on LWR Fuels. World Nuclear Association, Annual Symposium.

[Wei et al., 2008] Wei, X., Xu, G., Ren, Z., Wang, Y., Shen, G., and Han, G. (2008). Size-controlled synthesis of $BaTiO_3$ nanocrystals via a hydrothermal route. *Materials Letters*, 62(21–22):3666–3669.

[Wei et al., 2007] Wei, Z., Xia, T., Ma, J., Feng, W., Dai, J., Wang, Q., and Yan, P. (2007). Investigation of the lattice expansion for ni nanoparticles. *Materials Characterization*, 58(10):1019–1024.

[Willis et al., 2007] Willis, A. L., Chen, Z., He, J., Zhu, Y., Turro, N. J., and O'Brien, S. (2007). Metal Acetylacetonates as General Precursors for the Synthesis of Early Transition Metal Oxide Nanomaterials. *Journal of Nanomaterials*, 2007.

[Wu et al., 2008] Wu, D., Wu, X., Lv, Y., and Wang, H. (2008). Influence of solubility on the particle size of fluorides crystalline precipitated from aqueous solutions. *Materials Letters*, 62(17–18):3003–3006.

[Wu, 2008] Wu, H. (2008). *Inorganic Colloidal Nanocrystals: Synthesis and Bioapplications.* PhD thesis, UNIVERSITY OF FLORIDA.

[Wu et al., 2006] Wu, H., Yang, Y., and Cao, Y. C. (2006). Synthesis of Colloidal Uranium,àíDioxide Nanocrystals. *Journal of the American Chemical Society*, 128(51):16522–16523. PMID: 17177400.

[Wu et al., 2004] Wu, L., Wiesmann, H. J., Moodenbaugh, A. R., Klie, R. F., Zhu, Y., Welch, D. O., and Suenaga, M. (2004). Oxidation state and lattice expansion of CeO_{2-x} nanoparticles as a function of particle size. *Physical Review B*, 69(12):125415.

[Yongvanich et al., 2010] Yongvanich, N., Visuttipitukkul, P., Leksuma, P., Vutcharaammat, V., and Sangwanpanit, P. (2010). Sinterability and microstructure of bi-added sno2 nanomaterials Sinterability and Microstructure of Bi-Added SnO_2 Nanomaterials by Precipitation Method. *Journal of Metals, Materials and Minerals*, 20(3):67–72.

[Young and Cutler, 1970] Young, W. S. and Cutler, I. B. (1970). Initial Sintering with Constant Rates of Heating. *Journal of the American Ceramic Society*, 53(12):659–663.

[Yu et al., 2007] Yu, S., Sun, C.-J., Chow, G.-M., and Koch, C. (2007). *Chemical Synthesis of Nanostructured Particles and Films. Nanostructured Materials - Processing, Properties, and Applications (2nd Edition)*, volume Part I - Chapter 1. William Andrew Publishing.

[Zhang et al., 2007] Zhang, J., Zhao, Y., and Palosz, B. (2007). Comparative studies of compressibility between nanocrystalline and bulk nickel. *Applied Physics Letters*, 90(4):043112.

[Zhang et al., 1999] Zhang, W., Bao, X., Guo, X., and Wang, X. (1999). A high,Äêresolution solid,Äêstate NMR study on nano,Äêstructured HZSM,Äê5 zeolite. 60(1-2):89–94.

[Zhao et al., 2006] Zhao, S.-J., Albe, K., and Hahn, H. (2006). Grain size dependence of the bulk modulus of nanocrystalline nickel. *Scripta Materialia*, 55(5):473–476.

[Zhao et al., 2001] Zhao, Y. H., Sheng, H. W., and Lu, K. (2001). Microstructure evolution and thermal properties in nanocrystalline Fe during mechanical attrition. *Acta Materialia*, 49(2):365–375.

[Zhong et al., 2005] Zhong, L., Liu, C., Zachara, J. M., Kennedy, D. W., Szecsody, J. E., and Wood, B. (2005). Oxidative Remobilization of Biogenic Uranium(IV) Precipitates: effects of iron (II) and pH. *J. Environ. Qual.*, 34:1763 – 1771.

[Zumstein and Rousseau, 1989] Zumstein, R. C. and Rousseau, R. W. (1989). Agglomeration of copper sulfate pentahydrate crystals within well-mixed crystallizers. *Chemical Engineering Science*, 44(10):2149–2155.

[Zvoriste-Walters et al., 2013] Zvoriste-Walters, C. E., Heathman, S., Jovani-Abril, R., Spino, J. L., Janssen, A., and Caciuffo, R. (2013). Crystal size effect on the compressibility of nano-crystalline uranium dioxide. *Journal of Nuclear Materials*, 435(1–3):123–127.